von Karman Institute for Fluid Dynamics
Lecture Series 1998-03

29th Computational Fluid Dynamics

Feb. 23-27, 1998

Gas-Kinetic Schemes for Unsteady Compressible Flow Simulations

Kun Xu

The Hong Kong University of Science and Technology
Clear Water Bay, Kowloon, Hong Kong

Gas-Kinetic Schemes for Unsteady Compressible Flow Simulations

ABSTRACT

The development of gas-kinetic methods for compressible flow simulations have attracted much attention and become mature in the past few years. The gas-kinetic scheme not only gives accurate and robust numerical solutions for the unsteady compressible Euler and Navier-Stokes equations, but also provides a new tool to understand the underlying physical models for other shock capturing schemes, such as Flux Vector Splitting (FVS), Flux Difference Splitting (FDS) and Central Schemes. In this lecture, the BGK method based on the gas-kinetic Bhatnagar-Gross-Krook (BGK) model of the approximate Boltzmann equation will be fully analyzed, and all assumptions and approximations related to the numerical discretizations are justified by physical reasons. At the same time, a large number of numerical test cases are included.

Any finite volume shock capturing scheme basically solves a local Initial Value Problem (IVP). The accuracy, efficiency and robustness of the scheme depends on:
1. How close the initially reconstructed flow condition is to physical reality.
2. Whether the governing equations can describe all physical situations.
3. How accurately the IVP is solved.

We have to analyze any scheme in terms of the above three aspects. In this lecture, as a first attempt, from the discretized numerical schemes, we are going to analyze the real governing equations for the FVS and FDS schemes, from which the advantages and weaknesses of each approximation are clearly observed. The comparison between the gas-kinetic scheme and the Godunov method will also be presented. It is concluded that the Godunov fluxes lack dissipative mechanism in the discontinuous flow regions, especially in the multidimensional case. Due to a nonzero cell size and time step, the governing equations should be able to capture both equilibrium and non-equilibrium properties of the numerical fluid. The Euler equations cannot be used to describe nonequilibrium effects, and when solved by the Godunov method, spurious solutions, such as the carbuncle phenomena and odd-even decoupling, will automatically occur. The physical explanations for these phenomena will be presented in this lecture. In a certain sense, the BGK method presented in this lecture has a more fundamental physical basis than the Godunov method for the description of numerical fluid.

The lecture is largely self-contained and some remarks are based on the author's understanding of numerical schemes. At the end, it is hoped that this lecture note could provide a useful guidance to others to understand and develop more accurate and robust schemes in the future.

Contents

ACKNOWLEDGEMENT

The author wishes to thank all his collaborators (K. Prendergast, A. Jameson, L. Martinelli, C. Kim, S.H. Lui, M. Ghidaoui, T. Tang, and J.S Hu) for making the content of this lecture note more complete, and thank many colleagues and friends (A. Harten, A. Jameson, M. Salas, W.H. Hui, D.Y. Hsieh, S.Y. Cheng, C.W. Shu, B. van Leer, E. Tadmor, S. Osher, M. Hafez, and R. Jeltsch) for providing their unforgettable help in the past years. Special thanks to S.H. Lui and W.H. Hui for their helpful discussion and great effort to make the manuscript to the current form, to C. Kim, M. Ghidaoui, S. Shao and C.K. Chu for reviewing the manuscript and giving their valuable comments, and to H. Deconinck for his invitation and providing the opportunity for the author to summarize the research the author has participated in the past years.

The research related to some topics in this lecture note is supported by the Research Grant Council of Hong Kong through DAG 96/97.SC36 and RGC 97/98.HKUST6166/97P.

Chapter 1

Introduction

The development of numerical schemes based on the gas-kinetic theory for compressible flow simulations started in the 1960s. The Chu's method [14], based on the gas-kinetic BGK model, with discretized velocity space, is one of the earliest kinetic methods used for shock tube calculations. Another kinetic scheme used in early 70's is the Beam scheme [108], which is based on the collisionless Boltzmann equation, where the equilibrium states are replaced by three "particles" or "beams". In the 1980's and 90's, many researchers have contributed to gas-kinetic schemes. A partial list includes Reitz[102], Pullin[99], Deshpande[22], Elizarova and Chetverushkin[27], Croissille and Villedieu[19], Perthame[95], Macrossan[83], Kaniel[55], Chou and Baganoff[13] and Moschett and Pullin [86]. Pullin was the first to split the Maxwellian distribution into two parts and used the complete error function to obtain the numerical fluxes. The resulting scheme was named Equilibrium Flux Method (EFM). By applying the Courant-Isaacson-Reeves (CIR) upwind technique directly to the collisionless Boltzmann equation, Mandal and Deshpande derived the same scheme, which is named Kinetic Flux Vector Splitting (KFVS)[85]. Since the name KFVS scheme is closer to the name of Flux Vector Splitting (FVS) in the shock capturing community and they have the same underlying physical assumptions, the name KFVS will be used in this lecture to refer to these schemes, which are based on the collisionless Boltzmann equation in the gas evolution stage. In the past few years, great efforts have been paid to develop and extend new gas-kinetic schemes, which include the Peculiar Velocity based Upwind (PVU) method of Raghurama Rao and Deshpande[101] and the Least Square Kinetic Upwinding Method (LSKUM) [23], and many others. Perthame developed an efficient scheme using a square or half dome function to simplify the equilibrium gas distribution function. By combining the KFVS scheme with the multidimensional upwinding techniques developed by several researchers

at the University of Michigan and von Karman Institute [20, 21], Eppard and Grossman formulated several versions of first order multidimensional gas-kinetic schemes [29].

During the same period, new gas-kinetic schemes[128, 98, 137, 136, 135, 129, 59] based on the Bhatnagar-Gross-Krook (BGK) model [5] have been developed to model the gas evolution process more precisely. Schemes of this class are named BGK-type schemes in order to distinguish them from other Boltzmann-type schemes based on the collisionless Boltzmann equation. The BGK-type schemes take into account the particle collisions in the whole gas evolution process within a time step, from which a time-dependent gas distribution function and the resulting numerical fluxes at the cell interface are obtained. This approach avoids the ambiguity of adding *ad hoc* "collisions" for the KFVS or any other FVS schemes to reduce the numerical dissipations [86, 18]. Moreover, due to its specific governing equation, the BGK method gives Navier-Stokes solutions directly in smooth regions. In the discontinuous regions, the scheme provides a delicate dissipative mechanism to get a stable and crisp shock transition. Since the gas evolution process is a relaxation process from a nonequilibrium state to an equilibrium one, the entropy condition is always satisfied by the BGK method. Due to the dissipative nature in the BGK method, rarefaction shock, carbuncle phenomena or odd-even decoupling have never been observed, although they occasionally appear in the Godunov-type schemes, even the 1st-order Godunov method [76, 100, 35]. One purpose of this lecture is to point out explicitly the relation between spurious solutions and the Godunov method, and show the necessity to use the viscous governing equations directly to develop accurate and robust schemes. The multidimensionality of the BGK scheme will also be analyzed. Recently, the BGK-type has been extended to multicomponent inhomogeneous flows [129, 63] with applications to shock bubble interaction and the study of Rayleigh-Taylor instability. At the same time, hyperbolic conservation laws with source terms have been studied using the equivalent gas-kinetic approaches [130, 131].

Since the simulation of unsteady flows is emerging as an important area of practical interest, both the robustness and accuracy of a numerical scheme become important issues. Quite often, the requirements of robustness and accuracy of a numerical scheme are in conflict with each other. The simulation of a highly compressible flow with strong shock waves and extreme expansion waves requires a numerical scheme which is capable of handling both flow features. In the past decades, upwinding schemes have become the main stream of research in the area of unsteady compressible flow calculations. Although upwinding schemes have achieved great success, there are still existing many unsolved

problems. For examples, the post-shock oscillations, carbuncle phenomena and odd-even decoupling are occasionally observed in the scheme based on the exact Riemann solver; and more problems, such as negative density and rarefaction shocks, exist for the schemes based on the approximate Riemann solvers. Since the BGK model can be used to describe the Euler, Navier-Stokes, as well as free particle transport equations, the BGK scheme presented in this lecture has a larger regime of applicability than upwinding schemes. Based on the BGK method, the underlying physical models for the Flux Vector Splitting (FVS) and Flux Difference Splitting (FDS) schemes will be constructed, and all pathological behaviors will be explained.

For any scheme, we are basically solving a local Initial Value Problem (IVP) around the cell interface. The accuracy, efficiency and robustness of the scheme depend on

1. How close the initially reconstructed flow condition is to physical reality.
2. Whether the governing equations can describe all flow situations.
3. How accurately the IVP is solved.

All these points are related to the construction of the three stages in a high-order numerical scheme, *i.e.* reconstruction, gas-evolution and projection. A good numerical scheme has to compromise among these aspects. Any inappropriate approach in one of the above three aspects will definitely lead to a failure of the scheme in certain flow situations. For example, the gas inside a numerical shock layer stays in a highly non-equilibrium state and dissipation is extremely important to translate kinetic energy into thermal energy to construct a stable numerical shock transition. However, the Godunov method uses the inviscid Euler solution in these regions. The misuse of the governing equations leads to spurious solutions, such as the odd-even decoupling. It is true that the implicit dissipation is added in the projection stage of the Godunov method. But, as analyzed in this lecture, the projection dissipation is mesh oriented. The nonhomogeneity of the projection dissipation may yield spurious solutions. In this lecture, the dynamical effects in each stage of a numerical scheme will be analyzed in detail, and the implicit dissipative mechanism in the upwinding schemes will be explicitly presented. Basically, the Euler and the Navier-Stokes equations are only approximations to physical reality, the BGK model is also an approximation of reality. Since the BGK model can be applied to a wider class of physical conditions, it is not surprising to expect that the BGK method is more robust and accurate than the Godunov method. As pointed out by Roe [107], in fact it is not correct to think of the Godunov flux as an ideal to which all other flux formulas try to approximate in an inexpensive manner. The perfect

flux function has many tasks to perform and many pitfalls to avoid. The Godunov flux, or the exact Riemann solver, can hardly avoid all these pitfalls. The BGK scheme is not only a simple alternative to the Riemann solver or any other upwinding method, it has abundant physical basis to describe the numerical fluid. We can say that the pitfalls in the Godunov method are mostly due to its governing (Euler) equations. All these attempts to modify the Godunov-type flux function in hope to get a more robust and accurate scheme are actually trying to solve some other governing equations instead of the Euler, although it is not explicitly pointed out. The BGK method in certain ways avoids these weaknesses in Godunov method because it is simply not solving the Euler equations.

The conclusion of this lecture is that it is rather pointless to keep on developing new schemes by modifying the flux functions without constructing or using new governing equations. There is no physical reason to believe that the Euler equations are the correct physical model to properly describe the "numerical" fluid in the discretized space and time. The BGK method is one of the schemes which are based on more reliable governing equations for computational fluid. It also provides abundant information about how to connect the numerics with the physics in the design of numerical schemes. It is hoped that this lecture note will not only deepen our understanding of numerical schemes from a physical point of view, but also give some guidance to future research in the CFD community.

Chapter 2

Gas-Kinetic Theory and Finite Volume Formulation

There are two ways to describe flow motion. The first one is based on macroscopic quantities, such as mass, momentum and energy densities, as well as the physical law governing these quantities, such as the Euler, Navier-Stokes or higher order approximate equations supplied by the equation of state. Another type of description comes from microscopic considerations, *i.e.* the gas kinetic theory. The fundamental quantity in this description is the particle distribution function $f(x_i, u_i, t)$, which gives the number density of molecules in the six-dimensional phase space $(x_i, u_i) = (x, y, z, u, v, w)$. The evolution equation for the gas distribution function f is the Boltzmann equation. Physically, the gas kinetic equation provides more information about the gas flow and has larger applicability than the macroscopic counterpart.

2.1 Two Descriptions of Gas Flow and Governing Equations

Before we get the relation between the Boltzmann equation and the hydrodynamic equations, let us first introduce the macroscopic description of gas flow. Hydrodynamic Equations can be described as equations for the mass, momentum and energy densities,

$$\rho(x_j, t) \quad ; \quad \rho(x_j, t) U_i(x_j, t) \quad ; \quad \frac{\rho U^2}{2} + \rho\epsilon(x_j, t), \tag{2.1}$$

where ϵ is the internal energy density, U_i is the velocity of the hydrodynamic flow, and $U^2 = U_1^2 + U_2^2 + U_3^2$ is the square of the macroscopic velocity.

The Navier-Stokes equations merely state the laws of the conservation of mass, momentum and energy, supplied with the constitutive relations, equation of state, and the definition of transport coefficients. The conservation laws for these functions can be written in the following form[68],

Equation of continuity

$$\frac{\partial \rho}{\partial t} + \frac{\partial \rho U_j}{\partial x_j} = 0, \tag{2.2}$$

Equation of momentum

$$\frac{\partial \rho U_i}{\partial t} + \frac{\partial \rho U_i U_j}{\partial x_j} = -\frac{\partial p}{\partial x_i} + \frac{\partial \sigma_{ij}}{\partial x_j} + \rho F_i \tag{2.3}$$

Equation of energy

$$\frac{\partial}{\partial t}[\frac{\rho U^2}{2} + \rho\epsilon] + \frac{\partial}{\partial x_i}[U_i(\frac{\rho U^2}{2} + \rho\epsilon + p)] = \rho F_i U_i + \frac{\partial}{\partial x_i}(\sigma_{ij}U_j - q_i). \tag{2.4}$$

The closure of the equations (2.2-2.4) is based on two hypotheses, which are

1). The existence of a local thermodynamic equilibrium. This allows us to use the second law of thermodynamics, which holds for quasi-static processes,

$$Tds = d\epsilon + pd(\frac{1}{\rho}),$$

and the empirical equation of state,

$$p = p(\rho, T) \qquad ; \qquad \epsilon = \epsilon(\rho, T),$$

where s and T are entropy density and temperature.

2). The existence of two linear dissipative relations: Newton's formula for the force of internal friction, and Fick's formula for the vector of thermal flux q_i. Newton's formula is used in generalized form for the viscous stress tensor σ_{ij}. These formulas have the form

$$\sigma_{ij} = \eta[\frac{\partial U_i}{\partial x_j} + \frac{\partial U_j}{\partial x_i} - \frac{2}{3}\delta_{ij}\frac{\partial U_k}{\partial x_k}] + \zeta\delta_{ij}\frac{\partial U_k}{\partial x_k};$$

$$q_i = -\kappa\frac{\partial T}{\partial x_i}.$$

The first relation expresses the viscous stress tensor in terms of the derivatives of the velocity, and the second links the thermal flux vector with the gradient of the temperature.

Within the framework of phenomenological theory the coefficients of viscosity η, ζ, and the coefficient of thermal conductivity κ are measured experimentally as functions of ρ and T. As a result, we have a closed set of equations for the "hydrodynamic" variables of ρ, U_i and T. In order to compare the effects from both the viscous term and the heat conduction term, a useful number is defined, which is the Prandtl number,

$$\mathrm{Pr} = \frac{\eta C_p}{\kappa},$$

where C_p is the specific heat at constant pressure. The Prandtl number is practically constant for air, and the value is 0.72 at the common temperature. From a theoretical point of view, the justification of the above Navier-Stokes equations is largely based on the kinetic theory of gases.

Another picture to describe flow motion is based on particles' motion, or the statistical description of a fluid. For example, the fluid density is defined as a collection of individual particles

$$\rho = \sum_i m n_i, \tag{2.5}$$

where m is the molecular mass and n_i is the particle number density at a certain velocity. However, due to the large number of particles in a small volume in common situations, such as $\sum_i n_i = 2.7\times 10^{19}$ moleculars in 1 cubic centimeter at 1 atmosphere and $T = 0^o$, to follow each individual particle is impossible. Instead, a continuous distribution function is used to describe the probability of particles to be located in a certain velocity interval. For the hydrodynamics purpose, n_i is approximated by a gas distribution function,

$$f(x_i, t, u_i),$$

where (x_i, t) is the location of any point in space and time, $u_i = (u, v, w)$ is particle velocity with three components in the x, y, and z directions, and the relation between n_i and f is

$$m n_i = f(x_i, t, u_i).$$

As a result, the sum in Eq.(2.5) can be replaced by the integral

$$\rho = \int\int\int f du dv dw,$$

in the particle velocity space. For molecules with internal motion, such as rotation and vibration, the distribution function f can take these internal motion into account as well through additional variables ξ_i. The dimension and formulation for ξ_i are defined below.

For monotonic gas, the internal degree of freedom N is equal to 0. For diatomic gases, under the normal pressure and temperature, N is equal to 2 which accounts for two independent rotational degrees of freedom. Equipartition principle in statistical mechanics shows that each degree of freedom shares an equal amount of energy $\frac{1}{2}kT$, where k is the Boltzmann constant and T the temperature. Then, the specific heat ratios C_v and C_p for the gases in equilibrium state have the forms

$$C_v = \frac{N+3}{2}R \quad ; \quad C_p = \frac{(N+3)+2}{2}R, \tag{2.6}$$

where $R = k/m$ is the gas constant, m is the mass of each molecule, and the 3 accounts for the molecular motion in x, y and z directions. From the above equations, we can obtain the ratio of the principal specific heats, which is commonly denoted by γ,

$$\gamma = \frac{C_p}{C_v} = \frac{(N+3)+2}{N+3}. \tag{2.7}$$

So, γ is 5/3 for monotonic gas ($N = 0$), and 7/5 for diatomic gas ($N = 2$).

The thermodynamic aspect of the Navier-Stokes equations is based on the assumption that the departure of the gas from local equilibrium state is sufficiently small. Although we do not know the real gas distribution function f exactly in the real flow situation, in classical physics we do know the corresponding equilibrium state g locally once we know the mass, momentum and energy densities. In the following we are going to define the equilibrium distribution and present all its physical properties. In order to understand the internal variable ξ_i inside the gas distribution function, let's first write down the Maxwell-Boltzmann distribution g for the equilibrium state,

$$\begin{aligned} g &= \rho(\frac{\lambda}{\pi})^{\frac{N+3}{2}} e^{-\lambda[(u_i-U_i)^2+\xi_i^2]} \\ &= \rho(\frac{\lambda}{\pi})^{\frac{N+3}{2}} e^{-\lambda[(u-U)^2+(v-V)^2+(w-W)^2+\xi_1^2+...+\xi_N^2]}, \end{aligned} \tag{2.8}$$

where $\xi_i = (\xi_1, \xi_2, ..., \xi_N)$ are the components of the internal particle velocity in N dimensions, λ is a function of temperature, molecule mass and Boltzmann constant, with the relation $\lambda = m/2kT$, ρ is the density, $U_i = (U, V, W)$ is the corresponding macroscopic flow velocity with three components in the x, y, and z directions, and (u, v, w) are the three components of the microscopic particle velocity. In the above equation, the parameters λ, U_i and ρ which determine g uniquely are functions of space and time.

Taking moments of the equilibrium state g, the mass, momentum and energy densities at any point in space and time can be obtained. For example, the macroscopic and microscopic descriptions are related by

$$\begin{pmatrix} \rho \\ \rho U_i \\ \rho\epsilon \end{pmatrix} = \int g \begin{pmatrix} 1 \\ u_i \\ \frac{1}{2}(u_i^2 + \xi^2) \end{pmatrix} dudvdwd\xi. \tag{2.9}$$

More specifically,

$$\begin{pmatrix} \rho \\ \rho U \\ \rho V \\ \rho W \\ \rho\epsilon \end{pmatrix} = \int_{-\infty}^{\infty} g \begin{pmatrix} 1 \\ u \\ v \\ w \\ \frac{1}{2}(u^2 + v^2 + w^2 + \xi_1^2 + ... + \xi_N^2) \end{pmatrix} dudvdwd\xi_1...d\xi_N, \tag{2.10}$$

from which the total energy density $\rho\epsilon$ can be expressed as

$$\rho\epsilon = \frac{1}{2}\rho(U^2 + V^2 + W^2 + \frac{N+3}{2\lambda}),$$

which includes both kinetic and thermal energy densities. The detail formulation of the integrations of the Maxwellian distribution function can be found in Appendix B. Note that Eq.(2.8) describes the gas distribution function g in 3-Dimensions and the value of N can be obtained in terms of γ from Eq.(2.7). If we re-define the internal variable ξ_i as a vector in K dimensions, in the 3-Dimensional case we have

$$K = N = \frac{-3\gamma + 5}{\gamma - 1}.$$

In this lecture, we only give 1-D and 2-D flow simulations. In these cases, the distribution function g has to be modified as follows. For 1-D gas flow, the macroscopic average velocities in y and z directions are equal to zero with $(V, W) = (0, 0)$. So, the random motion of particles in y and z directions can be included in the internal variable ξ of the molecules. As a result, the internal degree of freedom becomes $N + 2$, which is denoted again by K with the relation $K = N + 2$. The distribution function g in the 1-Dimensional case goes to

$$g = \rho(\frac{\lambda}{\pi})^{\frac{N+3}{2}} e^{-\lambda[(u-U)^2+v^2+w^2+\xi_1^2+...+\xi_N^2]} \tag{2.11}$$

$$= \rho(\frac{\lambda}{\pi})^{\frac{N+3}{2}} e^{-\lambda[(u-U)^2+(v^2+w^2+\xi_1^2+...+\xi_N^2)]}$$

$$= \rho(\frac{\lambda}{\pi})^{\frac{K+1}{2}} e^{-\lambda[(u-U)^2+\xi^2]},$$

where the dimension of ξ is K. Substitue $N = K - 2$ into Eq.(2.7), we get the relation between K and γ in the 1-D case,

$$K = \frac{3-\gamma}{\gamma-1}.$$

For example, for diatomic gas with $N = 2$ and $\gamma = 1.4$, K is equal to 4, and the total energy density goes to

$$\rho\epsilon = \frac{1}{2}\rho(U^2 + \frac{K+1}{2\lambda}).$$

In 2-Dimensional flow calculations, K is equal to $N+1$, and the equilibrium distribution function is

$$g = \rho(\frac{\lambda}{\pi})^{\frac{N+3}{2}} e^{-\lambda[(u-U)^2+(v-V)^2+w^2+\xi_1^2+...+\xi_N^2]} \tag{2.12}$$

$$= \rho(\frac{\lambda}{\pi})^{\frac{K+2}{2}} e^{-\lambda[(u-U)^2+(v-V)^2+\xi^2]}.$$

Then, the relation between γ and K becomes

$$K = \frac{4-2\gamma}{\gamma-1}.$$

For diatomic gas, K is equal to 3 in the 2-D case and the total energy density becomes

$$\rho\epsilon = \frac{1}{2}\rho(U^2 + V^2 + \frac{K+2}{2\lambda}).$$

In all cases from the 1-D to 3-D, the pressure p is related to ρ and λ through the following relation,

$$p = nkT = \frac{\rho}{m}k\frac{m}{2k\lambda} = \frac{\rho}{2\lambda},$$

where n is the particle number density, k is the Boltzmann constant, and m is the molecule mass. Note that the pressure is independent of the internal degree of freedom N.

Due to the unique format of the equilibrium distribution function g in classical statistical physics, at each point in space and time, there is a one to one correspondence between g and the macroscopic densities, *e.g.* mass, momentum and energy. So, from macroscopic flow variables at any point in space and time, we can construct an unique equilibrium state. However, in real physical situation, gas does not necessarily stay in the Local Thermodynamic Equilibrium (LTE) state, such as gas inside a shock or boundary layer, even though we can still construct a local equilibrium state there from the corresponding macroscopic flow variables. Usually, we do not know the explicit form of the gas distribution function f in extremely dissipative flow regions, such as that inside a strong shock wave[1]. What we know is the time evolution of f, the so-called the Boltzmann Equation,

$$f_t + u_i f_{x_i} + a_i f_{u_i} = Q(f, f). \tag{2.13}$$

Here f is the real gas distribution function, a_i is the external force term acting on the particle in i-th direction, and $Q(f, f)$ is the collision operator. From the physical constraints of the conservation of mass, momentum and energy during particle collisions, the following compatibility condition has to be satisfied,

$$\int \psi_\alpha Q(f, f) d\Xi = 0, \tag{2.14}$$

where $d\Xi = dudvdwd\xi_1 d\xi_2 ... d\xi_K$ and $\psi_\alpha = (1, u, v, w, \frac{1}{2}(u^2 + v^2 + w^2 + \xi^2))^T$. For convenience, the following notations will be used,

$$\xi^2 = \xi_1^2 + \xi_2^2 + ... + \xi_K^2 \qquad ; \qquad d\xi = d\xi_1 d\xi_2 ... d\xi_K.$$

The gas kinetic theory suggests that the Navier-Stokes equations are valid if the length scale Δ of the flow is much larger than the mean free path $\bar{l}$ of the molecules, i.e.

$$K_n = \frac{\bar{l}}{\Delta} \ll 1,$$

where K_n is the Knudsen number. Since shock waves and boundary layers are different physical phenomena, the characteristic length scales will be different. For example, in a boundary layer, the significant length scale is the thickness of the boundary layer,

$$\Delta \sim \frac{L}{\mathrm{Re}^{1/2}},$$

[1]We should always be aware of the differences between the local equilibrium state g and the real gas distribution function f in different flow situations.

where $\mathrm{Re} = UL/\nu$ is the Reynolds number, $\nu = \eta/\rho$ is the kinematic viscosity coefficient, U is the upstream velocity, and L is the typical scale of the problem, *e.g.* the length of the flat plate. Since the mean free path of the particle can be approximated as[140],

$$\bar{l} = \frac{\nu}{c}(\frac{\pi\gamma}{2})^{1/2}, \tag{2.15}$$

where c is the speed of sound, the condition for the validity of the Navier-Stokes equations becomes

$$K_n \sim \frac{M}{\mathrm{Re}^{1/2}} \ll 1,$$

where $M = U/c$ is the Mach number. On the other hand, for a shock wave, the thickness of a shock front is,

$$\Delta \sim L/\mathrm{Re},$$

and the condition for the validity of the Navier-Stokes equations goes to

$$K_n \sim M \ll 1, \tag{2.16}$$

which means that the shock strength cannot be extremely high. Note that the physical shock thickness is usually on the order of particle mean free path[2].

Assuming further that the spatial and temporal variations of the distribution function f are small on the scale of the mean free path and the mean time interval between collisions, it is possible to find the first order approximations to the viscous stress tensor and the heat flux from the Boltzmann equation, which are in agreement with the Navier-Stokes equations. It is also possible to obtain the exact format for η, ζ and κ in the Navier-Stokes equations, in particular to show that $\zeta = 0$ for a monatomic gas[62]. Thus the Navier-Stokes equations may be regarded as the leading term in an asymptotic expansion of the full Boltzmann equation in the limit of $K_n \simeq 0$. From the Boltzmann equation, the quantities ν and κ can be derived as functions of the basic quantities describing the molecules [10]. For example, the viscous stress σ_{ij} and the heat flux q_i can be obtained from the gas distribution function f, such that

$$\sigma_{ij} = -(\int (u_i - U_i)(u_j - U_j) f du dv dw d\xi - p\delta_{ij}),$$

[2]In numerical simulations, the numerical shock thickness is usually on the order of cell size, which is equivalent to the mean free path for the numerical fluid in discontinuous regions being the cell size $\bar{l} \sim \Delta x$, instead of the physical mean free path $\bar{l}$ (Eq.(2.15)) in the real fluid.

and

$$q_i = \frac{1}{2}\int (u_i - U_i)\left((u-U)^2 + (v-V)^2 + (w-W)^2 + \xi^2\right) f du dv dw d\xi, \qquad (2.17)$$

where p is the local pressure. The viscous stress σ_{ij} and heat conducting q_i terms go to zero if and only if $f = g$ for the flow in equilibrium state.

Remark(2.1)

In the Boltzmann equation (2.13), the advection term on the left hand side always drives f away from local equilibrium distribution; the collision term on the right hand side $Q(f,f)$ pushes f back to equilibrium. Although, $Q(f,f)$ does not change the local mass, momentum and energy, it does re-distribute particles in the phase space (u_i, ξ), and subsequently change the transport coefficients of the particle system, *e.g.* viscosity and heat-conductivity. The real flow evolution is governed by the competition and balance between the convection and collision terms. As analyzed in the next chapter, the projection stage for the construction of constant states inside each numerical cell can be physically approximated as a process governed by the reduced Boltzmann equation $f_t = Q(f,f)$, where the mass, momentum and energy are conserved in the collisional process due to $\int Q(f,f)\psi_\alpha du dv dw d\xi = 0$. In other words, the collision term does not change the total energy, but it does re-distribute the energy between kinetic and thermal ones.

Remark(2.2)

For any shock capturing method, the numerical shock region usually spans over a few mesh points. So, the mean free path of the "numerical fluid" in these regions, which is proportional to the shock thickness, is on the order of the cell size, *i.e.* $\bar{l} \sim \Delta x$. As a result, the numerics amplifies the thickness of shock layer, and Eq.(2.15) requires that the artificial viscosity coefficient is on the order of $\nu \sim \Delta x$. The BGK method, presented in this lecture, could consistently capture the amplified numerical shock region from the controllable particle collision time τ, which also ranges from the physical one to the numerical one $\tau \sim \Delta t$, where Δt is the time step. The robustness and accuracy of the BGK method is mainly due to its ability to capture both equilibrium and nonequilibrium gas flow.

2.2 Bhatnagar-Gross-Krook (BGK) Model of the Boltzmann Equation

One of the main functions of the particle collision term is to drive the gas distribution function f back to the equilibrium state g corresponding to the local values of $\rho, \rho U_i$ and $\rho\epsilon$. The collision theory assumes that during a time dt, a fraction of dt/τ of molecules in a given small volume undergoes collision, where τ is the average time interval between successive particle collisions for the same particle. The collision term in the BGK model alters the velocity-distribution function from f to g. This is equivalent to assuming that the rate of changes df/dt of f due to collisions is $-(f-g)/\tau$, so the Boltzmann equation without external forcing term becomes [5],

$$\frac{\partial f}{\partial t} + u_i \frac{\partial f}{\partial x_i} = -\frac{f-g}{\tau}. \tag{2.18}$$

At the same time, due to the mass, momentum and energy conservation in particle collisions, the collision term $(g-f)/\tau$ satisfies the compatibility condition,

$$\int \frac{g-f}{\tau} \psi_\alpha d\Xi = 0, \tag{2.19}$$

where $d\Xi = dudvdwd\xi$ and $\psi_\alpha = (1, u_i, \frac{1}{2}(u_i^2 + \xi^2))^T$. Eq.(2.18) is a nonlinear integro-differential equation, since the distribution function f appears in a nonlinear fashion in g, where $\rho, \rho U_i, \rho\epsilon$ for the determination of g are integrals of the function f. The above BGK model coincides in form with the equations in the theory of relaxation processes and is therefore sometimes called the relaxation model.

If τ is a local constant, Eq.(2.18) may be written in integral form[62],

$$f(x_i, t, u_i, \xi) = \frac{1}{\tau}\int_{t_0}^{t} g(x_i - u_i(t-t'), t', u_i, \xi) e^{-(t-t')/\tau} dt' + e^{-(t-t_0)/\tau} f_0(x_i - u_i(t-t_0), t_0, u_i, \xi), \tag{2.20}$$

where f_0 is the real gas distribution function f at t_0, and g is the equilibrium state in (x, t). As a special case, we examine a gas whose state at time t_0 is described by a gas distribution function $f(x_i, t_0)$, which does not depend on the spatial coordinates. It follows from the conservation laws that the mass ρ, momentum ρU_i and energy $\rho\epsilon$ are constant in space and time and nothing will change macroscopically. Then, the corresponding equilibrium state g is a constant in space and time. From Eq.(2.20), we

have

$$f(x_i,t) = (1 - e^{-(t-t_0)/\tau})g + e^{-(t-t_0)/\tau} f(x_i,t_0). \tag{2.21}$$

Thus, the distribution function tends to the equilibrium state g exponentially, with a characteristic relaxation time τ equals to the time interval between collisions. For example, the denser the gas is, the faster the equilibrium is attained. From this example, we can observe that the gas-kinetic description provides more information than the macroscopic descriptions. Although, all macroscopic quantities are homogeneous and time independent, the particle distribution actually is a function of time. Consequently, the dissipative property of the gas system is also changing with time. The evolution from f to g is a process of increasing of entropy. So, the dissipative character in this gas system is a function of time.

The detail derivation from the BGK model to the Navier-Stokes equations is given in Appendix A. A similar derivation is given in [125]. The explicit expressions for the coefficients η , ζ and κ in the Navier-Stokes equations can be obtained. Due to the fact that all molecules, regardless of the velocities, have the same particle collision time τ in the BGK model, the BGK equation only gives the Navier-Stokes equations with a fixed Prandtl number which is equal to 1. For a state close to equilibrium, Eq.(2.18) confirms the obvious fact that the rate of approach to equilibrium is proportional to its deviation from the equilibrium. The validity of this assertion has been confirmed by comparison with the solution of the full Boltzmann equation [9]. In order to understand the reason why the BGK model can capture the Navier-Stokes solutions accurately, such as the laminar boundary layer, we are going to give two simple examples to illustrate the dissipative characters of the model and derive the dissipative coefficients. Because of the smallness of τ in the BGK model, in a gas whose state is not varying rapidly with time, $f - g$ will be small. Therefore, the distribution function can be written as

$$f = g - \tau \frac{\partial g}{\partial t} - \tau u_i \frac{\partial g}{\partial x_i}. \tag{2.22}$$

For a gas with uniform density and temperature, streaming along the x-direction with velocities U which is a function of z alone (see part (a) in Fig.(2.1)), Eq.(2.22) goes to

$$f = g - \tau w \frac{\partial U}{\partial z} \frac{\partial g}{\partial U}. \tag{2.23}$$

According to the definition and the condition $W = 0$, the viscous stress in the x-direction

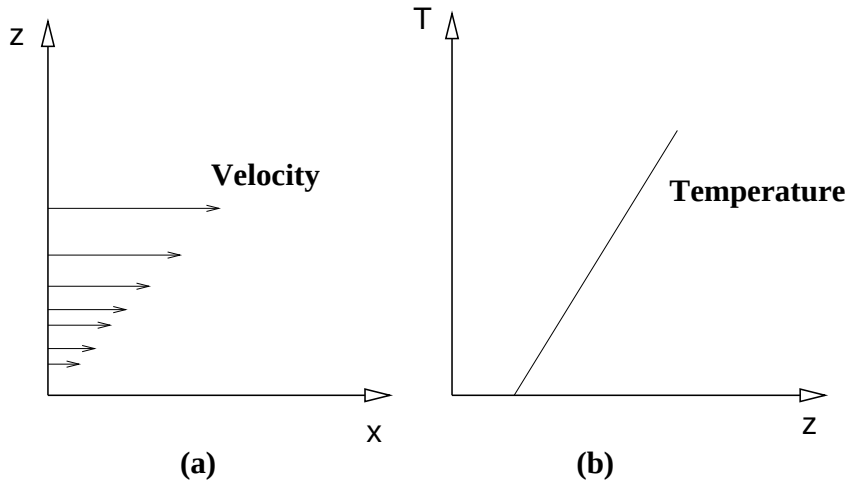

Figure 2.1: Linearly distributed steady velocity and temperature field.

across a plane $z =$ constant is

$$\sigma_{xz} = -\int (u-U) w f du dv dw d\xi. \tag{2.24}$$

Substitute Eq.(2.23) into (2.24), with the formation of equilibrium state

$$g = \rho(\frac{\lambda}{\pi})^{(K+3)/2} e^{-\lambda((u-U)^2+v^2+w^2+\xi^2)}, \tag{2.25}$$

and the definition $\sigma_{xz} = \eta \partial U/\partial z$ in the Navier-Stokes equations, we have

$$\begin{aligned} \eta &= \tau \int (u-U) w^2 \frac{\partial g}{\partial U} du dv dw d\xi \\ &= \tau \frac{\partial}{\partial U} \left(\int (u-U) w^2 g du dv dw d\xi \right) + \tau \int w^2 g du dv dw d\xi, \end{aligned} \tag{2.26}$$

where the first integral in the bracket vanishes, and the second term is equal to the pressure p. So, we have

$$\eta = \tau p, \tag{2.27}$$

which is consistent with the results in Appendix A[3].

[3]As analyzed in chapter 6, the lack of this kind of dissipative property for the shear wave in upwinding schemes based on the inviscid Euler equations, *e.g.* Godunov, Roe, Osher ...schemes, automatically lead to spurious solutions, such as carbuncle phenomena and odd-even decoupling.

Similarly, for a gas at rest and uniform in pressure, but with a temperature which is a function of z (part (b) of Fig.(2.1)), Eq.(2.22) becomes

$$f = g - \tau w \frac{\partial T}{\partial z} \frac{\partial g}{\partial T}.$$

With the equilibrium state

$$g = \rho(\frac{\lambda}{\pi})^{(K+3)/2} e^{-\lambda(u^2+v^2+w^2+\xi^2)}, \tag{2.28}$$

and the definition of heat flux $-\kappa \partial T/\partial z$ in Eq.(2.17), we have

$$\begin{aligned} \kappa &= \tau \frac{\partial}{\partial T} \int \frac{1}{2}(u^2+v^2+w^2+\xi^2) w^2 g du dv dw d\xi \qquad (2.29) \\ &= \tau \frac{\partial}{\partial T}(\frac{K+5}{2}\frac{p}{2\lambda}) \\ &= \tau \frac{\partial}{\partial T}(\frac{K+5}{2}\frac{pkT}{m}) \\ &= \tau \frac{K+5}{2}\frac{pk}{m}, \end{aligned}$$

where $\lambda = m/2kT$ is used in the above equation. The heat conducting coefficient obtained in this simple case is identical to the result from a rigorous proof (Appendix A). Further, from the above expressions η and κ, we can get that the Prandtl number for the BGK model,

$$\Pr = \frac{\eta C_p}{\kappa} = 1,$$

where $R = k/m$ and $C_p = (K+5)R/2$ (Eq.(2.6)) have been used. In conclusion, in regions where the flow is smooth, the BGK model can recover the Navier-Stokes equations exactly with $\Pr = 1$. Since in the continuum regime the behavior of the fluid depends very little on the nature of individual particles, the most important properties are: conservation, symmetry (Galilean invariant) and dissipation. The BGK model satisfies all these requirements [71].

The BGK model has been applied to a number of problems of nonequilibrium flow. Two successful applications of the BGK model are the study of shock structure and linearized Couette flow. One is related to discontinuous flow and the other to a continuous one. The internal structure of shock waves has been studied by various investigators since

the work of Rankine in 1870. The study of this problem has the distinct advantage that it does not involve the complicating effect of molecular interaction with solid surfaces. Although the structure of shock waves can be obtained theoretically from the solution of the original Boltzmann equation, an exact solution valid for a general range of Mach numbers has never been obtained. However, the shock structure obtained from the BGK model [72] provides useful information both to shock physics, and to the capturing of numerical shock structure in shock capturing schemes.

For any shock capturing scheme, the numerical shock wave will not have zero thickness as described by the Euler equations. Density, velocity, temperature, and other quantities of interest vary continuously in a few numerical cells through the wave. Since the Chapman-Enskog theory, which leads from the Boltzmann equation to the Navier-Stokes equations, depends on the continuous assumption and the slight departure of the gas distribution function from the local equilibrium state, theoretically the Navier-Stokes equations could only give an accurate description of weak shock structure. If there is a similarity between the numerical shock and the physical shock, the von Neumann and Richtmyer artificial viscosity concept based on the Navier-Stokes equations can only be applied to weak shock too. This is probably one of the direct reasons why no uniform viscous term can be found to capture all strengths of numerical shocks [91]. Thus, based on the artificial viscosity concept, in order to capture a steady and oscillation free shock transition, delicate dissipation has to be applied according to the shock strength. It is definitely a difficult problem to nail down the explicit form of dissipation. For upwinding schemes, dissipation is added mostly during the projection and reconstruction stages. Fortunately, the projection dissipation cannot simply be described by a second-order viscous term in the Navier-Stokes equations. Although, the Navier-Stokes equations can be obtained from the BGK model, in strong nonequilibrium flow regions, the BGK model is an equation more physically applicable than the Navier-Stokes equations. Therefore, as a governing equation, the BGK model provides abundant physical mechanism to construct numerical scheme for both "smooth" and "discontinuous" flow.

2.3 Entropy Condition

It is well-known that the Boltzmann equation, which is based on and derived from the reversible laws of mechanics, describes irreversible processes. For nonlinear gas system, thermodynamic irreversibility is accompanied by dissipation in the system and an

increase of entropy. The rigorous proof of entropy (H-theorem) for the Boltzmann equation can be found in [10]. In this section, only the entropy condition for the BGK model will be presented since the main part of the lecture is about the BGK model for the construction of gas-kinetic schemes.

The Boltzmann H-theorem states that if we define

$$\mathcal{H} = \int f \ln f d\Xi$$

as the entropy density (the real entropy is defined as $s = -k\mathcal{H}$), where $d\Xi = dudvdwd\xi$, and

$$\mathcal{H}_i = \int u_i f \ln f d\Xi$$

as the entropy flux in direction i, where f is the gas distribution function in the BGK model, the entropy condition implies the following inequality,

$$\frac{\partial \mathcal{H}}{\partial t} + \frac{\partial \mathcal{H}_i}{\partial x_i} \leq 0. \tag{2.30}$$

In order to prove the above inequality, let's multiply $(1 + \ln f)$ on both sides of the BGK model (2.18) and take an integration with respect to $d\Xi$,

$$\int (\frac{\partial f}{\partial t} + u_i \frac{\partial f}{\partial x_i})(1 + \ln f) d\Xi = \int \frac{g - f}{\tau}(1 + \ln f) d\Xi, \tag{2.31}$$

which gives

$$\frac{\partial}{\partial t} \int f \ln f d\Xi + \frac{\partial}{\partial x_i} \int u_i f \ln f d\Xi = \frac{1}{\tau} \int (g - f)(1 + \ln f) d\Xi. \tag{2.32}$$

From the compatibility condition (2.19), and the fact that $\ln g$ can be expressed as a sum of conservative moments of the collision term, we have

$$\int (g - f) \ln g d\Xi = 0.$$

With the definitions of $\mathcal{H}$ and $\mathcal{H}_i$, and the relations of $\int (g-f) d\Xi = 0$ and $\int (g-f) \ln g d\Xi = 0$, Eq.(2.32) goes to

$$\begin{aligned} \frac{\partial \mathcal{H}}{\partial t} + \frac{\partial \mathcal{H}_i}{\partial x_i} &= \frac{1}{\tau} \int (g - f) \ln f d\Xi \\ &= \frac{1}{\tau} \int (g - f)(\ln f - \ln g) d\Xi \\ &\leq 0. \end{aligned} \tag{2.33}$$

Therefore, it is proved that the BGK model satisfies the entropy condition, and the particle system will move towards the equilibrium state due to particle collisions.

Boltzmann's H-theorem is of basic importance because it shows that the Boltzmann equation ensures irreversibility. The entropy condition guarantees the dissipative property in the gas system. Thus, it is not surprising that most schemes based on the gas-kinetic theory satisfy the entropy condition automatically.

2.4 Gas-Kinetic Formulation for Conservation Laws

From the BGK model, most well-known viscous conservation laws can be recovered to a certain degree by selecting the appropriate equilibrium state in the BGK model. The inviscid hyperbolic system corresponds to the state with local equilibrium distribution function. In the following, some examples will be given.

Linear Advection-Diffusion Equation

The linear advection-diffusion equation in 1-D is written as

$$U_t + cU_x = \nu U_{xx}, \tag{2.34}$$

where ν is the viscosity coefficient. The above equation can be derived from the 1-D BGK model by adopting the equilibrium state,

$$g = U(\frac{\lambda}{\pi})^{1/2} e^{-\lambda(u-c)^2},$$

and the conservation constraint,

$$\int_{-\infty}^{\infty} (f - g) du = 0.$$

From the Chapman-Enskog expansion, to the first order, f is given as

$$f = g - \tau(g_t + ug_x). \tag{2.35}$$

Substitute the above equation into the BGK model and integrate with respect to u, we get

$$U_t + cU_x = \frac{\tau}{2\lambda} U_{xx} - \frac{3\tau^3}{4\lambda^2} U_{xxxx}.$$

The $4th$-order derivative in the above equation has a very nice property of stabilizing a numerical scheme [42]. Thus, if we take the collision time in the BGK model as $\tau = 2\nu\lambda$,

the advection-diffusion equation is recovered from the BGK model. As a special example, if we set $c = 0$ in the above equilibrium state g, the diffusion equation can be recovered.

Burgers' Equation

In order to get Burgers' equation,

$$U_t + UU_x = 0, \tag{2.36}$$

we need to define the equilibrium state g in the following way,

$$g = (\frac{\lambda}{\pi})^{1/2} U e^{-\lambda(u-U/2)^2}, \tag{2.37}$$

where the compatibility condition becomes

$$\int_{-\infty}^{\infty} (f - g) du = 0.$$

Shallow Water Equations

The 2-D shallow water equations are

$$\begin{array}{c} \rho_t + (\rho U)_x + (\rho V)_y = 0, \\ (\rho U)_t + (\rho U^2 + \frac{G}{2}\rho^2)_x + (\rho UV)_y = 0, \\ (\rho V)_t + (\rho VU)_x + (\rho V^2 + \frac{G}{2}\rho^2)_y = 0, \end{array} \tag{2.38}$$

where G is the gravitational constant. In order to recover the above equations, the equilibrium state g in the BGK model can be chosen as

$$g = \frac{1}{G\pi} e^{-\lambda[(u-U)^2 + (v-V)^2]}, \tag{2.39}$$

where

$$\lambda = \frac{1}{G\rho}.$$

The compatibility condition in this case is

$$\int (g - f) \begin{pmatrix} 1 \\ u \\ v \end{pmatrix} du dv = 0. \tag{2.40}$$

The Euler and Navier-Stokes Equations

For the 1-D Euler and Navier-Stokes equations, the BGK model is

$$f_t + uf_x = \frac{g-f}{\tau}, \tag{2.41}$$

and the equilibrium state g is the Maxwell-Boltzmann distribution,

$$g = \rho(\frac{\lambda}{\pi})^{\frac{K+1}{2}} e^{-\lambda((u-U)^2+\xi^2)}.$$

With the definition ψ_α ,

$$\psi_\alpha = (1, u, \frac{1}{2}(u^2+\xi^2))^T,$$

the compatibility condition between f and g is

$$\int (g-f)\psi_\alpha du d\xi = 0, \qquad\qquad \alpha = 1, 2, 3. \tag{2.42}$$

For a local equilibrium state with $f = g$, the Euler equations can be obtained by taking the moments of ψ_α to Eq.(2.41). This yields

$$\int \begin{pmatrix} 1 \\ u \\ \frac{1}{2}(u^2+\xi^2) \end{pmatrix} (g_t + ug_x) du d\xi = 0,$$

and the corresponding Euler equations are

$$\begin{pmatrix} \rho \\ \rho U \\ \frac{1}{2}\rho(U^2 + \frac{K+1}{2\lambda}) \end{pmatrix}_t + \begin{pmatrix} \rho U \\ \rho U^2 + \frac{\rho}{2\lambda} \\ \frac{1}{2}\rho(U^3 + \frac{(K+3)U}{2\lambda}) \end{pmatrix}_x = 0,$$

where the pressure p is $\rho/2\lambda$.

To first order in τ, the Chapman-Enskog expansion[62] gives

$$f = g - \tau(g_t + ug_x).$$

Taking moments of ψ_α again to the BGK equation with the new f, we get

$$\int \begin{pmatrix} 1 \\ u \\ \frac{1}{2}(u^2+\xi^2) \end{pmatrix} (g_t + ug_x) du d\xi = \tau \int \begin{pmatrix} 1 \\ u \\ \frac{1}{2}(u^2+\xi^2) \end{pmatrix} (g_{tt} + 2ug_{xt} + u^2 g_{xx}) du d\xi.$$

After integrating out all the moments, the corresponding Navier-Stokes equations can be expressed as

$$\left(\begin{array}{c}\rho\\ \rho U\\ \frac{1}{2}\rho(U^2+\frac{K+1}{2\lambda})\end{array}\right)_t+\left(\begin{array}{c}\rho U\\ \rho U^2+\frac{\rho}{2\lambda}\\ \frac{1}{2}\rho(U^3+\frac{(K+3)U}{2\lambda})\end{array}\right)_x=\tau\left(\begin{array}{c}0\\ \frac{2K}{K+1}\frac{\rho}{2\lambda}U_x\\ \frac{K+3}{4}\frac{\rho}{2\lambda}(\frac{1}{\lambda})_x+\frac{2K}{K+1}\frac{\rho}{2\lambda}UU_x\end{array}\right)_x.$$

In the 3-D case, the derivation is given in Appendix A.

2.5 Finite Volume Gas-kinetic Scheme

There are three stages in a high resolution numerical scheme: the initial reconstruction, gas evolution, and projection. In all these stages, how to correctly capture the gas evolution from the reconstructed initial condition plays a fundamental role in the determination of the quality of the scheme. The finite-volume gas-kinetic scheme for compressible flow simulations uses the Boltzmann equation as the governing equation and focuses on the evaluation of time-dependent gas distribution function f at a cell interface, from which the numerical fluxes can be computed, such as these fluxes across cell boundaries in Fig.(2.2). Since the Boltzmann equation is a scalar equation and a single distribution function f includes all information about the macroscopic flow variables as well as their transport coefficients, the schemes in two and three-dimensions can be constructed similarly. As a consequence, the 2-D BGK scheme presented in chapter 4 is probably a multidimensional method, at least in the gas evolution stage, because $\partial/\partial x$ and $\partial/\partial y$ terms in the Navier-Stokes equations are both included in the evolution of gas distribution function across a cell interface.

In the following, the 1-D finite volume scheme will be outlined. The Boltzmann equation in 1-D case can be written as

$$f_t+uf_x=Q(f,f). \tag{2.43}$$

The connection between f and macroscopic variable W is

$$W=(\rho,\rho U,\rho\epsilon)^T=\int\psi_\alpha f du d\xi,$$

and the corresponding fluxes are

$$F(W)=(F_\rho,F_{\rho U},F_{\rho\epsilon})^T=\int u\psi_\alpha f du d\xi, \tag{2.44}$$

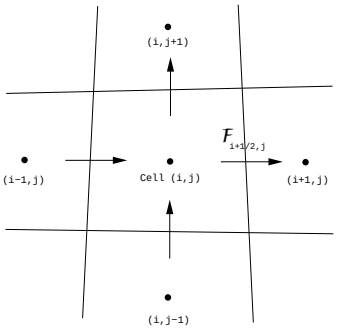

Figure 2.2: Interface fluxes by a finite volume gas-kinetic scheme

where $\psi_\alpha = (1, u, \frac{1}{2}(u^2 + \xi^2))^T$.

In order to develop a finite volume gas-kinetic scheme, take moments of ψ_α in Eq.(2.43) and integrate it with respect to $dud\xi$ in phase space, dx in a numerical cell $[x_{j-1/2}, x_{j+1/2}]$, and dt in a time step $[t^n, t^{n+1}]$,

$$\int (f_t + uf_x)\psi_\alpha dud\xi dxdt = \int Q(f, f)\psi_\alpha dud\xi dxdt,$$

from which we can get

$$W_j^{n+1} - W_j^n = \frac{1}{\Delta x}\int_{t^n}^{t^{n+1}} \Big(F_{j-1/2}(t) - F_{j+1/2}(t)\Big)\, dt + \frac{1}{\Delta x}\int_{t^n}^{t^{n+1}} \int_{x_{j-1/2}}^{x_{j+1/2}} \int Q(f, f)\psi_\alpha dud\xi dxdt.$$

Due to the compatibility condition(2.42), the term $\int Q(f, f)\psi_\alpha dud\xi$ in the above equation is precisely zero. Therefore, the flow variables can be updated according to

$$W_j^{n+1} - W_j^n = \frac{1}{\Delta x}\int_{t^n}^{t^{n+1}} \Big(F_{j-1/2}(t) - F_{j+1/2}(t)\Big)\, dt, \tag{2.45}$$

where $F_{j+1/2}$ is the numerical flux across a cell interface, and is obtained from the integration of the particle distribution function, shown in (2.44). In the 2-D and 3-D cases, similar finite volume formulation can be obtained.

The time dependent flux function across a cell interface is evaluated from the gas distribution function f which is obtained by solving the Boltzmann equation with the collision term. Although, the collision term has no direct influence on the update of

conservative variables inside each cell, as shown in Eq.(2.45), it does affect the interface flux and consequently affects the dissipative properties in the whole flow system. The BGK scheme solves the BGK model $f_t + uf_x = (g - f)/\tau$ directly for the time dependent distribution function f at a cell interface. This unsplitting scheme for the Boltzmann equation distinguishes it from Kinetic Flux Vector Splitting (KFVS) scheme, where the collisionless Boltzmann equation $f_t + uf_x = 0$ is solved in the gas evolution stage. In the following chapters, the numerical discretizations for both KFVS and BGK schemes will be presented. At the same time, the dynamical mechanism in the splitting schemes, *e.g.* the FVS and KFVS schemes, will be analyzed.

Chapter 3

Gas-Kinetic Flux Vector Splitting Method

The Euler equations are the moments of the Boltzmann equation when the velocity distribution function is a Maxwellian, and the collision term in the Boltzmann equation vanishes in this situation. The Boltzmann equation with vanishing collision term is called collisionless Boltzmann equation. Based on the collisionless Boltzmann equation, a very large number of kinetic schemes have been developed. A partial list of researchers include Sander and Prendergast (1974) [108], Pullin (1981) [99], Deshpande (1986) [22], Perthame (1992) [96], Macrossan [84], Estivalezes and Villedieu [30], Mandal and Deshpande [85], Eppard and Grossman [29], Chou and Baganoff [13], Moschetta and Pullin [86], and many others. Although the collisionless Boltzmann equation and the Euler equations have different gas dynamical property, it can still be used to approximate the Euler equations. One of the main reason is that artificial collisions have been added in the projection stage, *i.e.* the preparation of initial Maxwellian distribution functions in each time step.

3.1 Collisionless Boltzmann Equation

It is well-known that the Euler equations can be derived from the Boltzmann equation with a local equilibrium distribution function. For an equilibrium state, f is equal to the Maxwellian distribution g, the collision term $Q(f, f)$ goes to zero automatically, *i.e.* $Q(g, g) \equiv 0$. So, in 1-D case, once $f = g$ holds, the Boltzmann equation becomes

$$f_t + uf_x = 0. \tag{3.1}$$

Since there is no collision term on the right hand side of the above equation, this equation is called the collisionless Boltzmann equation[1]. With the initial condition of the gas distribution function $f_0(x,0)$ at time $t = 0$, the exact solution of the collisionless Boltzmann equation is

$$f = f_0(x - ut, t). \tag{3.2}$$

For example, for the same initial condition as the Riemann problem, two constant equilibrium states at $x \leq 0$ and $x > 0$ can be constructed,

$$\begin{aligned} f_0 &= \begin{cases} g_l, & x \leq 0 \\ g_r, & x > 0 \end{cases} \\ &= g_l(1 - \mathrm{H}(x)) + g_r \mathrm{H}(x), \end{aligned} \tag{3.3}$$

where $\mathrm{H}(x)$ is the Heaviside function. As stated in the last chapter, the equilibrium states g_l and g_r have one to one correspondence with the macroscopic flow variables. For example, in the equilibrium state g,

$$g = \rho(\frac{\lambda}{\pi})^{K+1} e^{-\lambda((u-U)^2+\xi^2)}, \tag{3.4}$$

there are 3 unknowns, ρ, U and λ, and λ can be obtained from the macroscopic variables $(\rho, \rho U, \rho\epsilon)$ through the relation

$$\lambda = \frac{K+1}{4} \frac{\rho}{\rho\epsilon - \frac{1}{2}\rho U^2}. \tag{3.5}$$

Hence, from the initial condition in Eq.(3.3), the exact solution from the collisionless Boltzmann equation is

$$f(x,t) = f_0(x - ut) = g_l(1 - \mathrm{H}(x - ut)) + g_r \mathrm{H}(x - ut). \tag{3.6}$$

Since $t > 0$, the above equation can be reformulated as

$$\begin{aligned} f(x,t) &= g_l(1 - \mathrm{H}(\frac{x}{t} - u)) + g_r \mathrm{H}(\frac{x}{t} - u) \\ &= f(\frac{x}{t}), \end{aligned} \tag{3.7}$$

[1]The collisionless Boltzmann equation itself cannot keep the initial equilibrium state in its time evolution process.

which is a similarity solution! So, similar to the Riemann solution of the Euler equations, the collisionless Boltzmann equation also provides a similarity solution for the case with two constant initial states. Although this similarity solution from the collisionless Boltzmann equation is commonly referred to as an approximate Riemann solution [41], it provides a different gas evolution picture. The scheme based on the solution (Eq.(3.7)) for the flux evaluation at a cell interface is so-called Kinetic Flux Vector Splitting (KFVS) scheme. The analysis in section(3.4) shows that the real governing equations for the KFVS scheme are different from the Euler equations. Without the help from the projection stage, *i.e.* the preparation of initial equilibrium states at the beginning of each time step, the KFVS would never approximate the Euler solutions.

Before we analyze the underlying dynamical effect in the collisionless Boltzmann equation, let's calculate the exact solutions of Eq.(3.1) under the following initial condition

$$W_0(x) = \begin{cases} (\rho_l = 1.0, \rho_l U_l = 0.0, \rho_l \epsilon_l = 2.5)\,, & x \le 0 \\ (\rho_r = 0.125, \rho_r U_r = 0.0, \rho_r \epsilon_r = 0.25), & x > 0 \end{cases} \tag{3.8}$$

from which two Maxwellians of g_l and g_r in Eq.(3.3) can be constructed. Based on the solution (3.6), the mass, momentum and energy densities at any point in space x and a fixed time t can be obtained by taking the moments of $f(x,t)$,

$$\begin{pmatrix} \rho(x,t) \\ \rho U(x,t) \\ \rho \epsilon(x,t) \end{pmatrix} = \int_{-\infty}^{\infty} f(x,t) \begin{pmatrix} 1 \\ u \\ \frac{1}{2}(u^2+\xi^2) \end{pmatrix} du d\xi. \tag{3.9}$$

The density distribution from $1st$-moment in the above equation is plotted in Fig.(3.1). The solid line refers to the exact solution from the similarity solution of the Euler equations and the $\times$ symbol is the solution from the collisionless Boltzmann equation (3.7)[2]. There are many differences between these two curves. No contact discontinuity wave is formed in the collisionless Boltzmann solution and the shock and rarefaction waves are quite smeared. This figure shows the differences between the Euler solution and the collisionless Boltzmann solution even with the same initial condition.

Remark(3.1)

It is true that *if* the flow remains in a local equilibrium state, Eq.(3.1) is the correct description of the flow motion. However, even with an initial local equilibrium state,

[2]Note that both curves are analytic solutions under the same initial condition, one is obtained from solving the Euler equations, and the other from the collisionless Boltzmann equation.

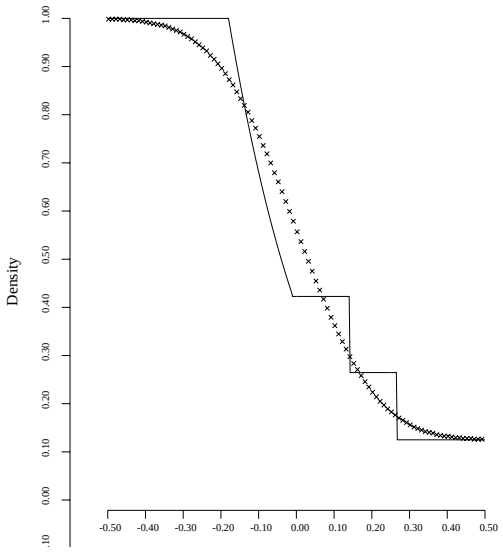

Figure 3.1: Exact Euler (solid line) and collisionless Boltzmann ($\times$ symbol) solutions for the same initial condition

the collisionless Boltzmann equation drives the gas distribution function, such as that in Eq.(3.7), away from its equilibrium assumptions. In other words, the collisionless model cannot keep the equilibrium state. Physically, the mechanism for bringing the distribution function close to a Maxwellian is the collisions suffered by the molecules of the gas, the so-called collision term in the Boltzmann equation. However, the collisionless Boltzmann equation ignores this dynamical process. Other Flux Vector Splitting (FVS) schemes using $F = F^+ + F^-$, such as Steger-Warming and van Leer [114, 123], have a similar gas evolution mechanism.

3.2 Kinetic Flux Vector Splitting Scheme

Although the KFVS scheme lacks particle collisions in the gas evolution stage, it still gives reasonable numerical solutions, which are different from particle free stream solutions. The reason is that in the projection and reconstruction stages of a numerical scheme, artificial particle collisions are introduced. In this section, the KFVS scheme is presented and a physical analysis of this scheme is given in section (3.4).

3.2.1 1st-order KFVS

The one-dimensional space is divided uniformly by numerical cells. Each cell occupies a small space $x \in [x_{j-1/2}, x_{j+1/2}]$, where $j + 1/2$ denotes the cell interface between cells j and $j + 1$, and the cell center is located at x_j. With the initial mass, momentum and

energy densities inside each cell j,

$$W_j = (\rho_j, \rho_j U_j, \rho_j \epsilon_j), \tag{3.10}$$

an equilibrium state g_j, which is

$$g_j = \rho_j (\frac{\lambda_j}{\pi})^{\frac{K+1}{2}} e^{-\lambda_j[(u-U_j)^2+\xi^2]},$$

can be obtained. For example, λ_j is given by

$$\lambda_j = \frac{K+1}{4} \frac{\rho_j}{\rho_j \epsilon_j - \frac{1}{2}\rho_j U_j^2}. \tag{3.11}$$

So, under the following initial condition around a cell interface $x_{j+1/2}$,

$$\begin{aligned} f_0(x) &= \begin{cases} g_j, & x \le x_{j+1/2} \\ g_{j+1}, & x > x_{j+1/2} \end{cases} \\ &= g_j(1 - \mathrm{H}(x - x_{j+1/2})) + g_{j+1}\mathrm{H}(x - x_{j+1/2}), \end{aligned} \tag{3.12}$$

the solution f based on the collisionless Boltzmann equation (3.1) at $x_{j+1/2}$ and time t becomes

$$f(x_{j+1/2}, t) = f_0(x - ut) \mid_{x=x_{j+1/2}} = \begin{cases} g_j, & u > 0 \\ g_{j+1}, & u < 0 \ . \end{cases} \tag{3.13}$$

From the above distribution function, the numerical fluxes for the mass, momentum and energy across the cell interface can be constructed, which are

$$\begin{aligned} F_{W,j+1/2} = \begin{pmatrix} F_\rho \\ F_{\rho U} \\ F_{\rho\epsilon} \end{pmatrix}_{j+1/2} &= \int u\psi_\alpha f(x_{j+1/2}, t) du d\xi \\ &= \int_{u>0} \int u\psi_\alpha g_j du d\xi + \int_{u<0} \int u\psi_\alpha g_{j+1} du d\xi \end{aligned} \tag{3.14}$$

where ψ_α stands for the moments $\psi_\alpha = (1, u, \frac{1}{2}(u^2 + \xi^2))^T$.

The evaluation of the moments of the equilibrium state in Eq.(3.14) is straightforward by using the recursive relations in Appendix B. In the following, the details of the numerical formulations are presented,

$$\begin{pmatrix} F_{\rho,j+1/2} \\ F_{\rho U,j+1/2} \\ F_{\rho\epsilon,j+1/2} \end{pmatrix} = \rho_j \begin{pmatrix} \frac{U_j}{2}\mathrm{erfc}(-\sqrt{\lambda_j}U_j) + \frac{1}{2}\frac{e^{-\lambda_j U_j^2}}{\sqrt{\pi\lambda_j}} \\ \left(\frac{U_j^2}{2} + \frac{1}{4\lambda_j}\right)\mathrm{erfc}(-\sqrt{\lambda_j}U_j) + \frac{U_j}{2}\frac{e^{-\lambda_j U_j^2}}{\sqrt{\pi\lambda_j}} \\ \left(\frac{U_j^3}{4} + \frac{K+3}{8\lambda_j}U_j\right)\mathrm{erfc}(-\sqrt{\lambda_j}U_j) + \left(\frac{U_j^2}{4} + \frac{K+2}{8\lambda_j}\right)\frac{e^{-\lambda_j U_j^2}}{\sqrt{\pi\lambda_j}} \end{pmatrix}$$

$$+\rho_{j+1} \begin{pmatrix} \frac{U_{j+1}}{2}\mathrm{erfc}(\sqrt{\lambda_{j+1}}U_{j+1}) - \frac{1}{2}\frac{e^{-\lambda_{j+1} U_{j+1}^2}}{\sqrt{\pi\lambda_{j+1}}} \\ \left(\frac{U_{j+1}^2}{2} + \frac{1}{4\lambda_{j+1}}\right)\mathrm{erfc}(\sqrt{\lambda_{j+1}}U_{j+1}) - \frac{U_{j+1}}{2}\frac{e^{-\lambda_{j+1} U_{j+1}^2}}{\sqrt{\pi\lambda_{j+1}}} \\ \left(\frac{U_{j+1}^3}{4} + \frac{K+3}{8\lambda_{j+1}}U_{j+1}\right)\mathrm{erfc}(\sqrt{\lambda_{j+1}}U_{j+1}) - \left(\frac{U_{j+1}^2}{4} + \frac{K+2}{8\lambda_{j+1}}\right)\frac{e^{-\lambda_{j+1} U_{j+1}^2}}{\sqrt{\pi\lambda_{j+1}}} \end{pmatrix}, \tag{3.15}$$

where the complementary error function (a special case of the incomplete gamma function) is defined by

$$\mathrm{erfc}(x) = \frac{2}{\sqrt{\pi}}\int_x^\infty e^{-t^2}dt.$$

Like sine and cosine functions, $\mathrm{erfc}(x)$, or its double precision $\mathrm{derfc}(x)$, is a given function in FORTRAN. Using the above numerical fluxes, the flow variables $\rho_j, \rho_j U_j, \rho_j \epsilon_j$ inside each cell can be updated as

$$\begin{pmatrix} \rho_j \\ \rho_j U_j \\ \rho_j \epsilon_j \end{pmatrix}^{n+1} = \begin{pmatrix} \rho_j \\ \rho_j U_j \\ \rho_j \epsilon_j \end{pmatrix}^{n} + \sigma \begin{pmatrix} F_{\rho,j-1/2} - F_{\rho,j+1/2} \\ F_{\rho U,j-1/2} - F_{\rho U,j+1/2} \\ F_{\rho\epsilon,j-1/2} - F_{\rho\epsilon,j+1/2} \end{pmatrix}, \tag{3.16}$$

where n is the step number and

$$\sigma = \frac{\Delta t}{\Delta x},$$

with Δt the stepsize in time, and Δx the mesh size in space.

Before we give a detailed numerical analysis of the KFVS method, let's first apply the above scheme to some standard test cases. In the following, Sod, Sjögreen and blast wave test cases are presented.

• Sod Shock Tube [113]: This test case is a one dimensional shock tube problem with two different initial constant states in the left and right parts of the tube — $\rho_l = 1, \rho_l U_l = 0, \rho_l \epsilon_l = 2.5$ and $\rho_r = 0.125, \rho_r U_r = 0, \rho_r \epsilon_r = 0.25$. This is a standard Riemann problem with a similarity solution. There are three waves, shock, contact

discontinuity and rarefaction emerging from the location of the initial discontinuity. The results from the 1st-order KFVS scheme and 100 grid points are shown in Fig(3.2) for the density, velocity and pressure distributions, where the solid lines are the exact solutions. Comparing Fig.(3.2) with (3.1), we can clearly observe that the numerical solution from the collisionless Boltzmann equation is different from the exact solution of the same equation. Basically, the preparation of Maxwellian distribution functions at the beginning of each time step is equivalent to adding pseudo-particle collisions into the collisionless Boltzmann method to capture the contact discontinuity wave.

• Sjögreen Supersonic Expansion Case [26]: Sjögreen test case is about the supersonic expansion of gas. This test has initial conditions $\rho_l = 1, \rho_l U_l = -2, \rho_l \epsilon_l = 3$ and $\rho_r = 1, \rho_r U_r = 2, \rho_r \epsilon_r = 3$, and a strong expansion wave is formed at the center of the region. The results from the KFVS scheme are shown in Fig(3.3). Some upwinding schemes based on the approximate Riemann solvers have difficulties in this case[100].

• Woodward-Colella Test Case [126]: This case is about strong blast waves interactions. The initial condition consists of three constant states between reflecting walls. The initial condition is $\rho_l = 1.0, \rho_l U_l = 0, \rho_l \epsilon_l = 2500$ for $0 < x \leq 0.1$, $\rho_m = 1.0, \rho_m U_m = 0.0, \rho_m \epsilon_m = 0.025$ for $0.2 < x \leq 0.9$ and $\rho_r = 1.0, \rho_r U_r = 0.0, \rho_r \epsilon_r = 250$ for $0.9 < x \leq 1$. Two strong blast waves develop, collide, and produce new contact discontinuities. The density, velocity and pressure profiles are shown in Fig(3.4), where 400 mesh points are used.

From the above three test cases, we can observe the diffusive character of the 1st-order KFVS scheme, and similar simulation results are obtained from any other first order scheme, such as the Godunov method. But, as analyzed in section (3.4), the reason for the diffusivity in the KFVS scheme is not only from the truncation error of the numerical discretization, but also from the intrinsic dissipative nature in the governing equation itself.

3.2.2 2nd-order KFVS

There are many ways to extend 1st-order KFVS to higher orders. In the following, we present an extension, which is consistent with the BGK scheme developed in the next chapter. In order to have a higher order scheme, we need first to construct higher order initial conditions. For simplicity, the location of a cell interface between cells j and $j+1$ is assumed to be $x_{j+1/2} = 0$. The initial distribution around a cell interface can be obtained from the interpolated macroscopic flow variables. For example, by using a

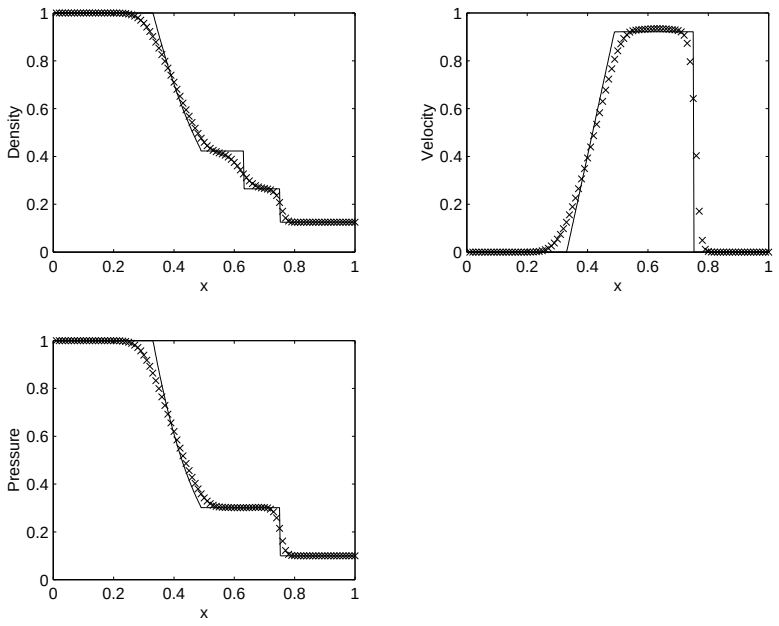

Figure 3.2: Sod test case solutions using the 1st-order KFVS scheme

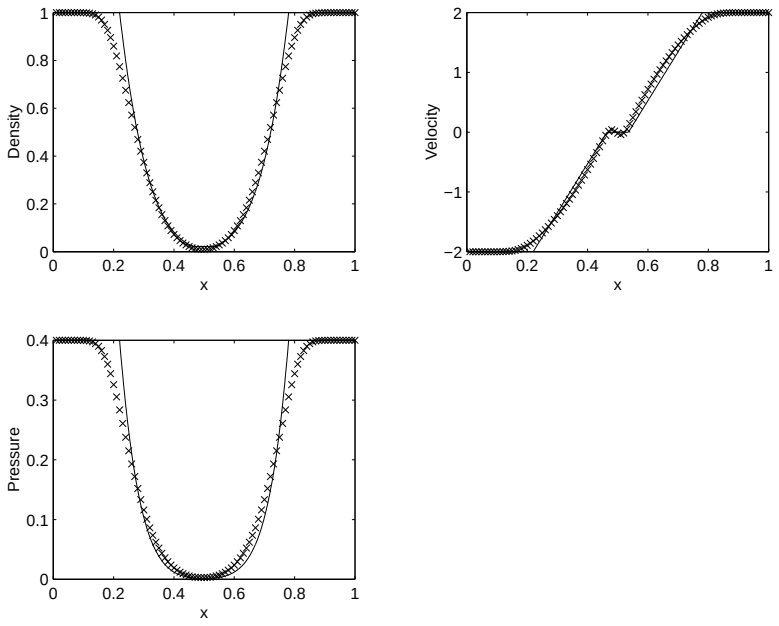

Figure 3.3: Sj*ö*green test case solutions using the 1st-order KFVS scheme

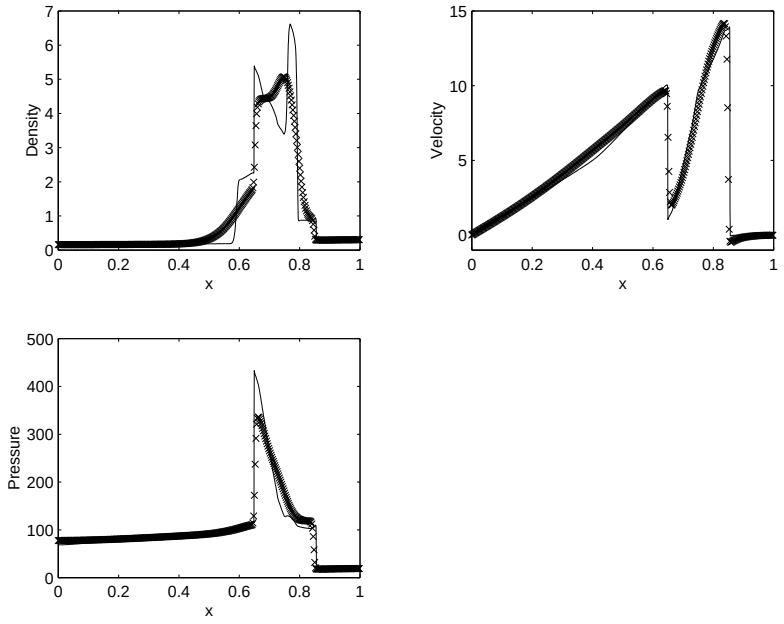

Figure 3.4: Woodward-Colella test case solutions using the 1st-order KFVS scheme

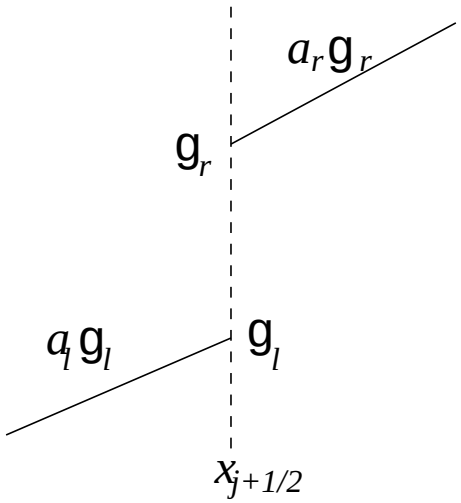

Figure 3.5: Initial gas distribution function for the 2nd-order KFVS scheme.

nonlinear limiter on the conservative variables directly, a second-order accurate initial condition on the left and right sides of a cell interface can be constructed,

$$W = \begin{cases} W_l + \frac{\partial W_l}{\partial x} x, & x \le 0, \\ W_r + \frac{\partial W_r}{\partial x} x, & x \ge 0, \end{cases} \tag{3.17}$$

from which the equivalent initial gas distribution function f_0 can be obtained (see Fig.(3.5)),

$$f_0(x) = \begin{cases} g_l(1 + a_l x), & x \le 0 \ , \\ g_r(1 + a_r x), & x \ge 0 \end{cases} \tag{3.18}$$

where the terms a_l and a_r in Eq.(3.18) are based on the Taylor expansion of the Maxwellian distribution function and have the form

$$a_l = a_{l1} + a_{l2}u + a_{l3}\frac{1}{2}(u^2 + \xi^2) \quad \text{and} \quad a_r = a_{r1} + a_{r2}u + a_{r3}\frac{1}{2}(u^2 + \xi^2). \tag{3.19}$$

Based on the relations between macroscopic variables and microscopic gas distribution function, we have

$$\begin{aligned} W_l + \frac{\partial W_l}{\partial x} x &= \int_{-\infty}^{\infty} \psi_\alpha g_l (1 + a_l x) du d\xi, \\ W_r + \frac{\partial W_r}{\partial x} x &= \int_{-\infty}^{\infty} \psi_\alpha g_r (1 + a_r x) du d\xi, \end{aligned} \tag{3.20}$$

from which we get

$$W_l = \int \psi_\alpha g_l du d\xi \quad , \quad W_r = \int \psi_\alpha g_r du d\xi, \tag{3.21}$$

and

$$\frac{\partial W_l}{\partial x} = \int \psi_\alpha g_l a_l du d\xi \quad , \quad \frac{\partial W_r}{\partial x} = \int \psi_\alpha g_r a_r du d\xi, \tag{3.22}$$

where $\psi_\alpha = (1, u, \frac{1}{2}(u^2 + \xi^2))^T$. Once ρ, U, λ in both equilibrium states g_l and g_r are obtained by solving Eq.(3.21), Eq.(3.22) on the both sides of a cell interface can be expressed as

$$M \begin{pmatrix} a_1 \\ a_2 \\ a_3 \end{pmatrix} = \frac{1}{\rho} \begin{pmatrix} \frac{\partial \rho}{\partial x} \\ \frac{\partial (\rho U)}{\partial x} \\ \frac{\partial (\rho \epsilon)}{\partial x} \end{pmatrix}, \tag{3.23}$$

where the symmetric matrix M has the form

$$M = \begin{pmatrix} 1 & U & \frac{1}{2}(U^2 + \frac{K+1}{2\lambda}) \\ U & U^2 + \frac{1}{2\lambda} & \frac{1}{2}(U^3 + \frac{(K+3)U}{2\lambda}) \\ \frac{1}{2}(U^2 + \frac{K+1}{2\lambda}) & \frac{1}{2}(U^3 + \frac{(K+3)U}{2\lambda}) & \frac{1}{4}(U^4 + \frac{(K+3)U^2}{\lambda} + \frac{(K^2+4K+3)}{4\lambda^2}) \end{pmatrix}. \tag{3.24}$$

In equations (3.23) and (3.24), (ρ, U, λ), (a_1, a_2, a_3), and $(\partial\rho/\partial x, \partial(\rho U)/\partial x, \partial(\rho\epsilon)/\partial x)$ stand for the corresponding values on both sides. The solutions of Eq.(3.23) are

$$a_3 = \frac{4\lambda^2}{K+1}(\mathcal{B} - 2U\mathcal{A}),$$

$$a_2 = 2\lambda(\mathcal{A} - \frac{a_3 U}{2\lambda}),$$

$$a_1 = \frac{1}{\rho}\frac{\partial\rho}{\partial x} - a_2 U - a_3(\frac{U^2}{2} + \frac{K+1}{4\lambda}), \tag{3.25}$$

where

$$\mathcal{A} = \frac{1}{\rho}(\frac{\partial(\rho U)}{\partial x} - U\frac{\partial\rho}{\partial x}),$$

$$\mathcal{B} = \frac{1}{\rho}(2\frac{\partial(\rho\epsilon)}{\partial x} - (U^2 + \frac{K+1}{2\lambda})\frac{\partial\rho}{\partial x}).$$

As an alternative, the values of (a_1, a_2, a_3) can be obtained directly by the Taylor-expansion of the Maxwellian distribution function in terms of the macroscopic flow variables. For example, the direct Taylor expansion of g gives

$$a_1 = \frac{1}{\rho}\frac{\partial\rho}{\partial x} - 2\lambda U\frac{\partial U}{\partial x} + (\frac{K+1}{2\lambda} - U^2)\frac{\partial\lambda}{\partial x} \tag{3.26}$$

$$a_2 = 2\lambda\frac{\partial U}{\partial x} + 2U\frac{\partial\lambda}{\partial x} \tag{3.27}$$

$$a_3 = -2\frac{\partial\lambda}{\partial x} \tag{3.28}$$

where $\partial\lambda/\partial x$ can be expressed as

$$\frac{\partial\lambda}{\partial x} = \frac{K+1}{4}\frac{1}{(\epsilon - \frac{1}{2}U^2)^2}(-\frac{\partial\epsilon}{\partial x} + U\frac{\partial U}{\partial x}), \tag{3.29}$$

and the derivatives of $\partial\epsilon/\partial x$ and $\partial U/\partial x$ are related to the gradients of the conservative variables

$$\frac{\partial\epsilon}{\partial x} = \frac{1}{\rho}\frac{\partial(\rho\epsilon)}{\partial x} - \frac{\epsilon}{\rho}\frac{\partial\rho}{\partial x},$$

and

$$\frac{\partial U}{\partial x} = -\frac{U}{\rho}\frac{\partial \rho}{\partial x} + \frac{1}{\rho}\frac{\partial(\rho U)}{\partial x}.$$

Once the initial gas distribution functions in Eq.(3.18) are obtained, based on the collisionless Boltzmann equation the time evolution of the gas distribution function at the cell interface $x = 0$ is

$$f_{i+1/2} = f_0(x - ut) \mid_{x=0} = \begin{cases} g_l(1 - a_l ut), & u \geq 0 \\ g_r(1 - a_r ut), & u < 0 \ , \end{cases} \tag{3.30}$$

from which, the corresponding mass, momentum and energy fluxes can be obtained,

$$\begin{aligned} \begin{pmatrix} F_\rho \\ F_{\rho U} \\ F_{\rho\epsilon} \end{pmatrix}_{j+1/2} &= \int_{u>0}\int u \begin{pmatrix} 1 \\ u \\ \frac{1}{2}(u^2 + \xi^2) \end{pmatrix} g_l(1 - a_l ut) du d\xi \\ &+ \int_{u<0}\int u \begin{pmatrix} 1 \\ u \\ \frac{1}{2}(u^2 + \xi^2) \end{pmatrix} g_r(1 - a_r ut) du d\xi. \end{aligned} \tag{3.31}$$

The moments of a Maxwellian in the above equation can be obtained using the recursive relation in Appendix B. Once we get the fluxes, the flow variables inside each cell can be updated through

$$W_j^{n+1} = W_j^n + \frac{1}{\Delta x}\int_0^{\Delta t}(F_{W,j-1/2} - F_{W,j+1/2})dt,$$

where Δt is the CFL time step.

In the following numerical test cases, the van Leer limiter is used for the reconstruction of initial conservative variables inside each cell. The van Leer limiter stands for

$$L(s, r) = (\text{sign}(s) + \text{sign}(r))\frac{sr}{|s| + |r|}, \tag{3.32}$$

where s and r represent the slopes of conservative variables. For example, for the construction of density distribution, we have

$$s = \frac{\rho_{j+1} - \rho_j}{x_{j+1} - x_j} \quad \text{and} \quad r = \frac{\rho_j - \rho_{j-1}}{x_j - x_{j-1}},$$

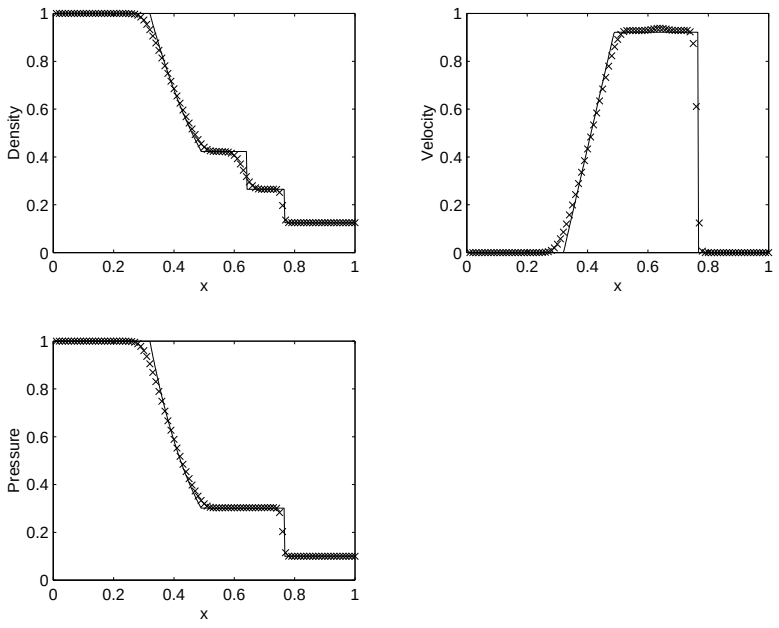

Figure 3.6: Sod test case using the 2nd-order KFVS scheme

where ρ_j is the cell averaged value. After implementing the limiter, linear distributed macroscopic variables inside each cell can be obtained. The density distribution in cell j becomes

$$\bar{\rho}(x) = \rho_j + L(s,r)(x - x_j) \quad \text{for} \quad x_{j-1/2} \leq x \leq x_{j+1/2}.$$

Similar equations can be found for the momentum and energy.

For the same shock tube test cases, the simulation results from the current 2nd-order KFVS scheme are shown in Fig.(3.6)-Fig.(3.8). From these figures, we can clearly observe the improvement of the accuracy of shock, contact discontinuity and rarefaction waves. For the 2-D forward step problem, the density and pressure contours obtained from the 2nd-order KFVS scheme are shown in Fig.(3.9). We can compare these results with those from the BGK method in the next chapter, where the same limiter is used for the construction of initial condition. Similar to other Flux Vector Splitting (FVS) schemes [124] for the Navier-Stokes solutions, the KFVS scheme usually gives a much poorer result than those obtained from the Godunov or FDS schemes. Even for the Euler solutions, the 2nd-order FDS scheme usually gives less dissipative results than those from the 2nd-order FVS scheme. The reason for this will be explained later.

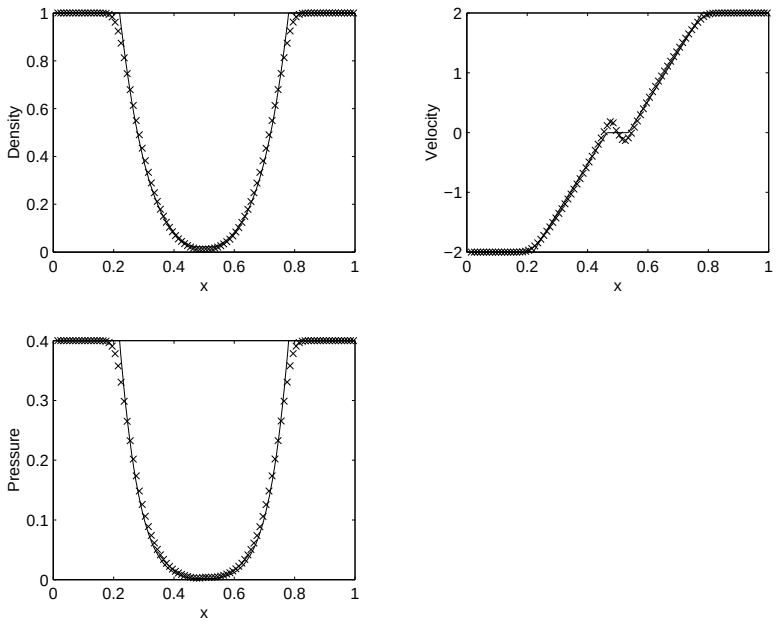

Figure 3.7: Sjögreen test case using the 2nd-order KFVS scheme

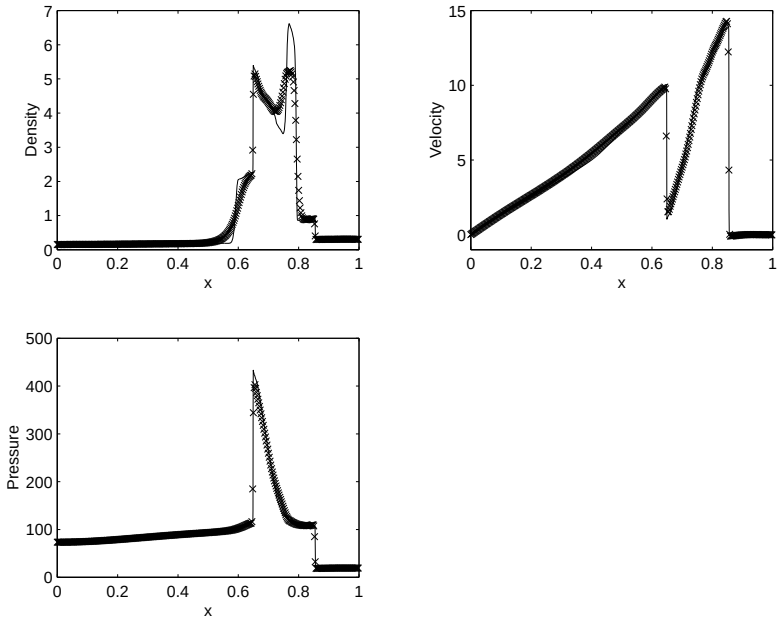

Figure 3.8: Woodward-Colella test case using the 2nd-order KFVS scheme

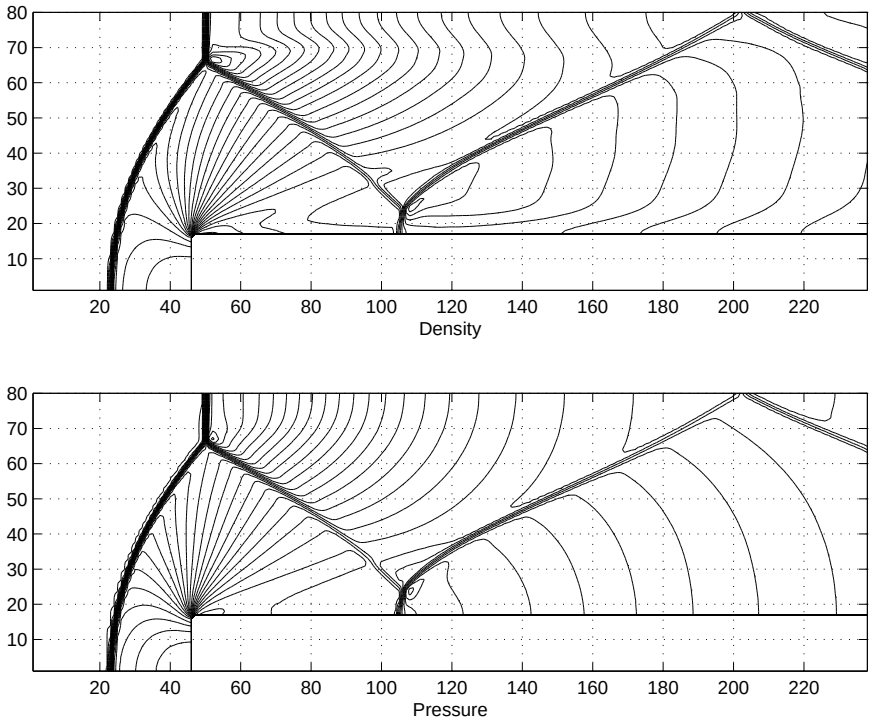

Figure 3.9: Density and pressure distributions from the 2nd-order KFVS Scheme using the van Leer limiter for the construction of initial conservative variables.

3.3 Positivity

For the gas-kinetic scheme, the positivity property is closely related to the positive gas distribution function f, *i.e.* $f \geq 0$. For the 1st-order KFVS scheme, the positivity condition can be rigorously proved. In other words, if the initial state in each cell has positive density and pressure, after the evolution and projection stages, the updated flow variables inside each cell will also have positive density and pressure. Numerically, for the 1st-order KFVS method, we have never observed negative density or pressure once the initial condition is physically reasonable, even in the case of flow expanding into a vacuum. Practically, positivity is an important property for any numerical scheme, especially in the inviscid flow simulation of high speed flows, *e.g.* to keep density and pressure positive at rear parts of flying objects in aerodynamics. Although positivity is a basic and natural requirement for any numerical scheme to be used in real engineering applications, there are not many schemes which could satisfy this property. Currently, there are probably three 1st-order schemes which can be proved to be positive, namely, Godunov, Lax-Friedrichs, and KFVS schemes. For the AUSM+ scheme[76], the proof is only valid in certain flow situations. Many popular methods, such as Roe's approximate

Riemann solver, lack this property and unphysical solutions are occasionally obtained [26, 100]. A scheme which satisfies the positivity requirement is not necessarily a good one, because the positivity requirement is only one of the requirements for a truly accurate and robust method. However, if a scheme could easily violate this basic requirement, it will definitely have limited applications. For example, for hypersonic flow calculations, it is extremely important to keep the pressure and density positive. In the literature, for the case of high Mach number flow passing over a cylinder, the majority of papers only present the solution for the front half of the cylinder. Numerically, to keep a positive density in the rear part of the cylinder is more difficult than capturing the shocks. This case will be used to test our BGK method in the next chapter. In the following, we give a rigorous proof of the positivity of the KFVS scheme [118]. Similar analysis can be found in the literature [95, 30].

The numerical scheme (3.16) can be split into two steps. In the first step we consider the case when there is only gas flowing out of cell j. This gives

$$\begin{pmatrix} \rho_j^* \\ \rho_j^* U_j^* \\ \rho_j^* \epsilon_j^* \end{pmatrix} = \begin{pmatrix} \rho_j \\ \rho_j U_j \\ \rho_j \epsilon_j \end{pmatrix} + \sigma \begin{pmatrix} \int_{u<0} u g_j du d\xi - \int_{u>0} u g_j du d\xi \\ \int_{u<0} u^2 g_j du d\xi - \int_{u>0} u^2 g_j du d\xi \\ \int_{u<0} \frac{u}{2}(u^2+\xi^2) g_j du d\xi - \int_{u>0} \frac{u}{2}(u^2+\xi^2) g_j du d\xi \end{pmatrix}, \quad (3.33)$$

where $\sigma = \Delta t/\Delta x$. The second step is to add the correction terms:

$$\begin{pmatrix} \tilde{\rho}_j \\ \tilde{\rho}_j \tilde{U}_j \\ \tilde{\rho}_j \tilde{\epsilon}_j \end{pmatrix} = \begin{pmatrix} \rho_j^* \\ \rho_j^* U_j^* \\ \rho_j^* \epsilon_j^* \end{pmatrix} + \sigma \begin{pmatrix} \int_{u>0} u g_{j-1} du d\xi - \int_{u<0} u g_{j+1} du d\xi \\ \int_{u>0} u^2 g_{j-1} du d\xi - \int_{u<0} u^2 g_{j+1} du d\xi \\ \int_{u>0} \frac{u}{2}(u^2+\xi^2) g_{j-1} du d\xi - \int_{u<0} \frac{u}{2}(u^2+\xi^2) g_{j+1} du d\xi \end{pmatrix}, \quad (3.34)$$

where the notation $(\rho, \rho U, \rho\epsilon)^{n+1} = (\tilde{\rho}, \tilde{\rho}\tilde{U}, \tilde{\rho}\tilde{\epsilon})$ has been used. It can be verified that $(\tilde{\rho}_j, \tilde{\rho}_j \tilde{U}_j, \tilde{\rho}\tilde{\epsilon}_j)$ obtained by (3.16) are exactly the same as those obtained by using (3.33) and (3.34). In order to simplify the notation, ρU is denoted by m in the following lemmas.

Lemma 3.3.1 *Assume that $\rho_j^*, m_j^*, \rho_j^* \epsilon_j^*$ are computed by (3.33). If $\rho_j \geq 0$ and $\rho_j^2 \epsilon_j \geq \frac{1}{2}(m_j)^2$ for all integers j, then*

$$\rho_j^* \geq 0, \qquad \rho_j^* \epsilon_j^* \geq \frac{1}{2} \rho_j^* \left(U_j^*\right)^2 \quad (3.35)$$

for all j, provided that the following CFL condition is satisfied:

$$\sigma \leq \frac{1}{\max_j \left(|U_j| + c_j\right)}, \tag{3.36}$$

where $c_j = \sqrt{\gamma/2\lambda_j}$ is the local speed of sound.

Proof. It follows from (3.33) that

$$\begin{aligned}
\rho_j^* &= \rho_j - \sigma\rho_j \left\{ \frac{1}{2} U_j \alpha_j + \beta_j \right\}, \\
m_j^* &= m_j - \sigma\rho_j \left\{ \left(\frac{U_j^2}{2} + \frac{1}{4\lambda_j} \right) \alpha_j + u_j \beta_j \right\}, \\
\rho_j^* \epsilon_j^* &= \rho_j \epsilon_j - \sigma\rho_j \left\{ \left(\frac{U_j^3}{4} + \frac{K+3}{8\lambda_j} U_j \right) \alpha_j + \left(\frac{U_j^2}{2} + \frac{K+2}{4\lambda_j} \right) \beta_j \right\},
\end{aligned}$$

where

$$\alpha_j = \operatorname{erfc}\left(-\sqrt{\lambda_j} U_j\right) - \operatorname{erfc}\left(\sqrt{\lambda_j} U_j\right); \quad \beta_j = \frac{e^{-\lambda_j U_j^2}}{\sqrt{\pi\lambda_j}}. \tag{3.37}$$

For ease of notation, we drop the subscript j in the remaining part of the proof. It follows from (3.37) that

$$0 \leq U\alpha \leq 2|U|, \qquad \beta \leq \frac{1}{\sqrt{\pi\lambda}}.$$

If σ satisfies (3.36), then

$$\rho^* \geq \rho\sigma \left\{ \max_j \left(|U_j| + c_j \right) - \left(|U| + \frac{1}{\sqrt{\pi\lambda}} \right) \right\} \geq 0.$$

Furthermore, we observe that

$$(\rho^*)^2 \epsilon^* - \frac{1}{2} (m^*)^2 = A\sigma^2 - B\sigma + C,$$

where, by direct calculations

$$\begin{aligned}
A &= \left(\frac{K+1}{16\lambda} U^2 - \frac{1}{32\lambda^2} \right) \rho^2\alpha^2 + \frac{K+2}{4\lambda} \rho^2\beta^2 + \frac{2K+3}{8\lambda} U\rho^2\alpha\beta; \\
B &= \frac{K+1}{4\lambda} \rho^2 U\alpha + \frac{2K+3}{4\lambda} \rho^2\beta; \\
C &= \rho\epsilon - \frac{1}{2} m^2 = \frac{K+1}{4\lambda} \rho^2.
\end{aligned}$$

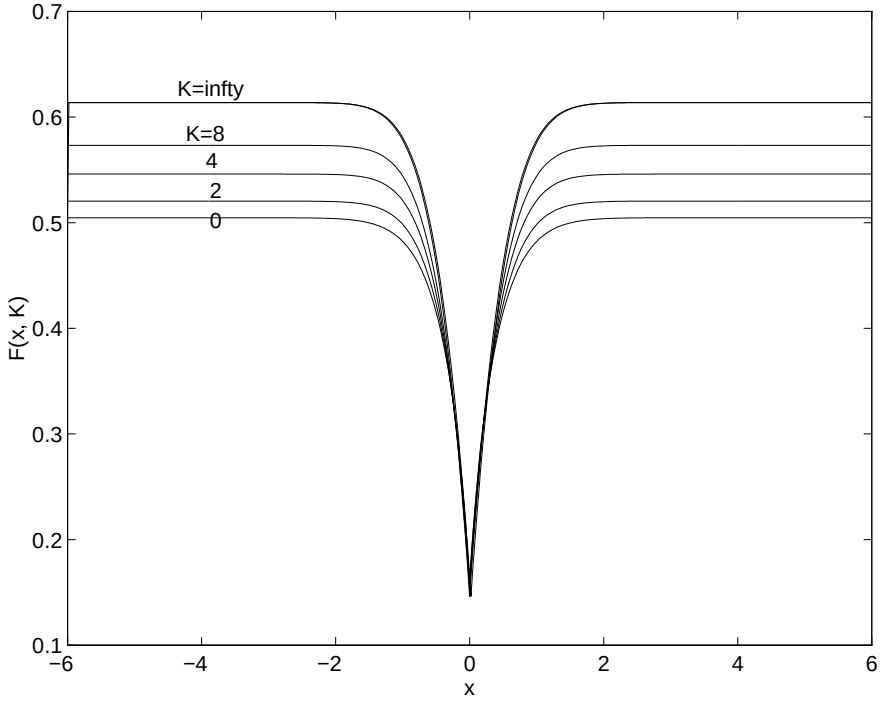

Figure 3.10: The function $F(x, K)$, with $K = 0, 2, 4, 8, \infty$.

The last equation indicates that $C \geq 0$. It follows from Jensen's inequality and the integral formulation (3.33) that $A \geq 0, B \geq 0$. Direct calculation also shows that $B^2 - 4AC \geq 0$. These facts imply that there are two positive roots for the quadratic equation $A\sigma^2 - B\sigma + C = 0$. In order that $(\rho^*)^2\epsilon^* \geq \frac{1}{2}(m^*)^2$, σ should satisfy $\sigma \leq \sigma_1$, where σ_1 is the smaller root of the quadratic equation. Direct calculation gives

$$\sigma_1 = \left(\frac{1}{2}U\alpha + \frac{2K+3}{2K+2}\beta + \frac{1}{K+1}\sqrt{\frac{K+1}{8\lambda}\alpha^2 + \frac{1}{4}\beta^2} \right)^{-1}.$$

Now introduce the following function:

$$\begin{aligned} F(x,K) &= |x| + \sqrt{\frac{K+3}{2K+2}} - \frac{1}{2}x\Big(\mathrm{erfc}(-x) - \mathrm{erfc}(x)\Big) - \frac{2K+3}{2K+2}\frac{e^{-x^2}}{\sqrt{\pi}} \\ &\quad - \frac{1}{K+1}\sqrt{\frac{K+1}{8}\Big(\mathrm{erfc}(-x) - \mathrm{erfc}(x)\Big)^2 + \frac{e^{-2x^2}}{4\pi}}. \end{aligned}$$

It can be shown that $F(x, K)$ is always positive for any $x \in \mathbf{R}$ and for any positive K. This can also be seen from Figure 3.10 where we have plotted $F(x, K)$ for several

values of K. Since $\gamma = (K+3)/(K+1)$, $F(x,K) \geq 0$ indicates that

$$\sigma_1 \geq \frac{1}{|U| + \sqrt{\frac{\gamma}{2\lambda}}}.$$

This completes the proof of this lemma. □

Lemma 3.3.2 *Assume that $\tilde{\rho}_j, \tilde{m}_j, \tilde{\rho}_j\tilde{\epsilon}_j$ be computed by (3.34). If ρ_j^*, m_j^* and $\rho_j^*\epsilon_j^*$ used in (3.34) satisfy $\rho_j^* \geq 0$ and $(\rho_j^*)^2\epsilon_j^* \geq \frac{1}{2}(m_j^*)^2$ for all integers j, then for any choice of $\sigma > 0$ the following positivity-preserving properties hold*

$$\tilde{\rho}_j \geq 0, \qquad (\tilde{\rho}_j)^2\,\tilde{\epsilon}_j \geq \frac{1}{2}\,(\tilde{m}_j)^2 \tag{3.38}$$

for all j.

Proof. It follows from Lemma 3.3.1 that $\rho_j^* \geq 0$, $(\rho_j^*)^2\epsilon_j^* \geq \frac{1}{2}\left(m_j^*\right)^2$. It is observed from (3.34) that $\tilde{\rho}_j \geq \rho_j^* \geq 0$. Similar to the proof of Lemma 3.3.1, we can write $\tilde{\rho}_j^2\tilde{\epsilon}_j - \frac{1}{2}\,(\tilde{m}_j)^2$ in the following form:

$$\tilde{\rho}_j^2\tilde{\epsilon}_j - \frac{1}{2}\,(\tilde{m}_j)^2 = A\sigma^2 + B\sigma + C,$$

where the coefficients A, B, and C are obtained from (3.34). Using the facts that $(\rho_j^*)^2\epsilon_j^* \geq \frac{1}{2}\left(m_j^*\right)^2$ and

$$\int_{u>0} \frac{u}{2}(u^2+\xi^2)g_{j-1}dud\xi \geq \int_{u>0} \frac{1}{2}u^3 g_{j-1}dud\xi;$$
$$\int_{u<0} \frac{u}{2}(u^2+\xi^2)g_{j+1}dud\xi \leq \int_{u<0} \frac{1}{2}u^3 g_{j+1}dud\xi,$$

we can show that $A \geq 0, B \geq 0$ and $C \geq 0$. This completes the proof of (3.38). □

Combining Lemmas 3.1 and 3.2, we conclude that the collisionless approach is positivity-preserving as long as the standard CFL condition is satisfied.

Remark(3.2)

Lemma 3.3.2 shows that the positivity-preserving analysis for the numerical scheme (3.16) can be determined by analyzing the simplified scheme (3.33). In other words, the

CFL condition is obtained by considering the scheme (3.16) with the following assumption:

$$\rho_{j-1} = 0, \qquad \rho_j > 0, \qquad \rho_{j+1} = 0. \tag{3.39}$$

For high-order schemes, a similar theorem about positivity can be proved with a limitation on the slopes of the initial reconstruction data and the specific techniques to extend the KFVS scheme from 1st to 2nd order[30].

3.4 Physical and Numerical Analysis

The gas evolution model in the KFVS scheme is based on the collisionless Boltzmann equation. However, the exact free stream solution in Fig.(3.1) and the numerical solution in Fig.(3.2) are different. What is the main reason for their deviation? In this section, we are going to analyze the KFVS scheme. This analysis can be equally applied to any other Flux Vector Splitting (FVS) scheme once $F_{j+1/2} = F^+(W_j) + F^-(W_{j+1})$ is used for the flux construction, such as van Leer splitting [123] and Steger-Warming splitting [114]. The difference is that instead of free particle transport, they have free wave penetrations.

In most of the current literature, the KFVS scheme is regarded as an approximate Riemann solver for the numerical solution of the Euler equations. It is observed that as the time step Δt and cell size Δx approach zero, the numerical solution of the KFVS scheme suggests that the scheme converges to the Euler solution. However, with finite cell size and time step, it is noticed that the KFVS scheme usually gives more diffusive results than Flux Difference Splitting (FDS) scheme. In this section, a underlying physical model for the KFVS scheme is constructed to explain its dissipative characters. The way to derive the real governing equations from the discretized numerical schemes is an important issue we should face in order to better develop and understand numerical methods. Although, it is very helpful to use the words "implicit dissipation" to conceal our ignorance in the understanding of dissipative mechanism in the upwinding schemes, it also prevents us from getting a complete understanding of these schemes. In the CFD community, there are many methods for the numerical solution of compressible flow. Do we really find any principles or useful guidance to lead us to more reliable methods? Or, could we have any confidence to say that this new scheme can avoid spurious solutions instead of saying that it works for this test case? It seems that we have not had this kind of confidence yet. One of the main purposes of this lecture is to get a better understanding to what we are really doing in a numerical scheme.

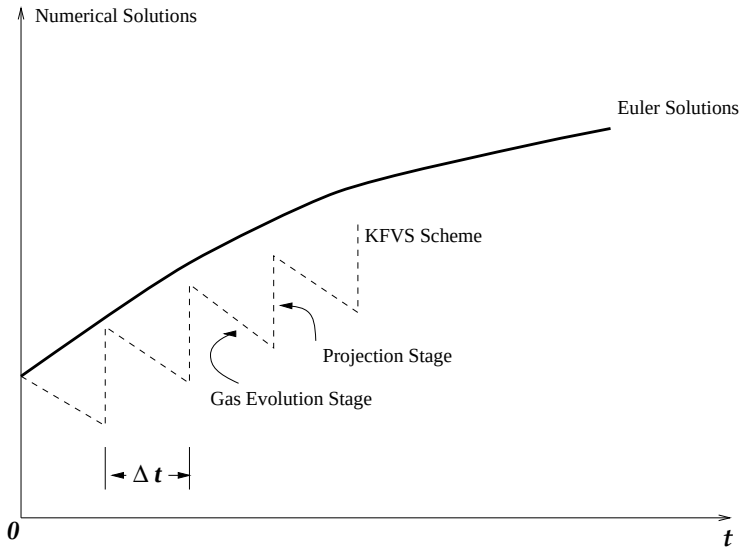

Figure 3.11: KFVS Solutions vs Euler solution, where Δt is the CFL time step.

From numerical observations, it is well-known that the KFVS and FVS schemes give very dissipative results for the Navier-Stokes solutions[82, 124], such as in the laminar boundary layer calculations, especially with coarse meshes. It is also observed that the steady state flow structures from the KFVS scheme in the multidimensional case could probably depend on the cell size. To explain this, we need a clear understanding of the underlying physical model in the discretized KFVS scheme.

In the gas evolution stage of the KFVS scheme, the particles can transport freely. For example, gas in high temperature region can freely move into low temperature region without suffering any particle collisions. As a result, the free penetration of particles strongly and easily smears any temperature gradients and removes the possible formation of contact discontinuity waves. Similarly, the "shock" from collisionless Boltzmann equation will also be smeared due to the free transport of particles across the "shock" front even though the shock has self-steepening mechanism. Numerically, the contact discontinuity waves from the KFVS scheme are still obtained, which means that the particles are not absolutely moving freely as described in the collisionless Boltzmann equation. The numerical particles do suffer some kind of collisions to reduce the dissipation to a lower level. In order to understand this, we need to take a careful look at the two stages in a 1st-order numerical scheme: the gas evolution stage and the projection

stage. In the gas evolution stage, the collisionless Boltzmann equation

$$\frac{\partial f}{\partial t} + u\frac{\partial f}{\partial x} = 0, \tag{3.40}$$

is solved with the exact solution shown in Eq.(3.13). However, in the projection stage, the flow variables are averaged inside each cell, and the averaging is based on the mass, momentum and energy conservations. More specifically, instead of keeping the nonequilibrium solution from the collisionless Boltzmann equation inside each cell, an equilibrium state is constructed with the same mass, momentum and energy densities inside each cell. The above conservative property in the projection stage makes it identical to the dynamical effects from the collision term $Q(f, f)$ in the Boltzmann equation, where the local mass, momentum and energy are conserved during the course of particle collisions. Therefore, dynamically, the projection stage is actually a physical process solving the following equation,

$$f_t = Q(f, f), \tag{3.41}$$

to translate a non-equilibrium state to an equilibrium one. Since the particle collision time τ in $Q(f, f)$ is much shorter than the time step $\tau \ll \Delta t$, the Maxwellian distribution is obtained instantaneously inside each cell. If we combine the gas evolution and projection stages to form a uniform KFVS scheme, the real governing equation of the KFVS scheme will be a modified "BGK" model,

$$\frac{\partial f}{\partial t} + u\frac{\partial f}{\partial x} = \frac{g - f}{\Delta t}, \tag{3.42}$$

where the real physical collision time in BGK model is replaced by the time step Δt. The dynamical effect from the two numerical stages in the 1st-order KFVS scheme is qualitatively described in Fig.(3.11), where the free transport in the gas evolution stage always evolves the system away from the Euler solution (f becomes more and more different from the Maxwellian), the projection stage drives the system back to approach the Euler solution (the preparation of the equilibrium state). The characteristic time interval in the KFVS scheme is the time step.

The underlying macroscopic governing equation (3.42) for the KFVS is identical to that from the BGK model, except the collision time τ is replaced by the CFL time step Δt. All theoretical results related to the BGK model can be applied to the above model equation. The first and direct consequence is that the KFVS scheme satisfies the entropy

condition. It is true that entropy-violating solutions have never been observed in the KFVS scheme. Also, the above governing equation for the KFVS scheme tells us that the numerical viscosity coefficient η in the KFVS scheme is

$$\eta = p\Delta t, \tag{3.43}$$

where p is the local pressure, and the corresponding heat conduction coefficient κ is

$$\kappa = \frac{K+5}{2}\frac{k}{m}p\Delta t. \tag{3.44}$$

Since the time step is related to the cell size by the CFL condition, the dissipative coefficients in the KFVS scheme will be proportional to the cell size. In regions where the flow is smooth, we conclude that the KFVS scheme is solving the "Navier-Stokes" equations and the dissipative coefficients are proportional to the time step. In discontinuous region, we cannot figure out the corresponding governing equations for the macroscopic variables from the "BGK" model of Eq.(3.42), because the standard Chapman-Enskog expansion is only correct in smooth flow regions. Although there is uncertainty about the explicit dissipative term in KFVS scheme for the macroscopic equations in the discontinuous regions, the free particle transport inside each time step will equalize the particle mean free path $\bar{l}$ to the cell size Δx. Physically, this is critically important for the robustness of the KFVS scheme[3]. The numerical shock thickness ($\sim \Delta x$) does require that the numerical mean free path be equal to the cell size ($\bar{l} \sim \Delta x$). So, numerics and physics match perfectly for discontinuous solutions in the KFVS scheme. Although free particle transport makes the KFVS scheme extremely robust and provides a reasonable mechanism to construct the numerical shock structure, the large mean free path also poisons the Navier-Stokes solutions in the smooth regions, such as in laminar boundary layer calculations.

For any numerical method, besides numerical modeling errors, there are also truncation errors. For the 1st-order KFVS method, the coefficient of the leading truncation error in solving Eq.(3.42) is also proportional to Δx. So, the macroscopic equation solved

[3]KFVS is probably the most robust scheme. Although the Godunov method in the 1-D case satisfies positivity, entropy condition, it can still give glitches in rarefaction waves [120] and develop odd-even decoupling in the 2-D case. The KFVS scheme also has the entropy and positivity property, gives much smoother rarefaction waves, and avoids carbuncle and odd-even decoupling completely. As far as accuracy is concerned, the KFVS scheme is worse than the Godunov method in certain flow situations, especially for the Navier-Stokes solutions. However, this weakness in the KFVS scheme can be fixed by including particle collisions in the gas evolution stage, such as in the BGK scheme, and at the same time, robustness can be kept.

by the 1st-order KFVS scheme is

$$W_t + F(W)_x = \alpha_p \Delta x W_{xx} + \alpha_t \Delta x W_{xx},$$

where α_p is related to the numerical modeling viscosity coefficient in Eq.(3.43)-(3.44), and α_t is the numerical discretization error in solving Eq.(3.42). For the 2nd-order KFVS scheme, the truncation error will be reduced, and the coefficient in the numerical dispersive term will be proportional to $(\Delta x)^2$. However, the numerical modeling dissipation from the governing equation will remain the same even though the collision time could be reduced to one half of a time step if an intermediate stage is added inside each time step for a 2nd order accuracy. Therefore, for a 2nd-order scheme, the real governing equation becomes

$$W_t + F(W)_x = \frac{\alpha_p}{2} \Delta x W_{xx} + \alpha_h (\Delta x)^2 W_{xxx},$$

where α_h is the coefficient for high order truncation terms.

Suppose we are interested in solving the Navier-Stokes equations by a 2nd-order KFVS scheme. With an additional physical viscous term νW_{xx}, the governing equation changes to

$$W_t + F(W)_x = \frac{\alpha_p}{2} \Delta x W_{xx} + \nu W_{xx} + \alpha_h (\Delta x)^2 W_{xxx},$$

where ν is the physical viscosity which is determined by the Reynolds number. As a result, the accuracy of the numerical solution for the Navier-Stokes equations depends on the ratio of the physical viscosity coefficient and the numerical modeling viscosity coefficient. With the definition,

$$\delta = \frac{\nu}{\alpha_p \Delta x},$$

if δ is larger, *i.e.* with a smaller mesh size, the KFVS scheme could give accurate Navier-Stokes solutions, such as the case presented in the paper by Chou and Baganoff[13], where a large number of grid points have been used for shock structure calculations. Numerically, with such a refined mesh, we can hardly distinguish the numerical behavior from different schemes so long as the schemes are consistent with the governing equation. So, in some sense, the conclusion in [13] is misleading. For a reasonable mesh size, such as a few points in the boundary layer, the KFVS scheme could hardly give accurate Navier-Stokes solution, because δ will not be a large number anymore in this situation.

In conclusion, the physical requirement for the transition from the Boltzmann equation to the Euler equations is based on the assumption of a local equilibrium state. It is

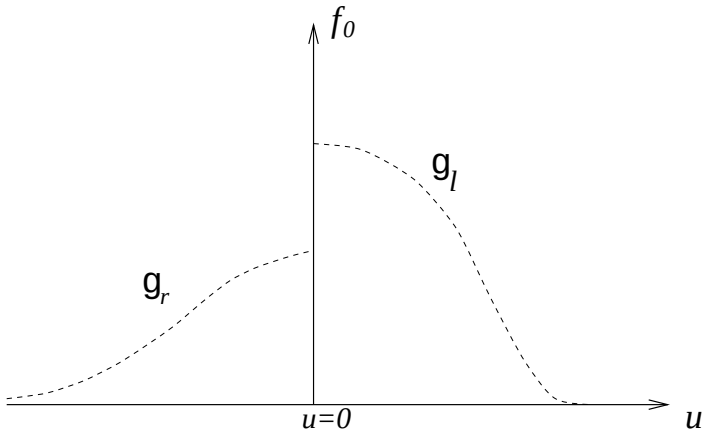

Figure 3.12: The gas distribution function at a cell interface for flux evaluation in the KFVS scheme

true that, at the beginning of each time step, the gas distribution in the KFVS scheme is a Maxwellian distribution function inside each cell, but the real gas distribution function which is used to evaluate the numerical fluxes across the cell boundary is not Maxwellian at all — it is composed of "two half-Maxwellians" in $u \geq 0$ and $u \leq 0$ regions separately, see Fig.(3.12)[4]. This non-equilibrium distribution does not correspond to the Euler solutions at all. Physically, molecules in the real gas suffer many collisions during a CFL time step. Because of particle collisions, the flow could evolve to the equilibrium state.

3.5 Summary

In this chapter, the KFVS scheme has been introduced and analyzed. For all flux vector splitting schemes, the drawback of poor resolution of the contact discontinuity wave and the slip surface is due to the intrinsic free particle or wave transport dynamics in the gas evolution stage. For example, the particles or waves in high temperature region can easily move to the lower temperature region and eliminate the possible formation of contact discontinuity wave. Since the laminar boundary layer can be regarded as contact or slip regions, it gets smeared easily by using the FVS schemes. Although the strong smearing can be much reduced with the help of the projection mechanism (pseudo-collisions) in a numerical scheme, the intrinsic viscosity coefficient ($\sim \Delta x$) due to the numerical modeling in the KFVS and FVS schemes is always there. In order to

[4]For the FVS scheme, the flux function $F_{j+1/2} = F_j^+ + F_{j+1}^-$ does not corresponding to any equilibrium state although the equilibrium assumption is used to decompose $F_j = F_j^+ + F_j^-$ inside each cell.

capture the correct Navier-Stokes solutions, such as the correct boundary layer, we have to modify the free transport mechanism in the KFVS scheme, in other words we have to include real particle collisions in the gas evolution stage directly. However, without using any reasonable particle collisional model, any *ad hoc* fixes to the FVS scheme will eventually fail in certain flow situations[86, 35]. In the next chapter, we are going to include particle collisions in the gas evolution stage, and this inclusion is based on the BGK model of the Boltzmann equation.

Chapter 4

Gas-Kinetic BGK Method

As analyzed in the last chapter, the KFVS scheme is based on the collisionless Boltzmann equation in the gas evolution stage. Due to free transport dynamics in this stage, it cannot properly capture the contact discontinuity wave and slip lines. The artificial collisions with the collision time equal to the time step Δt help the KFVS scheme to capture these waves. In order to include real particle collisions into the gas evolution model to reduce over-diffusivity in the KFVS scheme, we have to use a physical model to approximate particle collisions. In this chapter, the Bhatnagar-Gross-Krook (BGK) model [5] will be used in the gas evolution stage to construct the numerical fluxes across a cell interface.

Basically, the KFVS scheme can be regarded as a splitting scheme for the Boltzmann equation, where the Boltzmann equation is solved in two steps,

$$f_t + u_i \frac{\partial f}{\partial x_i} = 0, \qquad \text{in the gas evolution stage}$$

and

$$f_t = Q(f, f), \qquad \text{in the projection stage.}$$

The over-diffusivity in the KFVS scheme is closely related to the splitting error. The gas-kinetic BGK scheme presented in this chapter is an unsplitting scheme for the Boltzmann equation, where the following equations are solved

$$f_t + u_i \frac{\partial f}{\partial x_i} = \frac{g - f}{\tau}, \qquad \text{in the gas evolution stage}$$

and

$$f_t = Q(f, f), \qquad \text{in the projection stage.}$$

This chapter provides an excellent example to illustrate the importance of the unsplitting scheme for hyperbolic conservation laws with a source term[1]. As analyzed in the last chapter, the KFVS scheme does converge to the Euler solution mathematically as the cell size and time step approach zero. However, in practical numerical calculations finite cell size and time step are used. It is thus necessary to decouple the relation between viscosity coefficients and time step or cell size in the KFVS scheme in the smooth flow regions, and keep the coupling in the discontinuous regions once the numerical resolution determined by the cell size cannot resolve the flow structure.

The development of the BGK method started in the summer of 1990[128], and the early results were published in two papers [98, 137]. After that, the original scheme has further been developed and simplified in [136, 135, 134]. At the same time, the BGK method has been extended to multicomponent flow [129] and hyperbolic conservation laws with source terms, such as the Euler equations with heat transfer [130]. Currently, extensions of the BGK scheme to chemical reactive and multiphase flows are under investigation. In recent years, the BGK method has found its way in many applications, which include astrophysics [127], aerodynamics [59], hydraulic engineering [32], and physical science [63, 64]. Also, a modified BGK method has been successfully applied to incompressible flow calculations [79]. Since most hyperbolic equations can be recovered by an equivalent BGK model, the numerical techniques presented in this chapter for the Euler and the Navier-Stokes equations can be naturally extended to other conservation laws. In the numerical part, extensive test cases for both inviscid and viscous flow equations are presented.

4.1 1st-order BGK Method

4.1.1 Numerical Formulation

The BGK model in the 1-D case is

$$f_t + uf_x = \frac{g - f}{\tau}, \tag{4.1}$$

and the compatibility condition is

$$\int\int \frac{g - f}{\tau}\psi_\alpha du d\xi = 0, \qquad \alpha = 1, 2, 3, \tag{4.2}$$

[1]The collision term in the BGK model can be regarded as a source term.

where

$$\psi_\alpha = (1, u, \frac{1}{2}(u^2 + \xi^2))^T.$$

Again, the notations $d\xi = d\xi_1 d\xi_2 ... d\xi_K$ and $\xi^2 = \xi_1^2 + \xi_2^2 + ... + \xi_K^2$ have been used.

For the initial condition of two constant states around a cell interface $x = 0$,

$$\begin{aligned} f_0 &= \begin{cases} g_l, & x \le 0 \\ g_r, & x > 0 \end{cases} \\ &= g_l(1 - \mathrm{H}(x)) + g_r \mathrm{H}(x), \end{aligned} \tag{4.3}$$

and with the assumption of constant equilibrium state g_0 in space and time, the solution f of the BGK model at $x = 0$ is[2],

$$f = (1 - e^{-t/\tau})g_0 + e^{-t/\tau}\left(g_l \mathrm{H}(u) + g_r(1 - \mathrm{H}(u))\right), \tag{4.4}$$

where the equilibrium state g_0 is constructed by applying the compatibility condition (4.2) along the line $(x = 0, t)$,

$$\begin{aligned} \int\int_{-\infty}^{+\infty} \psi_\alpha g_0 du d\xi &= \int\int_{-\infty}^{\infty} \psi_\alpha f_0(-ut) du d\xi \\ &= \int\int_{u>0} \psi_\alpha g_l du d\xi + \int\int_{u<0} \psi_\alpha g_r du d\xi. \end{aligned} \tag{4.5}$$

The underlying physical assumption in the above equation is that the left and right moving particles collapse at a cell interface to form an equilibrium state g_0.

The solution (4.4) is different from the solution based on the collisionless Boltzmann equation. In the limit of $\tau \to 0$, Eq.(4.4) goes to $f = g_0$, which is an exact Maxwellian distribution function for the Euler equations at the cell interface. Physically, in this limiting case, the use of $f = g_0$ is identical to the assumption in the Godunov method, where an equilibrium state is always obtained at the cell interface in the construction of flux functions from the flow variables. For $\tau \to \infty$, f is equal to f_0, which recovers the distribution function in the KFVS scheme. So, in some sense, Eq.(4.4) makes a bridge between the KFVS (or FVS) scheme and the Godunov method. In the current 1st-order BGK scheme, $e^{-t/\tau}$ can be assumed to be a constant.

[2]For the BGK model, with the initial condition of two constant states separated at $x = 0$, there is no similarity solution. This is due to the fact that a characteristic time scale τ is involved in the BGK equation.

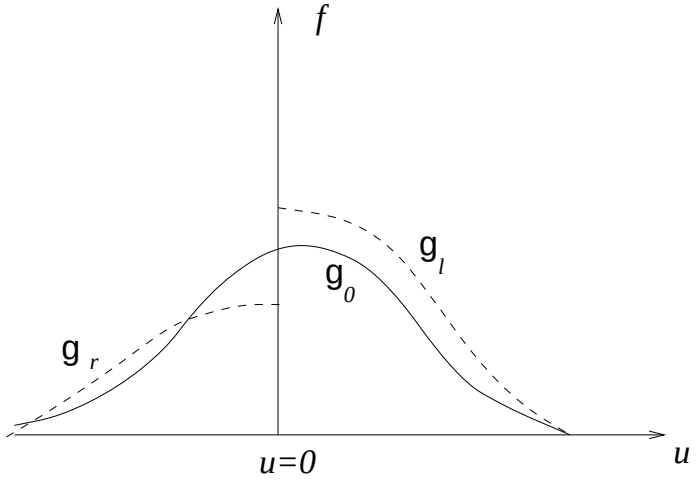

Figure 4.1: Schematic model for the gas distribution function at cell interface

The distribution function at a cell interface for the 1st-order BGK method is based on the combination of two functions: the nonequilibrium state from the initial gas distribution function f_0 and the equilibrium state g_0 constructed from f_0, see Fig.(4.1). With the definition $e^{-t/\tau} = \eta$, the final distribution function f at $x = 0$ is

$$f_{j+1/2} = (1 - \eta)g_0 + \eta f_0. \tag{4.6}$$

The positivity property for the above scheme has been analyzed in [118].

The numerical formulation for the 1st-order BGK scheme is the following:

1. Given the initial mass, momentum and energy densities $\{\rho_j^n, \rho_j^n U_j^n, \rho_j^n \epsilon_j^n\}$ in each cell j, compute U_j^n and λ_j^n for the construction of the Maxwellian distribution function g_j,

$$g_j = \rho_j (\frac{\lambda_j}{\pi})^{\frac{K+1}{2}} e^{-\lambda_j[(u-U_j)^2+\xi^2]},$$

where λ_j is determined by

$$\lambda_j = \frac{K+1}{4} \frac{\rho_j}{\rho_j \epsilon_j - \frac{1}{2}\rho_j U_j^2}$$

and $K = 4$ for $\gamma = 1.4$.

2. Compute the numerical fluxes from f_0, which are denoted as $\{F^0_{\rho,j+1/2}, F^0_{\rho U,j+1/2}, F^0_{\rho\epsilon,j+1/2}\}$.

$$\begin{pmatrix} F^0_{\rho,j+1/2} \\ F^0_{\rho U,j+1/2} \\ F^0_{\rho\epsilon,j+1/2} \end{pmatrix} = \int\int_{u>0} u\psi_\alpha g_j du d\xi + \int\int_{u<0} u\psi_\alpha g_{j+1} du d\xi$$

$$= \rho_j \begin{pmatrix} \frac{U_j}{2}\mathrm{erfc}(-\sqrt{\lambda_j}U_j) + \frac{1}{2}\frac{e^{-\lambda_j U_j^2}}{\sqrt{\pi\lambda_j}} \\ \left(\frac{U_j^2}{2} + \frac{1}{4\lambda_j}\right)\mathrm{erfc}(-\sqrt{\lambda_j}U_j) + \frac{U_j}{2}\frac{e^{-\lambda_j U_j^2}}{\sqrt{\pi\lambda_j}} \\ \left(\frac{U_j^3}{4} + \frac{K+3}{8\lambda_j}U_j\right)\mathrm{erfc}(-\sqrt{\lambda_j}U_j) + \left(\frac{U_j^2}{4} + \frac{K+2}{8\lambda_j}\right)\frac{e^{-\lambda_j U_j^2}}{\sqrt{\pi\lambda_j}} \end{pmatrix}$$

$$+\rho_{j+1} \begin{pmatrix} \frac{U_{j+1}}{2}\mathrm{erfc}(\sqrt{\lambda_{j+1}}U_{j+1}) - \frac{1}{2}\frac{e^{-\lambda_{j+1} U_{j+1}^2}}{\sqrt{\pi\lambda_{j+1}}} \\ \left(\frac{U_{j+1}^2}{2} + \frac{1}{4\lambda_{j+1}}\right)\mathrm{erfc}(\sqrt{\lambda_{j+1}}U_{j+1}) - \frac{U_{j+1}}{2}\frac{e^{-\lambda_{j+1} U_{j+1}^2}}{\sqrt{\pi\lambda_{j+1}}} \\ \left(\frac{U_{j+1}^3}{4} + \frac{K+3}{8\lambda_{j+1}}U_{j+1}\right)\mathrm{erfc}(\sqrt{\lambda_{j+1}}U_{j+1}) - \left(\frac{U_{j+1}^2}{4} + \frac{K+2}{8\lambda_{j+1}}\right)\frac{e^{-\lambda_{j+1} U_{j+1}^2}}{\sqrt{\pi\lambda_{j+1}}} \end{pmatrix}.$$

3. Obtain the total mass, momentum and energy densities at the cell interface from the collapsed left and right moving particles,

$$\begin{pmatrix} \bar{\rho}_{j+1/2} \\ \bar{\rho}_{j+1/2}\bar{U}_{j+1/2} \\ \bar{\rho}_{j+1/2}\bar{\epsilon}_{j+1/2} \end{pmatrix}$$

$$= \int\int_{u>0} \psi_\alpha g_j du d\xi + \int\int_{u<0} \psi_\alpha g_{j+1} du d\xi$$

$$= \rho_j \begin{pmatrix} \frac{1}{2}\mathrm{erfc}(-\sqrt{\lambda_j}U_j) \\ \frac{1}{2}U_j\mathrm{erfc}(-\sqrt{\lambda_j}U_j) + \frac{1}{2}\frac{e^{-\lambda_j U_j^2}}{\sqrt{\pi\lambda_j}} \\ \frac{1}{2}\left(\frac{U_j^2}{2} + \frac{K+1}{4\lambda_j}\right)\mathrm{erfc}(-\sqrt{\lambda_j}U_j) + \frac{U_j}{4}\frac{e^{-\lambda_j U_j^2}}{\sqrt{\pi\lambda_j}} \end{pmatrix}$$

$$+\rho_{j+1} \begin{pmatrix} \frac{1}{2}\mathrm{erfc}(\sqrt{\lambda_{j+1}}U_{j+1}) \\ \frac{1}{2}U_{j+1}\mathrm{erfc}(\sqrt{\lambda_{j+1}}U_{j+1}) - \frac{1}{2}\frac{e^{-\lambda_{j+1} U_{j+1}^2}}{\sqrt{\pi\lambda_{j+1}}} \\ \frac{1}{2}\left(\frac{U_{j+1}^2}{2} + \frac{K+1}{4\lambda_{j+1}}\right)\mathrm{erfc}(\sqrt{\lambda_{j+1}}U_{j+1}) - \frac{U_{j+1}}{4}\frac{e^{-\lambda_{j+1} U_{j+1}^2}}{\sqrt{\pi\lambda_{j+1}}} \end{pmatrix},$$

from which $(\bar{\rho}_{j+1/2}, \bar{U}_{j+1/2}, \bar{\lambda}_{j+1/2})$ in g_0 can be obtained.

4. Compute the numerical fluxes $\{F^1_{\rho,j+1/2}, F^1_{\rho U,j+1/2}, F^1_{\rho\epsilon,j+1/2}\}$ from the equilibrium states g_0,

$$\begin{pmatrix} F^1_{\rho,j+1/2} \\ F^1_{\rho U,j+1/2} \\ F^1_{\rho\epsilon,j+1/2} \end{pmatrix} = \int\int_{-\infty}^{\infty} u\psi_\alpha g_0 du d\xi$$

$$= \bar{\rho}_{j+1/2} \begin{pmatrix} \bar{U}_{j+1/2} \\ \bar{U}^2_{j+1/2} + \frac{1}{2\lambda_{j+1/2}} \\ \frac{1}{2}\bar{U}^3_{j+1/2} + \frac{K+3}{4\lambda_{j+1/2}}\bar{U}_{j+1/2} \end{pmatrix}.$$

5. The final fluxes across the cell interface is

$$\begin{pmatrix} F_{\rho,j+1/2} \\ F_{\rho U,j+1/2} \\ F_{\rho\epsilon,j+1/2} \end{pmatrix} = (1-\eta) \begin{pmatrix} F^1_{\rho,j+1/2} \\ F^1_{\rho U,j+1/2} \\ F^1_{\rho\epsilon,j+1/2} \end{pmatrix} + \eta \begin{pmatrix} F^0_{\rho,j+1/2} \\ F^0_{\rho U,j+1/2} \\ F^0_{\rho\epsilon,j+1/2} \end{pmatrix},$$

where η is a local constant $\eta \in [0,1]$.

4.1.2 Physical and Numerical Analysis

Remark(4.1)

For the 1st-order BGK scheme, it can be proved that the evolution process from f_0 to g_0 is a process with increase of entropy. In other words, it satisfies the H-theorem in the gas evolution stage. With the definition of entropy ($s = -k\mathcal{H}$, k is Boltzmann constant), we have

$$\begin{aligned} \Delta\mathcal{H} &= \int g_0 \ln g_0 du d\xi - \int f_0 \ln f_0 du d\xi \\ &= \int (g_0 - f_0) \ln g_0 du d\xi + \int f_0 (\ln(g_0/f_0) du d\xi \\ &= \int f_0 \ln(g_0/f_0) du d\xi \\ &\leq \int f_0 (g_0/f_0 - 1) du d\xi \\ &= \int (g_0 - f_0) du d\xi \\ &= 0. \end{aligned}$$

The entropy increasing property in the gas evolution stage, along with the dissipative property in the projection stage, prevents the formation of any unphysical rarefaction shock in the gas-kinetic BGK scheme.

Remark(4.2)

The construction of the equilibrium state g_0 at a cell interface is based on the assumption that left and right moving particles towards a cell interface collapse totally and instantaneously. A Maxwellian distribution function is constructed there from the total mass, momentum and energy densities of the collapsed particles. If $\eta = 0$ is assumed, an exact Maxwellian $f = g_0$ will be the distribution at a cell interface, and this scheme

is called Totally Thermalized Transport (TTT) method [128]. Similar analysis has been obtained in [84]. Inside the numerical shock layer, the TTT scheme gives an inappropriate representation of the flow physics, where a non-equilibrium state is interpreted as an equilibrium one. So, the TTT scheme will definitely fail in numerical shock regions. The scheme with both g_0 and f_0 ($\eta \neq 0, 1$) is called Partially Thermalized Transport (PTT) method in [128]. As we will show in the next section, due to the special dissipative nature in the 1st-order BGK scheme, the above scheme surprisingly gives oscillation-free solutions in the slowly moving shock case. At the same time, a crisp shock transition (2 or 3 points) is captured. It is worthy to study the specific dissipative nature in the 1st-order BGK method. This dissipation due to non-Maxwellian distribution (discontinuous at $u = 0$) is unique and cannot be obtained from the Navier-Stokes type dissipations, such as the simple introduction of a νW_{xx} term. The method based on the blending of equilibrium and non-equilibrium states to evaluate fluxes has been successfully extended to inhomogeneous flow calculations[63].

Remark(4.3)

The distribution function f in Eq.(4.6) corresponds to a physically realizable state with positive density and pressure. This can easily be proved. Since $g_0 > 0, f_0 > 0$ and $\eta \in [0, 1]$, f is a strictly positive function with $f > 0$ for all particle velocities. Therefore, f has a positive density and temperature at the cell interface due to the following relations

$$\int f du d\xi > 0 \ ; \ \int u^2 f du d\xi - \frac{(\int u f du d\xi)^2}{\int f du d\xi} > 0.$$

However, positive density and pressure at a cell interface does not mean that the final scheme will keep the density and pressure positive inside each cell in the next time step. In the case of $\eta = 1$, where f is equal to the nonequilibrium distribution function f_0, the positivity has been rigorously proved in the last chapter. However, the general proof of positivity for the BGK method is very difficult. The difficulty is mainly due to the variation of η in a real flow situation, and an inappropriate choice of the value η will not keep the scheme positive. For example, the choice of $f = g_0$ with $\eta = 0$ is only correct in smooth flow regions. In the discontinuous region, one possible way is to estimate the range of the value η, where the scheme could have the positivity property by keeping a certain amount of non-equilibrium state. It is probably very difficult to estimate this parameter η; physically, η should depend on the strength of a shock wave.

Numerically, we find that if the Mach number of the shock wave is less than 15, even with $\eta = 0$, the kinetic scheme could still keep the positivity. With $\eta = 0.01$, we can extend the Mach number up to 30 and keep the scheme positive[118]. In real numerical simulations, in the discontinuous region, with the value of η on the order of 0.5 or even larger, it seems that the BGK method could satisfy the positivity for any Mach number. It has been shown recently, at least up to $M = 10^4$, that the BGK scheme could have positive solution[127]. Positivity is one of the essential requirements for any numerical scheme. However, even equipped with this property, the scheme cannot be guaranteed to be robust. In other words, a positive scheme does not necessarily mean that the underlying dynamical basis for the numerical fluid is reasonable, such as KFVS, Lax-Friedrichs, and even the Godunov method (more detail analysis will be given in Chapter 6). Furthermore, a positive scheme does not guarantee that the scheme could avoid numerical instabilities to blow up the program, such as the carbuncle phenomena and odd-even decoupling in the Godunov method.

4.1.3 Numerical Examples

In the following, we are going to apply the 1st-order BGK method to a few test cases.

Example 1 (Slowly Moving Shocks): We take the following initial data [100] that gives a Mach-3 shock moving to the right with a shock speed $s = 0.1096$,

$$W_1 = \begin{pmatrix} 3.86 \\ -3.1266 \\ 27.0913 \end{pmatrix} \quad \text{if} \quad 0 \leq 0.5; \qquad W_2 = \begin{pmatrix} 1.0 \\ -3.44 \\ 8.4168 \end{pmatrix} \quad \text{if} \quad 0.5 \leq x \leq 1, \tag{4.7}$$

where W represents the mass, momentum and energy densities. We have used $100, 200$ and 400 mesh points in the calculations with the CFL number 0.65. The parameter η in Eq.(4.6) is equal to 0.5. The output time is at $t = 0.95$. The density and momentum distributions around the shock front are shown in Fig(4.2) and Fig(4.3). From these figures, we observe that there is a momentum spike and its peak value is independent of mesh size (the explanation for this will be given in Chapter 6). At the same time, there are no oscillations generated even with two or three mesh points in the shock layer.

Remark(4.4)

For a slowly moving shock, the 1st-order BGK method could give both non-oscillatory and crisp numerical shock transition, which can hardly be obtained using any other

upwinding or central scheme, even the original Godunov method. However, if we reduce the number η in Eq.(4.6) to a much smaller number, such as $\eta = 0.01$, post-shock oscillations will be formed. This means that the dissipation provided in f is not enough to cope with the dissipation needed to keep a steady shock structure. This is physically reasonable because the gas in the shock regions should stay in a highly non-equilibrium state, and an equilibrium representation is inappropriate. Arora and Roe [2] pointed out the oscillatory behavior of the BGK scheme in the case with a small value of η, but they failed to mention that with a reasonable η, the smooth shock transition and oscillation free profile can be maintained by the 1st-order BGK method. From this test case, we can realize the importance of keeping the non-equilibrium property in the gas distribution function in the discontinuous region. The use of the equilibrium distribution function g_0 to represent non-equilibrium physics in the numerical shock layer, such as the Godunov and the TTT methods, will automatically lead to oscillations. The dissipative mechanism provided by the combination of two half Maxwellians with a whole Maxwellian in the BGK scheme is very special. The BGK method is more close to other physical models, such as the Mott-Smith model [88] in the construction of a numerical shock structure.

Remark(4.5)

To capture the nonequilibrium property in a fluid is a tough and challenging step. The slowly moving shock case challenges the validity of the upwinding concept in the construction of shock capturing schemes. In order to capture a smooth and sharp numerical shock structure, nonequilibrium and dissipative flow property has to be considered; the characteristic concept lacks its physical basis here because the equations are not hyperbolic anymore. The real reason for the capturing of shocks in the upwinding schemes is due to the dissipations provided in the initial condition, rather than the capturing of wave propagation in the gas evolution stage. More analysis will be given in chapter 6.

Example 2 (Stationary Shock): We take the following initial data [53] that gives a stationary shock,

$$W_1 = \begin{pmatrix} 2/3 \\ 1/\sqrt{2} \\ 8/14 \end{pmatrix} \quad \text{if} \quad 0 \le 0.5; \qquad W_2 = \begin{pmatrix} 2 \\ 1/\sqrt{2} \\ 23/14 \end{pmatrix} \quad \text{if} \quad 0.5 \le x \le 1. \tag{4.8}$$

We also use $100, 200$ and 400 mesh points in this calculation. The parameter η is again taking the value of 0.5. The output time is at $t = 2$. The density and momentum

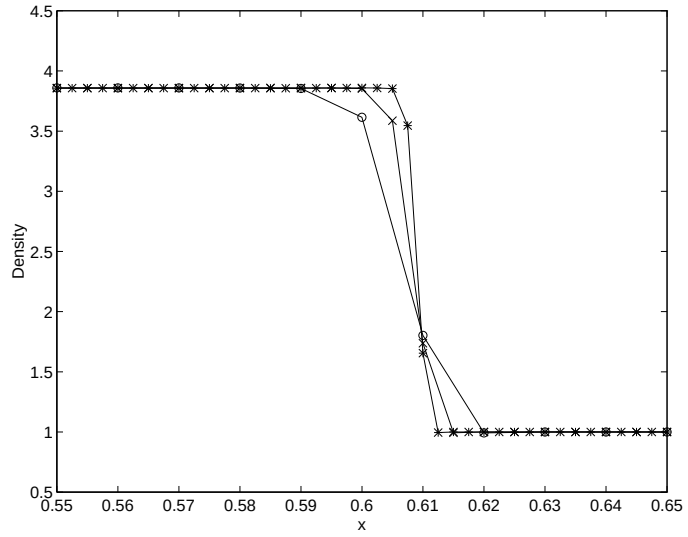

Figure 4.2: Density distribution for Example 1 using the BGK scheme,___o___$\Delta x = 0.01$, ___x___$\Delta x = 0.005$ and ___$*$___$\Delta x = 0.0025$

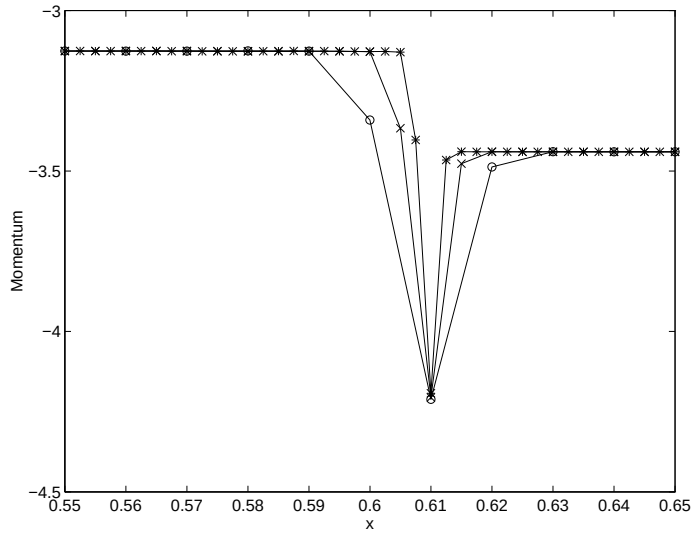

Figure 4.3: Momentum distribution for Example 1 using the BGK scheme,___o___$\Delta x = 0.01$, ___x___$\Delta x = 0.005$ and ___$*$___$\Delta x = 0.0025$

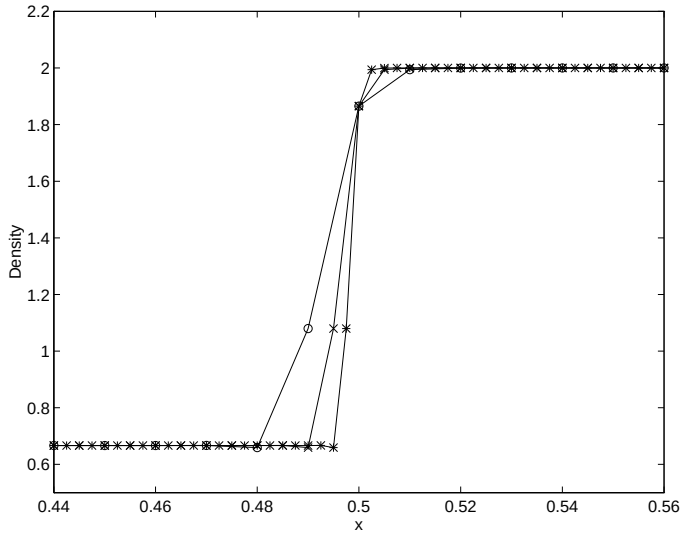

Figure 4.4: Density distribution for Example 2 using the BGK scheme, ___o___$\Delta x = 0.01$, ___x___$\Delta x = 0.005$ and ___$*$___$\Delta x = 0.0025$

distributions around the shock front are shown in Fig(4.4) and Fig(4.5). Note that the shock location is slightly off the center of the correct location because a small amount of mass has been carried away initially when the shock is settling down to its final numerical structure. In this case, we do not observe any oscillations either.

Example 3 (Strong Rarefaction Wave): The initial condition for the vacuum apparition case [30] is

$$(\rho, U, p) = \begin{cases} (1, -5, 0.4) & 0 \leq x < 100, \\ (1, 5, 0.4) & 100 \leq x \leq 200. \end{cases}$$

The CFL number is 0.65 and 200 grid points are used. It is observed numerically that the BGK method with both $\eta = 1$ and $\eta = 0$ can keep the density and pressure positive in this case. As a result, the whole scheme is positive for any value of $\eta \in [0, 1]$ in this case [118]. With $\eta = 0$, the numerical results for density, velocity and pressure at $t = 10$ are shown in Fig.(4.6). Even with $\rho \sim 10^{-11}$, the internal energy is still positive in our calculations. Note that conservative variables are used in the BGK method, the pressure is a passive quantity derived from conservative variables. This test case is an extreme case for a strong expansion wave.

Remark(4.6)

It is commonly true that we can use special test cases to validate or test different schemes. However, before we set up a special test case, we should realize clearly the applicability of the original equations we are trying to solve. It is rather pointless to

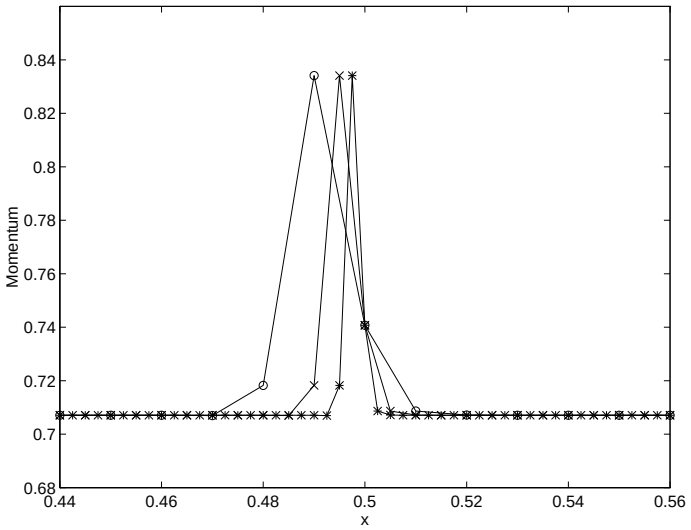

Figure 4.5: Momentum distribution for Example 2 using the BGK scheme,___o___$\Delta x = 0.01$, ___x___$\Delta x = 0.005$ and ___$*$___$\Delta x = 0.0025$

set up more and more stronger expansion waves in order to prove the advantage of any specific flow solver. As we know, as $\rho \to 0$, the flow motion can only be described by rarefied gas dynamics, such as the collisionless Boltzmann equation or the BGK model. The Euler and Navier-Stokes equations give inappropriate description here. So, it is not surprising that gas-kinetic schemes are much more robust for rarefaction wave than any other shock capturing scheme based on the inviscid Euler or viscous Navier-Stokes equations.

4.2 2nd-order BGK Method in 1-D Case

A numerical scheme basically solves an IVP locally. Therefore, we need to know both the initial condition and the governing equations. The reconstruction stage is a process to prepare the initial data, and the gas evolution stage is a process to get the solution of the governing equations under this initial condition.

4.2.1 Initial Reconstruction

For a high resolution scheme, reconstruction techniques are used to interpolate the cell averaged mass, momentum and energy densities. Simple polynomial expansion usually generates spurious overshoot and undershoot, or even oscillations if large variations in data are present initially. The most successful and reliable interpolation techniques known so far is the TVD principle[39], and this concept can be dated back to Boris and

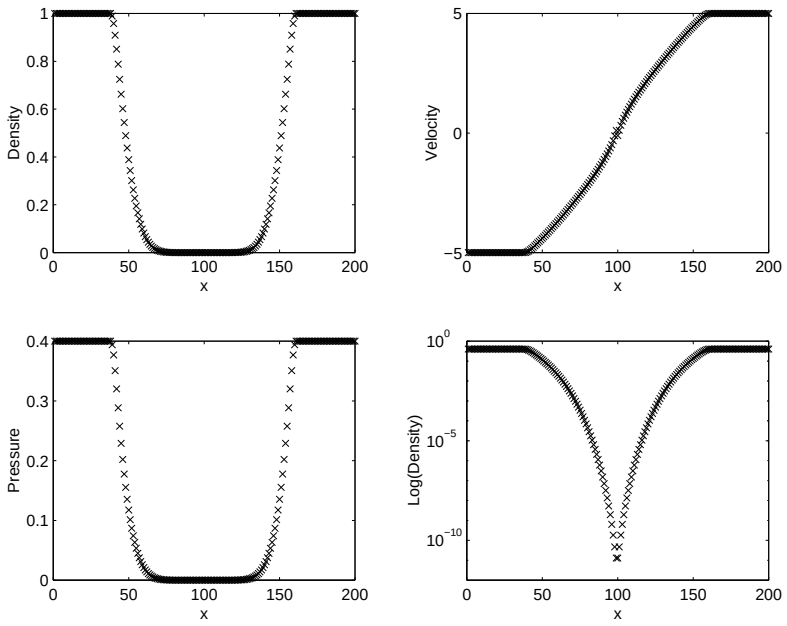

Figure 4.6: Strong expansion wave case using 1st-order BGK method

Book [7].

For the BGK method, the reconstruction techniques are applied to the conservative variables directly. Let $x_j = jh$ $(j = 0, 1, 2, ...)$ be a uniform mesh and h the mesh size. Let $x_{j+\frac{1}{2}} = (j + \frac{1}{2})h$ be the interface between cells j and $j + 1$. The cell averaged mass, momentum and energy densities are denoted by W_j, and its interpolated value in cell j is $\bar{W}_j(x)$, where $\bar{W}_j(x_{j-1/2})$ and $\bar{W}_j(x_{j+1/2})$ are two pointwise values in cell j at the locations $x_{j-1/2}$ and $x_{j+1/2}$. To second order accuracy, the interpolated value in the j-th cell can be formally written as

$$\bar{W}_j(x) = W_j + L(s_{j+}, s_{j-})(x - x_j) \quad \text{for} \quad x_{j-1/2} \leq x \leq x_{j+1/2},$$

where all standard nonlinear limiters can be used in the construction of $L(s_{j+}, s_{j-})$. For example, with $s_{j+} = (W_{j+1} - W_j)/h$ and $s_{j-} = (W_j - W_{j-1})/h$, the MUSCL limiter is

$$L(s_{j+}, s_{j-}) = S(s_{j+}, s_{j-}) \min(\frac{1}{2}|s_{j+} + s_{j-}|, 2|s_{j+}|, 2|s_{j-}|),$$

and the van Leer limiter stands for

$$L(s_{j+}, s_{j-}) = S(s_{j+}, s_{j-}) \frac{2|s_{j+}||s_{j-}|}{|s_{j+}| + |s_{j-}|},$$

where $S(s_{j+}, s_{j-})$ is the sign function. These two limiters are commonly used in flow calculations for the BGK scheme. After data reconstruction, the flow variables at the two end points $x_{j-1/2}$ and $x_{j+1/2}$ in the cell j become

$$\bar{W}_j(x_{j-1/2}) = W_j - \frac{1}{2}hL(s_{j+}, s_{j-}) \text{ and } \bar{W}_j(x_{j+1/2}) = W_j + \frac{1}{2}hL(s_{j+}, s_{j-}).$$

At the same time, to the second order of accuracy, the value of the reconstructed $\bar{W}$ at cell center x_j is equal to the cell averaged initial value, such that $\bar{W}_j(x_j) = W_j$.

4.2.2 The Gas Evolution Stage

For 1-D gas flow, the BGK model is

$$f_t + uf_x = \frac{g - f}{\tau}, \tag{4.9}$$

where both f and g are functions of space x, time t, particle velocity u and internal variable ξ. Due to the mass, momentum and energy conservations in the process of particle collisions, f and g satisfy the compatibility condition,

$$\int\int \frac{g - f}{\tau}\psi_\alpha d\Xi = 0, \qquad \alpha = 1, 2, 3. \tag{4.10}$$

where $d\Xi = dud\xi$ and

$$\psi_\alpha = (1, u, \frac{1}{2}(u^2 + \xi^2))^T. \tag{4.11}$$

Physically, the particle collision time τ depends on the local macroscopic flow variables, such as temperature and density. However, due to the finite cell size and time step, the particle collision time used in the calculation will also include an artificial term to account for the fact that the smallest numerical shock thickness is the cell size instead of the physical shock thickness. In other words, in the discontinuous shock region, the mean free path for the numerical fluid should be at least on the same scale as the cell size.

For the BGK model, the equivalent integral solution of f at the cell interface $x_{j+1/2}$ and time t is [62],

$$f(x_{j+1/2}, t, u, \xi) = \frac{1}{\tau}\int_0^t g(x', t', u, \xi)e^{-(t-t')/\tau}dt' + e^{-t/\tau}f_0(x_{j+1/2} - ut), \tag{4.12}$$

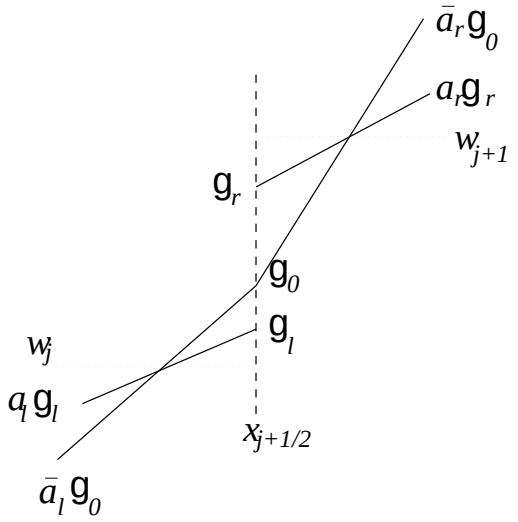

Figure 4.7: Initial condition for the 2nd-order BGK method

where $x' = x_{j+1/2} - u(t - t')$ is the trajectory of a particle motion, f_0 is the real gas distribution function f at the beginning of each time step ($t = 0$), and g is the corresponding equilibrium state in space and time around the point $(x_{j+1/2}, t = 0)$. Both g and f_0 must be specified in Eq.(4.12) in order to obtain the solution f.

For the second-order scheme, f_0 and g around the cell interface $x_{j+1/2}$ are constructed as

$$f_0 = \begin{cases} g_l \left(1 + a_l(x - x_{j+1/2})\right), & x \leq x_{j+1/2}, \\ g_r \left(1 + a_r(x - x_{j+1/2})\right), & x \geq x_{j+1/2}, \end{cases} \tag{4.13}$$

and

$$g = g_0 \left(1 + (1 - \mathrm{H}(x - x_{j+1/2}))\bar{a}_l(x - x_{j+1/2}) + \mathrm{H}(x - x_{j+1/2})\bar{a}_r(x - x_{j+1/2}) + \bar{A}t\right), \tag{4.14}$$

where g_l, g_r and g_0 are local Maxwellian distribution functions located to the left, to the right and in the middle of a cell interface, $a_l, a_r, \bar{a}_l$ and $\bar{a}_r$ the corresponding slopes, and $\mathrm{H}(x)$ the Heaviside function. The schematic description of the initial data for both f_0 and g are shown in Fig.(4.7). The dependence of $a_l, a_r, ..., \bar{A}$ on the particle velocities is obtained from the Taylor expansion of a Maxwellian and have the form

$$a_l = a_{1l} + a_{2l}u + a_{3l}\frac{1}{2}(u^2 + \xi^2) = a_{\alpha l}\psi_\alpha,$$

$$a_r = a_{1r} + a_{2r}u + a_{3r}\frac{1}{2}(u^2 + \xi^2) = a_{\alpha r}\psi_\alpha,$$

$$\bar{a}_r = \bar{a}_{1r} + \bar{a}_{2r}u + \bar{a}_{3r}\frac{1}{2}(u^2+\xi^2) = \bar{a}_{\alpha r}\psi_\alpha,$$

$$\bar{a}_l = \bar{a}_{1l} + \bar{a}_{2l}u + \bar{a}_{3l}\frac{1}{2}(u^2+\xi^2) = \bar{a}_{\alpha l}\psi_\alpha,$$

$$\bar{A} = \bar{A}_1 + \bar{A}_2u + \bar{A}_3\frac{1}{2}(u^2+\xi^2) = \bar{A}_\alpha\psi_\alpha,$$

where all coefficients $a_{1l}, a_{2l}, ..., \bar{A}_3$ are local constants. The idea of interpolating f_0 separately in the regions $x \le x_{j+1/2}$ and $x \ge x_{j+1/2}$ originates from the following physical consideration: for a non-equilibrium gas flow, since the cell size is usually much larger than the thickness of a discontinuity, physical quantities can change dramatically in space. For example, across a shock front, the upstream and downstream gas distribution functions could be two different Maxwellians. Therefore, we need the splitting of f_0 to capture this possible physical reality.

In the reconstruction stage described in Section(4.2.1), we have obtained $\bar{\rho}_j(x), \bar{\rho}_j\bar{U}_j(x)$ and $\bar{\rho}_j\bar{\epsilon}_j(x)$ in each cell $x_{j-1/2} \le x \le x_{j+1/2}$. The left and right side pointwise values at the cell interface $x_{j+1/2}$ are

$$\left(\bar{\rho}_j(x_{j+1/2}) \ , \ \bar{\rho}_{j+1}(x_{j+1/2})\right),$$

$$\left(\bar{\rho}_j\bar{U}_j(x_{j+1/2}) \ , \ \bar{\rho}_{j+1}\bar{U}_{j+1}(x_{j+1/2})\right),$$

$$\left(\bar{\rho}_j\bar{\epsilon}_j(x_{j+1/2}) \ , \ \bar{\rho}_{j+1}\bar{\epsilon}_{j+1}(x_{j+1/2})\right).$$

By using the relation between the gas distribution function f_0 and the macroscopic variables, we get

$$\int \psi_\alpha g_l d\Xi = \begin{pmatrix} \bar{\rho}_j(x_{j+1/2}) \\ \bar{\rho}_j\bar{U}_j(x_{j+1/2}) \\ \bar{\rho}_j\bar{\epsilon}_j(x_{j+1/2}) \end{pmatrix} \ ; \ \int \psi_\alpha a_l g_l d\Xi = \begin{pmatrix} \frac{\bar{\rho}_j(x_{j+1/2})-\bar{\rho}_j(x_j)}{\Delta x^-} \\ \frac{\bar{\rho}_j\bar{U}_j(x_{j+1/2})-\bar{\rho}_j\bar{U}_j(x_j)}{\Delta x^-} \\ \frac{\bar{\rho}_j\bar{\epsilon}_j(x_{j+1/2})-\bar{\rho}_j\bar{\epsilon}_j(x_j)}{\Delta x^-} \end{pmatrix}$$

and

$$\int \psi_\alpha g_r d\Xi = \begin{pmatrix} \bar{\rho}_{j+1}(x_{j+1/2}) \\ \bar{\rho}_{j+1}\bar{U}_{j+1}(x_{j+1/2}) \\ \bar{\rho}_{j+1}\bar{\epsilon}_{j+1}(x_{j+1/2}) \end{pmatrix} \ ; \ \int \psi_\alpha a_r g_r d\Xi = \begin{pmatrix} \frac{\bar{\rho}_{j+1}(x_{j+1})-\bar{\rho}_{j+1}(x_{j+1/2})}{\Delta x^+} \\ \frac{\bar{\rho}_{j+1}\bar{U}_{j+1}(x_{j+1})-\bar{\rho}_{j+1}\bar{U}_{j+1}(x_{j+1/2})}{\Delta x^+} \\ \frac{\bar{\rho}_{j+1}\bar{\epsilon}_{j+1}(x_{j+1})-\bar{\rho}_{j+1}\bar{\epsilon}_{j+1}(x_{j+1/2})}{\Delta x^+} \end{pmatrix}, \tag{4.15}$$

where $\Delta x^- = x_{j+1/2} - x_j$ and $\Delta x^+ = x_{j+1} - x_{j+1/2}$. With the definition of the Maxwellian distribution functions

$$g_l = \rho_l (\frac{\lambda_l}{\pi})^{\frac{K+1}{2}} e^{-\lambda_l((u-U_l)^2+\xi^2)},$$

$$g_r = \rho_r (\frac{\lambda_r}{\pi})^{\frac{K+1}{2}} e^{-\lambda_r((u-U_r)^2+\xi^2)},$$

and from Eq.(4.15), all parameters in g_l and g_r can be uniquely determined, for example

$$\begin{pmatrix} \rho_l \\ U_l \\ \lambda_l \end{pmatrix} = \begin{pmatrix} \bar{\rho}_j(x_{j+1/2}) \\ \bar{U}_j(x_{j+1/2}) \\ \frac{(K+1)\bar{\rho}_j(x_{j+1/2})}{4\left(\bar{\rho}_j\bar{\epsilon}_j(x_{j+1/2}) - \frac{1}{2}\bar{\rho}_j\bar{U}_j^2(x_{j+1/2})\right)} \end{pmatrix}$$

and

$$\begin{pmatrix} \rho_r \\ U_r \\ \lambda_r \end{pmatrix} = \begin{pmatrix} \bar{\rho}_{j+1}(x_{j+1/2}) \\ \bar{U}_{j+1}(x_{j+1/2}) \\ \frac{(K+1)\bar{\rho}_{j+1}(x_{j+1/2})}{4\left(\bar{\rho}_{j+1}\bar{\epsilon}_{j+1}(x_{j+1/2}) - \frac{1}{2}\bar{\rho}_{j+1}\bar{U}_{j+1}^2(x_{j+1/2})\right)} \end{pmatrix}.$$

On the right hand side of a cell interface, once g_r is obtained from the above equations, the slope a_r can be computed from

$$\frac{1}{\rho_r}\begin{pmatrix} \frac{\bar{\rho}_{j+1}(x_{j+1}) - \bar{\rho}_{j+1}(x_{j+1/2})}{\Delta x^+} \\ \frac{\bar{\rho}_{j+1}\bar{U}_{j+1}(x_{j+1}) - \bar{\rho}_{j+1}\bar{U}_{j+1}(x_{j+1/2})}{\Delta x^+} \\ \frac{\bar{\rho}_{j+1}\bar{\epsilon}_{j+1}(x_{j+1}) - \bar{\rho}_{j+1}\bar{\epsilon}_{j+1}(x_{j+1/2})}{\Delta x^+} \end{pmatrix} \equiv \frac{1}{\rho_r}\begin{pmatrix} (\frac{\partial \rho}{\partial x})^r \\ (\frac{\partial(\rho U)}{\partial x})^r \\ (\frac{\partial(\rho \epsilon)}{\partial x})^r \end{pmatrix} = M^r_{\alpha\beta}\begin{pmatrix} a_{1r} \\ a_{2r} \\ a_{3r} \end{pmatrix}, \tag{4.16}$$

where the matrix $M^r_{\alpha\beta} = \frac{1}{\rho_r}\int \psi_\alpha \psi_\beta g_r d\Xi$ has the form

$$M^r_{\alpha\beta} = \begin{pmatrix} 1 & U_r & \frac{1}{2}(U_r^2 + \frac{K+1}{2\lambda_r}) \\ U_r & U_r^2 + \frac{1}{2\lambda_r} & \frac{1}{2}(U_r^3 + \frac{(K+3)U_r}{2\lambda_r}) \\ \frac{1}{2}(U_r^2 + \frac{K+1}{2\lambda_r}) & \frac{1}{2}(U_r^3 + \frac{(K+3)U_r}{2\lambda_r}) & \frac{1}{4}(U_r^4 + \frac{(K+3)U_r^2}{\lambda_r} + \frac{(K^2+4K+3)}{4\lambda_r^2}) \end{pmatrix}.$$

From Eq.(4.16), $(a_{1r}, a_{2r}, a_{3r})^T$ can readily be obtained,

$$a_{3r} = \frac{4\lambda_r^2}{K+1}(2(\frac{\partial \epsilon}{\partial x})^r - 2U_r(\frac{\partial U}{\partial x})^r),$$

$$a_{2r} = 2\lambda_r((\frac{\partial U}{\partial x})^r - \frac{U_r}{2\lambda_r}a_{3r}),$$

$$a_{1r} = \frac{1}{\rho_r}(\frac{\partial \rho}{\partial x})^r - U_r a_{2r} - (\frac{U_r^2}{2} + \frac{K+1}{4\lambda_r})a_{3r}, \tag{4.17}$$

where

$$(\frac{\partial U}{\partial x})^r = \frac{1}{\rho_r}((\frac{\partial(\rho U)}{\partial x})^r - U_r(\frac{\partial \rho}{\partial x})^r),$$

$$(\frac{\partial \epsilon}{\partial x})^r = \frac{1}{\rho_r}((\frac{\partial(\rho \epsilon)}{\partial x})^r - \frac{1}{2}(U_r^2 + \frac{K+1}{2\lambda_r})(\frac{\partial \rho}{\partial x})^r).$$

On the left hand side, since the matrix $M^l_{\alpha\beta} = \frac{1}{\rho_l}\int \psi_\alpha \psi_\beta g_l d\Xi$ has the same structure as $M^r_{\alpha\beta}$, $(a_{1l}, a_{2l}, a_{3l})^T$ can be obtained similarly.

After determining f_0, the corresponding values of ρ_0, U_0 and λ_0 in g_0

$$g_0 = \rho_0(\frac{\lambda_0}{\pi})^{\frac{K+1}{2}} e^{-\lambda_0((u-U_0)^2+\xi^2)}$$

can be determined as follows. Taking the limit $t \to 0$ in Eq.(4.12) and substituting its solution into Eq.(4.10) yield

$$\int\int g_0 \psi_\alpha d\Xi = \int_{u>0}\int \psi_\alpha g_l d\Xi + \int_{u<0}\int \psi_\alpha g_r d\Xi, \qquad \alpha = 1,2,3. \tag{4.18}$$

Since λ_0 in g_0 can be found from $\rho_0, \rho_0 U_0$ and $\rho_0 \epsilon_0$ through the relation

$$\lambda_0 = (K+1)\rho_0/(4(\rho_0\epsilon_0 - \frac{1}{2}\rho_0 {U_0}^2)),$$

we only need to know $(\rho_0, \rho_0 U_0, \rho_0 \epsilon_0)^T$, which can be expressed as moments of g_l and g_r. By introducing the notation

$$\rho_l < ... >_{>0} = \int_{u>0}\int (...) g_l d\Xi,$$

$$\rho_r < ... >_{<0} = \int_{u<0}\int (...) g_r d\Xi,$$

Eq.(4.18) is equivalent to

$$\begin{pmatrix} \rho_0 \\ \rho_0 U_0 \\ \rho_0 \epsilon_0 \end{pmatrix} = \begin{pmatrix} \rho_l < u^0 >_{>0} + \rho_r < u^0 >_{<0} \\ \rho_l < u^1 >_{>0} + \rho_r < u^1 >_{<0} \\ 1/2(\rho_l < u^2 + \xi^2 >_{>0} + \rho_r < u^2 + \xi^2 >_{<0}) \end{pmatrix}. \tag{4.19}$$

A complete table of moments of the Maxwellian is included in Appendix B. After obtaining g_0, $\bar{a}_l$ and $\bar{a}_r$ of g in Eq.(4.14) can be found through the relation

$$\frac{1}{\rho_0}\begin{pmatrix} \frac{\bar{\rho}_{j+1}(x_{j+1}) - \rho_0}{\Delta x^+} \\ \frac{\bar{\rho}_{j+1}\bar{U}_{j+1}(x_{j+1}) - \rho_0 U_0}{\Delta x^+} \\ \frac{\bar{\rho}_{j+1}\bar{\epsilon}_{j+1}(x_{j+1}) - \rho_0 \epsilon_0}{\Delta x^+} \end{pmatrix} = \bar{M}^0_{\alpha\beta}\begin{pmatrix} \bar{a}_{1r} \\ \bar{a}_{2r} \\ \bar{a}_{3r} \end{pmatrix},$$

and

$$\frac{1}{\rho_0}\begin{pmatrix} \frac{\rho_0-\bar{\rho}_j(x_j)}{\Delta x^-} \\ \frac{\rho_0 U_0-\bar{\rho}_j\bar{U}_j(x_j)}{\Delta x^-} \\ \frac{\rho_0\epsilon_0-\bar{\rho}_j\bar{\epsilon}_j(x_j)}{\Delta x^-} \end{pmatrix} = \bar{M}^0_{\alpha\beta}\begin{pmatrix} \bar{a}_{1l} \\ \bar{a}_{2l} \\ \bar{a}_{3l} \end{pmatrix}.$$

The matrix $\bar{M}^0_{\alpha\beta} = \frac{1}{\rho_0}\int \psi_\alpha\psi_\beta g_0 d\Xi$ has the same structure as $M^r_{\alpha\beta}$, which is

$$\bar{M}^0_{\alpha\beta} = \begin{pmatrix} 1 & U_0 & \frac{1}{2}(U_0^2+\frac{K+1}{2\lambda_0}) \\ U_0 & U_0^2+\frac{1}{2\lambda_0} & \frac{1}{2}(U_0^3+\frac{(K+3)U_0}{2\lambda_0}) \\ \frac{1}{2}(U_0^2+\frac{K+1}{2\lambda_0}) & \frac{1}{2}(U_0^3+\frac{(K+3)U_0}{2\lambda_0}) & \frac{1}{4}(U_0^4+\frac{(K+3)U_0^2}{\lambda_0}+\frac{(K^2+4K+3)}{4{\lambda_0}^2}) \end{pmatrix}.$$

Therefore, $(\bar{a}_{1r},\bar{a}_{2r},\bar{a}_{3r})^T$ and $(\bar{a}_{1l},\bar{a}_{2l},\bar{a}_{3l})^T$ can be obtained by following the procedure in Eq.(4.17).

Up to this point, we have obtained the initial gas distribution function f_0 and the corresponding equilibrium state g_0 at the cell interface $x_{j+1/2}$. At the same time, all spatial slopes in the expression of f_0 and g, *i.e.* a_l, a_r and $\bar{a}_l, \bar{a}_r$, are determined from the slopes of the reconstructed macroscopic variables (see Fig.(4.7)). For the Navier-Stokes solutions, the slopes of $\bar{a}_l$ and $\bar{a}_r$ are related to the the viscosity and heat conduction effects [137], and the validation of the Navier-Stokes solutions from the BGK scheme will be presented in the numerical part. After substituting Eq.(4.13) and Eq.(4.14) into Eq.(4.12), the final gas distribution function at a cell interface can be expressed as

$$\begin{aligned} f(x_{j+1/2},t,u,\xi) &= (1-e^{-t/\tau})g_0 \\ &\quad + \left(\tau(-1+e^{-t/\tau})+te^{-t/\tau}\right)\left(\bar{a}_l\mathrm{H}(u)+\bar{a}_r(1-\mathrm{H}(u))\right)ug_0 \\ &\quad +\tau(t/\tau-1+e^{-t/\tau})\bar{A}g_0 \\ &\quad +e^{-t/\tau}\left((1-uta_l)\mathrm{H}(u)g_l+(1-uta_r)(1-\mathrm{H}(u))g_r\right). \end{aligned} \tag{4.20}$$

The only unknown term in the above equation is $\bar{A}$. Since both f (Eq.(4.20)) and g (Eq.(4.14)) contain the common $\bar{A}$, applying the compatibility constraint at $x_{j+1/2}$ and integrating it over the whole time step Δt yield

$$\int_0^{\Delta t}\int (g-f)\psi_\alpha dt d\Xi = 0,$$

which gives

$$\bar{M}^0_{\alpha\beta}\bar{A}_\beta = \frac{1}{\rho_0}\int \left[\gamma_1 g_0+\gamma_2 u\left(\bar{a}_l\mathrm{H}[u]+\bar{a}_r(1-\mathrm{H}[u])\right)g_0\right.$$

$$
\begin{aligned}
&+ \quad \gamma_3 \left(\mathrm{H}[u] g_l + (1 - \mathrm{H}[u]) g_r\right) \\
&+ \quad \gamma_4 u \left(a_l \mathrm{H}[u] g_l + a_r (1 - \mathrm{H}[u]) g_r)\right] \psi_\alpha d\Xi, \qquad (4.21)
\end{aligned}
$$

where

$$
\begin{aligned}
\gamma_0 &= \Delta t - \tau(1 - e^{-\Delta t/\tau}), \\
\gamma_1 &= -(1 - e^{-\Delta t/\tau})/\gamma_0, \\
\gamma_2 &= \left(-\Delta t + 2\tau(1 - e^{-\Delta t/\tau}) - \Delta t e^{-\Delta t/\tau}\right)/\gamma_0, \\
\gamma_3 &= (1 - e^{-\Delta t/\tau})/\gamma_0, \\
\gamma_4 &= \left(\Delta t e^{-\Delta t/\tau} - \tau(1 - e^{-\Delta t/\tau})\right)/\gamma_0. \qquad (4.22)
\end{aligned}
$$

All moments of the Maxwellian on the right hand side of Eq.(4.21) can be obtained from the table in Appendix B and $(\bar{A}_1, \bar{A}_2, \bar{A}_3)^T$ can subsequently be evaluated.

Finally, the time-dependent numerical fluxes across the cell interface can be computed as

$$
\begin{pmatrix} \mathcal{F}_\rho \\ \mathcal{F}_{\rho U} \\ \mathcal{F}_{\rho\epsilon} \end{pmatrix}_{j+1/2} = \int u \begin{pmatrix} 1 \\ u \\ \frac{1}{2}(u^2 + \xi^2) \end{pmatrix} f(x_{j+1/2}, t, u, \xi) d\Xi, \qquad (4.23)
$$

where $f(x_{j+1/2}, t, u, \xi)$ is given in Eq.(4.20). By integrating the above equation for a whole time step, we get the total mass, momentum and energy transport. These fluxes satisfy the consistency condition of $\mathcal{F}(U, U) = \mathcal{F}(U)$ for a homogeneous uniform flow, where $\mathcal{F}(U)$ are the corresponding Euler fluxes.

4.3 2-D BGK Method

In the 2-Dimensional case, the BGK scheme is designed to solve the following the 2-D compressible Navier-Stokes equations in smooth regions:

$$
\begin{pmatrix} \rho \\ \rho U \\ \rho V \\ \rho\epsilon \end{pmatrix}_t + \begin{pmatrix} \rho U \\ \rho U^2 + p \\ \rho UV \\ (\rho\epsilon + p)U \end{pmatrix}_x + \begin{pmatrix} \rho V \\ \rho UV \\ \rho V^2 + p \\ (\rho\epsilon + p)V \end{pmatrix}_y = \begin{pmatrix} 0 \\ s_{1x} \\ s_{2x} \\ s_{3x} \end{pmatrix}_x + \begin{pmatrix} 0 \\ s_{1y} \\ s_{2y} \\ s_{3y} \end{pmatrix}_y, \qquad (4.24)
$$

where

$$
s_{1x} = \tau p[2\frac{\partial U}{\partial x} - \frac{2}{5}(\frac{\partial U}{\partial x} + \frac{\partial V}{\partial y})],
$$

$$s_{1y} = \tau p(\frac{\partial U}{\partial y} + \frac{\partial V}{\partial x}),$$

$$s_{2x} = \tau p(\frac{\partial V}{\partial x} + \frac{\partial U}{\partial y}),$$

$$s_{2y} = \tau p[2\frac{\partial V}{\partial y} - \frac{2}{5}(\frac{\partial U}{\partial x} + \frac{\partial V}{\partial y})],$$

$$s_{3x} = \tau p[2U\frac{\partial U}{\partial x} + V(\frac{\partial V}{\partial x} + \frac{\partial U}{\partial y}) - \frac{2}{5}U(\frac{\partial U}{\partial x} + \frac{\partial V}{\partial y}) + \frac{7}{4}\frac{\partial}{\partial x}(\frac{1}{\lambda})],$$

$$s_{3y} = \tau p[U(\frac{\partial U}{\partial y} + \frac{\partial V}{\partial x}) + 2V\frac{\partial V}{\partial y} - \frac{2}{5}V(\frac{\partial U}{\partial x} + \frac{\partial V}{\partial y}) + \frac{7}{4}\frac{\partial}{\partial y}(\frac{1}{\lambda})].$$

The BGK model in the 2-D case is

$$f_t + uf_x + vf_y = \frac{g - f}{\tau},$$

and the compatibility condition is

$$\int\int \frac{g - f}{\tau}\psi_\alpha d\Xi = 0, \qquad \alpha = 1, 2, 3, 4, \tag{4.25}$$

where $d\Xi = dudvd\xi$ and

$$\psi_\alpha = (1, u, v, \frac{1}{2}(u^2 + v^2 + \xi^2))^T. \tag{4.26}$$

In order to use the BGK model to obtain the time dependent gas distribution function f, we need to reconstruct the initial conditions for both f and g at the beginning of each time step, and the construction depends on the initial distribution of the macroscopic variables. From the cell averaged mass, momentum and energy densities, we can reconstruct the initial data in each cell (i, j) using nonlinear limiters. For example, in the 2-D case, for the cell (i, j), the cell center is at $(x_{i,j}, y_{i,j})$ and cell averaged flow variables are $W_{i,j}$. After reconstruction, the flow distribution in this cell can be written as

$$\bar{W}_{i,j}(x, y) = W_{i,j} + L_x(W, W)(x - x_{i,j}) + L_y(W, W)(y - y_{i,j}),$$

where $W_{i,j}$ is the cell averaged initial data, and $L_x(W, W), L_y(W, W)$ the nonlinear limiters, such that

$$L_x(W, W) = L_x\left(\frac{W_{i+1,j} - W_{i,j}}{x_{i+1,j} - x_{i,j}}, \frac{W_{i,j} - W_{i-1,j}}{x_{i,j} - x_{i-1,j}}\right),$$

and

$$L_y(W,W) = L_x\left(\frac{W_{i,j+1}-W_{i,j}}{x_{i,j+1}-x_{i,j}}, \frac{W_{i,j}-W_{i,j-1}}{x_{i,j}-x_{i,j-1}}\right).$$

From the above initial condition, in the gas evolution stage, the BGK scheme could generate "waves" moving in any direction, not necessarily parallel to the cell interface. In other words, the time evolution of f takes into account both gradients of flow variables in the x and y directions. Basically, the BGK method provides a multidimensional gas evolution scheme, it is different from directional splitting schemes, where Eq.(4.24) is solved in two parts, *i.e.*

$$W_t + F(W)_x = S_x$$

in x-direction and

$$W_t + G(W)_y = S_y$$

in the y-direction.

Let's define the center of the cell boundary between cells (i,j) and $(i+1,j)$ as $(x_{i+1/2,j}, y_{i+1/2,j})$. For simplicity, $(x_{i+1/2,j} = 0, y_{i+1/2,j} = 0)$ is assumed. In order to evaluate the fluxes across the cell interface between (i,j) and $(i+1,j)$, the initial gas distribution function f_0 can be constructed as

$$\begin{aligned} f_0(x,y,0) &= \begin{cases} g_l(1+a_l x + b_l y), & x<0 \\ g_r(1+a_r x + b_r y), & x>0 \end{cases} \\ &= g_l(1+a_l x + b_l y)(1-\mathrm{H}(x)) + g_r(1+a_r x + b_r y)\mathrm{H}(x), \end{aligned} \tag{4.27}$$

where g_l and g_r are local Maxwellians at the left and right sides of the cell interface, and have the general forms

$$g_l = \rho_l(\frac{\lambda_l}{\pi})^{(K+2)/2} e^{-\lambda_l((u-U_l)^2+(v-V_l)^2+\xi^2)},$$

and

$$g_r = \rho_r(\frac{\lambda_r}{\pi})^{(K+2)/2} e^{-\lambda_r((u-U_r)^2+(v-V_r)^2+\xi^2)}.$$

The terms a_l, b_l, a_r and b_r in Eq.(4.27) are from the Taylor expansion of a Maxwellian and have the form

$$a_l = a_{1l} + a_{2l}u + a_{3l}v + a_{4l}\frac{1}{2}(u^2+v^2+\xi^2),$$

$$b_l = b_{1l} + b_{2l}u + b_{3l}v + b_{4l}\frac{1}{2}(u^2 + v^2 + \xi^2),$$

$$a_r = a_{1r} + a_{2r}u + a_{3r}v + a_{4r}\frac{1}{2}(u^2 + v^2 + \xi^2),$$

$$b_r = b_{1r} + b_{2r}u + b_{3r}v + b_{4r}\frac{1}{2}(u^2 + v^2 + \xi^2).$$

With the relation between macroscopic variables and microscopic gas distribution function,

$$\bar{W} = \int \psi_\alpha f_0 d\Xi,$$

both g_l and g_r as well as their slopes in Eq.(4.27) can be obtained from the reconstructed initial data in cells (i, j) and $(i+1, j)$. For example, in cell (i, j), with the reconstructed data $\bar{W}_{i,j}(x, y) = W_{i,j} + L_x(x - x_{i,j}) + L_y(y - y_{i,j})$, we can obtain g_l first from the macroscopic variable $\bar{W}_{i,j}(x_{i+1/2,j}, y_{i+1/2,j})$. At the same time, a_l and b_l can be obtained using the relations

$$\frac{1}{\rho_l}L_x = \frac{1}{\rho_l}\begin{pmatrix} (\partial\rho/\partial x)^l \\ (\partial(\rho U)/\partial x)^l \\ (\partial(\rho V)/\partial x)^l \\ (\partial(\rho\epsilon)/\partial x)^l \end{pmatrix} = \frac{1}{\rho_l}\int \psi_\alpha a_l g_l d\Xi = M_l \begin{pmatrix} a_{1l} \\ a_{2l} \\ a_{3l} \\ a_{4l} \end{pmatrix}, \tag{4.28}$$

and

$$\frac{1}{\rho_l}L_y = \frac{1}{\rho_l}\begin{pmatrix} (\partial\rho/\partial y)^l \\ (\partial(\rho U)/\partial y)^l \\ (\partial(\rho V)/\partial y)^l \\ (\partial(\rho\epsilon)/\partial y)^l \end{pmatrix} = \frac{1}{\rho_l}\int \psi_\alpha b_l g_l d\Xi = M_l \begin{pmatrix} b_{1l} \\ b_{2l} \\ b_{3l} \\ b_{4l} \end{pmatrix}. \tag{4.29}$$

The matrix $M_l = \frac{1}{\rho_l}\int \psi_\alpha \psi_\beta g_l d\Xi$ is a function of the parameters (U_l, V_l, λ_l) in g_l, which has the form

$$M_l = \begin{pmatrix} 1 & U_l & V_l & \mathcal{B}_1 \\ U_l & U_l^2 + 1/2\lambda_l & U_l V_l & \mathcal{B}_2 \\ V_l & U_l V_l & V_l^2 + 1/2\lambda_l & \mathcal{B}_3 \\ \mathcal{B}_1 & \mathcal{B}_2 & \mathcal{B}_3 & \mathcal{B}_4 \end{pmatrix}, \tag{4.30}$$

where

$$\mathcal{B}_1 = \frac{1}{2}(U_l^2 + V_l^2 + (K+2)/2\lambda_l),$$

$$\mathcal{B}_2 = \frac{1}{2}(U_l^3 + V_l^2 U_l + (K+4)U_l/2\lambda_l),$$

$$\mathcal{B}_3 = \frac{1}{2}(V_l^3 + U_l^2 V_l + (K+4)V_l/2\lambda_l)$$

and

$$\mathcal{B}_4 = \frac{1}{4}\left((U_l^2+V_l^2)^2 + (K+4)(U_l^2+V_l^2)/\lambda_l + (K^2+6K+8)/4\lambda_l^2\right).$$

The above symmetric matrix can be easily inverted, and the solutions for a_l and a_r in Eq.(4.28) can be expressed as

$$a_{4l} = \frac{4\lambda_l^2}{K+2}\left(2(\frac{\partial \epsilon}{\partial x})^l - 2U_l(\frac{\partial U}{\partial x})^l - 2V_l(\frac{\partial V}{\partial x})^l\right),$$

$$a_{3l} = 2\lambda_l\left((\frac{\partial V}{\partial x})^l - \frac{V_l}{2\lambda_l}a_{4l}\right),$$

$$a_{2l} = 2\lambda_l\left((\frac{\partial U}{\partial x})^l - \frac{U_l}{2\lambda_l}a_{4l}\right),$$

$$a_{1l} = \frac{1}{\rho_l}(\frac{\partial \rho}{\partial x})^l - U_l a_{2l} - V_l a_{3l} - \frac{1}{2}\left(U_l^2 + V_l^2 + \frac{K+1}{2\lambda_l}\right)a_{4l},$$

where

$$(\frac{\partial U}{\partial x})^l = \frac{1}{\rho_l}\left((\frac{\partial(\rho U)}{\partial x})^l - U_l(\frac{\partial \rho}{\partial x})^l\right),$$

$$(\frac{\partial V}{\partial x})^l = \frac{1}{\rho_l}\left((\frac{\partial(\rho V)}{\partial x})^l - V_l(\frac{\partial \rho}{\partial x})^l\right),$$

$$(\frac{\partial \epsilon}{\partial x})^l = \frac{1}{\rho_l}\left((\frac{\partial(\rho \epsilon)}{\partial x})^l - \frac{1}{2}(U_l^2 V_l^2 + \frac{K+2}{2\lambda_l})(\frac{\partial \rho}{\partial x})^l\right).$$

If $\partial/\partial x$ is changed to $\partial/\partial y$ in the above equations, the parameters in b_l, *i.e.* $(b_{1l}, b_{2l}, b_{3l}, b_{4l})$ in Eq.(4.29) can be obtained. Based on the similar equations, g_r, a_r and b_r in the initial gas distribution function f_0 (Eq.(4.27)) at the right hand side of the cell interface can be obtained. Therefore, all terms for the initial gas distribution function f_0 have been obtained explicitly from the reconstructed macroscopic initial data.

The equilibrium state g around the cell interface $(x = 0, y = 0)$ is assumed to be

$$g(x,y,t) = g_0(1 + \bar{a}_l x(1 - \mathrm{H}(x)) + \bar{a}_r x \mathrm{H}(x) + \bar{b}y + \bar{A}t). \tag{4.31}$$

where

$$g_0 = \rho_0(\frac{\lambda_0}{\pi})^{\frac{K+2}{2}} e^{-\lambda_0[(u-U_0)^2+(v-V_0)^2+\xi^2]},$$

$$\bar{a}_l = \bar{a}_{1l} + \bar{a}_{2l}u + \bar{a}_{3l}v + \bar{a}_{4l}\frac{1}{2}(u^2+v^2+\xi^2),$$

$$\bar{a}_r = \bar{a}_{1r} + \bar{a}_{2r}u + \bar{a}_{3r}v + \bar{a}_{4r}\frac{1}{2}(u^2+v^2+\xi^2),$$

$$\bar{b} = \bar{b}_1 + \bar{b}_2u + \bar{b}_3v + \bar{b}_4\frac{1}{2}(u^2+v^2+\xi^2),$$

and

$$\bar{A} = \bar{A}_1 + \bar{A}_2u + \bar{A}_3v + \bar{A}_4\frac{1}{2}(u^2+v^2+\xi^2).$$

Similar to the 1-D case, at time $t = 0$, g_0 can be obtained from g_l and g_r of f_0 using the compatibility condition,

$$\int \psi_\alpha g_0 d\Xi = \int_{u>0}\int \psi_\alpha g_l d\Xi + \int_{u<0}\int \psi_\alpha g_r d\Xi.$$

More specifically, with the definitions

$$\int_{u>0}\int (...)g d\Xi = \rho < ... >_{u>0},$$

and

$$\int_{u<0}\int (...)g d\Xi = \rho < ... >_{u<0},$$

we have

$$\begin{aligned} W_0 = \begin{pmatrix} \rho_0 \\ \rho_0 U_0 \\ \rho_0 V_0 \\ \rho_0 \epsilon_0 \end{pmatrix} &= \rho_l \begin{pmatrix} < u^0v^0 >_{>0} \\ < u^1v^0 >_{>0} \\ < u^0v^1 >_{>0} \\ 1/2(< u^2v^0 >_{>0} + < u^0v^2 >_{>0} + < u^0v^0\xi^2 >_{>0}) \end{pmatrix} \\ &+ \rho_r \begin{pmatrix} < u^0v^0 >_{<0} \\ < u^1v^0 >_{<0} \\ < u^0v^1 >_{<0} \\ 1/2(< u^2v^0 >_{<0} + < u^0v^2 >_{<0} + < u^0v^0\xi^2 >_{<0}) \end{pmatrix} \end{aligned} \quad (4.32)$$

Once $W_0 = (\rho_0, \rho_0U_0, \rho_0V_0, \rho_0\epsilon_0)$ is obtained, g_0 is totally determined. For example, λ_0 can be expressed as

$$\lambda_0 = \frac{K+2}{4}\frac{\rho_0}{\rho_0\epsilon_0 - \frac{1}{2}\rho_0(U_0^2+V_0^2)}.$$

Now, connecting W_0 at the cell interface to values $\bar{W}_{i,j}(x_{i,j}, y_{i,j})$ and $\bar{W}_{i+1,j}(x_{i+1,j}, y_{i+1,j})$ in the x-direction, we can get the slopes of the macroscopic variables on both sides of the cell interface, from which $\bar{a}_l$ and $\bar{a}_r$ terms in Eq.(4.31) can be obtained by using the similar techniques of obtaining a_l and a_r terms in f_0. In the y-direction at $x = 0$ and $t = 0$, the term $\bar{b}$ in Eq.(4.31) can be obtained from the following compatibility condition,

$$\frac{\partial}{\partial y} \int \psi_\alpha (g - f_0) d\Xi = 0.$$

As a result, it gives

$$\begin{aligned} \frac{1}{\rho_0} \int_{-\infty}^{\infty} \psi_\alpha \bar{b} g_0 d\Xi &= M^0_{\alpha\beta} \begin{pmatrix} \bar{b}_1 \\ \bar{b}_2 \\ \bar{b}_3 \\ \bar{b}_4 \end{pmatrix} \\ &= \frac{1}{\rho_0} \left(\int_{u>0} \int \psi_\alpha b_l g_l d\Xi + \int_{u<0} \int \psi_\alpha b_r g_r d\Xi \right), \end{aligned} \tag{4.33}$$

where the matrix

$$M^0_{\alpha\beta} = \frac{1}{\rho_0} \int \psi_\alpha \psi_\beta g_0 d\Xi$$

has the same structure as M_l in Eq.(4.30). So, $(\bar{b}_1, \bar{b}_2, \bar{b}_3, \bar{b}_4)$ can be obtained similarly.

Substituting both f_0 in Eq.(4.27) and g in Eq.(4.31) into the integral solution of the BGK model, we have

$$\begin{aligned} f(x_{i+1/2,j}, y_{i+1/2,j}, t, u, v, \xi) &= \frac{1}{\tau} \int_0^t g(x', y', t', u, \xi) e^{-(t-t')/\tau} dt' \\ &\quad + e^{-t/\tau} f_0(x_{i+1/2,j} - ut, y_{i+1/2,j} - vt), \end{aligned} \tag{4.34}$$

where $x' = x_{i+1/2,j} - u(t - t')$ and $y' = y_{i+1/2,j} - v(t - t')$ are the trajectory of a particle motion. With the definition $(x_{i+1/2,j} = 0, y_{i+1/2,j} = 0)$, f goes to

$$\begin{aligned} f(0,0,t) &= (1 - e^{-t/\tau}) g_0 \\ &\quad + \left(\tau(-1 + e^{-t/\tau}) + te^{-t/\tau} \right) \left((\bar{a}_l \mathrm{H}(u) + \bar{a}_r (1 - \mathrm{H}(u)))u + \bar{b}v \right) g_0 \\ &\quad + \tau(t/\tau - 1 + e^{-t/\tau}) \bar{A} g_0 \\ &\quad + e^{-t/\tau} \left((1 - uta_l - vtb_l) \mathrm{H}(u) g_l + (1 - uta_r - vtb_r)(1 - \mathrm{H}(u)) g_r \right). \end{aligned} \tag{4.35}$$

The only unknown in the above equation is $\bar{A}$, which can be obtained by using the compatibility condition at $(x = 0, y = 0)$ in whole time step Δt, namely

$$\int\int_0^{\Delta t} \begin{pmatrix} 1 \\ u \\ v \\ \frac{1}{2}(u^2 + v^2 + \xi^2) \end{pmatrix} (g(0,0,t) - f(0,0,t)) dt d\Xi = 0. \tag{4.36}$$

The above equation gives

$$\begin{aligned} M^0_{\alpha\beta}\bar{A}_\beta &= \frac{1}{\rho_0}\int \left[\gamma_1 g_0 + \gamma_2 \left(u\left(\bar{a}_l \mathrm{H}[u] + \bar{a}_r(1 - \mathrm{H}[u])\right) + \bar{b}v\right) g_0 \right. \\ &+ \gamma_3 \left(\mathrm{H}[u] g_l + (1 - \mathrm{H}[u]) g_r\right) \\ &+ \left. \gamma_4 \left((a_l u + b_l v)\mathrm{H}[u] g_l + (a_r u + b_r v)(1 - \mathrm{H}[u]) g_r\right)\right] \psi_\alpha d\Xi, \end{aligned} \tag{4.37}$$

and $\bar{A}_\beta = (\bar{A}_1, \bar{A}_2, \bar{A}_3, \bar{A}_4)^T$ can be obtained from the above equation. The parameters $(\gamma_0, \gamma_1, \gamma_2, \gamma_3, \gamma_4)$ have the same values as those presented in Eq.(4.22). From the above analysis, we can observe the close relation between the 1-D and the 2-D BGK schemes. Basically, there is not much difference from the 1-D to the 3-D cases in the current BGK formulation.

Once the explicit gas distribution function $f(0, 0, t)$ in Eq.(4.35) at the center of a cell interface is obtained, the mass, momentum and energy transports in a time step Δt across the boundary can be evaluated. The time dependent numerical flux functions are

$$\begin{pmatrix} F_\rho \\ F_{\rho U} \\ F_{\rho V} \\ F_{\rho\epsilon} \end{pmatrix}_{i+1/2,j} = \int u \begin{pmatrix} 1 \\ u \\ v \\ \frac{1}{2}(u^2 + v^2 + \xi^2) \end{pmatrix} f(0,0,t) d\Xi.$$

Note that $f(0, 0, t)$ gives the time-dependent particle distribution function at a cell interface, the corresponding macroscopic variables are not necessarily propagating in the x-direction. The $\partial/\partial y$ effects are explicitly included in f through the b_l, b_r and $\bar{b}$ terms. For the fluxes across the cell interface between cells (i, j) and $(i, j+1)$, similar techniques can be developed.

4.4 Numerical Analysis

One of the obvious improvement of the BGK scheme over the KFVS scheme is the inclusion of particle collisions in the gas evolution stage. Due to this fact, the BGK

scheme has much less numerical dissipation than the KFVS method.

Remark(4.7)

Eq.(4.35) gives explicitly the time-dependent gas distribution function f at the cell boundary. In order to understand this formulation, several limiting cases will be discussed below.

In the hydrodynamic limit of $\tau << \Delta t$ and in a smooth region, such as

$$g_l = g_r = g_0, \quad a_l = a_r = \bar{a}_l = \bar{a}_r \equiv \bar{a}, \quad \text{and} \quad b_l = b_r = \bar{b},$$

to first order in τ, Eq.(4.35) goes to

$$f = g_0(1 - \tau(u\bar{a} + v\bar{b}) + (t - \tau)\bar{A}). \tag{4.38}$$

In this case, Eq.(4.37) for the determination of $\bar{A}$ is reduced to[128],

$$\int \psi_\alpha \bar{A} g_0 du dv d\xi = -\int \psi_\alpha (u\bar{a} + v\bar{b}) g_0 du dv d\xi. \tag{4.39}$$

Substituting Eq.(4.38) into the definition of the stress tensor,

$$\sigma_{ij} = -\int (u_i - U_i)(u_j - U_j) f du dv d\xi,$$

we can get the shear stress. For example, σ_{xy} from f in Eq.(4.38) becomes

$$\sigma_{xy} = \tau p(\frac{\partial U}{\partial y} + \frac{\partial V}{\partial x}),$$

where τp corresponds to the dynamic viscosity coefficient and p is the local pressure. Therefore, in the smooth region, the current scheme can give the Navier-Stokes solution once the initial condition of $\partial U/\partial y$ and $\partial V/\partial x$ are properly reconstructed. The current scheme in the 2-D case is different from directional splitting methods, where all terms, such as $\partial U/\partial y$ and $\partial V/\partial x$, are included in the final flux formulation through the terms $\bar{a}$ and $\bar{b}$.

Remark(4.8)

In the limit of $\tau \to \infty$, the solution of the gas distribution function f in Eq.(4.35) reduces to

$$\begin{aligned} f &= f_0(x - ut, y - vt) \\ &= (1 - ua_l t - vb_l t)\mathrm{H}(u) g_l + (1 - ua_r t - vb_r t)(1 - \mathrm{H}(u)) g_r. \end{aligned}$$

This is precisely the 2-D KFVS scheme in the last chapter. As analyzed before, the two "half" Maxwellians are important for the robustness of the scheme in discontinuous regions.

Remark(4.9)

Similar to any hybrid scheme, the full BGK scheme presented in Eq.(4.35) can be simplified. For example, as presented in [134], for the Navier-Stokes solution the distribution function at a cell interface can be constructed as

$$\begin{aligned} f &= g_0\left(1+\bar{A}(t-\tau)-\tau(u\bar{a}_l\mathrm{H}(u)+u\bar{a}_r(1-\mathrm{H}(u))+v\bar{b})\right) \\ &\quad +\mathcal{L}(.)(f_0-g_0), \end{aligned}$$

where $\bar{A}$ is obtained from

$$\int \psi_\alpha \bar{A} g_0 du dv d\xi = -\int \psi_\alpha \left(u(\bar{a}_l\mathrm{H}(u)+\bar{a}_r(1-\mathrm{H}(u)))+v\bar{b}\right) g_0 du dv d\xi,$$

and $\mathcal{L}(.)$ is an adaptive limiter to control the numerical dissipation. Similar method has been successfully extended and applied to inhomogeneous flow calculations [63].

Remark(4.10).

From gas-kinetic theory, the collision time should depend on macroscopic flow variables, such as density and temperature. For Euler calculations, as a common practice the collision time τ is composed of two parts,

$$\tau = C_1\Delta t + \Delta t \mathrm{Min}(1, C) \tag{4.40}$$

where

$$C = C_2\frac{|\rho_l/\lambda_l-\rho_r/\lambda_r|}{|\rho_l/\lambda_l+\rho_r/\lambda_r|},$$

and Δt is the CFL time step[3]. For the Navier-Stokes solution, the collision time will be chosen according to the real physical viscosity coefficient ν, such that

$$\tau = \frac{\nu\rho}{p},$$

[3]For the KFVS scheme, there is only one particle collision in each time step. For the BGK method, if $C_1 = 0.01$, there will be 100 collisions in the smooth flow regions, which means that the artificial viscosity coefficient in the BGK method is reduced to 1/100 of the value in the KFVS scheme. Mathematically, we can also change $C_1\Delta t$ to $\tilde{C}_1(\Delta t)^2$ in order to show that the scheme has a consistent second order accuracy. Numerically, it does not make any differences because C_1 and $\tilde{C}_1$ can be two different constants.

where ρ and p are local density and pressure. In Eq.(4.40), the first term on the right hand side gives a limiting threshold for the collision time to avoid the blowing up the program, such as the evaluations of $\Delta t/\tau$ and $e^{-\Delta t/\tau}$, it also provides a background dissipation for the numerical fluid. The second term is related to the pressure jump in the reconstructed initial data, which introduces additional artificial dissipation if high pressure gradients are present in the fluid. For the Euler calculations, since the mesh size is not small enough to resolve the physical discontinuity, artificial dissipation has to be added to expand the thickness of the discontinuity to a few cell sizes. For shock tube test cases, numerical results are not sensitive to the choices of the values of C_1 and C_2. For example, C_1 can take the values from 0.01 to 0.1, the numerical results will be equally good. In the test cases in the next section, $C_1 = 0.05$ and $C_2 = 5$ are usually used. Numerically, the additional term in the collision time can be considered as a limiter imposed in the temporal domain for higher order time evolution model, which is similar to the conventional limiter imposed in the spatial domain in the reconstruction stage. For the Godunov method, since the flux function in the Riemann solver is independent of time, the temporal limiter is not needed for the 1st-order gas evolution model. The concept of limiters needs to be extended to both space and time if a numerical scheme couples them and has a uniformly high order of accuracy. The obvious advantage of the BGK-type scheme is the explicit dissipative mechanism, which avoids the ambiguity of implicit viscosities in other upwinding flux constructions, such as AUSM, HLLE and CUSP[75, 18, 49]. Also, it is very unlikely that an excellent scheme can be developed which is robust, accurate and free of any tunable parameters. Fluid in the smooth and discontinuous regions have totally different dynamical behaviors, even have different governing equations. Starting from a fixed governing equations, such as the Euler equations, it is impossible to describe the flow motion correctly in all situations. For example, the Godunov method has no tunable free parameter, but it treats the shock region with equilibrium states and this mal-representation triggers instabilities, such as carbuncle phenomena and odd-even decoupling. The detail analysis is given in chapter 6. The BGK scheme can describe the numerical fluid in both the smooth and discontinuous regions by the variation of the collision time. The change of collision time is numerically necessary and physically reasonable.

Remark(4.11).

For a two dimensional flow, the linearized form of the Navier-Stokes equations is

$$W_t + AW_x + BW_y = S.$$

It is well known that the difficulties in the development of multidimensional upwind schemes for the Navier-Stokes equations is due to the fact that the matrices A and B do not commute: $[A, B] \equiv AB - BA \neq 0$. Physically, it means that an infinite number of waves will be present in the flow. Therefore, the necessity of wave modeling follows [21]. However, for the BGK model

$$f_t + uf_x + vf_y = (g - f)/\tau,$$

the particle velocities are independent variables and the non-commuting difficulty is eliminated. Thus, in the BGK scheme, particles can move in all directions. Theoretically, it is exactly a multidimensional gas evolution model.

The BGK scheme can be simplified to become a directional splitting scheme. Everything we need to do here is to delete all terms related $b_l, b_r, \bar{b}$ in both f_0 and g in the construction of the 2-D BGK fluxes.

Remark(4.12).

The full Boltzmann scheme gives time-dependent fluxes, which may handicap the convergence of the scheme to a steady state. Thus, for steady state calculations, the relaxation process must be simplified in order to yield time independent numerical fluxes. The easiest way to achieve this is to keep only the pointwise values and ignore all high-order spatial and temporal slopes in the expansion of f and g. Similar to the JST scheme [50], we can write the BGK solution as

$$f = g_0 + \epsilon^{(2)}(f_0 - g_0), \tag{4.41}$$

where $\epsilon^{(2)}$ is the adaptive coefficient to control the dissipation in the scheme.

Remark(4.13).

The BGK model only recovers the Navier-Stokes equations with a fixed Prandtl number, which is $\Pr = 1$. In order to simulate flows with arbitrary Prandtl number, we have to modify either the viscosity or heat conductivity coefficients. Since the explicit form of the gas distribution function f at the cell interface has been obtained, according to Eq.(2.17) the heat conducting flux can be evaluated. As a simple way, we can fix the Prandtl number by changing this term when we evaluate the energy flux in Eq.(5.40)[4].

[4]For thermal boundary layers, perfect numerical solutions from the BGK method have been obtained

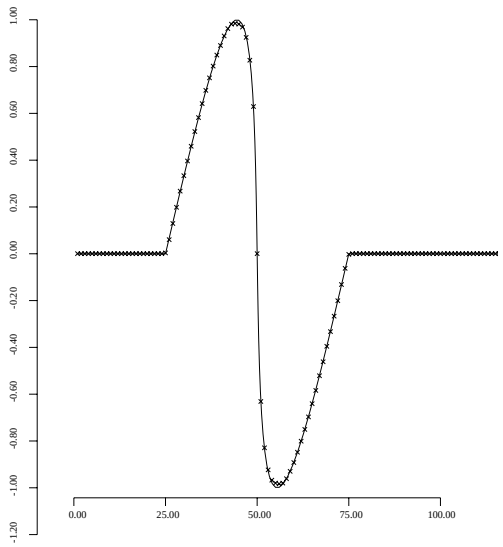

Figure 4.8: Burgers' equation with sine wave

4.5 Numerical Experiments

The BGK scheme has been applied to many test cases ranging from a simple advection-diffusion equation to unsteady hypersonic flow computations. In all test cases, entropy-violating solutions have never been obtained from the BGK method. Unless otherwise stated, in all of the numerical examples reported here, $\gamma = 1.4$ and the van Leer limiter is used for the construction of conservative variables inside each numerical cell.

4.5.1 Inviscid Flows

Case(1) Burgers' Equation

In the case of Burgers' equation, two different initial profiles, *e.g.* a sine wave and a stair wave, are tested. The formation and propagation of discontinuities are compared with the analytical solutions at two different times for each test case (Fig.(4.8)-(4.11)). Judging from the comparison ([42, 138]), one may confirm the higher resolution property of the BGK scheme.

Case(2) Shallow Water Equations

The initial condition in the 1-D case for the shallow water equation is

$$(\rho_l = 1.0, U_l = 0.0)|_{x<0.5} \qquad \text{and} \qquad (\rho_r = 0.125, U_r = 0.0)|_{x\geq 0.5}.$$

The simulation results with 200 grid points at time $T = 0.3$ are shown in Fig.(4.12),

for different Prandtl numbers by C. Kim.

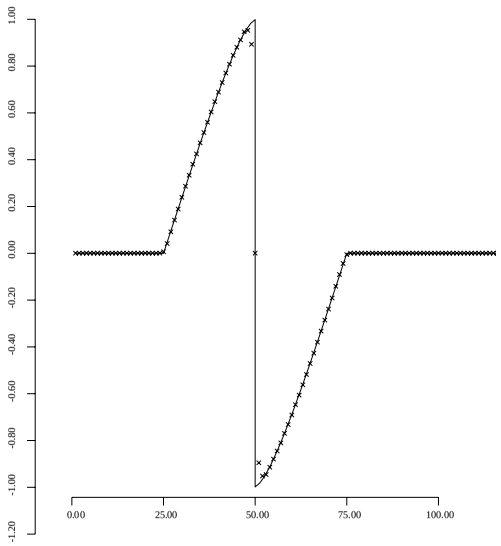

Figure 4.9: Burgers' equation with sine wave

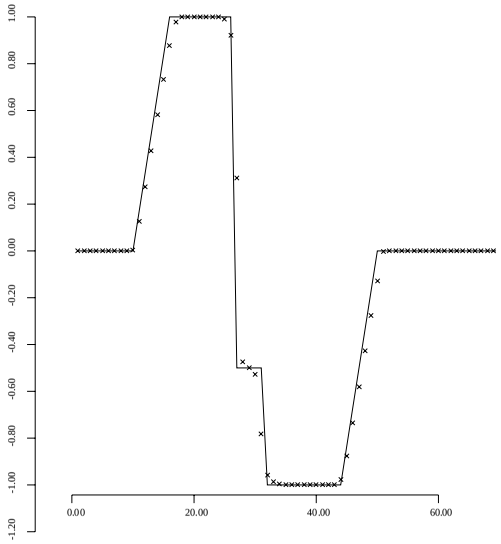

Figure 4.10: Burgers' equation in stair case

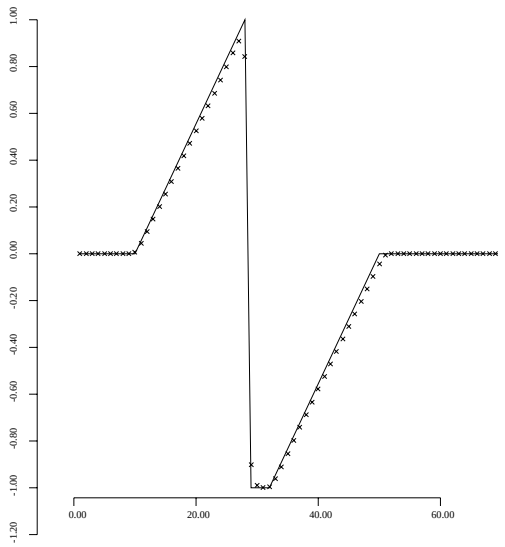

Figure 4.11: Burgers' equation in stair case

where the solid line is the exact solution. From this test case, we observe that the BGK scheme gives accurate results in both discontinuous and smooth regions. In the 2-D case, we simulate the break-down of the dam of a reservoir, where the initial water surface height inside the reservoir is 1.0 and outside is 0.2. The simulation result is shown in Fig.(4.13) for the water height distribution after the dam-break.

Case(3) 1-D Shock Tube Problems

Sjögreen Test Case

The Sjögreen test case is given in the paper by Einfeldt *et. al.* [26]. In that paper, the authors analyzed the weakness of non-positive conservative schemes for the simulation of flows with large kinetic energy. They showed that no scheme whose interface flux derived from a linearized Riemann solution could be positively conservative. For example, some well-known schemes may fail to reproduce correctly the strong expansion profiles. The results from the BGK scheme are shown in Fig.(4.14). The ability to handle strong rarefaction wave is one of the advantages of gas-kinetic schemes.

Sod, Lax-Harten, Blast Wave and Shu-Osher Test Cases

The results for the Sod, Lax-Harten, Blast wave and Shu-Osher test cases are shown in Fig.(4.15)-(4.18). The simulation results of Shu-Osher case can be improved if $4th$-order ENO techniques are used for the initial reconstruction at the beginning of each time step [135], but the robustness of the scheme is not as good as the current BGK scheme with van Leer or MUSCL limiters.

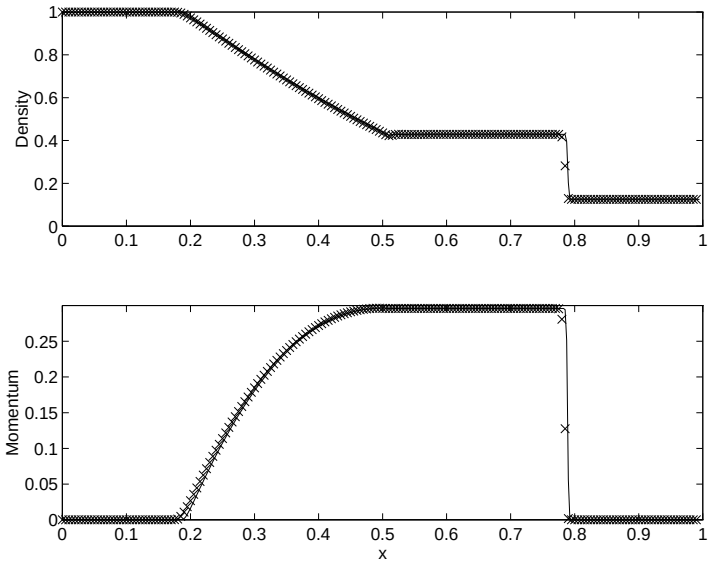

Figure 4.12: Shock tube test case with 200 grid points for shallow water equations

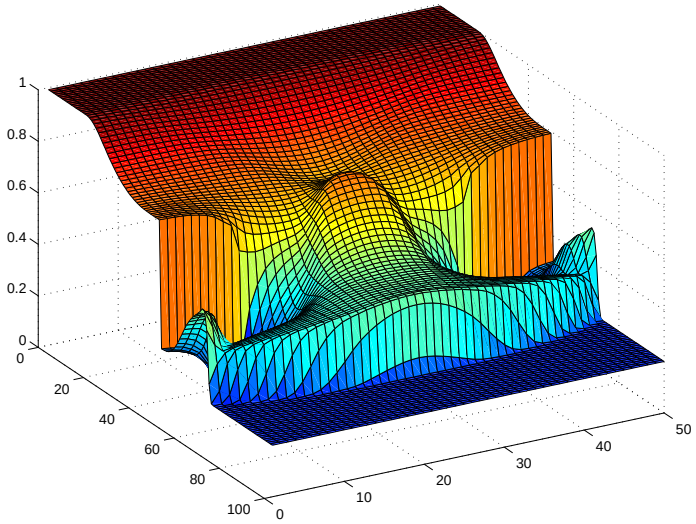

Figure 4.13: 2-D dam-break problem with 50×100 mesh points

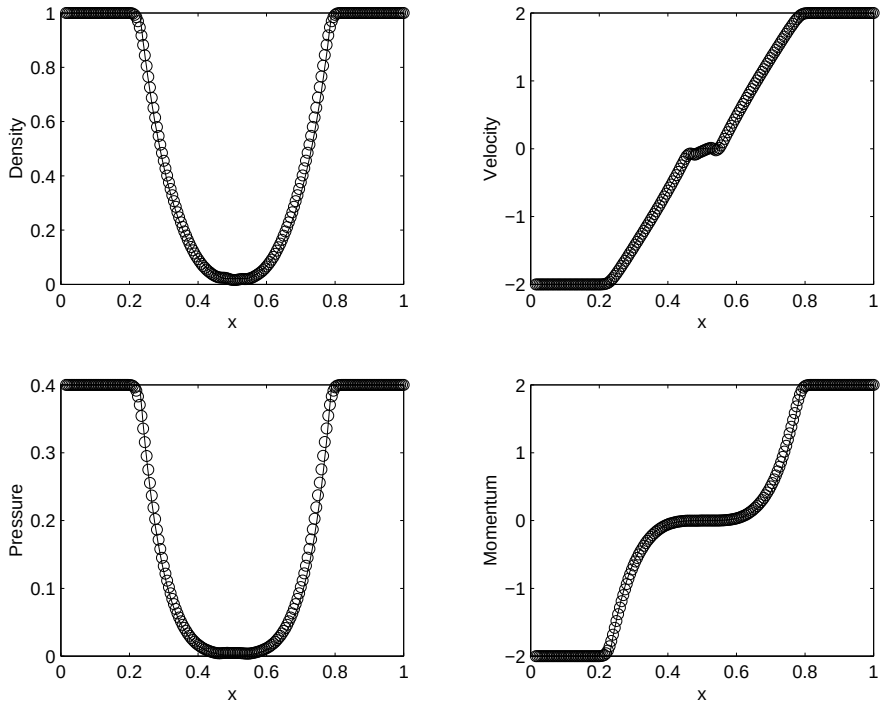

Figure 4.14: Sjögreen test for strong rarefaction wave

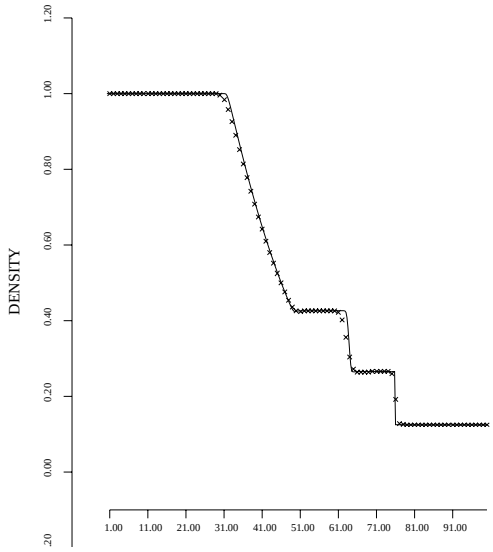

Figure 4.15: Sod case with MUSCL limiter (100 cells)

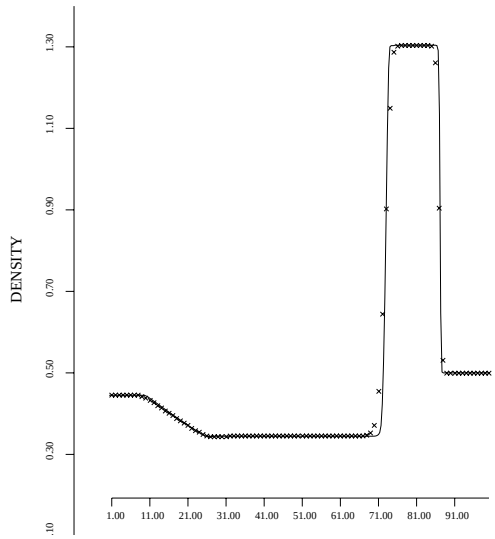

Figure 4.16: Lax-Harten case with MUSCL limiter (100 cells)

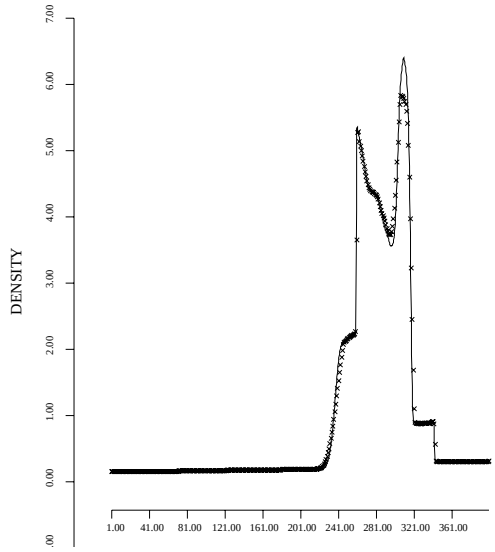

Figure 4.17: Blast-Wave case with MUSCL limiter (400 cells). The solid line is obtained from 800 mesh points and BGK method

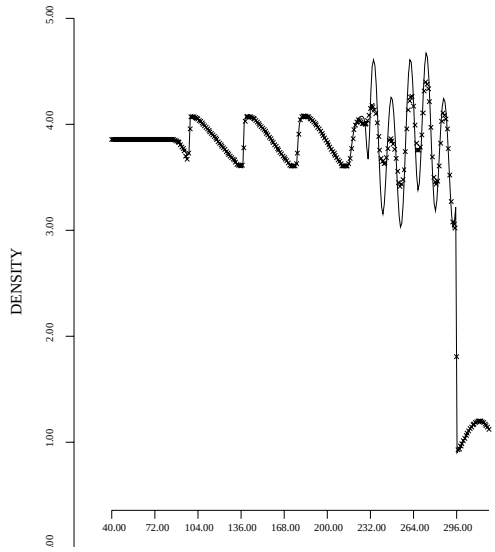

Figure 4.18: Shu-Osher case with MUSCL limiter (400 cells)

Case(4) 2-D Flow Problems

Forward Facing Step with Mach 3

The forward-facing step test is carried out on a uniform mesh with 240×80 cells. The computed density and pressure distributions are presented in Fig.(4.19). Notice that the BGK scheme does not require any special treatment at the corner, and does not produce "dog-leg" around the corner.

Double Mach Reflection

The double Mach reflection problem is calculated on a computational domain with 360×120 cells. The problem is set up by driving a strong shock down a tube which contains a wedge. The computed density and pressure distributions after the collision between the shock and the wedge are shown in Fig.(4.20). The kinked Mach phenomenon found in [106, 35, 76] was never observed in the BGK scheme.

An Impulsively Started Cylinder

Strong shocks, and expansions as well as subsonic flow regions are presented in both the steady and unsteady hypersonic flows induced by the impulsive start of a cylinder. A monotonic numerical scheme is needed to crisply capture the shock without generating spurious oscillations. Moreover, a numerical scheme should be capable of maintaining positivity of the flow variables, to avoid the occurrence of unphysical negative values for quantities such as density and/or pressure in regions of low density and low pressure created by extreme expansions. In the present case, an initial Mach number of $M = 3.5$ is chosen for the hypersonic flow, and all flow features discussed above will be present.

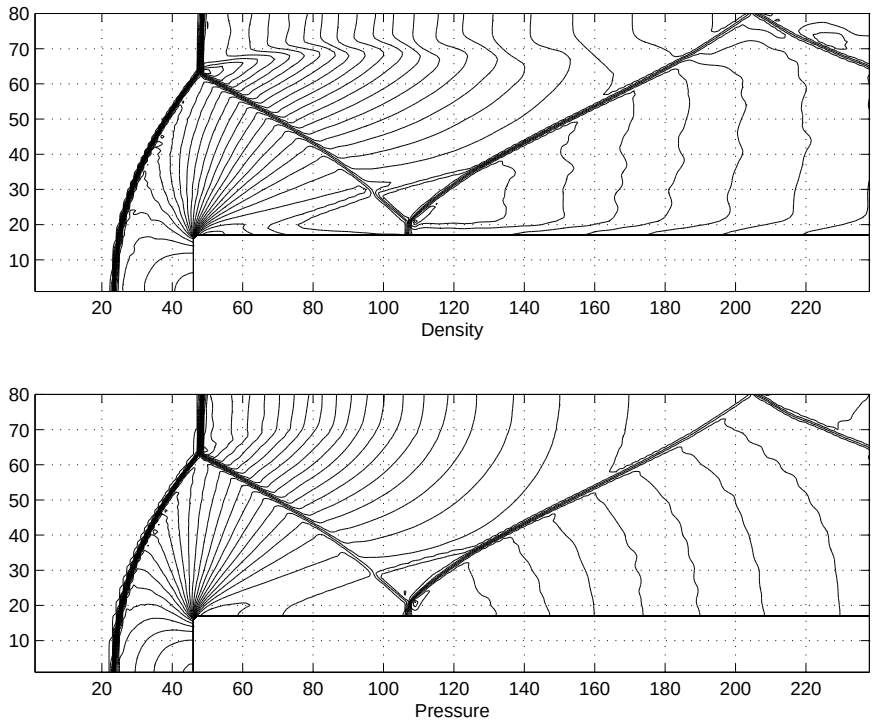

Figure 4.19: Density and pressure distributions from the 2-D BGK method with van Leer limiter

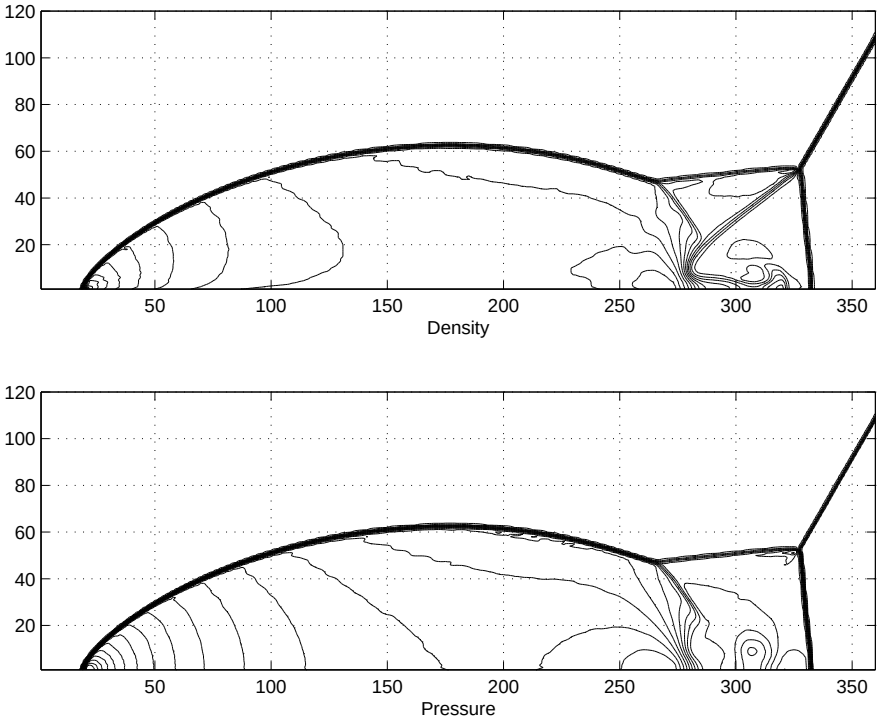

Figure 4.20: Density and pressure distributions from the 2-D BGK method with van Leer limiter

Because the very high expansion in the rear part of cylinder produces a vacuum-like low pressure and low density region, this problem imposes a particular difficulty not only for unsteady but also for steady flow computations.

If the kinetic energy is so large that the difference between the total energy and the kinetic energy is in the range of round off error, one should limit the lower bound of the difference with the order of round-off to avoid meaningless computations. This problem is solely caused by the finite precision of the hardware and not by the numerical scheme. The round-off error is usually of the order $O(10^{-12}) \sim O(10^{-16})$. The present computations were performed using a Silicon Graphics INDIGO 2 workstation with an observed round-off error of order $O(10^{-18})$. Thus a lower bound of 10^{-16} was selected.

Most first-order schemes have severe difficulties in maintaining positive pressure and/or density, and generally need *ad hoc* fixes. Most of the second order schemes simply fail. The BGK-type scheme, however, does not seem to have any particular difficulty in preserving positivity during the whole time integration. This finding is verified for both first and second order schemes.

180×50 cells were used in the current calculation. The grid distribution is uniform in the angular direction (180 cells) while the cells in the radial direction grid (50 cells) are slightly clustered to the surface. The ratio of outer radius to inner radius is 10, and all the calculations were carried out using a CFL number of 0.5. Fig.(4.21) shows the computed density, pressure and Mach number distributions along the symmetry line and the upper surface of the cylinder at times of $T = 6.0, 7.0, 8.0$ corresponding to a free stream Mach number of $M = 3.5$. It can be seen that the results at three different times practically collapse to a single curve. This indicates that the computed results at $T = 6.0$ have reached a steady state. Fig.(4.22) shows the density, pressure and Mach number contours at $T = 6.0$.

Notice that the bow shock wave is captured with two interior points. Also, the expansion in the rear part of the cylinder creates an even higher Mach number. Our results show a much higher Mach number than the result in [80]. This again indicates that the BGK scheme may yield a less diffusive solution with consequently higher accuracy, although it is intrinsically solving the viscous flow equations.

Shock Diffraction around a Corner

This is about a strong shock of Mach number 5.09 diffracting around a corner [100]. Fig.(4.23) and Fig.(4.24) show the density and entropy contours by the BGK method. There are no detections or entropy-fix in our calculation. It is well known that the

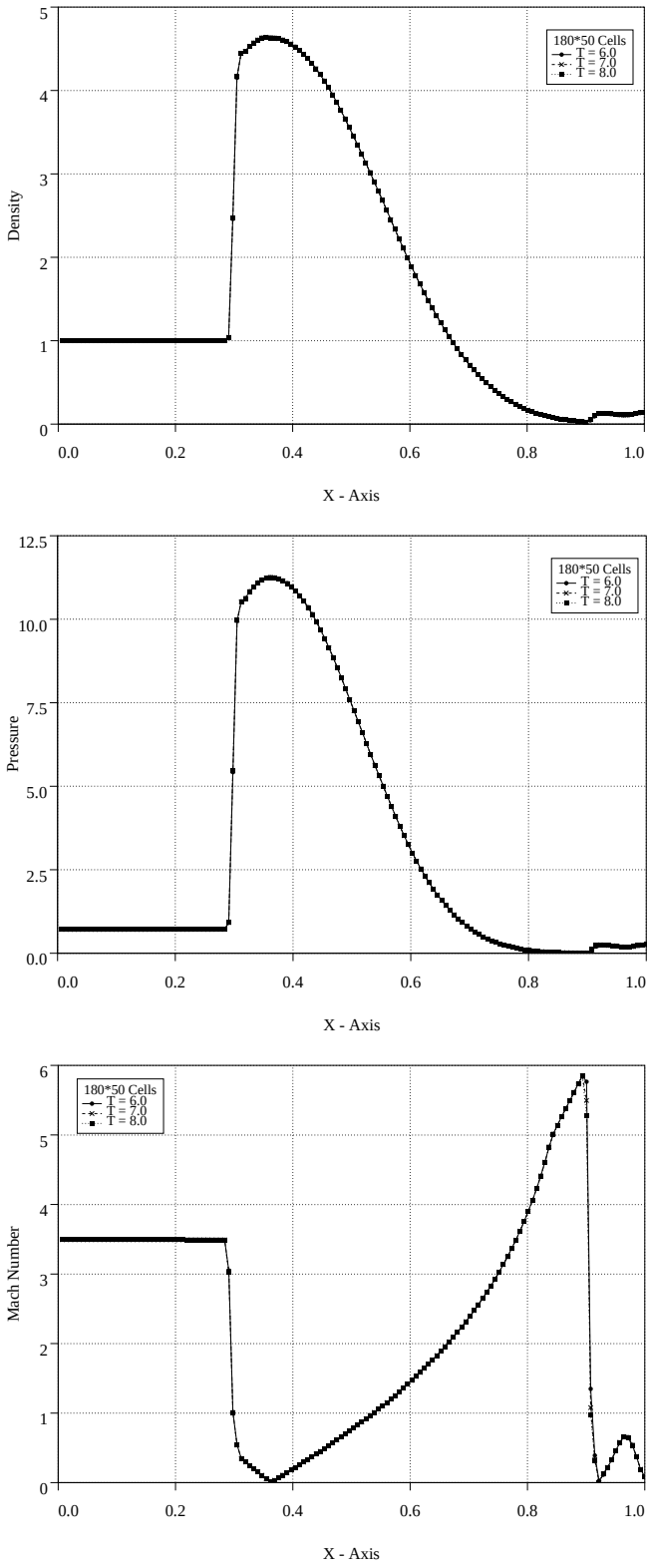

Figure 4.21: Density, pressure and Mach number distributions for $M = 3.5$

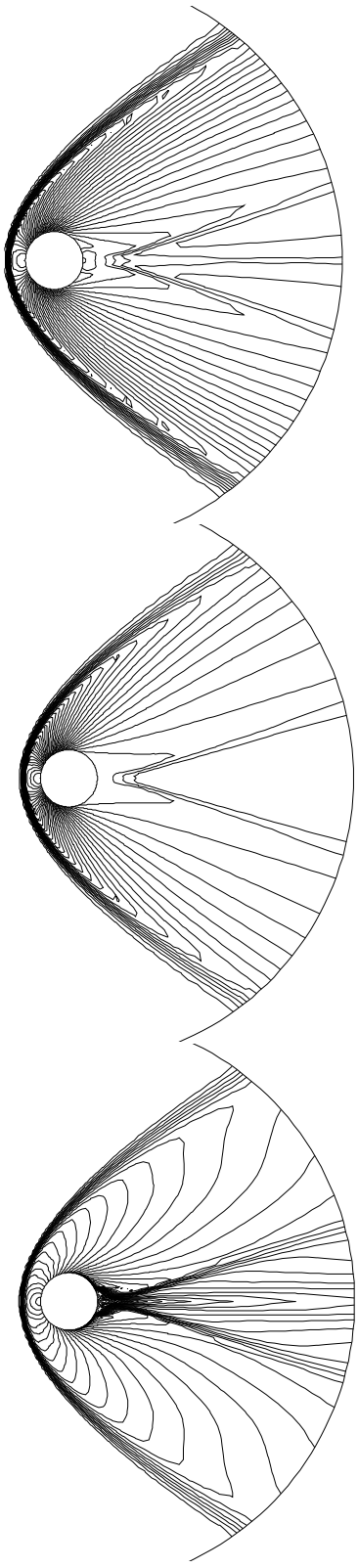

Figure 4.22: Density, pressure and Mach number contours for $M = 3.5$

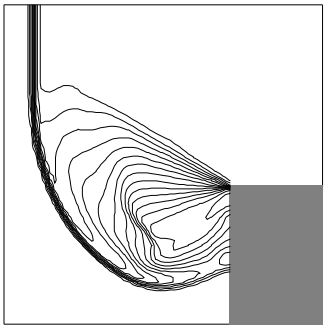

Figure 4.23: Density distribution on a mesh 70×70

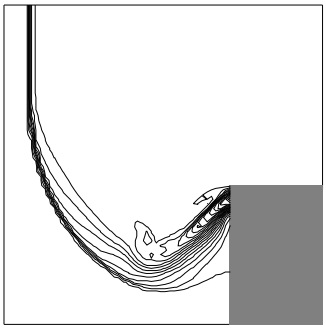

Figure 4.24: Entropy distribution on a mesh 70×70

original Godunov scheme, the Roe scheme without an entropy-fix and the Osher scheme could yield a "shock" at the rarefaction corner.

Regular Shock Reflection

The computational domain is rectangular of length 4 and height 1 divided into 60×20 rectangular grids with $\Delta x = 1/15$ and $\Delta y = 1/20$. Dirichlet conditions are imposed on the left and upper boundaries as

$$\begin{aligned} (\rho, u, p)|_{(0,y,t)} &= (1.0, 2.9, 0, 1/4) \\ (\rho, u, p)|_{(x,1,t)} &= (1.69997, 2.61934, -0.50633, 1.52819) \end{aligned}$$

The bottom boundary is a reflecting wall and supersonic outflow condition is applied along the right boundary [15]. We iterate 1000 time steps, at which the solution reaches a steady state. In Fig.(4.25), we show the pressure contours as well as pressure distribution along the middle line in the y-direction.

Steady Airfoil Calculations with Multigrid Techniques

Steady state transonic flow calculations for NACA0012, RAE2822 and Korn airfoils using the simplified relaxation scheme (4.41) are presented. In these calculations, the selective parameter $\epsilon^{(2)}$ is determined by a switching function calculated from local pres-

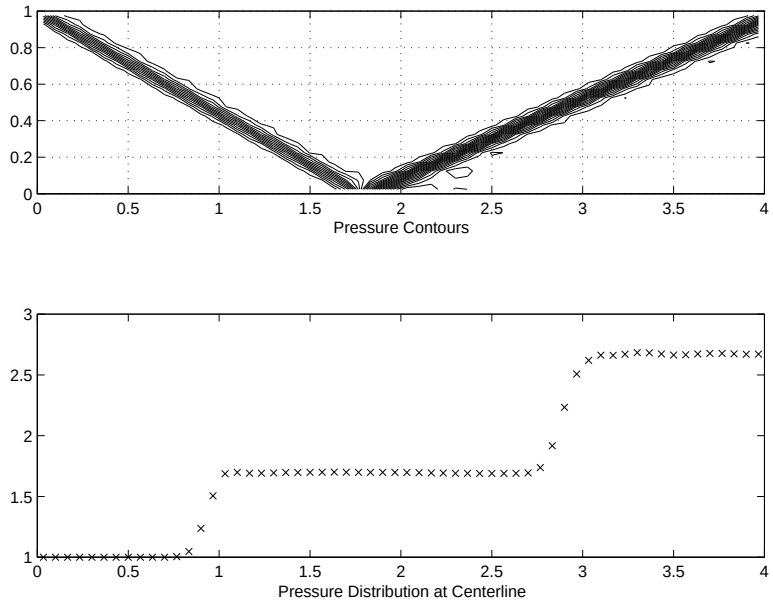

Figure 4.25: Regular shock reflection

sure gradients. Using subscripts i and j to label the mesh cells, the switching function for fluxes in the i direction is

$$\epsilon^{(2)} = 1 - e^{-\alpha \max(P_{i+1,j}, P_{i,j})} \tag{4.42}$$

where α is a constant,

$$P_{i,j} = \frac{|\Delta p_{i+1/2,j} - \Delta p_{i-1/2,j}|}{|\Delta p_{i+1/2,j}| + |\Delta p_{i-1/2,j}|}$$

and

$$\Delta p_{i+1/2,j} = p_{i+1,j} - p_{i,j}.$$

In the following calculations, the parameter α in (4.42) is set to be $\alpha = 0.5$. Also the van Leer limiter is again used in the current formulation for the interpolation of the left and right states. The computational domain is an O-mesh with 160 cells in the circumferential direction and 32 cells in the radial direction. This is a fine enough mesh to produce accurate answers with standard high resolution difference schemes [49, 42, 48]. For the NACA0012 airfoil, three initial conditions of different Mach numbers of $0.8, 0.8$ and 0.85, and different angles of attack $0.0, 1.25$ and 1.0 degrees are used. Similarly, a Mach number of 0.75 and angle of attack of 3.0 degrees have been used for the airfoil RAE2822 calculation. The simulation results after 100 multigrid cycles are presented in Fig.(4.26).

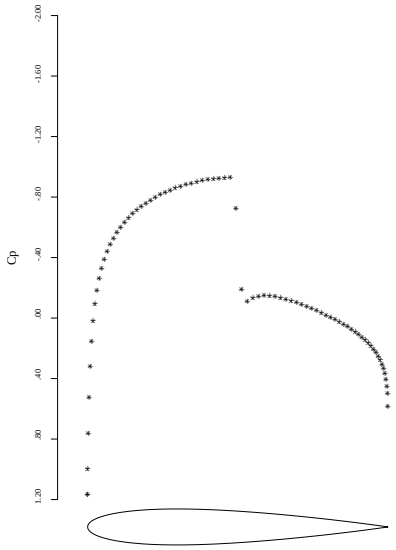

Figure 1: NACA 0012 with $M = 0.80, \alpha = 0.00$, $C_L = 0.0000, C_D = 0.0079, C_M = 0.0000$, Grid 161×33 and RES. $0.470E-04$

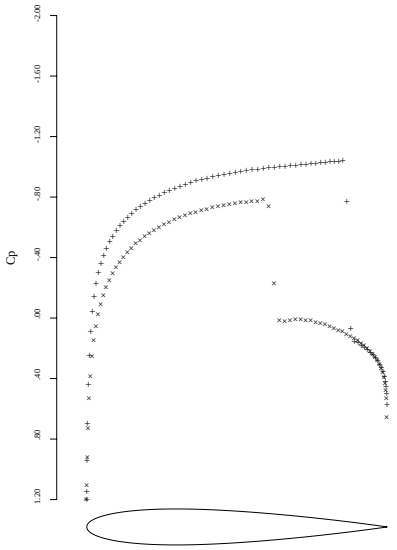

Figure 3: NACA 0012 with $M = 0.85, \alpha = 1.00$, $C_L = 0.3978, C_D = 0.0587, C_M = -0.1363$, Grid 161×33 and RES. $0.653E-03$

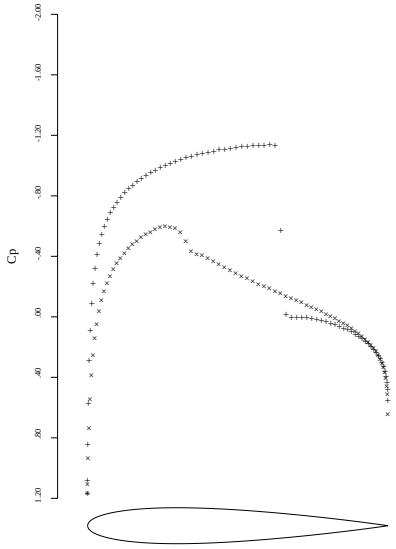

Figure 2: NACA 0012 with $M = 0.8, \alpha = 1.25$, $C_L = 0.3724, C_D = 0.0232, C_M = -0.0424$, Grid 161×33 and RES. $0.197E-03$

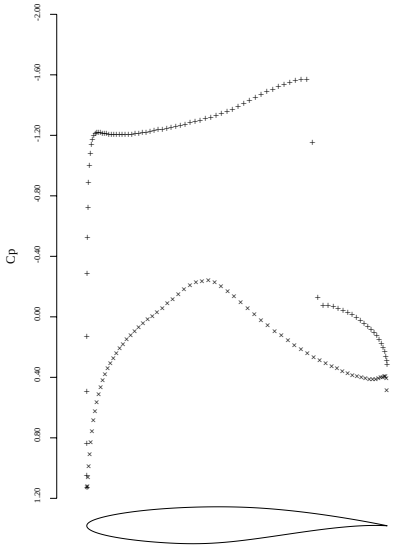

Figure 4: RAE 2822 with $M = 0.75, \alpha = 3.00$, $C_L = 1.1325, C_D = 0.0471, C_M = -0.1970$, Grid 161×33 and RES. $0.126E-02$

Figure 4.26: Steady state flow calculations around airfoils

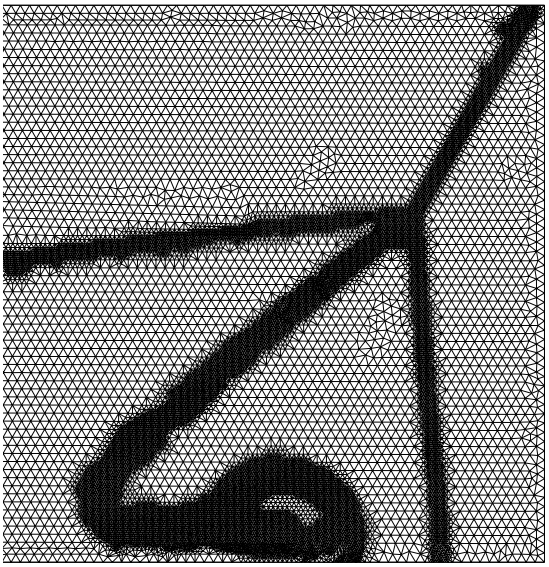

Figure 4.27: Unstructure adaptive mesh for double Mach reflection problem

Adaptive Unstructure Mesh

Recently, the BGK scheme has also been implemented on an unstructured mesh [58, 60, 59]. For the same Double Mach Reflection problem, with the adaptive unstructured mesh, the resolved density distributions are shown in Fig.(4.27)-(4.28). We clearly observe a shear instability around the slip line, and its interaction with the boundary.

In all cases we observe diffusion at contact discontinuities. Physically, the thickness of any contact discontinuity should increase on the order of $\sqrt{t}$ (t is the time), and it should be wider than the shock front. It is pointed out in chapter 6 that the smearing of contact discontinuities is mainly caused by the projection and reconstruction dynamics in the scheme.

4.5.2 Laminar Boundary Layer Calculation

As analyzed in the last section, the BGK scheme directly solves the Navier-Stokes equations in smooth flow regions. In the following, we are going to apply the BGK method to a standard laminar boundary layer. In this case, the viscosity coefficient is given initially. So, we have to change the collision time according to the real physical viscosity coefficient. The numerical results are compared with the exact Blasius solutions [109].

In the BGK model, the corresponding kinematic viscosity coefficient is,

$$\nu = \frac{\tau p}{\rho}.$$

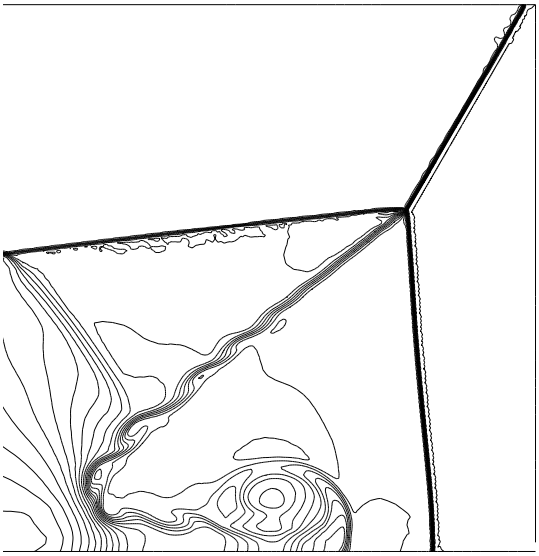

Figure 4.28: Density distribution around triple point region

With the relation $p = \rho/2\lambda$, we get

$$\tau = 2\lambda\nu.$$

This is the collision time used in the following calculations, where ν is known according to the Reynolds number Re and λ is the same quantity appearing in the equilibrium state g_0 at a cell interface.

Many gas-kinetic schemes claim to give accurate Navier-Stokes solutions, such as those presented in [86, 13], although most of them are dynamically similar to the KFVS scheme. It is probably favorable to get a standard and reasonable test case in order to compare different schemes. As analyzed in last chapter, the artificial dissipation is proportional to cell size in the KFVS scheme. It is hard to compare different schemes if different mesh sizes are used, especially in these cases with a fine mesh. In the following, we design a standard test case for this purpose.

The numerical mesh for the Navier-Stokes test case is rectangular and with 320×120 grid points in the xy plane, with the cell size $\Delta x = 1.0$ and $\Delta y = 1.0$. The flat plate is placed at the lower boundary ranging from $x = 80$ to $x = 320$ with total length $L = 240$. The inflow boundary condition at the left boundary is

$$(\rho, U, V, p)|_{x=0,y,t} = (1, 3, 0, \frac{9}{\gamma M^2}),$$

where M is the Mach number and $\gamma = 1.4$. In this test case, the Reynolds number is

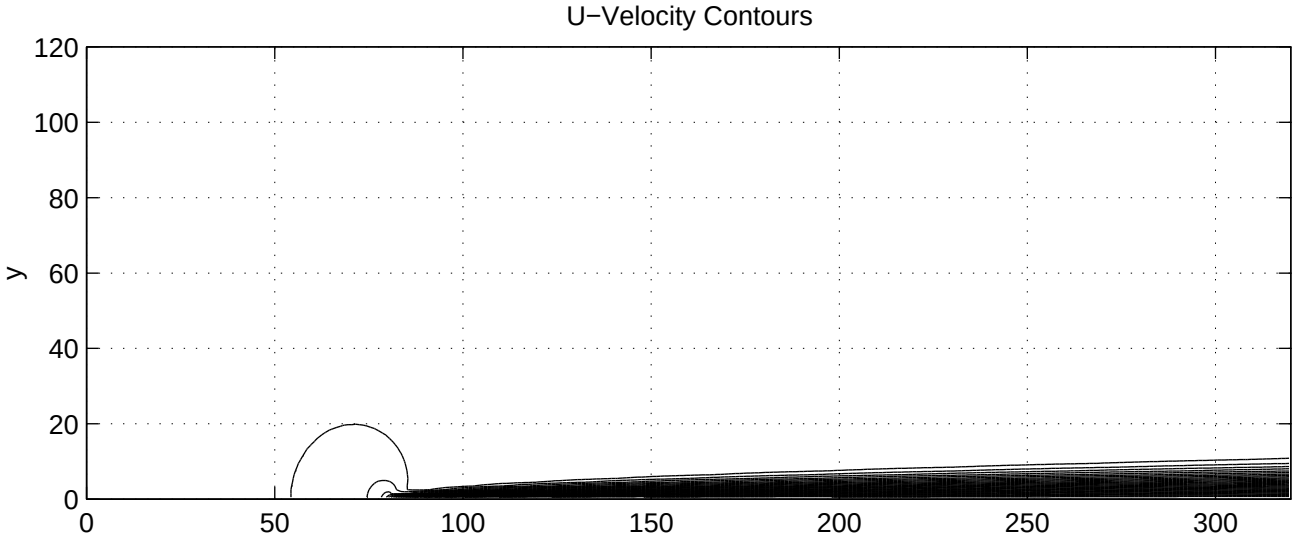

Figure 4.29: U-velocity contour for laminar boundary layer case (Re = 9580)

defined as

$$\mathrm{Re} = \frac{UL}{\nu},$$

and ν can be changed according to Re. No-slip boundary condition is imposed on the flat plate. Appropriate nonreflecting boundary condition, based on the one-dimensional Riemann invariants normal to the grid, is used at the upper boundary. Simple extrapolation of the conservation variables are used on the right boundary. The output U and V velocities in the boundary layer are taken at $x = 150, 200, 250$ and 300.

The first test case is for $\nu = 0.0750$ and the upstream Mach number $M = 0.15$. In this case, the corresponding Reynolds number is 9580. Fig.(4.29) shows the U-velocity contours in the whole computational domain obtained from the BGK method. At different locations of $x = 150, 200, 250$ and 300, along the y-direction, U and V velocities after the transformations are plotted in Fig.(4.30) and Fig.(4.31), where the solid lines are the exact Blasius solutions. As we can see, the BGK method gives accurate Navier-Stokes solutions, even with just a few points in the boundary layer[5].

If the viscosity coefficient is reduced to $\nu = 0.05$, the Reynolds number becomes $Re = 14370$. In this case, the relative boundary layer thickness is reduced. At the same output locations, the transformed U-velocity is shown in Fig.(4.32). Even with 5 points

[5]The V-velocity in the first cell next to the flat plate is overshooting. It is probably due to the large cell size and artificial heating in the reconstruction stage, where the van Leer limiter is used for the construction of flow variables. The viscous heating at the boundary generates hot gases with higher pressure to push the gas away from the flat plate. Perfect results without over-shooting can be obtained if adaptive mesh is used in the boundary layer (C. Kim, private communication).

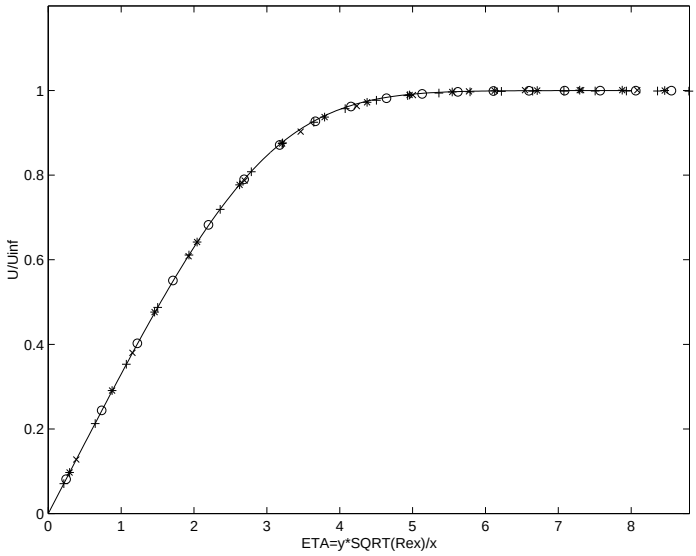

Figure 4.30: U-velocity in the boundary layer (Re = 9580), where the solid line is the exact solution, and the numerical solutions x: $x = 150$; *: $x = 200$; o: $x = 250$; +: $x = 300$

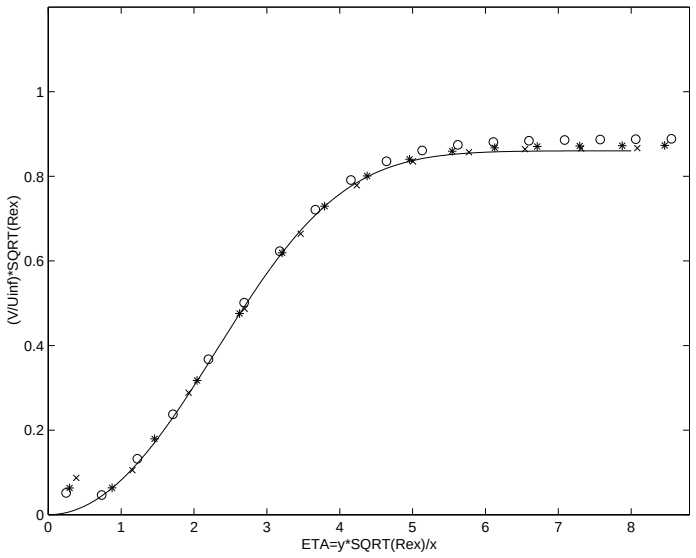

Figure 4.31: V-velocity in the boundary layer (Re = 9580), where the solid line is the exact solution, and the numerical solutions x: $x = 150$; *: $x = 200$; o: $x = 250$

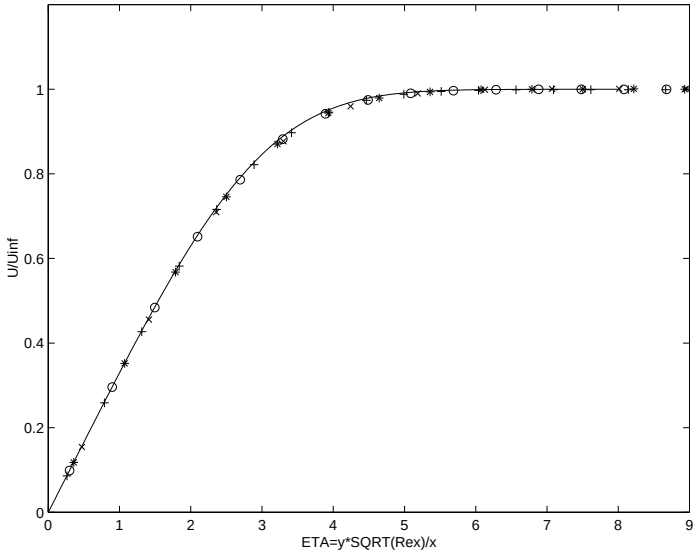

Figure 4.32: U-velocity in the boundary layer (Re = 14370), where the solid line is the exact solution, and the numerical solutions x: $x = 150$; *: $x = 200$; o: $x = 250$; +: $x = 300$

in the boundary layer at $x = 150$, the U velocity is still captured correctly.

With even smaller $\nu = 0.025$, the Reynolds number goes to $Re = 28740$ and the boundary layer is even thinner. In this case, the U-velocity plot is shown in Fig.(4.33). Even with 4 points in the boundary layer at $x = 150$, the U-velocity is well captured. From this test case, we clearly observe that the BGK scheme solves the Navier-Stokes equations accurately. Therefore, in the smooth region, the BGK method gives Navier-Stokes solutions automatically. This is one of the main reasons for the BGK scheme to avoid instabilities suffered by many upwinding schemes in the shock regions in the 2-D case. In discontinuous regions, it is very hard to obtain the explicit viscosity term from the BGK scheme, since the Chapman-Enskog expansion is only correct for smooth solutions.

4.6 Summary

In this chapter, we have presented the BGK scheme for solving compressible flow equations, and presented extensive numerical results. It is the first time that the compatibility condition and the BGK model are solved consistently in the BGK scheme.

The exact preservation of isolated contact and shear waves for the convective-flux model has been pursued with great efforts in the CFD community. This property prevents the contamination of a boundary layer due to excessive artificial dissipation. However, the clear capturing of a slip line is accompanied by instabilities (discussed in chapter

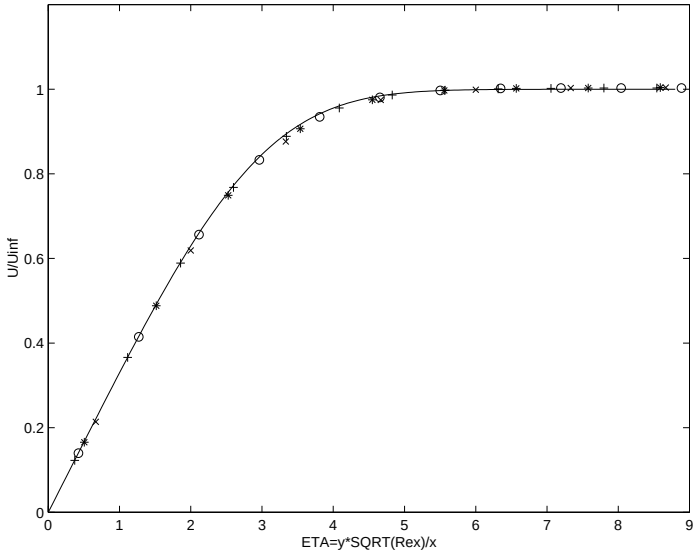

Figure 4.33: U-velocity in the boundary layer (Re = 28740), where the solid line is the exact solution, and the numerical solutions x: $x = 150$; *: $x = 200$; o: $x = 250$; +: $x = 300$

6). Different from the above approach, the BGK scheme is solving the viscous equations directly, and the inviscid solution is only a limiting case where the viscosity coefficient is small. As a result, the BGK scheme is vrey robust and always gives entropy-satisfying solutions. Numerically, due to the finite cell size and time step, artificial dissipation has to be included in any scheme. If the inviscid Euler equations are solved in the gas evolution stage, it is very difficult to model and control the necessary dissipations. Even though we are solving the viscous equations in the BGK method, the numerical results look less dissipative than those schemes solving the inviscid Euler equations if the same initial reconstruction is used for the conservative variables at the beginning of each time step. In the next chapter, the extension of the BGK method to multicomponent flows and hyperbolic conservation laws with source terms will be discussed.

Chapter 5

Extensions of the BGK Method

This chapter concerns the extension of the BGK method to multicomponent flow computations and to the Euler equations with heat transfer. The essential point in developing such an extended BGK method is to construct and obtain the corresponding BGK model first.

5.1 Multicomponent BGK Scheme

5.1.1 Introduction

The focus of this section is to solve the Euler equations for a two-component gas flow,

$$\begin{pmatrix} \rho^{(1)} \\ \rho^{(2)} \\ \rho U \\ \rho\epsilon \end{pmatrix}_t + \begin{pmatrix} \rho^{(1)}U \\ \rho^{(2)}U \\ \rho U^2 + P \\ U(\rho\epsilon + P) \end{pmatrix}_x = 0, \tag{5.1}$$

where $\rho = \rho^{(1)} + \rho^{(2)}$ is the total density, $\rho\epsilon$ the total energy, and U the average flow velocity. Each component has its specific heat ratio γ_i. The equation of state is $\epsilon_i = C_{vi}T$ and $P = P_1 + P_2$ is the total pressure. A detailed introduction to multicomponent flow equations can be found in [56]. A straightforward extension of finite volume schemes based on the Riemann solver to multicomponent flow calculations usually encounters two difficulties: the mass fraction $Y = \rho_1/\rho$ and $1 - Y = \rho_2/\rho$ may become negative and the pressure distribution may have oscillations through contact discontinuities. In order to reduce these difficulties, many methods have been developed, such as modifying the flux function [65], introducing nonconservative variables [56], or designing a specific numerical discretization to update Y for certain flow solvers [3]. Currently, hybrid schemes

have become popular for multicomponent flow calculations [57]. As we will see in Chapter 6, the oscillatory behavior at a material interface in shock capturing schemes is a natural consequence of the projection dynamics. In order words, the exchange of mass, momentum and energy between different components at a material interface naturally generates pressure wiggles. One possible way of reducing the pressure fluctuation is to efficiently dissipate it after its formation. We do not believe that any specific fixes for certain flow solvers can totally cure this problem, or any fixes can be generally applicable to other flows, *e.g.* three components flows. Recently, based on gas-kinetic theory, many lattice gas methods have been developed to study multicomponent gas flow [110, 36], such as for incompressible immiscible flow and phase transition problems [11]. Since there is no thermal energy involved here, the lattice gas method cannot be applied to compressible multicomponent flow calculations.

In this section, we are interested in extending the gas-kinetic BGK scheme developed in the last chapter to solve the multicomponent compressible Euler equations. Each component has its individual gas-kinetic BGK equation and the equilibrium states for each component are coupled by the physical requirements of total momentum and energy conservation in particle collisions. During each time step, the time dependent gas evolution of all components are obtained simultaneously. There are no specific numerical requirements imposed at the material interface in the current approach. Basically, each component is regarded as filling up the whole space and the multicomponent gas interactions are formulated everywhere, although the mass density for some components could be zero in certain flow regions. Gas kinetic theory can correctly describe particle transport in gas mixtures and the current approach is an initial attempt to capture these phenomena.

5.1.2 One-Dimensional Multicomponent BGK Method

The fundamental task in the construction of a finite-volume gas-kinetic scheme for multicomponent flow simulations is to evaluate the time-dependent gas distribution function f for each component at a cell interface, from which the numerical fluxes are evaluated. For a two-component gas flow, there are two macroscopic quantities in space x and time t, which are mass $(\rho^{(1)}(x,t), \rho^{(2)}(x,t))$, momentum $(\rho^{(1)}U^{(1)}(x,t), \rho^{(2)}U^{(2)}(x,t))$, and energy densities $(\rho^{(1)}\epsilon^{(1)}(x,t), \rho^{(2)}\epsilon^{(2)}(x,t))$, where the superscripts (1) and (2) refer to the component 1 and component 2 gases respectively. Generally, these two components have

different specific heat ratios ($\gamma^{(1)}, \gamma^{(2)}$). The governing equation for the time evolution of each component is the BGK model [10],

$$\begin{aligned} f_t^{(1)} + u f_x^{(1)} &= (g^{(1)} - f^{(1)})/\tau, \\ f_t^{(2)} + u f_x^{(2)} &= (g^{(2)} - f^{(2)})/\tau, \end{aligned} \tag{5.2}$$

where $f^{(1)}$ and $f^{(2)}$ are gas distribution functions for components 1 and 2, and $g^{(1)}$ and $g^{(2)}$ are the corresponding equilibrium states which $f^{(1)}$ and $f^{(2)}$ approach. Since we are solving the multicomponent Euler equations, the same collision time τ is assumed in the above two-component BGK model. For each component, the equilibrium state is a Maxwellian distribution with the general formulation,

$$g = \rho\,(\lambda/\pi)^{\frac{K+1}{2}}\, e^{-\lambda((u-U)^2+\xi^2)},$$

where λ is a function of temperature. $K^{(1)}$ and $K^{(2)}$ are the degrees of the internal variables ξ in the distribution functions, and are related to the specific heat ratios $\gamma^{(1)}$ and $\gamma^{(2)}$ (see chapter 2),

$$K^{(1)} = (5 - 3\gamma^{(1)})/(\gamma^{(1)} - 1) + 2 \qquad \text{and} \qquad K^{(2)} = (5 - 3\gamma^{(2)})/(\gamma^{(2)} - 1) + 2.$$

Due to the momentum and energy exchange in particle collisions between the two components, $g^{(1)}$ and $g^{(2)}$ in Eq.(5.2) are not independent functions. As a physical model, it is postulated that $g^{(1)}$ and $g^{(2)}$ have the same temperature and velocity. This assumption of no velocity slip is reasonable only if the density variation between the components is moderate as is generally the case with two gases. In some situations, the nonequilibrium particle transport in gas mixtures are important, especially when the molecular weights for each component are very different. In these cases, a modified BGK model is necessary [37] and the current scheme can also be extended there.

Instead of individual mass, momentum and energy conservation in a single component flow, for two component gas mixtures the compatibility condition is

$$\int [(g^{(1)} - f^{(1)})\phi_\alpha^{(1)} + (g^{(2)} - f^{(2)})\phi_\alpha^{(2)}] du d\xi = 0, \qquad \alpha = 1, 2, 3, 4 \tag{5.3}$$

where

$$\phi_\alpha^{(1)} = (1, 0, u, \frac{1}{2}(u^2 + \xi^2))^T$$

and

$$\phi_\alpha^{(2)} = (0, 1, u, \frac{1}{2}(u^2 + \xi^2))^T$$

are the moments for individual mass, total momentum, and total energy densities.

Based on Eq.(5.2) and Eq.(5.3), from the Chapman-Enskog expansion the diffusion equations between two components can be derived, for example

$$\frac{\partial \rho^{(1)}}{\partial t} + \frac{\partial (\rho^{(1)} U)}{\partial x} = \tau \frac{\partial}{\partial x} \left(\frac{\rho^{(2)}}{\rho^{(1)} + \rho^{(2)}} \frac{\partial}{\partial x} (\frac{\rho^{(1)}}{2\lambda}) - \frac{\rho^{(1)}}{\rho^{(1)} + \rho^{(2)}} \frac{\partial}{\partial x} (\frac{\rho^{(2)}}{2\lambda}) \right)$$

and

$$\frac{\partial \rho^{(2)}}{\partial t} + \frac{\partial (\rho^{(2)} U)}{\partial x} = \tau \frac{\partial}{\partial x} \left(\frac{\rho^{(1)}}{\rho^{(1)} + \rho^{(2)}} \frac{\partial}{\partial x} (\frac{\rho^{(2)}}{2\lambda}) - \frac{\rho^{(2)}}{\rho^{(1)} + \rho^{(2)}} \frac{\partial}{\partial x} (\frac{\rho^{(1)}}{2\lambda}) \right). \tag{5.4}$$

Here U and λ represent the common velocity and temperature in the equilibrium states $g^{(1)}$ and $g^{(2)}$. If the collision time for $f^{(1)}$ and $f^{(2)}$ in Eq.(5.2) are different, a similar diffusion equation can be derived [10]. Here the BGK model for multicomponent flow takes into account the effects of particle diffusion between different species, and the numerical scheme presented in this section is actually a flow solver for the above mass diffusion equations in the smooth flow regions. In other words, particle diffusion is unavoidable.

Due to the momentum and energy exchange in particle collisions, the maximum entropy criteria in the particle system requires that the equilibrium states $g^{(1)}$ and $g^{(2)}$ have a common velocity and temperature at any point in space and time. So for any given initial macroscopic variables in space and time,

$$W^{(1)} = (\rho^{(1)}, \rho^{(1)} U^{(1)}, \rho^{(1)} \epsilon^{(1)})^T \qquad \text{and} \qquad W^{(2)} = (\rho^{(2)}, \rho^{(2)} U^{(2)}, \rho^{(2)} \epsilon^{(2)})^T, \tag{5.5}$$

we can construct the corresponding equilibrium states,

$$g^{(1)} = \rho^{(1)} \left(\lambda_0/\pi\right)^{\frac{K^{(1)}+1}{2}} e^{-\lambda_0((u-U_0)^2+\xi^2)}$$

and

$$g^{(2)} = \rho^{(2)} \left(\lambda_0/\pi\right)^{\frac{K^{(2)}+1}{2}} e^{-\lambda_0((u-U_0)^2+\xi^2)}, \tag{5.6}$$

where the common values of λ_0 and U_0 can be obtained from the conservation requirements,

$$\rho^{(1)} U^{(1)} + \rho^{(2)} U^{(2)} = (\rho^{(1)} + \rho^{(2)}) U_0$$

and

$$\rho^{(1)}\epsilon^{(1)} + \rho^{(2)}\epsilon^{(2)} = \frac{\rho^{(1)} + \rho^{(2)}}{2}U_0^2 + \frac{(K^{(1)}+1)\rho^{(1)} + (K^{(2)}+1)\rho^{(2)}}{4\lambda_0}. \tag{5.7}$$

From the above two equations, U_0 and λ_0 can be obtained explicitly,

$$U_0 = \frac{\rho^{(1)}U^{(1)} + \rho^{(2)}U^{(2)}}{\rho^{(1)} + \rho^{(2)}} \tag{5.8}$$

and

$$\lambda_0 = \frac{1}{4}\frac{(K^{(1)}+1)\rho^{(1)} + (K^{(2)}+1)\rho^{(2)}}{\rho^{(1)}\epsilon^{(1)} + \rho^{(2)}\epsilon^{(2)} - \frac{1}{2}(\rho^{(1)} + \rho^{(2)})U_0^2}. \tag{5.9}$$

If both $W^{(1)}$ and $W^{(2)}$ in Eq.(5.5) are physically realizable states which satisfy

$$(\rho^{(1)} \geq 0, \rho^{(1)}\epsilon^{(1)} \geq \frac{1}{2}\rho^{(1)}{U^{(1)}}^2)$$

and

$$(\rho^{(2)} \geq 0, \rho^{(1)}\epsilon^{(2)} \geq \frac{1}{2}\rho^{(2)}{U^{(2)}}^2),$$

it can be proved that the value of λ_0 in Eq.(5.9) is a positive number. As a consequence, the equilibrium states are physical states with positive density and temperature. From thermodynamics, we know that the total entropy in the particle system with the equilibrium states $g^{(1)}$ and $g^{(2)}$ has the largest value among all possible particle distribution functions corresponding to the initial macroscopic states $W^{(1)}$ and $W^{(2)}$ in Eq.(5.5) under the momentum and energy exchangeable condition between different components.

Because of particle collisions, each component relaxes to a local equilibrium state in a time scale of the collision time τ. Since the CFL time step used in the current scheme is much larger than the collision time, the exchange of momentum and energy in particle collisions can be regarded as taking place instantaneously and the temperature and velocity of both components attain a common value. Therefore, from the numerical point of view at any point in space and time, it is fair enough to modify the individual macroscopic distribution in Eq.(5.5) to the equilibrium values

$$W^{(1)} = \left(\rho^{(1)}, \rho^{(1)}U^{(1)}, \rho^{(1)}\epsilon^{(1)}\right)^T = \left(\rho^{(1)}, \rho^{(1)}U_0, \frac{1}{2}\rho^{(1)}(U_0^2 + \frac{K^{(1)}+1}{2\lambda_0})\right)^T$$

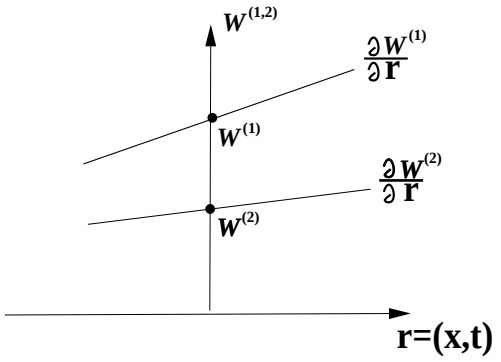

Figure 5.1: Linearly distributed macroscopic variables $\frac{\partial W^{(1,2)}}{\partial r}$ in $r = x$ or t

and

$$W^{(2)} = \left(\rho^{(2)}, \rho^{(2)}U^{(2)}, \rho^{(2)}\epsilon^{(2)}\right)^T = \left(\rho^{(2)}, \rho^{(2)}U_0, \frac{1}{2}\rho^{(2)}(U_0^2 + \frac{K^{(2)}+1}{2\lambda_0})\right)^T. \tag{5.10}$$

The equilibrium states $g^{(1)}$ and $g^{(2)}$ are coupled with the common temperature and velocity at any point in space and time $r = (x, t)$, as well as their slopes. As shown in Fig.(5.1), once we know $W^{(1)}$, $W^{(2)}$ and their linear slopes for the macroscopic variables,

$$W^{(1)} + \frac{\partial W^{(1)}}{\partial r} r = W^{(1)} + \left(\frac{\partial \rho^{(1)}}{\partial r}, \frac{\partial(\rho^{(1)}U^{(1)})}{\partial r}, \frac{\partial(\rho^{(1)}\epsilon^{(1)})}{\partial r}\right)^T r$$

and

$$W^{(2)} + \frac{\partial W^{(2)}}{\partial r} r = W^{(2)} + \left(\frac{\partial \rho^{(2)}}{\partial r}, \frac{\partial(\rho^{(2)}U^{(2)})}{\partial r}, \frac{\partial(\rho^{(2)}\epsilon^{(2)})}{\partial r}\right)^T r,$$

we can construct the equivalent gas distribution functions $g^{(1)}$ and $g^{(2)}$, and the corresponding slopes $(m^{(1)}, n^{(1)}, p^{(1)})$ and $(m^{(2)}, n^{(2)}, p^{(2)})$ in the expansion of the Maxwellian distribution functions,

$$\left[1 + \left(m^{(1)} + n^{(1)}u + p^{(1)}(u^2 + \xi^2)\right) r\right] g^{(1)},$$
$$\left[1 + \left(m^{(2)} + n^{(2)}u + p^{(2)}(u^2 + \xi^2)\right) r\right] g^{(2)}. \tag{5.11}$$

Due to the requirement of $g^{(1)}$ and $g^{(2)}$ having the same temperature and velocity at any point in space and time, as shown in Eq.(5.6), the variables $(m^{(1,2)}, n^{(1,2)}, p^{(1,2)})$ in equation (5.11) are not totally independent. Since $n^{(1)}, p^{(1)}, n^{(2)}, p^{(2)}$ depend only on the r-derivative of U_0 and λ_0, a common velocity and temperature in space and time require

$$n \equiv n^{(1)} = n^{(2)} \qquad \text{and} \qquad p \equiv p^{(1)} = p^{(2)}.$$

So, the connections between the macroscopic and the microscopic distributions can be reduced to

$$\begin{aligned}
\begin{pmatrix} \frac{\partial \rho^{(1)}}{\partial r} \\ \frac{\partial \rho^{(2)}}{\partial r} \\ \frac{\partial (\rho^{(1)} U^{(1)} + \rho^{(2)} U^{(2)})}{\partial r} \\ \frac{\partial (\rho^{(1)} \epsilon^{(1)} + \rho^{(2)} \epsilon^{(2)})}{\partial r} \end{pmatrix} &\equiv \begin{pmatrix} \omega_1 \\ \omega_2 \\ \omega_3 \\ \omega_4 \end{pmatrix} \\
&= \int \Big[\Big(m^{(1)} + nu + p(u^2 + \xi^2) \Big) g^{(1)} \phi_\alpha^{(1)} \\
&\quad + \Big(m^{(2)} + nu + p(u^2 + \xi^2) \Big) g^{(2)} \phi_\alpha^{(2)} \Big] du d\xi. \qquad (5.12)
\end{aligned}$$

The above four equations uniquely determine the four unknowns $(m^{(1)}, m^{(2)}, n, p)$ and the solutions can be obtained in the following: Define

$$\Pi_1 = \omega_3 - U_0(\omega_1 + \omega_2),$$

$$\Pi_2 = 2\omega_4 - (U_0^2 + \frac{K^{(1)} + 1}{2\lambda_0})\omega_1 - (U_0^2 + \frac{K^{(2)} + 1}{2\lambda_0})\omega_2.$$

The solutions of Eq.(5.12) are

$$p = \frac{2\lambda_0^2(\Pi_2 - 2U_0\Pi_1)}{(K^{(1)} + 1)\rho^{(1)} + (K^{(2)} + 1)\rho^{(2)}},$$

$$n = \frac{2\lambda_0}{\rho^{(1)} + \rho^{(2)}} \left(\Pi_1 - \frac{(\rho^{(1)} + \rho^{(2)})U_0}{\lambda_0} p \right),$$

$$m^{(1)} = \frac{1}{\rho^{(1)}} \left(\omega_1 - \rho^{(1)} U_0 n - \rho^{(1)} (U_0^2 + \frac{K^{(1)} + 1}{2\lambda_0}) p \right),$$

and

$$m^{(2)} = \frac{1}{\rho^{(2)}} \left(\omega_2 - \rho^{(2)} U_0 n - \rho^{(2)} (U_0^2 + \frac{K^{(2)} + 1}{2\lambda_0}) p \right).$$

The above solutions will be used a few times in the current two-component BGK solver to obtain both the spatial and temporal variations of the particle distribution functions.

For each cell j, the cell center is located at x_j and the cell interfaces are at $x_{j-1/2}$ and $x_{j+1/2}$. The cell averaged macroscopic variables are denoted as $W_j^{(1)}$ and $W_j^{(2)}$ for the mass, momentum and energy densities. In order to update the cell-averaged values $W_j^{(1,2)}$, we need to get the numerical fluxes across the cell interface. These fluxes are determined from the time-dependent gas distribution functions. The gas distribution function for each component at a cell interface can be obtained from the integral solution of the BGK model,

$$\begin{aligned} f^{(1)}(x_{j+1/2},t,u,\xi) &= \frac{1}{\tau}\int_0^t g^{(1)}(x',t',u,\xi)e^{-(t-t')/\tau}dt' \\ &\quad +e^{-t/\tau}f_0^{(1)}(x_{j+1/2}-ut) \end{aligned} \tag{5.13}$$

for component 1, and

$$\begin{aligned} f^{(2)}(x_{j+1/2},t,u,\xi) &= \frac{1}{\tau}\int_0^t g^{(2)}(x',t',u,\xi)e^{-(t-t')/\tau}dt' \\ &\quad +e^{-t/\tau}f_0^{(2)}(x_{j+1/2}-ut) \end{aligned} \tag{5.14}$$

for component 2, where $x_{j+1/2}$ is the cell interface and $x' = x_{j+1/2} - u(t-t')$ the particle trajectory. There are four unknowns in Eq.(5.13) and Eq.(5.14). Two of them are initial gas distribution functions $f_0^{(1)}$ and $f_0^{(2)}$ at the beginning of each time step $t = 0$, and the others are $g^{(1)}$ and $g^{(2)}$ in both space and time locally around $(x_{j+1/2}, t = 0)$. In order to obtain all these unknowns, the BGK scheme is summarized as follows.

(1) Modify the initial cell average conservative variables $W_j^{(1,2)}$ in each cell j to the equilibrium values according to Eq.(5.10) where the equilibrium velocity and temperature in each cell are obtained using Eq.(5.8) and Eq.(5.9). Then, apply the standard van Leer or MUSCL limiters to interpolate the equilibrium conservative variables $W_j^{(1,2)}$ in each cell j to get the reconstructed initial data

$$\bar{W}_j^{(1,2)}(x) = W_j^{(1,2)} + \frac{\bar{W}_j^{(1,2)}(x_{j+1/2}) - \bar{W}_j^{(1,2)}(x_{j-1/2})}{x_{j+1/2}-x_{j-1/2}}(x-x_j) \qquad \text{for} \qquad x\epsilon[x_{j-1/2}, x_{j+1/2}], \tag{5.15}$$

where $\left(\bar{W}_j^{(1,2)}(x_{j-1/2}), \bar{W}_j^{(1,2)}(x_{j+1/2})\right)$, are the reconstructed point-wise values at the cell interfaces $x_{j-1/2}$ and $x_{j+1/2}$.

(2) Based on the states $\left(\bar{W}_j^{(1,2)}(x_{j+1/2}), \bar{W}_{j+1}^{(1,2)}(x_{j+1/2})\right)$, use Eq.(5.8) and Eq.(5.9) on both sides of the cell interface $x_{j+1/2}$ to evaluate the equilibrium velocities U_0^l, U_0^r and "temperatures" λ_0^l, λ_0^r, and modify these reconstructed data to the new values according to Eq.(5.10), which are denoted as

$$\tilde{W}_j^{(1,2)}(x_{j+1/2}) \qquad \text{and} \qquad \tilde{W}_{j+1}^{(1,2)}(x_{j+1/2}). \tag{5.16}$$

Then, connect the above values in Eq.(5.16) to the cell centered values in Eq.(5.15),

$$\bar{W}_j^{(1,2)}(x_j) \qquad \text{and} \qquad \bar{W}_{j+1}^{(1,2)}(x_{j+1}), \tag{5.17}$$

to get the linear slopes of mass, momentum and energy densities for each component on both sides of the cell interface,

$$\frac{\tilde{W}_j^{(1,2)}(x_{j+1/2}) - \bar{W}_j^{(1,2)}(x_j)}{x_{j+1/2} - x_j} \qquad \text{and} \qquad \frac{\bar{W}_{j+1}^{(1,2)}(x_{j+1}) - \tilde{W}_{j+1}^{(1,2)}(x_{j+1/2})}{x_{j+1} - x_{j+1/2}}. \tag{5.18}$$

In order to translate the above macroscopic flow distributions into the equivalent microscopic gas distribution functions, we construct the initial distribution functions $f_0^{(1)}$ and $f_0^{(2)}$ in Eq.(5.13) and Eq.(5.14) as

$$f_0^{(1)} = \begin{cases} \left(1 + a_l^{(1)}(x - x_{j+1/2})\right) g_l^{(1)}, & x \le x_{j+1/2}, \\ \left(1 + a_r^{(1)}(x - x_{j+1/2})\right) g_r^{(1)}, & x \ge x_{j+1/2}, \end{cases} \tag{5.19}$$

for component 1, and

$$f_0^{(2)} = \begin{cases} \left(1 + a_l^{(2)}(x - x_{j+1/2})\right) g_l^{(2)}, & x \le x_{j+1/2}, \\ \left(1 + a_r^{(2)}(x - x_{j+1/2})\right) g_r^{(2)}, & x \ge x_{j+1/2}, \end{cases} \tag{5.20}$$

for component 2. $g_l^{(1)}, g_l^{(2)}$ can be obtained from the macroscopic densities $\tilde{W}_j^{(1,2)}(x_{j+1/2})$ in Eq.(5.16),

$$g_l^{(1)} = \rho_l^{(1)} \left(\lambda_0^l/\pi\right)^{\frac{K^{(1)}+1}{2}} e^{-\lambda_0^l((u-U_0^l)^2+\xi^2)}$$

and

$$g_l^{(2)} = \rho_l^{(2)} \left(\lambda_0^l/\pi\right)^{\frac{K^{(2)}+1}{2}} e^{-\lambda_0^l((u-U_0^l)^2+\xi^2)}. \tag{5.21}$$

Similarly, $g_r^{(1)}$ and $g_r^{(2)}$ can be found from $\tilde{W}_{j+1}^{(1,2)}(x_{j+1/2})$ in Eq.(5.16),

$$g_r^{(1)} = \rho_r^{(1)} \left(\lambda_0^r/\pi\right)^{\frac{K^{(1)}+1}{2}} e^{-\lambda_0^r((u-U_0^r)^2+\xi^2)}$$

and

$$g_r^{(2)} = \rho_r^{(2)} \left(\lambda_0^r/\pi\right)^{\frac{K^{(2)}+1}{2}} e^{-\lambda_0^r((u-U_0^r)^2+\xi^2)}. \tag{5.22}$$

The terms $a_{l,r}^{(1,2)}$ in Eq.(5.19) and Eq.(5.20) are composed of

$$a_{l,r}^{(1,2)} = m_{l,r}^{(1,2)} + n_{l,r}u + p_{l,r}(u^2+\xi^2),$$

which can be determined on both sides of a cell interface in terms of the slopes of macroscopic variables in Eq.(5.18) by using the techniques for solving Eq.(5.12) with $r = x$. At this point, all parameters in Eq.(5.19) and Eq.(5.20) for the initial gas distribution functions at the beginning of each time step are determined from the initial reconstructed macroscopic distributions.

(3) Assume the equilibrium states in Eq.(5.13) and Eq.(5.14) around $(x_{j+1/2}, t=0)$ are

$$\begin{aligned} g^{(1)} &= \Big(1 + (1-\mathrm{H}(x-x_{j+1/2}))(x-x_{j+1/2})\bar{a}_l^{(1)} \\ &\quad + \mathrm{H}(x-x_{j+1/2})(x-x_{j+1/2})\bar{a}_r^{(1)} + \bar{A}^{(1)}t\Big)\, g_0^{(1)}, \end{aligned} \tag{5.23}$$

and

$$\begin{aligned} g^{(2)} &= \Big(1 + (1-\mathrm{H}(x-x_{j+1/2}))(x-x_{j+1/2})\bar{a}_l^{(2)} \\ &\quad + \mathrm{H}(x-x_{j+1/2})(x-x_{j+1/2})\bar{a}_r^{(2)} + \bar{A}^{(2)}t\Big)\, g_0^{(2)}, \end{aligned} \tag{5.24}$$

where H is the Heaviside function. $g_0^{(1)}$ and $g_0^{(2)}$ are the initial equilibrium states located at the cell interface,

$$g_0^{(1)} = \rho_0^{(1)} \left(\lambda_0/\pi\right)^{\frac{K^{(1)}+1}{2}} e^{-\lambda_0((u-U_0)^2+\xi^2)}$$

and

$$g_0^{(2)} = \rho_0^{(2)} \left(\lambda_0/\pi\right)^{\frac{K^{(2)}+1}{2}} e^{-\lambda_0((u-U_0)^2+\xi^2)}. \tag{5.25}$$

The parameters $\bar{a}_{l,r}^{(1,2)}$ and $\bar{A}^{(1,2)}$ have the forms

$$\bar{a}_{l,r}^{(1,2)} = \bar{m}_{l,r}^{(1,2)} + \bar{n}_{l,r}u + \bar{p}_{l,r}(u^2+\xi^2) \qquad \text{and} \qquad \bar{A}^{(1,2)} = \bar{A}_a^{(1,2)} + \bar{A}_b u + \bar{A}_c(u^2+\xi^2).$$

Here $g_0^{(1)}$ and $g_0^{(2)}$ in Eq.(5.23) and (5.24) can be obtained self-consistently by taking the limits of $(t \to 0)$ in Eq.(5.13) and Eq.(5.14) and applying the compatibility condition at $(x = x_{j+1/2}, t = 0)$, giving

$$\begin{aligned}
\begin{pmatrix} \rho_0^{(1)} \\ \rho_0^{(2)} \\ (\rho_0^{(1)} + \rho_0^{(2)})U_0 \\ \rho_0^{(1)}\epsilon_0^{(1)} + \rho_0^{(2)}\epsilon_0^{(2)} \end{pmatrix} &\equiv \int \left(g_0^{(1)}\phi_\alpha^{(1)} + g_0^{(2)}\phi_\alpha^{(2)} \right) du d\xi \\
&= \int \Big[\Big(\mathrm{H}(u) g_l^{(1)} + (1 - \mathrm{H}(u)) g_r^{(1)} \Big) \phi_\alpha^{(1)} \\
&\quad + \Big(g_l^{(2)} \mathrm{H}(u) + g_r^{(2)} (1 - \mathrm{H}(u)) \Big) \phi_\alpha^{(2)} \Big] du d\xi. \qquad (5.26)
\end{aligned}$$

Using $g_{l,r}^{(1,2)}$ in Eq.(5.21) and Eq.(5.22), the right hand side of Eq.(5.26) can be evaluated explicitly. Therefore, $\rho_0^{(1)}$, $\rho_0^{(2)}$, λ_0, and U_0 in Eq.(5.25) can be obtained from Eq.(5.26). As a result, $g_0^{(1)}$ and $g_0^{(2)}$ are totally determined. Then, connecting the macroscopic variables

$$W_0^{(1)} = \left(\rho_0^{(1)}, \rho_0^{(1)} U_0, \rho_0^{(1)} \epsilon_0^{(1)} \right) \qquad \text{and} \qquad W_0^{(2)} = \left(\rho_0^{(2)}, \rho_0^{(2)} U_0, \rho^{(2)} \epsilon_0^{(2)} \right)$$

at the cell interface to the cell centered values in Eq.(5.17) on both sides, we can obtain the slopes for the macroscopic variables,

$$\frac{W_0^{(1,2)} - \bar{W}_j^{(1,2)}(x_j)}{x_{j+1/2} - x_j} \qquad \text{and} \qquad \frac{\bar{W}_{j+1}^{(1,2)}(x_{j+1}) - W_0^{(1,2)}}{x_{j+1} - x_{j+1/2}},$$

from which $\bar{a}_l^{(1)}$ and $\bar{a}_l^{(2)}$ on the left side and $\bar{a}_r^{(1)}$ and $\bar{a}_r^{(2)}$ on the right side in Eq.(5.23) and Eq.(5.24) can be obtained by using the same techniques for solving Eq.(5.12) with $r = x$. At this point, there are still two unknowns $\bar{A}^{(1,2)}$ for the time variation parts of the gas distribution functions in Eq.(5.23) and Eq.(5.24).

(4) Substituting Eq.(5.23), Eq.(5.24), Eq.(5.19), and Eq.(5.20) into the integral solutions Eq.(5.13) and Eq.(5.14), we get

$$\begin{aligned}
f^{(1)}(x_{j+1/2}, t, u, \xi) &= (1 - e^{-t/\tau}) g_0^{(1)} \\
&\quad + \Big(\tau(-1 + e^{-t/\tau}) + t e^{-t/\tau} \Big) \Big(\bar{a}_l^{(1)} \mathrm{H}(u) + \bar{a}_r^{(1)} (1 - \mathrm{H}(u)) \Big) u g_0^{(1)} \\
&\quad + \tau(t/\tau - 1 + e^{-t/\tau}) \bar{A}^{(1)} g_0^{(1)}
\end{aligned}$$

$$+e^{-t/\tau}\left((1-uta_l^{(1)})\mathrm{H}(u)g_l^{(1)}+(1-uta_r^{(1)})(1-\mathrm{H}(u))g_r^{(1)}\right) \tag{5.27}$$

and

$$\begin{aligned} f^{(2)}(x_{j+1/2},t,u,\xi) &= (1-e^{-t/\tau})g_0^{(2)} \\ &+\left(\tau(-1+e^{-t/\tau})+te^{-t/\tau}\right)\left(\bar{a}_l^{(2)}\mathrm{H}(u)+\bar{a}_r^{(2)}(1-\mathrm{H}(u))\right)ug_0^{(2)} \\ &+\tau(t/\tau-1+e^{-t/\tau})\bar{A}^{(2)}g_0^{(2)} \\ &+e^{-t/\tau}\left((1-uta_l^{(2)})\mathrm{H}(u)g_l^{(2)}+(1-uta_r^{(2)})(1-\mathrm{H}(u))g_r^{(2)}\right). \end{aligned} \tag{5.28}$$

In order to evaluate the unknowns $\bar{A}^{(1,2)}$ in the above two equations, we can use the compatibility condition at the cell interface $x_{j+1/2}$ on the whole CFL time step Δt,

$$\int_0^{\Delta t}\int[(g^{(1)}-f^{(1)})\phi_\alpha^{(1)}+(g^{(2)}-f^{(2)})\phi_\alpha^{(2)}]dud\xi dt=0,$$

from which we can get

$$\begin{aligned} \int[g_0^{(1)}\bar{A}^{(1)}\phi_\alpha^{(1)}+g_0^{(2)}\bar{A}^{(2)}\phi_\alpha^{(2)}]dud\xi &= \int\Big[\left(\bar{A}_a^{(1)}+\bar{A}_bu+\bar{A}_c(u^2+\xi^2)\right)g_0^{(1)}\phi_\alpha^{(1)} \\ &\quad+\left(\bar{A}_a^{(2)}+\bar{A}_bu+\bar{A}_c(u^2+\xi^2)\right)g_0^{(2)}\phi_\alpha^{(2)}\Big]dud\xi \\ &\equiv \begin{pmatrix} \frac{\partial\rho^{(1)}}{\partial t} \\ \frac{\partial\rho^{(2)}}{\partial t} \\ \frac{\partial(\rho^{(1)}U^{(1)}+\rho^{(2)}U^{(2)})}{\partial t} \\ \frac{\partial(\rho^{(1)}\epsilon^{(1)}+\rho^{(2)}\epsilon^{(2)})}{\partial t} \end{pmatrix} \\ &= \frac{1}{\gamma_0}\int\Big[\gamma_1g_0^{(1)}+\gamma_2u\left(\bar{a}_l^{(1)}\mathrm{H}(u)+\bar{a}_r^{(1)}(1-\mathrm{H}(u))\right)g_0^{(1)} \\ &+ \gamma_3\left(\mathrm{H}(u)g_l^{(1)}+(1-\mathrm{H}(u))g_r^{(1)}\right) \\ &+ \gamma_4u\left(a_l^{(1)}\mathrm{H}(u)g_l^{(1)}+a_r^{(1)}(1-\mathrm{H}(u))g_r^{(1)}\right)\Big]\phi_\alpha^{(1)}dud\xi \\ &+ \Big[\gamma_1g_0^{(2)}+\gamma_2u\left(\bar{a}_l^{(2)}\mathrm{H}(u)+\bar{a_r^{(2)}}(1-\mathrm{H}(u))\right)g_0^{(2)} \\ &+ \gamma_3\left(\mathrm{H}(u)g_l^{(2)}+(1-\mathrm{H}(u))g_r^{(2)}\right) \\ &+ \gamma_4u\left(a_l^{(2)}\mathrm{H}(u)g_l^{(2)}+a_r^{(2)}(1-\mathrm{H}(u))g_r^{(2)}\right)\Big]\phi_\alpha^{(2)}dud\xi, \end{aligned} \tag{5.29}$$

where γ_0 to γ_4 have the same values as those in Eq.(4.22).

Since all terms on the right hand side of Eq.(5.29) are known and the integral can be evaluated explicitly, the coefficients $(\bar{A}_a^{(1,2)}, \bar{A}_b, \bar{A}_c)$ can be determined from Eq.(5.29) using the techniques for solving Eq.(5.12) with $r = t$.

(5) Finally the time-dependent numerical fluxes for component 1 and component 2 gases across a cell interface can be obtained by taking the moments of the individual gas distribution functions $f^{(1)}$ and $f^{(2)}$ in Eq.(5.27) and Eq.(5.28) separately, which are

$$\begin{pmatrix} \mathcal{F}_{\rho^{(1)}} \\ 0 \\ \mathcal{F}_{\rho^{(1)}U^{(1)}} \\ \mathcal{F}_{\rho^{(1)}\epsilon^{(1)}} \end{pmatrix}_{j+1/2} = \int u\phi_\alpha^{(1)} f^{(1)}(x_{j+1/2}, t, u, \xi) du d\xi,$$

and

$$\begin{pmatrix} 0 \\ \mathcal{F}_{\rho^{(2)}} \\ \mathcal{F}_{\rho^{(2)}U^{(2)}} \\ \mathcal{F}_{\rho^{(2)}\epsilon^{(2)}} \end{pmatrix}_{j+1/2} = \int u\phi_\alpha^{(2)} f^{(2)}(x_{j+1/2}, t, u, \xi) du d\xi.$$

Integrating the above equations for the whole time step Δt, we can get the total mass, momentum and energy transports for each component, from which the flow variables in each cell can be updated. For the next time step, we go back to step(1) and repeat all above steps. From the above numerical procedures, we can observe the similarity of the BGK schemes for both the multicomponent flows and the single component flows.

5.1.3 Numerical Examples

Three shock tube test cases are presented in this section to validate the current approach for multicomponent flow calculations. In all calculations, the length of the numerical domain is equal to 100 and each cell size is $\Delta x = 1$. Different from any other approaches [56, 3], the van Leer's limiter is used in our scheme for the reconstruction of *conservative* variables for each component directly without imposing any specific numerical requirement for a smooth interface transition. The time step is determined by the common CFL condition where the CFL number is equal to 0.65. The collision time τ is the same as that for the single component BGK solver. Due to a non-zero collision time, which is a necessary condition from the numerical point of view, the particle diffusion and flow dissipation can be naturally captured.

CASE(1) The first test case is taken from [56, 65], and the initial condition is

$$W_L = (\rho_L, \rho_L U_L, E_L, \gamma_L) = (1.0, 0.0, 2.5, 1.4),$$

and

$$W_R = (\rho_R, \rho_R U_R, E_R, \gamma_R) = (0.125, 0.0, 0.5, 1.2).$$

In this calculation, the initial discontinuity is located at $x = 50$. The simulation results are shown in Fig.(5.2)-Fig.(5.4) for the total density ($\rho^{(1)} + \rho^{(2)}$), pressure, and velocity. In all these figures, the solid lines are the curves obtained from 400 grid points with the same BGK scheme. The pressure and velocity are very smooth across the material interface, although all conservative variables are used in the initial reconstruction. The pressure distribution in Fig.(5.3) is obtained as a passive variable from the conservative variables at the output time. Fig.(5.5) presents the average γ in each cell which is defined as $\gamma = (K + 3)/(K + 1)$ and the average K is $K = (\rho^{(1)}K^{(1)} + \rho^{(2)}K^{(2)})/(\rho^{(1)} + \rho^{(2)})$. Fig.(5.6) and Fig.(5.7) are the individual mass densities $\rho^{(1)}$ and $\rho^{(2)}$ for each component. Since we follow the time evolution of each component explicitly, the total mass for each component is precisely conserved. If there were no momentum and energy exchange between the two components through particle collisions, the physical problem would become the one in which each component expands into a vacuum, and the final results will be totally different from these results shown above. Also, as shown in Fig.(5.6) and Fig.(5.7), both $\rho^{(1)}$ and $\rho^{(2)}$ around the material interface reduce from certain values to zero. If we define $\varphi = \rho^{(1)} - \rho^{(2)}$, then according to the sign of φ, we know in each cell which component the gas is mostly composed of. If we define $\varphi = 0$ as the material interface, the function φ will be similar to the level set function [92]. However, φ is updated in our scheme according to a different physical model and the distribution of φ can be used as a measure of particle diffusion. At the same time, the material interface can be easily captured in multidimensional and multicomponent flow evolutions.

CASE(2) The second test case is taken from Abgrall's recent paper [3] with initial data

$$W_L = (\rho_L, \rho_L U_L, E_L, \gamma_L) = (14.54903, 0.0, 2.9 \times 10^7, 1.67),$$

and

$$W_R = (\rho_R, \rho_R U_R, E_R, \gamma_R) = (1.16355, 0.0, 2.5 \times 10^5, 1.40).$$

This example is interesting and very difficult for multicomponent flow solvers due to its large pressure variation. 100 mesh points are used for our BGK solver. Fig.(5.8)-

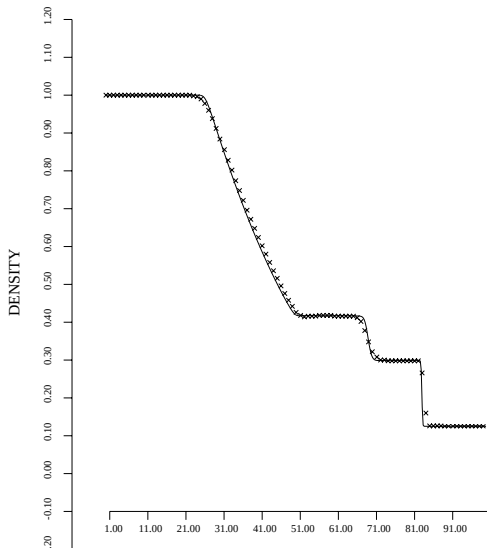

Figure 5.2: Total density distribution ($\rho^{(1)} + \rho^{(2)}$)

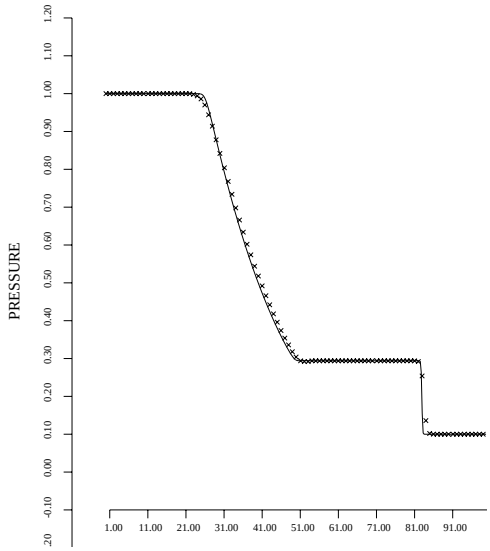

Figure 5.3: Pressure distribution

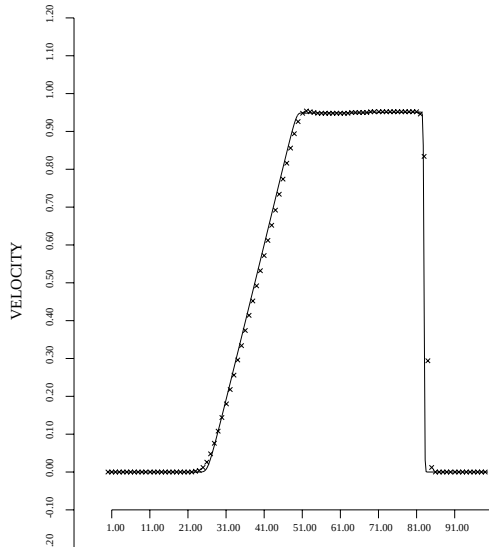

Figure 5.4: Velocity distribution

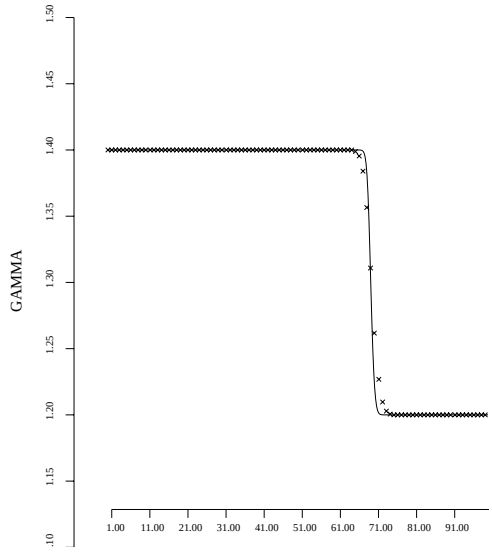

Figure 5.5: γ distribution

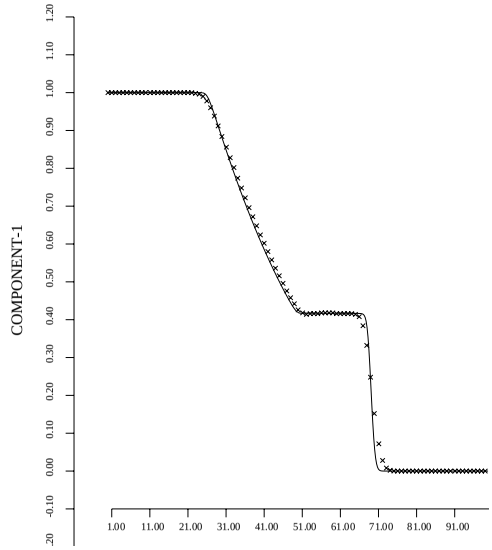

Figure 5.6: Density $\rho^{(1)}$ distribution

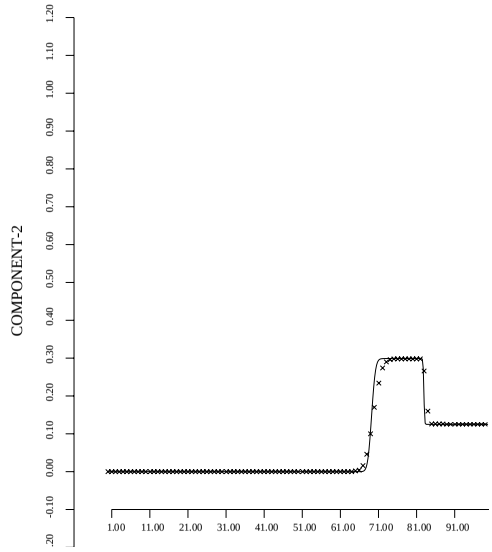

Figure 5.7: Density $\rho^{(2)}$ distribution

Fig.(5.13) show the total mass density ($\rho^{(1)} + \rho^{(2)}$), pressure, velocity, γ, $\rho^{(1)}$, and $\rho^{(2)}$ separately, where the solid lines are obtained from the same scheme with 400 grid points. The velocity and pressure are very smooth at the material interface, but a small wiggle appears at the end of the rarefaction wave. It seems that this wiggle is not caused by the current technique designed specifically for the two-component flow solver. Even for the single component BGK solver, if the initial data have extremely large density and pressure jump, a similar wiggle usually appears. It seems that this mechanism of the appearance of wiggle is inherent to the finite volume method.

For the test case of a shock-bubble interaction presented in [3], the current scheme has some difficulties. Because the gas-kinetic scheme is a scheme designed to describe the advection-diffusion equation, it can never keep a contact discontinuity sharp and stationary. Physical diffusion and heat conduction due to the particle transport in gases will naturally smear the contact discontinuity. So, before the shock interacts with the bubble, the bubble surface has already been smeared over a few cells and the thickness depends on the collision time. It seems that for the shock-interface interaction cases, a carefully designed scheme based on the approximate Riemann solver should be useful, at least in the 1-D case, since these schemes could keep the contact material interface sharp before the contact becomes involved in the interactions with shocks. However, for the general cases where the initial bubble surface is located in the middle of a numerical cell, the ability of any shock capturing scheme to keep a stationary material interface sharp and free of wiggles is doubtful. For these applications where advection-diffusion phenomena are important (not purely artificial diffusion), such as pollutant propagation and turbulent mixing layer, the gas-kinetic scheme will be suitable and the BGK model could naturally describe this kind of physical phenomena [111]. Another good application for the current scheme is that it can be applied to the gas-vacuum expansion problem which occurs in interstellar medium and confined plasma. As it is well-known, the Riemann solver has great difficulty in handling the gas-vacuum expansion case, where the density and temperature easily become negative. This is true especially for the approximate Riemann solver [26].

CASE(3) As a third case, we test the gas-vacuum expansion phenomena with initial data,

$$W_L = (\rho_L, \rho_L U_L, E_L, \gamma_L) = (1.0, 0.0, 2.5, 1.4),$$

$$W_R = (\rho_R, \rho_R U_R, E_R, \gamma_R) = (0.0, 0.0, 0.0, 0.0),$$

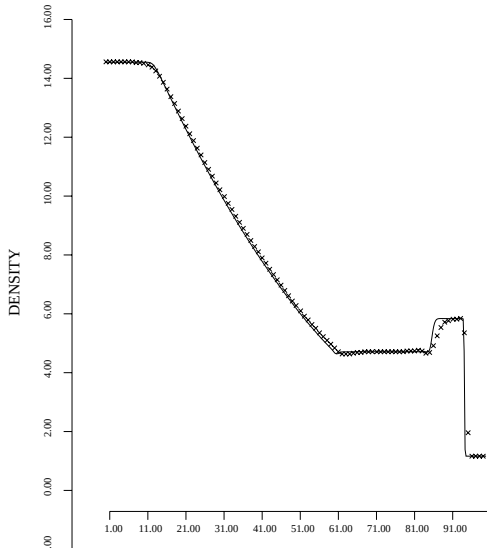

Figure 5.8: Total density distribution ($\rho^{(1)} + \rho^{(2)}$)

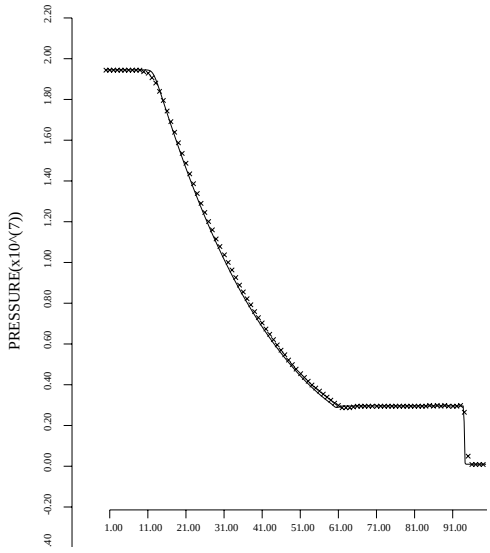

Figure 5.9: Pressure distribution

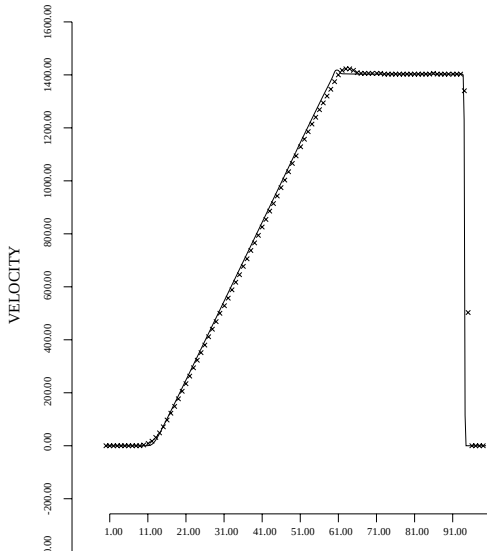

Figure 5.10: Velocity distribution

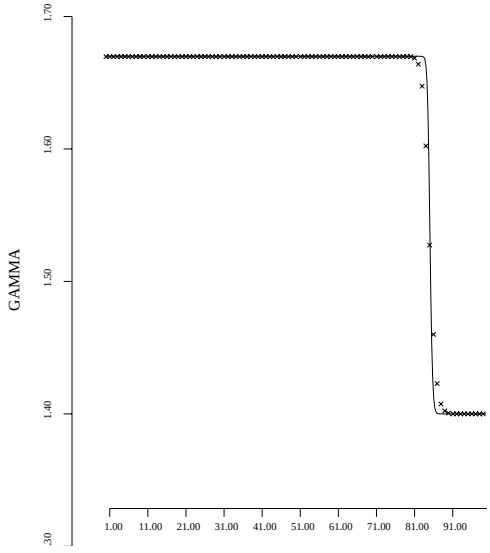

Figure 5.11: γ distribution

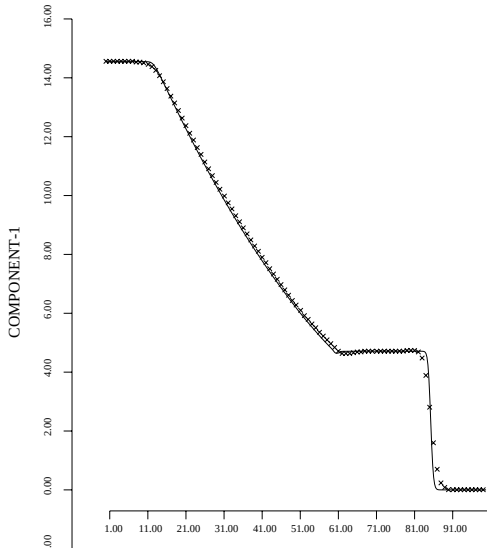

Figure 5.12: Density $\rho^{(1)}$ distribution

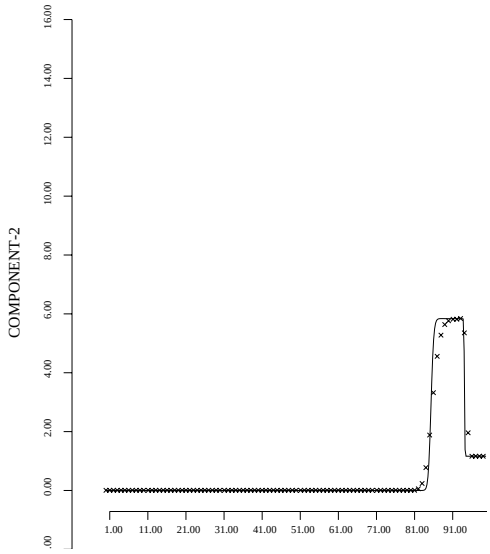

Figure 5.13: Density $\rho^{(2)}$ distribution

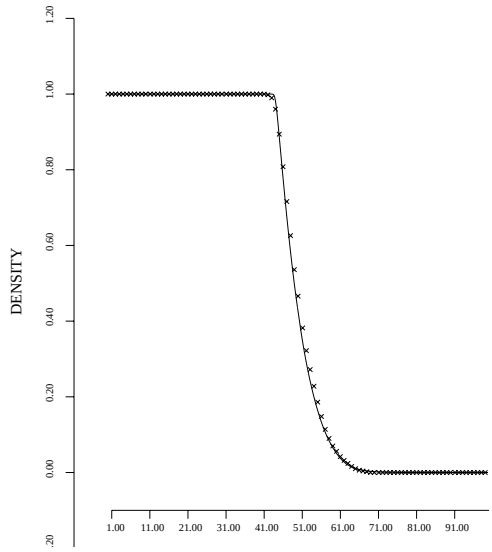

Figure 5.14: Density distribution $\rho^{(1)}$

where all flow variables on the right hand side are zero. 100 grid points are used here. The simulation results are shown in Fig(5.14) and Fig.(5.15) for the density and pressure distributions for the component 1 gas. The solid lines are obtained from the same scheme with 400 grid points. Comparing Fig.(5.14) with Fig.(5.6), we can observe clearly the effects of particle collisions between different components and the effects of dynamical coupling in the two component gas evolution.

5.1.4 Summary

In this section, we have developed a BGK scheme for multicomponent flow calculations. Since we have followed the time-evolution of the distribution function for each component explicitly, the total mass for each component is precisely conserved. Theoretically, it is possible to prove, at least in simple cases, that the current method keeps Y and $1 - Y$ positive throughout the flow calculation. Due to particle collisions between different components, individual momentum and energy for each components are exchangeable, but the total momentum and energy are precisely conserved. The current scheme can be extended to the three dimensional case without major modifications. The capturing of particle diffusion process in multicomponent gas flows by numerical methods is a tough problem, nevertheless the current approach is a starting point in this direction. By using a simplified BGK approach, Kotelnikov and Montgomery [63, 64] have recently successfully extended the BGK scheme to inhomogeneous flows and shock turbulent interaction calculations.

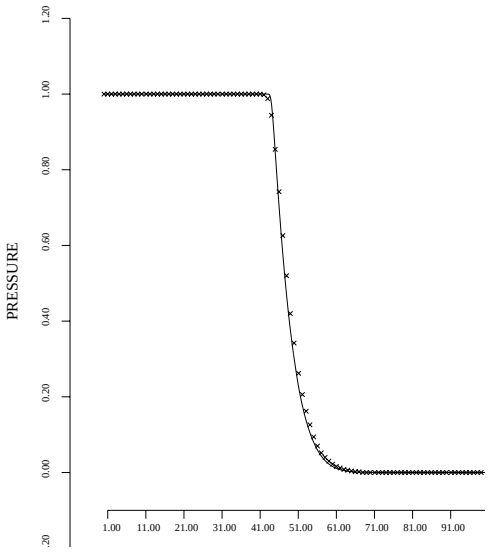

Figure 5.15: Pressure distribution

5.2 The Euler Equations with Heat Transfer

5.2.1 Introduction

Many numerical schemes have been developed to study and analyze hyperbolic equations with source terms [139, 70, 52, 53, 8, 16, 1, 93, 94]. As analyzed in Chapter 3 of this lecture notes, the BGK method gives an excellent example of an unsplitting scheme for the Boltzmann equation, where the KFVS scheme is basically a splitting technique. From the KFVS scheme, we find that the splitting error, resulting from particle free transport in the gas evolution stage.

Generally, a hyperbolic equation with source term in 1-D can be written as

$$W_t + F(W)_x = S(W), \tag{5.30}$$

where W is the vector of the flow variables, such as mass, momentum and energy densities, $F(W)$ the corresponding fluxes, and $S(W)$ the source term. If we integrate the above equation with respect to dx in a numerical cell j from $x_{j-1/2}$ to $x_{j+1/2}$, and dt in a time interval from t^n to t^{n+1},

$$\int_{t^n}^{t^{n+1}} \int_{x_{j-1/2}}^{x_{j+1/2}} (W_t + F(W)_x) dx dt = \int_{t^n}^{t^{n+1}} \int_{x_{j-1/2}}^{x_{j+1/2}} S(W) dx dt,$$

we get

$$W_j^{n+1} - W_j^n = \frac{1}{\Delta x} \int_{t^n}^{t^{n+1}} \Big(F_{j-1/2}(t) - F_{j+1/2}(t) \Big) dt + \frac{1}{\Delta x} \int_{x_{j-1/2}}^{x_{j+1/2}} \int_{t^n}^{t^{n+1}} S(W) dx dt, \tag{5.31}$$

where $\Delta x = x_{j+1/2} - x_{j-1/2}$ is the cell size and W_j the average value of W in cell j, *i.e.*

$$W_j = \frac{1}{\Delta x} \int_{x_{j-1/2}}^{x_{j+1/2}} W dx.$$

Eq.(6.9) can be written in a semi-discrete form,

$$\frac{dW_j}{dt} = \frac{1}{\Delta x} \Big(F_{j-1/2}(t) - F_{j+1/2}(t) \Big) + \frac{1}{\Delta x} \int_{x_{j-1/2}}^{x_{j+1/2}} S(W) dx, \tag{5.32}$$

where W_j^{n+1} can be obtained using the standard Runge-Kutta method.

The focus of this section is about how to evaluate the numerical fluxes across a cell interface once there is a source term on the right hand side of the hyperbolic equation. A standard splitting scheme solves

$$W_t + F(W)_x = 0 \tag{5.33}$$

to evaluate the numerical fluxes, where the source term effects are neglected in the calculation of the flux function, even though its effects could be implicitly included into the preparation of the initial data. The importance of including source terms into the gas evolution process can be observed from the following example. Suppose we are interested in the steady state solution of Eq.(5.32), which requires that

$$\Big(F_{j-1/2}(t) - F_{j+1/2}(t) \Big) + \int_{x_{j-1/2}}^{x_{j+1/2}} S(W) dx = 0. \tag{5.34}$$

Theoretically, the scheme could not keep the steady state solution without including the source term S into the flux functions $F_{j-1/2}$ and $F_{j+1/2}$. In other words, the flux functions have to include source term effects to compensate the effect from the last term on the left hand side of Eq.(5.34).

The focus of this work is to develop a generalized BGK scheme for the Euler equations with heat transfer. The current method implements the source term directly in the time evolution of the gas distribution function. In other words, Eq.(5.30) is solved directly for the flux evaluations across each cell interface. This scheme can also be applied to other hyperbolic conservation laws with source terms if the corresponding gas-kinetic BGK model can be obtained, such as the shallow water equations. However, it is rather naive to believe that a universal technique can be obtained for all hyperbolic conservation laws with source terms. Different source terms could have totally different dynamical

influence on the hyperbolic equations. The dynamical effects from different sources have to be analyzed case by case. For example, gravitational force and heat conduction could have completely different impacts on the gas evolution, especially in the long time behavior of the system.

Similar to most other schemes for hyperbolic conservation laws with source terms, the current approach does not alleviate the problem of the spurious solutions arising in the numerical approximation of the equation of the reactive flow [16] or any of the model system for reacting flow [70]. The main reason for the spurious solutions in this type of equations, as clearly analyzed by Leveque and Yee, is due to the lack of spatial resolution which triggers the spurious solutions. We believe that the only way to overcome this difficulty is to effectively resolve the subcell structure and the stiff source term effect *via* methodologies such as adaptive mesh refinement, front tracking, or subcell resolution[28, 8].

5.2.2 A Gas-kinetic Method for the Euler Equations with Heat Transfer

We consider the Euler equations for a fluid in contact with a constant temperature bath:

$$\begin{pmatrix} \rho \\ \rho U \\ \rho\epsilon \end{pmatrix}_t + \begin{pmatrix} \rho U \\ \rho U^2 + p \\ \rho U\epsilon + Up \end{pmatrix}_x = \begin{pmatrix} 0 \\ 0 \\ \rho(T_* - T)/\varepsilon \end{pmatrix}. \tag{5.35}$$

where T_* is the temperature of the constant temperature bath. We assume that the gas is a $\gamma-$law gas, *i.e.* $p = (\gamma - 1)\rho e$, and choose a unit of temperature so that $T = e$.

The generalized BGK model for the above equations can be constructed as

$$f_t + uf_x = \frac{g - f}{\tau} + \frac{s}{\varepsilon}, \tag{5.36}$$

where s is an additional source term which we define below. In the above equation, there are two relaxation times τ and ε, both being much smaller than the CFL time step Δt in smooth regions.

All f, g and s are functions of space x, time t, particle velocity u, and internal variable ξ. For the Euler equations, the equilibrium state g is a Maxwellian,

$$g = e^{\ln\Pi - \lambda((u-U)^2 + \xi^2)} = \rho(\frac{\lambda}{\pi})^{\frac{K+1}{2}} e^{-\lambda((u-U)^2+\xi^2)},$$

where $\Pi = \rho(\lambda/\pi)^{\frac{K+1}{2}}$ and K is the dimension of the internal variable ξ and is equal to

$$K = (3-\gamma)/(\gamma-1),$$

in the 1-D case. In the equilibrium state, λ is a function of the gas temperature T, *i.e.* $\lambda = (K+1)/4T$ with the definition of $T = e$. Due to mass, momentum and energy conservations in the course of particle collisions, f and g satisfy the compatibility condition

$$\int (f-g)\psi_\alpha d\Xi = 0, \qquad \forall x, t \tag{5.37}$$

where $d\Xi = dud\xi$ and

$$\psi_\alpha = (1, u, \frac{1}{2}(u^2+\xi^2))^T.$$

For the heat conducting Euler equations, the corresponding source term s can be constructed as, although this is not the only choice,

$$s = s_1 - s_2 = \rho(\frac{\lambda_*}{\pi})^{\frac{K+1}{2}} e^{-\lambda_*(u^2+\xi^2)} - \rho(\frac{\lambda}{\pi})^{\frac{K+1}{2}} e^{-\lambda(u^2+\xi^2)} \tag{5.38}$$

where $\lambda_* = (K+1)/4T_*$. For a local equilibrium flow, with the condition $\tau \leq \epsilon$, the Euler equations with heat transfer (5.35) can be recovered from the generalized BGK model(5.36) through

$$\int (g_t + ug_x)\psi_\alpha d\Xi = \int \frac{s}{\varepsilon}\psi_\alpha d\Xi.$$

The numerical discretization for Eq.(5.36) is based on its integral solution

$$\begin{aligned} f(x_{j+1/2}, t, u, \xi) &= \frac{1}{\tau}\int_0^t \left(g(x', t', u, \xi) + \frac{\tau}{\varepsilon} s(x', t', u, \xi) \right) e^{-(t-t')/\tau} dt' \\ &\quad + e^{-t/\tau} f_0(x_{j+1/2} - ut), \end{aligned} \tag{5.39}$$

where $x_{j+1/2}$ is the cell interface and $x' = x_{j+1/2} - u(t-t')$ the particle trajectory. The following part of this section is about the numerical evaluation of the time-dependent distribution $f(x_{j+1/2}, t, u, \xi)$ at the cell interface. Once this is obtained, the numerical fluxes for mass, momentum and energy across the cell interface can be obtained by taking moments of f,

$$F_{j+1/2}(t) = \begin{pmatrix} F_\rho(t) \\ F_{\rho U}(t) \\ F_{\rho\epsilon}(t) \end{pmatrix}_{j+1/2} = \int\int u\psi_\alpha f(x_{j+1/2}, t, u, \xi) d\Xi. \tag{5.40}$$

Then, a method of lines approach is used to solve Eq.(5.32) as an ODE.

There are three unknowns in the equation (5.39). The first one is the initial gas distribution function f_0 at the beginning of each time step $t = 0$. The other two are g and s, which are functions of (x, t) locally around the point $(x_{j+1/2}, t = 0)$. The numerical scheme for solving Eq.(5.39), along with the compatibility condition(5.37), is described as follows:

Step(1):

Use a nonlinear limiter to interpolate the initial conservative variables at $t = 0$,

$$W_j = (\rho_j, \rho_j U_j, \rho_j \epsilon_j),$$

we can get the reconstructed initial data in each cell

$$\bar{W}_j(x) = W_j + \frac{\bar{W}_j(x_{j+1/2}) - \bar{W}_j(x_{j-1/2})}{x_{j+1/2} - x_{j-1/2}}(x - x_j)$$

for $x \in [x_{j-1/2}, x_{j+1/2}]$.

Step(2):

Based on the reconstructed data in Step(1), around each cell interface $x_{j+1/2}$, construct the initial gas distribution function f_0,

$$f_0(x) = \begin{cases} g^l \left(1 + a^l(x - x_{j+1/2})\right), & x \le x_{j+1/2}, \\ g^r \left(1 + a^r(x - x_{j+1/2})\right), & x \ge x_{j+1/2}, \end{cases} \tag{5.41}$$

where the states g^l and g^r are the Maxwellian distribution functions which have a one-to-one correspondence with the conservative variables at the cell interface,

$$g^l = g^l(\bar{W}_j(x_{j+1/2})) \qquad \text{and} \qquad g^r = g^r(\bar{W}_{j+1}(x_{j+1/2})). \tag{5.42}$$

For example, with the definition

$$g^l = e^{\ln \Pi^l - \lambda^l((u-U^l)^2+\xi^2)} = \rho^l(\frac{\lambda^l}{\pi})^{\frac{K+1}{2}} e^{-\lambda^l((u-U^l)^2+\xi^2)}, \tag{5.43}$$

where $\Pi^l = \rho^l(\frac{\lambda^l}{\pi})^{\frac{K+1}{2}}$, all coefficients in g^l can be obtained as

$$\begin{pmatrix} \rho^l \\ U^l \\ \lambda^l \end{pmatrix} = \begin{pmatrix} \bar{\rho}_j(x_{j+1/2}) \\ \bar{U}_j(x_{j+1/2}) \\ \frac{(K+1)\bar{\rho}_j(x_{j+1/2})}{4\left(\bar{\rho}_j\bar{\epsilon}_j(x_{j+1/2}) - \frac{1}{2}\bar{\rho}_j\bar{U}_j^2(x_{j+1/2})\right)} \end{pmatrix}. \tag{5.44}$$

Similar equations can be found for the unknowns in g^r. The terms $a^{l,r}$ in Eq.(5.41) are obtained from the Taylor expansion of a Maxwellian and have the forms

$$a^{l,r} = m_1^{l,r} + m_2^{l,r} u + m_3^{l,r}(u^2 + \xi^2).$$

These coefficients $(m_1^{l,r}, m_2^{l,r}, m_3^{l,r})$ can be totally determined from the slopes of the reconstructed mass, momentum and energy densities in Step(1),

$$\left(\frac{\bar{W}_j(x_{j+1/2}) - \bar{W}_j(x_j)}{x_{j+1/2} - x_j}, \frac{\bar{W}_{j+1}(x_{j+1}) - \bar{W}_{j+1}(x_{j+1/2})}{x_{j+1} - x_{j+1/2}} \right),$$

and the derived variables, such as temperature and velocity slopes. The results are

$$m_1^{l,r} = \left(\frac{\partial \ln \Pi}{\partial x} \right)^{l,r} - \left(U^2 \frac{\partial \lambda}{\partial x} \right)^{l,r} - 2 \left(\lambda U \frac{\partial U}{\partial x} \right)^{l,r}$$

$$m_2^{l,r} = 2 \left(U \frac{\partial \lambda}{\partial x} \right)^{l,r} + 2 \left(\lambda \frac{\partial U}{\partial x} \right)^{l,r}$$

$$m_3^{l,r} = - \left(\frac{\partial \lambda}{\partial x} \right)^{l,r}.$$

So, all coefficients in Eq.(5.41) are obtained from the reconstructed data. For simplification, we use $x_{j+1/2} = 0$ in the rest of this section.

Step(3):

As a physical model, the equilibrium state g is assumed to be continuous across a cell interface

$$g = g_0 \left(1 + (1 - \mathrm{H}(x)) \bar{a}^l x + \mathrm{H}(x) \bar{a}^r x + \bar{A} t \right), \tag{5.45}$$

where $\mathrm{H}(x)$ is Heaviside function and g_0 is the equilibrium state located at $(x = 0, t = 0)$,

$$g_0 = e^{\ln \Pi_0 - \lambda_0((u-U_0)^2 + \xi^2)} = \rho_0 (\frac{\lambda_0}{\pi})^{\frac{K+1}{2}} e^{-\lambda_0((u-U_0)^2+\xi^2)}, \tag{5.46}$$

with $\Pi_0 = \rho_0 (\lambda_0/\pi)^{\frac{K+1}{2}}$, and ρ_0, λ_0 and U_0 in the above equation are obtained below by Eq.(5.48). In Eq.(5.45), $\bar{a}^l, \bar{a}^r$, and $\bar{A}$ are related to the Taylor expansions of a Maxwellian on the left and right sides of the cell interface,

$$\bar{a}^{l,r} = \bar{m}_1^{l,r} + \bar{m}_2^{l,r} u + \bar{m}_3^{l,r}(u^2 + \xi^2),$$

$$\bar{A} = \bar{A}_1 + \bar{A}_2 u + \bar{A}_3(u^2 + \xi^2). \tag{5.47}$$

Taking both limits of $(x \to 0, t \to 0)$ in Eq.(5.39) and (5.45), and applying the compatibility condition at $(x = 0, t = 0)$, g_0 can be uniquely determined in terms of f_0,

$$\begin{pmatrix} \rho_0 \\ \rho_0 U_0 \\ \rho_0 \epsilon_0 \end{pmatrix} = \int g_0 \psi_\alpha du d\xi = \int [g^l H(u) + g^r(1 - H(u))] \psi_\alpha d\Xi, \tag{5.48}$$

where

$$W_0 = (\rho_0, \rho_0 U_0, \rho_0 \epsilon_0)^T$$

is the "average " of the flow variables at the cell interface, from which g_0 is completely determined as shown in Eq.(5.44). Using W_0 and the cell centered values $W_j(x_j)$ and $W_{j+1}(x_{j+1})$, we get three slopes for the mass, momentum and energy separately in $x > 0$ and $x < 0$, from which $(\bar{a}^l, \bar{a}^r)$ of (5.47) can be determined,

$$\bar{a}^l = \bar{a}^l \left(\frac{W_0 - \bar{W}_j(x_j)}{x_{j+1/2} - x_j} \right) \qquad \text{and} \qquad \bar{a}^r = \bar{a}^r \left(\frac{\bar{W}_{j+1}(x_{j+1}) - W_0}{x_{j+1} - x_{j+1/2}} \right). \tag{5.49}$$

Now, the remaining unknown term in Eq.(5.45) is $\bar{A}$, which is related to the time-derivative of a Maxwellian and its coefficients can be expressed as

$$\bar{A}_1 = \frac{\partial \ln \Pi}{\partial t} - U_0^2 \frac{\partial \lambda}{\partial t} - 2\lambda_0 U_0 \frac{\partial U}{\partial t},$$

$$\bar{A}_2 = 2U_0 \frac{\partial \lambda}{\partial t} + 2\lambda_0 \frac{\partial U}{\partial t},$$

and

$$\bar{A}_3 = -\frac{\partial \lambda}{\partial t}. \tag{5.50}$$

Step(4):

The source term $(s = s_1 - s_2)$ is constructed as

$$s_1 = s_{10} \left(1 + (1 - \mathrm{H}(x)) \bar{a}_{s1}^l x + \mathrm{H}(x) \bar{a}_{s1}^r x + \bar{A}_{s1} t \right)$$

$$s_2 = s_{20} \left(1 + (1 - \mathrm{H}(x)) \bar{a}_{s2}^l x + \mathrm{H}(x) \bar{a}_{s2}^r x + \bar{A}_{s2} t \right), \tag{5.51}$$

where

$$s_{10} = \rho_0 (\frac{\lambda_*}{\pi})^{\frac{K+1}{2}} e^{-\lambda_*(u^2+\xi^2)},$$

$$s_{20} = \rho_0 (\frac{\lambda_0}{\pi})^{\frac{K+1}{2}} e^{-\lambda_0 (u^2+\xi^2)} \tag{5.52}$$

are determined by the values of ρ_0 and λ_0 in g_0. From the Taylor expansion of the source terms (Eq.(5.38)), $\bar{a}_{s1}^{l,r}$ and $\bar{a}_{s2}^{l,r}$ have the forms

$$\bar{a}_{s1}^{l,r} = \bar{\omega}_1^{l,r}$$

and

$$\bar{a}_{s2}^{l,r} = \bar{\sigma}_1^{l,r} + \bar{\sigma}_3^{l,r}(u^2 + \xi^2).$$

The coefficients in the above equations are related to the coefficients of $\bar{a}^{l,r}$ in Eq.(5.47) due to the relations between g and s. For s_1, we have

$$\bar{\omega}_1^{l,r} = \bar{m}_1^{l,r} + \bar{m}_2^{l,r} U_0 + \bar{m}_3^{l,r} (U_0^2 + \frac{1+K}{2\lambda_0}),$$

and for s_2,

$$\bar{\sigma}_1^{l,r} = \bar{m}_1^{l,r} + \bar{m}_2^{l,r} U_0 + \bar{m}_3^{l,r} U_0^2$$

and

$$\bar{\sigma}_3^{l,r} = \bar{m}_3^{l,r}.$$

So, all parameters in Eq.(5.51) at $t = 0$ are obtained. The remaining unknowns are

$$\bar{A}_{s1} = \bar{\Omega}_1$$

and

$$\bar{A}_{s2} = \bar{\Sigma}_1 + \bar{\Sigma}_3 (u^2 + \xi^2).$$

Again, due to the relations between g and s, the parameters $(\bar{\Omega}_1, \bar{\Sigma}_1, \bar{\Sigma}_3)$ in the above equations depend on the parameters of $\bar{A}$ in Eq.(5.47),

$$\bar{\Omega}_1 = \bar{A}_1 + \bar{A}_2 U_0 + \bar{A}_3 (U_0^2 + \frac{1+K}{2\lambda_0})$$

$$\bar{\Sigma}_1 = \bar{A}_1 + \bar{A}_2 U_0 + \bar{A}_3 U_0^2$$

and

$$\bar{\Sigma}_3 = \bar{A}_3.$$

Therefore, we have to obtain the values of $(\bar{A}_1, \bar{A}_2, \bar{A}_3)$ for the determination of both g (Eq.(5.45)) and s (Eq.(5.51)).

Step(5):

Substituting Eq.(5.45),(5.51) and (5.41) into the integral solution (5.39), we obtain the distribution function f at $x = 0$,

$$\begin{aligned} f(0,t) &= \gamma_0 \left(g_0 + \frac{\tau}{\varepsilon}(s_{10} - s_{20}) \right) \\ &+\gamma_1 \left[\left(\bar{a}^l \mathrm{H}(u) + \bar{a}^r (1 - \mathrm{H}(u)) \right) u g_0 \right. \\ &\left. + \frac{\tau}{\varepsilon} \left((\bar{a}^l_{s1} \mathrm{H}(u) + \bar{a}^r_{s1}(1 - \mathrm{H}(u)))us_{10} - (\bar{a}^l_{s2} \mathrm{H}(u) + \bar{a}^r_{s2}(1 - \mathrm{H}(u)))us_{20} \right) \right] \\ &+\gamma_2 \left(\bar{A} g_0 + \frac{\tau}{\varepsilon}(\bar{A}_{s1} s_{10} - \bar{A}_{s2} s_{20}) \right) \\ &+\gamma_3 \left((1 - uta^l)\mathrm{H}(u) g^l + (1 - uta^r)(1 - \mathrm{H}(u)) g^r \right), \end{aligned} \tag{5.53}$$

with

$$\gamma_0 = 1 - e^{-t/\tau},$$

$$\gamma_1 = \tau(-1 + e^{-t/\tau}) + te^{-t/\tau},$$

$$\gamma_2 = \tau(t/\tau - 1 + e^{-t/\tau}),$$

$$\gamma_3 = e^{-t/\tau}.$$

As pointed out in the last step, there are three unknowns $(\bar{A}_1, \bar{A}_2, \bar{A}_3)$ inside $(\bar{A}, \bar{A}_{s1}, \bar{A}_{s2})$ in (5.53). Three conditions are needed to determine them. Since the compatibility condition has to be satisfied everywhere in space and time, it can be integrated in a whole CFL time step Δt at $x = 0$

$$\int_0^{\Delta t} \int \left(f(0,t,u,\xi) - g(0,t,u,\xi) \right) \psi_\alpha dt d\Xi = 0, \tag{5.54}$$

where both f and g are known from Eq.(5.53) and (5.45). The above equation provides three conditions to determine the three unknowns $(\bar{A}_1, \bar{A}_2, \bar{A}_3)$. This numerical procedure is an important step in the BGK-type schemes to determine the time evolution of the flow variables. Due to the implicit property in the above integral, the BGK scheme uses the CFL time step Δt as the time step regardless of the stiffness of the relaxation time; otherwise, the numerical stability for the BGK model (5.36) requires $\Delta t \leq \tau$ and $\Delta t \leq \epsilon$. No iterations are necessary to solve Eq.(5.54) for $(\bar{A}_1, \bar{A}_2, \bar{A}_3)$ and the solutions

are obtained as follows. Define

$$
\begin{aligned}
(C_1, C_2, C_3)^T &= \frac{1}{\rho_0 \Gamma_5} \int \Big[-\Gamma_3 g_0 + \Gamma_1 u \left(\bar{a}^l \mathrm{H}(u) + \bar{a}^r (1 - \mathrm{H}(u)) \right) g_0 \\
&+ \Gamma_3 \left(\mathrm{H}(u) g^l + (1 - \mathrm{H}(u)) g^r \right) \\
&+ \Gamma_4 u \left(a^l \mathrm{H}(u) g^l + a^r (1 - \mathrm{H}(u)) g^r \right) \Big] \psi_\alpha d\Xi, \qquad (5.55)
\end{aligned}
$$

with

$$
\begin{aligned}
\Gamma_0 &= \Delta t - \tau (1 - e^{-\Delta t/\tau}), \\
\Gamma_1 &= \tau \left(-\Delta t + 2\tau (1 - e^{-\Delta t/\tau}) - \Delta t e^{-\Delta t/\tau} \right), \\
\Gamma_2 &= \frac{1}{2} \Delta t^2 - \tau \Delta t + \tau^2 (1 - e^{-\Delta t/\tau}), \\
\Gamma_3 &= \tau (1 - e^{-\Delta t/\tau}), \\
\Gamma_4 &= \tau \left(-\Delta t e^{-\Delta t/\tau} + \tau (1 - e^{-\Delta t/\tau}) \right), \\
\Gamma_5 &= \tau \left(\Delta t - \tau (1 - e^{-\Delta t/\tau}) \right).
\end{aligned}
$$

Since all terms on the right hand side of Eq.(5.55) are known, C_1, C_2 and C_3 are obtained explicitly. Then, from the definitions

$$
\tilde{C}_3 = C_3 + \frac{1}{2} \frac{\Gamma_2}{\Gamma_5} \left(\frac{\tau}{\varepsilon} \right) \frac{K+1}{2} \left(\frac{1}{\lambda_*} - \frac{1}{\lambda_0} \right) C_1,
$$

$$
B_1 = C_2 - U_0 C_1,
$$

$$
B_2 = 2\tilde{C}_3 - \left(U_0^2 + \frac{K+1}{2\lambda_0} \right) C_1,
$$

and

$$
\Gamma_* = \left(\frac{\tau}{\varepsilon} \right) \frac{\Gamma_2}{\Gamma_5},
$$

we have

$$
\bar{A}_3 = 2\lambda_0^2 \frac{B_2 - 2U_0 B_1}{(K+1)(1+\Gamma_*)}
$$

$$
\bar{A}_2 = 2(\lambda_0 B_1 - U_0 \bar{A}_3)
$$

$$
\bar{A}_1 = C_1 - U_0 \bar{A}_2 - (U_0^2 + \frac{K+1}{2\lambda_0}) \bar{A}_3.
$$

Now, all terms in the time dependent gas distribution function f in Eq.(5.53) are obtained, from which the numerical fluxes can be obtained.

5.2.3 Numerical Examples

Two numerical examples for the Euler equations with heat transfer are presented. In both cases, $\gamma = 1.4$ is used and the temperature bath has $T_* = 1.0$. The computational domain is from $x = -1$ to $x = 1$ with 200 equally divided cells and cell size $\Delta x = 0.01$. The van Leer limiter is used for all interpolations of the initial conservative variables, and the time step is given by taking CFL Number = 0.65 in all cases. In numerical calculations, the collision time τ can be defined in the same way as that used in Chapter 4.

Since we are concentrating on the construction of numerical flux functions by including the source term effects in this section, the second term in Eq.(5.32) is just treated implicitly. The update of flow variables is based on

$$W_j^{n+1} - W_j^n = \frac{1}{\Delta x}\int_0^{\Delta t}(F_{j-1/2} - F_{j+1/2})dt + \Delta t S(W_j^{n+1}), \tag{5.56}$$

where the time-dependent flux function $F_{j+1/2}$ is given by Eq.(5.40).

Case(1): Traveling Shock Waves

The first case is taken from Pember's paper[94]. We consider a traveling wave problem of the heat conducting Euler equations for which the states at $\pm\infty$ satisfy the isothermal shock relations,

$$(\rho_l = 2.5, p_l = 1.0, U_l = 1.1) \qquad \text{and} \qquad (\rho_r = 1.0, p_r = 0.4, U_r = 0.5).$$

The corresponding shock speed is

$$v_s = \frac{\rho_l U_l - \rho_r U_r}{\rho_l - \rho_r} = 1.5.$$

We numerically solve a series of traveling wave problems of this type in which ε alone is varied. The initial shock is located at $x = -0.8$, and it takes $t = 1.066$ to propagate from $x = -0.8$ to $x = 0.8$. We use three heat relaxation times $\Delta x/\varepsilon = 0.125, 1.0$, and 10^4, which range from less than, to considerably larger than the magnitude of the sound speed and the fluid velocities. The density distributions are shown in Fig.(5.16)-Fig(5.18) for these three cases and the solid lines are obtained from the same scheme with a refined

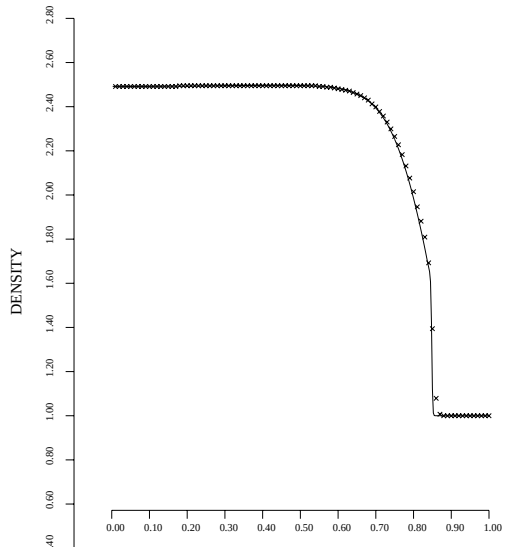

Figure 5.16: Density profile for a traveling shock wave with $\frac{\Delta x}{\varepsilon} = 0.125$

mesh $\Delta x = 0.0025$. As $\Delta x/\varepsilon \gg 1$, the relaxation process will become too fine to be fully resolved by the spatial resolution, *i.e.* the grid size. There are almost no differences between the results using $\Delta x/\varepsilon = 10^2$ and $\Delta x/\varepsilon = 10^4$, because in both cases the small subcell structure generated by ε is lost due to the finite cell size and numerical dissipation inside each cell. From the above numerical results, we conclude that the current BGK solver provides a smooth transition from mild to stiff relaxation.

Case(2): Shock Tube Problem

The second test case is taken from the paper [52], where the initial condition is

$$(\rho_l = 1.0, \rho_l\epsilon_l = 1.0, U_l = 0.0) \qquad \text{and} \qquad (\rho_r = 0.2, \rho_r\epsilon_r = 1.0, U_r = 0.0).$$

The initial discontinuity is located at $x = 0$. Fig.(5.19)-Fig.(5.22) show the density distributions at time $t = 0.5$ with different relaxation time $\Delta x/\varepsilon = (10^{-3}, 10^{-2}, 10^{-1}, 1)$, where the solid lines are obtained from the same scheme using a refined mesh $\Delta x = 0.0025$. From these figures, we can clearly observe the transition from three waves (rarefaction, contact, shock) to two waves (rarefaction, shock). With the increase of the coefficient $1/\varepsilon$, the contact discontinuity wave gets smeared due to heat conduction, and finally disappears.

When ε is on the order of the particle collision time, $\varepsilon \simeq \tau$, both relaxations are very stiff. The state with an even smaller ε is actually a physically unreasonable situation, since in this case the small structure inside Δx due to ε is covered by the large dissipative scale ($\simeq \Delta x$) determined by the collision time τ. The largest $\Delta x/\varepsilon$ we have tried is 10^2,

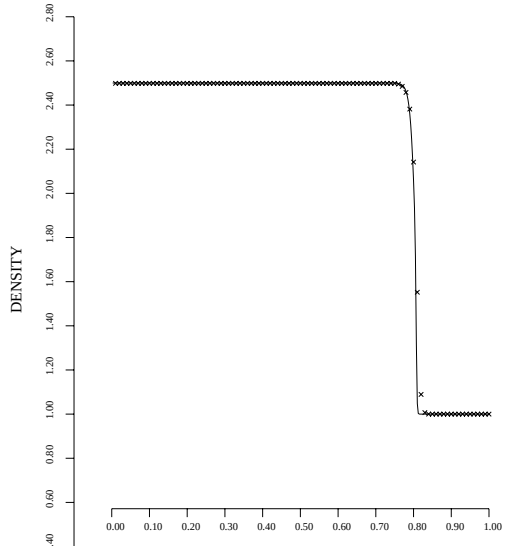

Figure 5.17: Density profile for a traveling shock wave with $\frac{\Delta x}{\varepsilon} = 1.0$

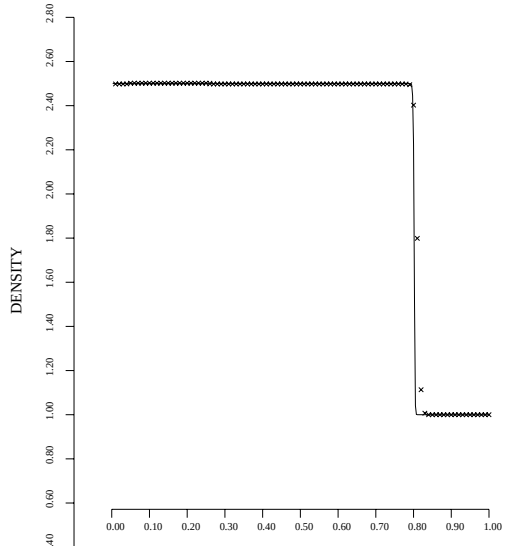

Figure 5.18: Density profile for a traveling shock wave with $\frac{\Delta x}{\varepsilon} = 10^4$

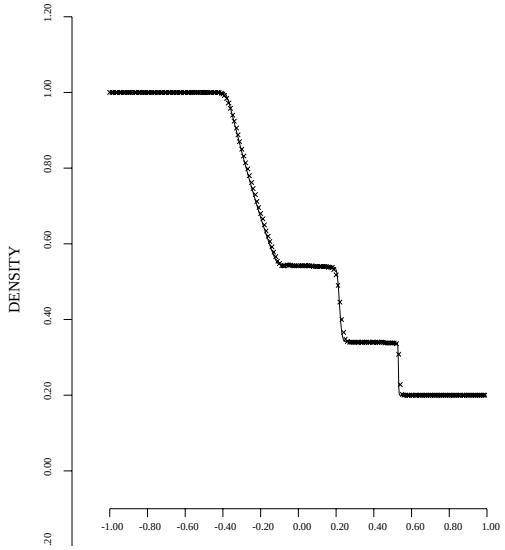

Figure 5.19: Density distribution with $\frac{\Delta x}{\varepsilon} = 10^{-3}$

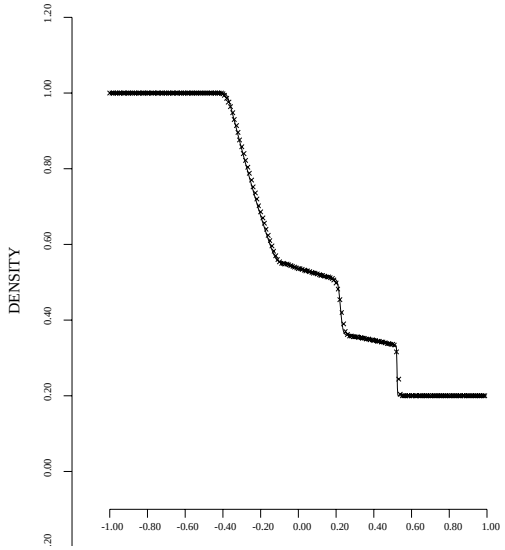

Figure 5.20: Density distribution with $\frac{\Delta x}{\varepsilon} = 10^{-2}$

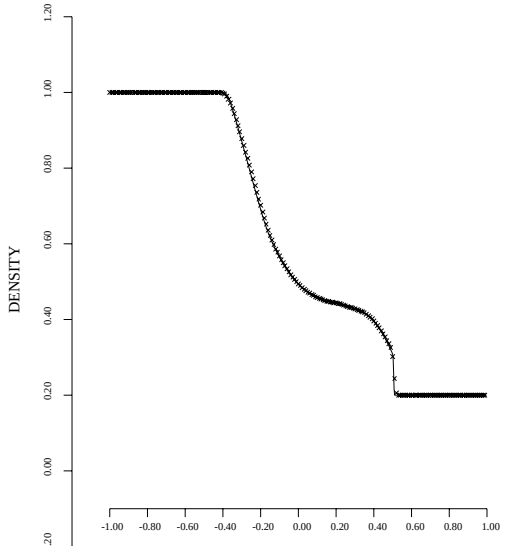

Figure 5.21: Density distribution with $\frac{\Delta x}{\varepsilon} = 10^{-1}$

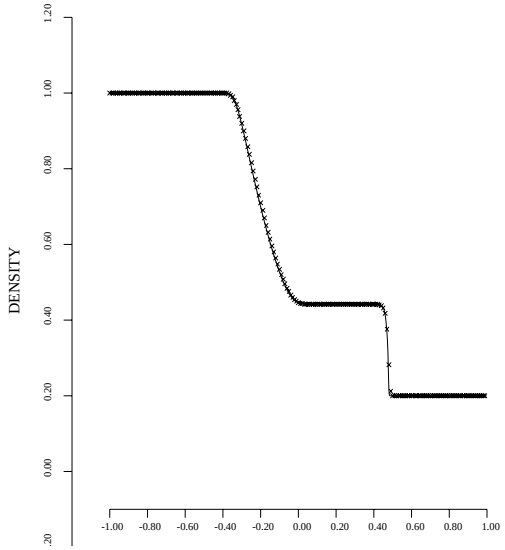

Figure 5.22: Density distribution with $\frac{\Delta x}{\varepsilon} = 1$

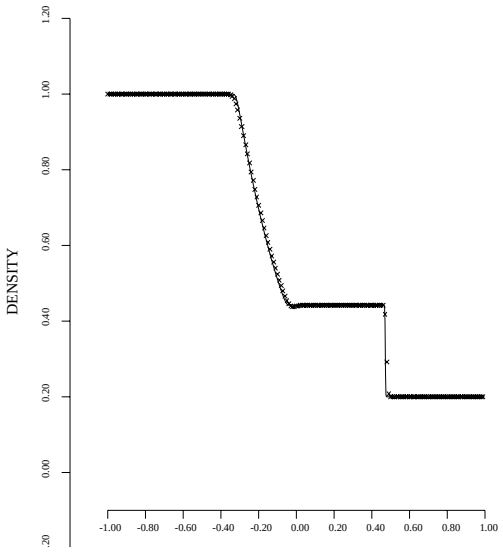

Figure 5.23: Density distribution with $\frac{\Delta x}{\varepsilon} = 10^2$

and the simulation results for the density, velocity, and pressure are shown in Fig.(5.23)-Fig.(5.25). Comparing Fig.(5.22) with Fig.(5.23), we can see the sharpening of the shock wave and rarefaction corners because of the transition from heat conducting Euler flow to isothermal flow. Even for a smaller ε, the rarefaction corner and shock wave will not be changed.

Remark(5.1)

Due to the finite cell size and time step, there are intrinsic dissipations for any numerical scheme. For the BGK method, theoretically we could choose the collision time τ according to the physical Reynolds number, and this is true once the corresponding flow structure can be resolved by the cell size and time step, or in regions with smooth flows. However, if the size of the flow structure given by this Reynolds number is smaller than the cell size, artificial viscosity has to be added. Therefore, the collision time in our scheme cannot be extremely small in any case, even for the Euler solutions. Any physical phenomena corresponding to finer temporal resolution, such as the structures obtained with $\varepsilon \ll \tau$, is definitely lost due to artificial dissipation. In other words, for any relaxation time ε, there is a lower bound limitation ε_ν, below that artificial relaxation takes place. So, it is rather pointless to take a very small relaxation time, such as $\varepsilon = 10^{-8}$, in the hope to prove the correctness and accuracy of a scheme. Although the numerical solutions are stable, they definitely correspond to the solutions with a much larger ε.

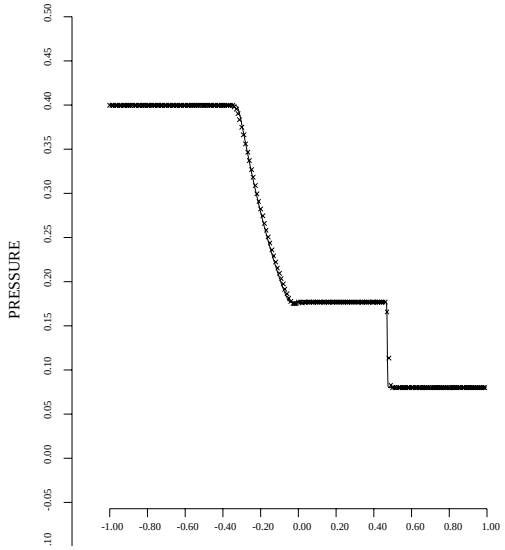

Figure 5.24: Pressure distribution with $\frac{\Delta x}{\varepsilon} = 10^2$

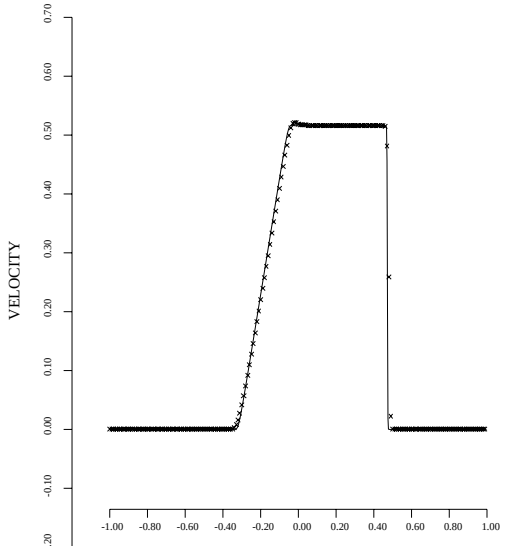

Figure 5.25: Velocity distribution with $\frac{\Delta x}{\varepsilon} = 10^2$

5.2.4 Summary

In this section, we have presented a BGK-type scheme for the Euler equations with heat transfer. The source term is included explicitly in the time-evolution of the gas distribution at a cell interface, from which the numerical fluxes are obtained. The numerical results validate the current approach in the capturing of the source term effects in the flow. The current method can also be extended to other hyperbolic conservation laws with source terms if the corresponding BGK model can be established.

5.3 Summary

In this Chapter, extensions of the BGK method to multicomponent flow and the Euler equations with heat transfer have been presented. Different from most upwinding schemes, the particle trajectory can be easily modified by including external source term effects in addition to the collision term. The extensions of the BGK method to chemical reactive flows and to the study of multicomponent particle diffusion phenomena are probably important applications of the gas-kinetic schemes in the future. Also, implementing turbulence modeling into the BGK scheme to study flow mixing and instability will become an interesting research project.

Chapter 6

Numerics and Physics

There are three stages in a high-resolution shock capturing scheme for compressible flow calculations: Reconstruction, Evolution and Projection. For a 1st-order scheme, there are two stages: evolution and projection (see Fig.(6.1)). In this chapter, we are going to analyze the dynamical effects in these stages, and explain the physical reasons behind these spurious solutions in shock capturing schemes, such as post-shock oscillations, carbuncle phenomena and odd-even decoupling. This chapter presents a general understanding of the numerical scheme, the advantages and weaknesses for different schemes can be analyzed in terms of their specific dynamical influence in different stages.

6.1 Reconstruction Dynamics

Theoretically, the flow is distributed continuously in space at any instant of time. In the numerical approach, we are looking at these data with limited resolution due to the finite cell size. What we can record is the cell-averaged flow distributions. As a principle, *the smallest resolvable scales are the cell size and time step.* With discretized initial data, in order to capture the flow evolution locally, we have to reconstruct a continuous initial condition and put it into the appropriate governing equations. In the respect of initial reconstruction, one of the simplest ways is to connect all cell averaged initial data[1], as shown in Fig.(6.2). Unfortunately, with this initial condition, the solution to the nonlinear governing equations, *e.g.* the Euler or Navier-Stokes equations, is too complicated to be implemented efficiently for numerical purpose. So, this initial reconstruction has to be simplified in order to get a simple solution around a cell interface. In order to apply the Taylor expansion technique, a continuous and smooth function has to be assumed

[1]The only use of the reconstructed initial condition here is to calculate numerical fluxes across a cell interface. Still, the cell averaged flow variables will be updated in order to have a conservative scheme.

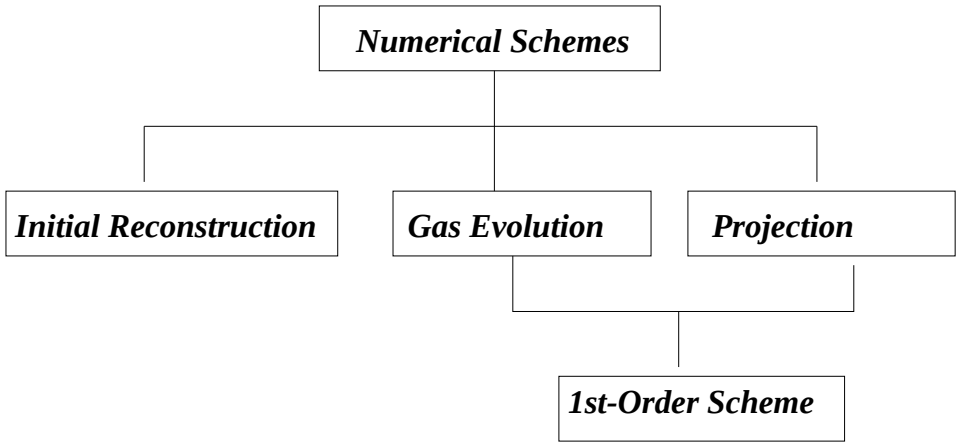

Figure 6.1: Schematic Description of Numerical Schemes

across a cell interface. In this case, the flow variables W are approximated locally in the following form,

$$W(x,t) = W(x_0,t_0) + \frac{\partial W}{\partial x}(x-x_0) + \frac{\partial W}{\partial t}(t-t_0),$$

where the relation between $\partial W/\partial x$ and $\partial W/\partial t$ depends on the governing equations for the temporal and spatial variations of W. For example, a linearly distributed flow variables can be constructed initially, as shown in Fig.(6.3). This is the fundamental idea underlying the central schemes. For the Euler equations, from this initial data, we can construct numerical fluxes across the cell interface explicitly, *i.e.* Lax-Wendroff scheme. There are two intrinsic weaknesses in the above initial condition: (1). If there are high gradients in the flow distribution, the interpolated flow variables at these locations away from the central point $(i+1/2)$ can easily become unphysical, such as negative density or pressure. These wrong information could propagate to the cell interface $(i+1/2)$ to effect the numerical fluxes. (2). The initial reconstructed data inside each cell are not self-consistent. For example, the initial data inside cell j will be different when the numerical solutions are evaluated at the left boundary $x_{j-1/2}$ and the right boundary $x_{j+1/2}$. Thus, before using any governing equation, the traditional central scheme has errors in the initial condition already. Although the above initial condition is perfectly correct in regions with smooth flow and the central schemes behave very well, the inappropriate initial condition causes the failure of the central scheme in discontinuous flow

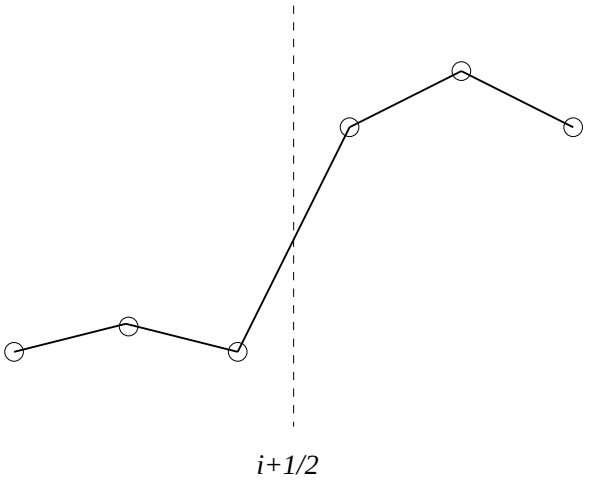

Figure 6.2: The simplest initial condition without using any limiter

calculations. With this inappropriate initial condition, even with the exact solution of the governing equations in the gas evolution stage, *i.e.* the exact generalized Riemann solver for the Euler equations, oscillations will still be generated in discontinuous regions.

As another choice, we can totally ignore the slopes of flow variables inside each cell in the reconstructed initial date, such as shown in Fig.(6.4). The numerical gas with this initial condition stays in a more stable state than those with any other initial reconstruction. Comparing Fig.(6.3) with Fig.(6.4), the constant initial data maximizes the entropy inside each cell. In other words, it reduces the kinetic energy inside each cell to the minimum level with the conditions of total mass, momentum and energy conservation inside each cell, *i.e.* $\int_{\text{cell}_j} \frac{1}{2}\rho U^2|_{\text{Fig.(6.3)}} d\Omega \geq \int_{\text{cell}_j} \frac{1}{2}\rho U^2|_{\text{Fig.(6.4)}} d\Omega$. Therefore, dynamically the time evolution of the numerical fluid from the initial condition in Fig.(6.4) will be different from that in Fig.(6.3), and the former one does not have enough kinetic energy to generate oscillations. The capturing of numerical shocks in upwinding schemes is mainly due to the dissipation included in the initial condition, otherwise no shocks could be captured since there is not enough dissipation in the gas evolution stage. In order to get a physically reasonable and mathematically tractable initial condition in both smooth and discontinuous flow regions, nonlinear limiters have to be introduced in the initial data reconstruction. This is one of the fundamental ideas for the development of modern shock capturing schemes, and it started from the work by Boris and Book [7]. With nonlinear limiters, the general initial data can be constructed as that shown

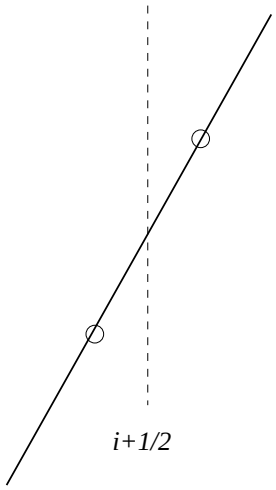

Figure 6.3: Linearly distributed initial data around a cell interface

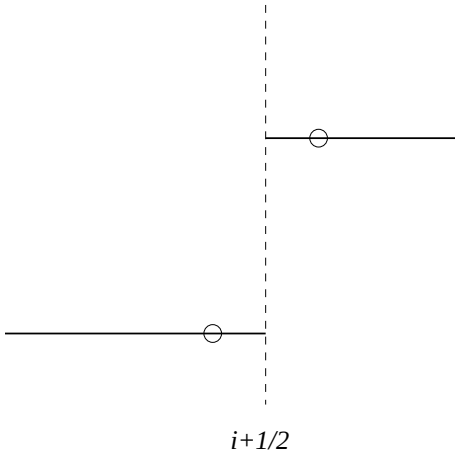

Figure 6.4: Constant initial data around a cell interface

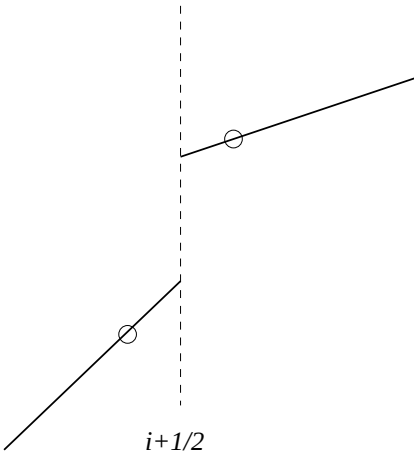

Figure 6.5: A general data reconstruction between two extremes

in Fig.(6.5), which goes to the continuous distribution in the smooth region and the step distribution in the discontinuous region. The BGK method uses this kind of initial data for the conservative variables. Some schemes based on the generalized Riemann solvers use the same initial condition[4], and the differences between the BGK method and the generalized Riemann solver will become clear when we discuss the gas evolution stage in the next section. In conclusion, the simplest initial reconstruction is shown in Fig.(6.2). However, we cannot find any simple solution under this initial condition for most nonlinear differential equations. So, a nonlinear limiter is introduced to simplify this kind of initial data.

Once we get the initial condition, we have to use reasonable governing equations to describe the time evolution of the numerical fluid. Physically, there is no granted reason to believe that the Euler equations are the appropriate equations to describe the time evolution of numerical fluid, even though they are perfectly correct for the inviscid physical fluid. The correctness of the equations depends on the fluid situations in the discretized space, it could be the Euler, the Navier-Stokes equations or the Boltzmann equation. Since the BGK model can be shown to be correct in both the Navier-Stokes and the free-molecular limit with quite general physical description of a fluid, it stands on a firm physical basis. Currently, new schemes are continuously being developed. Without using appropriate governing equations for the numerical fluid, any progress through *ad hoc* fixes of the flux function will not make qualitative changes.

6.2 Gas Evolution Dynamics

The dynamical effects from the reconstruction stage were discussed in the last section. In this section, the dynamical influence from the gas evolution stage will be discussed. Basically, different flow solvers correspond to different underlying governing equations, and these equations may be different from the ones we are supposed to solve. The current approach to get a better flux function for the Euler equations is actually a process to solve new governing equations which are more appropriate for the numerical fluid, even though it is not explicitly realized yet.

The gas evolution stage determines the time evolution of the numerical fluid around a cell interface. Theoretically, the time evolution process can be described by the Euler equations, the Navier-Stokes equations, or the Boltzmann equation. In order to make the numerical fluid as close as possible to the real physical fluid, the choice of governing equations should depend closely on the real flow situation. Because of the finite cell size and time step, the numerical fluid is intrinsically dissipative, especially in discontinuous regions. So, the corresponding dissipated governing equations have to be solved.

There are mainly two kind of numerical discretizations for the Euler equations, *e.g.* the FVS and FDS methods. The FVS methods and the equivalent KFVS scheme have been analyzed clearly in Chapter 3, where the FVS scheme can be regarded as solving the collisionless Boltzmann equation in the gas evolution stage. The splitting errors between the collision (projection stage) and free transport (evolution stage) create large dissipation in the FVS scheme. Due to the free particle or wave transport in most FVS schemes, their solutions deviate from the Euler solutions, and this deviation can never be eliminated by simply increasing the mathematical order of the initial interpolation without modifying particle or wave propagation model in the gas evolution stage.

The main purpose of this section is to re-examine dynamics in the exact Riemann solver and the FDS scheme. It is realized that the exact Riemann solver is not adequate to capture the whole spectrum of physical fluid. The reason for spurious solutions from the Riemann solver, such as the odd-even decoupling and carbuncle phenomena in the 2-D case, will be explained. In order to develop more robust and accurate schemes for compressible flow calculations, both equilibrium and nonequilibrium fluid behaviors have to be captured in the gas evolution stage.

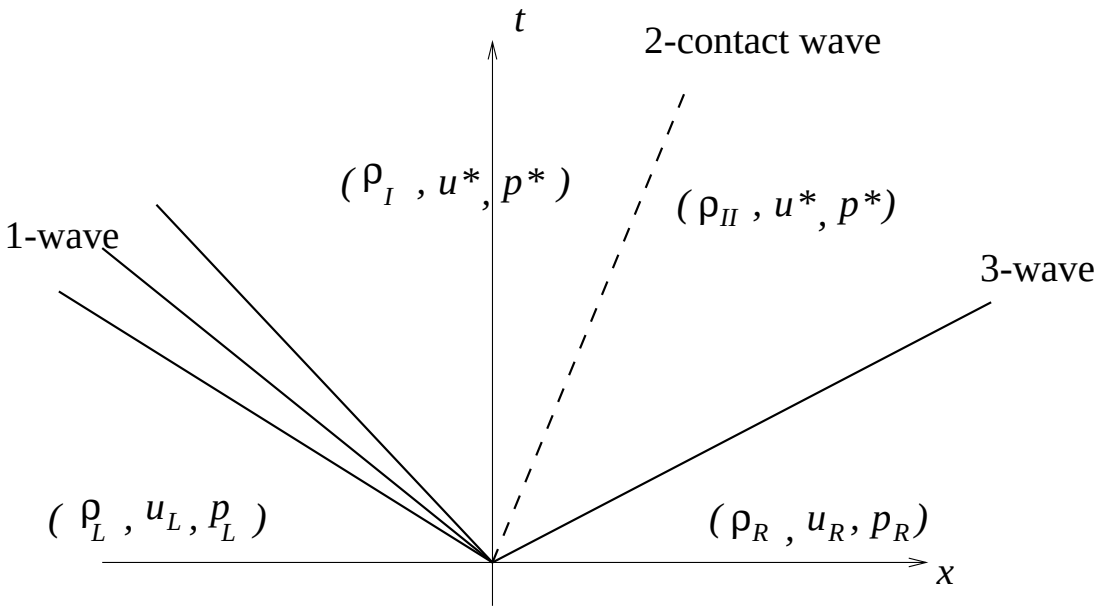

Figure 6.6: Solution of the Riemann problem in the (x, t)-plane

6.2.1 Exact Riemann solver and Anomalous Phenomena

The Riemann problem is defined as an Initial Value Problem (IVP) for the Euler equations in the 1-D case. With the following initial condition at $t = 0$,

$$(\rho, U, P)(x, 0) = \begin{cases} (\rho_L, U_L, P_L), & x < 0, \\ (\rho_R, U_R, P_R), & x > 0, \end{cases} \tag{6.1}$$

the entropy-satisfying solutions are the following: the left state (ρ_L, U_L, P_L) is connected to the right state (ρ_R, U_R, P_R) by a 1-shock or 1-rarefaction wave, a 2-contact discontinuity, and a 3-shock or a 3-rarefaction wave. The 2-contact discontinuity separates two constant states (ρ_I, U^*, P^*) and (ρ_{II}, U^*, P^*) so that (U, P) are continuous across the contact discontinuity. For example, in Fig.(6.6), the 1-wave is a rarefaction and the 3-wave a shock. There is standard technique to obtain the solution around a contact discontinuity [121].

Once the solution from the Riemann solver is obtained, the values, for example (ρ_I, U^*, P^*) in Fig.(6.6) at $x = 0$, can be used to construct the fluxes. The Godunov method uses these fluxes across each cell interface to update the flow variables inside each cell. In order to understand the Godunov method, we have to understand the underlying assumption in the process of obtaining the fluxes. All advantages and weaknesses in the Godunov method can be attributed to this underlying assumption. For the Euler

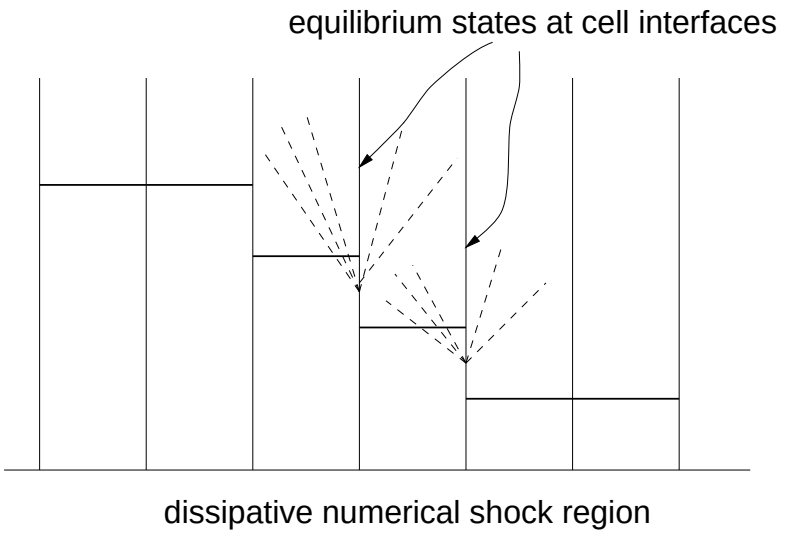

Figure 6.7: Godunov gas evolution model

equations, it is obvious that once we know (ρ, U, P), the corresponding fluxes are

$$\begin{pmatrix} \mathcal{F}_\rho \\ \mathcal{F}_{\rho U} \\ \mathcal{F}_{\rho\epsilon} \end{pmatrix} = \begin{pmatrix} \rho U \\ \rho U^2 + P \\ \frac{1}{2}\rho U^3 + \frac{\gamma}{\gamma-1} PU \end{pmatrix}. \tag{6.2}$$

For example, in Fig.(6.6), the time-dependent fluxes at $x = 0$ are $(\rho_I U^*, \rho_I U^{*2} + P^*, \frac{1}{2}\rho_I U^{*3} + \frac{\gamma}{\gamma-1} P^* U^*)^T$. From the flow variables (ρ, U, P) to the fluxes $(F_\rho, F_{\rho U}, F_{\rho\epsilon})$, the equilibrium state is assumed. In other words, for the Godunov method whatever the real physical flow situations is, the state (ρ_I, U^*, P^*) at the cell interface is always corresponding to the local equilibrium state with a Maxwellian gas distribution function, even for the flow inside a numerical shock layer, see Fig.(6.7). It is well known that the intermediate points in the numerical shock region have to be regarded as points inside the shock structure, which corresponds to the highly nonequilibrium and dissipative region, and the inclusion of nonequilibrium properties is crucial in the capturing of a stable shock transition. However, the applying of the Riemann solver here in the gas evolution stage mis-interprets this region as an inviscid flow region with equilibrium states. From Fig.(6.7), it will not be difficult to realize that there will not be enough numerical dissipation to capture the discontinuous shock structure in the Godunov method. Without the dissipation provided in the projection stage (discussed later), it is impossible for the Godunov method to have a shock capturing ability. Unfortunately, in the multidimensional case, the projection dissipation is not equally added in all directions in the

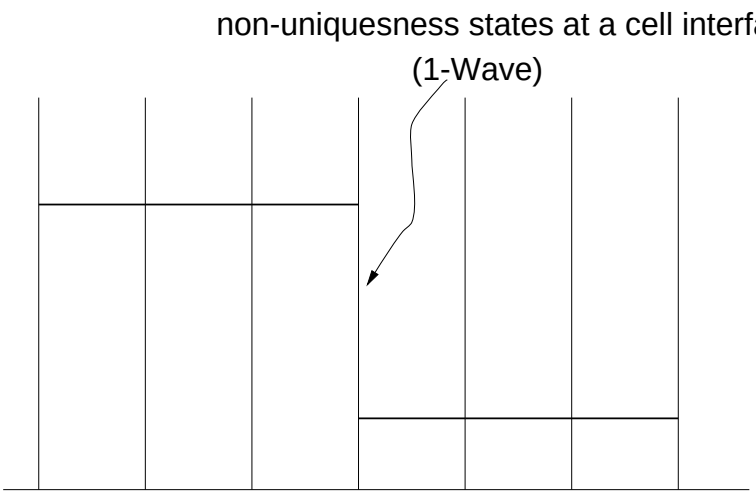

Figure 6.8: Shock front is located exactly at a cell interface

Godunov method, and this fact triggers the instability. It is true that, if the shock is located exactly at a cell interface, the Godunov method could capture the stationary shock exactly, such as that shown in Fig.(6.8). However, it is only a special case. If we look at the Riemann solution in this situation, we cannot even find a unique state (ρ, U, P) at a cell interface. Therefore, in this case the Godunov method uses the continuous fluxes directly, which avoids constructing any equilibrium state at the cell interface and avoids making mistakes. For an unsteady flow, once the shock is away from the cell interface, the weakness of the Godunov method emerges. Inside the numerical shock region, instead of smearing and dissipating different waves, the Riemann solver always generates characteristic waves to propagate away from the shock region to form oscillations. Ignoring the nonequilibrium or dissipative property of a numerical fluid is one of the direct reasons for the 2-D carbuncle phenomena and odd-even decoupling [76].

In the 1-D case, there is always projection dissipation to support the numerical shock structure, as will be analyzed in section(6.3). However, in the 2-D case, if the shock front is aligned with the numerical mesh, the projection dissipation could only be provided in one direction. Due to the lack of dissipation in the other direction, the Godunov method automatically generates instability. The following is the detail explanation:
In order to have the carbuncle phenomena or odd-even decoupling to happen, the numerical fluid has to satisfy the following conditions [100, 76].

1. Shock propagates and is aligned with the mesh.

2. The mass flux due to a pressure difference is not zero, such as $D^{(p)} \neq 0$ in the

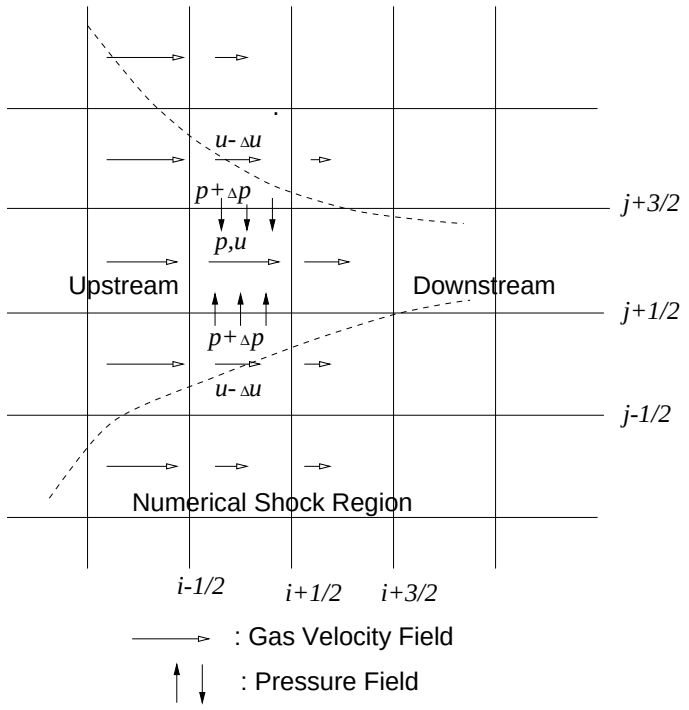

Figure 6.9: Schematic explanations of a carbuncle phenomena

dissipative term $\mathcal{D}(W_j, W_{j+1}) = \mathcal{D}^{(\rho)}\Delta\rho + \mathcal{D}^{(U)}\Delta U + \mathcal{D}^{(p)}\Delta p$ of the full mass flux function $F^{(\rho)}_{j+1/2} = \frac{1}{2}[(\rho U)_j + (\rho U)_{j+1}] - \frac{1}{2}\mathcal{D}(W_j, W_{j+1})$.

3. The variations of density and pressure are out of phase.

From point 1, if the shock is aligned with the mesh, the projection dissipation can only be provided in one direction due to the velocity differences in this direction. For example, if the shock is propagating in the x-direction, there will be no projection dissipation in the y-direction because even inside the shock layer, the velocities in different cells in the y-direction are almost equal to each other. As we know, the projection dissipation is proportional to the square of velocity differences $(\mathbf{U}_1 - \mathbf{U}_2)^2$, which is shown in Eq.(6.7).

Suppose there is a stationary numerical shock in the x-direction, which is shown in Fig.(6.9). Due to the conservative relation for the shock wave, we have

$$\frac{U^2}{2} + \frac{\gamma}{\gamma - 1}\frac{P}{\rho} = \text{constant},$$

in the x-direction, from which

$$U\Delta U + \frac{\gamma}{\gamma - 1}\frac{\rho\Delta P - P\Delta\rho}{\rho^2} = 0,$$

can be obtained. If ΔP and $\Delta\rho$ are out of phase (point 3 above), such that $\Delta P = -\beta\Delta\rho$, where β is a positive constant, we have

$$U\Delta U + \frac{\gamma}{\gamma - 1}\frac{(\rho + \beta P)\Delta P}{\rho^2} = 0.$$

So, once there are some perturbations at the shock front, an increase in pressure corresponds to a decrease in velocity. As shown in Fig.(6.9), the fluid in central cells have a slightly larger velocity and thus a slightly lower pressure. Physically, due to the velocity differences, the shear viscosity will strongly take effect and reduce the velocity differences, and a stable shock front can be formed from the dynamical balance between advection and dissipation. However, numerically, solving the inviscid Euler solver in the y-direction will give different answers here. The exact 1-D Riemann solver in the y-direction does not recognize the x-component velocity differences at all due to its inviscid nature. In other words, the velocity differences between the fluid in cells (i, j) and $(i, j-1), (i, j+1)$ in Fig.(6.9) will not make any differences in the flux function. The main dynamical effect involved in the Riemann solver in this situation is the pressure difference. Since the surrounding cells have a higher pressure, they will push the fluid towards the center. As a consequence, the fluid in the central cells passes through an even narrower region. According to the Bernoulli equation, the fluid speed goes up due to the convergence of streamlines, and the pressure in central cells becomes even lower. Therefore, the Euler fluxes or the exact Riemann solver in the y-direction will amplify the initial perturbations, and the fluid speed can easily go up and penetrate the shock layer to form an instability. This explanation validates Liou's conjecture [76], that $\mathcal{D}^{(p)} \neq 0$ is accompanied by an instability. Otherwise, if $\mathcal{D}^{(p)} = 0$, the pressure difference in the y-direction will not push the fluid towards the central cells, and no instability will be formed. Unfortunately, for any physical fluid, $\mathcal{D}^{(p)} \neq 0$ always holds. So, the carbuncle phenomena or odd-even decoupling is intrinsically rooted in the Godunov method. Any fixes to artificially make $\mathcal{D}^{(p)} = 0$ will eventually become a failure. For moving shocks, it is easy to generate initial perturbations where the odd-even decoupling forms quickly. One possible cure for the instability is to include a dissipative mechanism, such as an artificial shear stress. However, an inappropriate artificial shear stress would probably poison the Navier-Stokes solution and sacrifice one of the advantages of the FDS scheme. Fortunately, the BGK method includes the physical viscous term directly.

In the cases where the shock front is not aligned with the numerical mesh, the pro-

jection dissipation will take effect automatically in the shock regions in both directions in the 2D case. Thus, the spurious phenomenon will not be present. In conclusion, the odd-even decoupling and carbuncle phenomena are due to the intrinsic inviscid nature of the Euler equations, which could happen for FDS schemes, such as the Godunov, Roe, and Osher's methods. For the FVS and KFVS schemes, the carbuncle and odd-even decoupling can be avoided because they are not solving the inviscid Euler equations in the gas evolution stage, which is analyzed in chapter 3.

6.2.2 Flux Vector Splitting, Flux Difference Splitting, and BGK Schemes

A recent trend in the development of upwind schemes has centered around the construction of hybrid flux-splitting formulations which seek to combine the accuracy of FDS approaches in the resolution of shear layers with the robustness of FVS in the capturing of strong discontinuities. In the past few years, great efforts have been taken to combine the FVS and FDS schemes, see [24] and references therein. However, untill now there have been few great successes. The main reason for the unsuccessful attempts is that there is a lack of physical principle (or governing equation) to combine FVS and FDS fluxes.

The weakness of the Godunov method or FDS scheme results from inadequate dissipation in the inviscid Euler solution in the shock region. As pointed out before, the Riemann solution corresponds an equilibrium state at the cell interface, regardless of the real physical situation. The successful part of the Godunov method in capturing numerical shocks is largely due to the projection dissipation. However, in the multidimensional case, the projection dissipation is not uniformly added in each direction. The ability to capture a stable discontinuous solution for the FDS scheme in the multidimensional case is rather fragile, especially in cases where high resolution calculation on a fine mesh is required[2]. Even for the "multidimensional" scheme (if there is one for the Euler equations), similar spurious phenomena are doomed to happen. For the numerical solution in smooth regions, such as a boundary layer, the absence of dissipation in the Riemann solver becomes an advantage, where the boundary solutions can be captured accurately.

On the other hand, for the Flux Vector Splitting scheme, the governing equation in the gas evolution stage is the collisionless Boltzmann equation. The free transport in the gas evolution stage, naturally introduces large dissipation in the FVS scheme.

[2]Fine mesh corresponds to less dissipation added in the projection stage.

Although the large dissipation, or more precisely the nonequilibrium property in the FVS scheme, could help to capture a stable and robust numerical shock structure, the contact discontinuities and slip lines are badly smeared. As a consequence, the Navier-Stokes solution cannot be properly obtained from FVS schemes [124, 82].

In order to develop a robust and accurate scheme for unsteady compressible flows, we have to in some ways combine the good properties from both FDS and FVS schemes. In other words, we need to use FDS in continuous regions and FVS in discontinuous regions to construct a hybrid scheme. For example, starting from the FVS scheme, in order to reduce the free penetration of different waves or particles, the correlation or collisions between left and right moving waves have to be introduced. The construction of the common $M_{1/2}, U_{1/2}$ terms in AUSM-type schemes is largely based on this physical reason[75]. Similarly, Moschetta and Pullin [86] tried to use Osher's flux function to replace linearly degenerate wave in the KFVS scheme. From the FDS scheme, additional dissipations are usually introduced to stabilize discontinuous solutions [17]. The dynamical effects of using two waves instead of three waves in the HLLE scheme is basically to smear some waves and introduce dissipations [25]. A good hybrid scheme depends on a smart weight function to identify where the flow is smooth, where the flow is discontinuous, and make a smooth transition between them. No uniform criteria have been obtained so far. One direct way to avoid using the hybrid philosophy in the designing of robust and accurate scheme is to include "smart" viscous term in the governing equation directly. In other words, even though the additional dissipation in the scheme can smear the contact discontinuity or the slip line, the scheme is equally good if the dissipative effect is physically correct and could generate the exact Navier-Stokes solution in the smooth region. At the same time, the artificial dissipation is large enough to stabilize the discontinuous solutions, such as the BGK method.

From the above analysis, we know that the Riemann solver cannot capture all flow situations, such as the nonequilibrium shock region. *Perfect Riemann solvers have not and will never be found by solving the inviscid Euler equations numerically.* In order to have a reliable scheme, we have to have the correct governing equations for the numerical fluid, where both equilibrium and non-equilibrium flow properties have to be considered. The BGK model naturally provides such an equation and the BGK method gives a genuine nonlinear combination of FVS and FDS schemes. For example, in the discontinuous region, the BGK method has a non-Maxwellian distribution to capture the dissipative flow behavior, and in the continuous region, it gives a "Lax-Wendroff"

type central scheme for the Navier-Stokes equations.

6.2.3 Central and Upwind Schemes

As analyzed before, any numerical scheme basically solves an IVP locally around each cell interface. In order to get a good numerical method, we need both a reasonable initial condition and a correct governing equation. In this section, we are going to compare the central and upwind schemes in terms of initial condition and gas evolution. It is recognized that the oscillatory behavior in central schemes is mainly due to an inappropriate initial condition, rather than an absence of any upwinding mechanism. For example, let's look at the 1-D linear advection equation

$$u_t + au_x = 0,$$

where $a > 0$. The exact solution for the above equation is $u = u_0(x - at)$, which means that the initial curve u_0 propagates in the x-direction with constant speed. For the initial condition with linear distributed data across a cell interface, such as that shown in Fig.(6.10), the generalized Riemann solution moves the whole curve a distance $a\Delta t$ in a time step Δt. After each time step, the projection stage averages u inside each cell. From the exact upwinding solution, we find that the oscillations automatically form in the averaged u after a single step. For a square wave, the oscillations will appear at two corners (see Fig.(6.11)), which is identical to the numerical results from the Lax-Wendroff scheme. In other words, the Lax-Wendroff scheme is basically a generalized Riemann solver for an initial condition which is continuous across a cell interface.

For the nonlinear system. Suppose that we have the following initial conditions around the cell boundary $x_{j+1/2}$ at $t = 0$,

$$\text{IVP1:} \quad \begin{cases} \rho = \rho_{j+1/2} + \frac{\partial \rho}{\partial x}|_{j+1/2}(x - x_{j+1/2}), \\ \rho U = (\rho U)_{j+1/2} + \frac{\partial (\rho U)}{\partial x}|_{j+1/2}(x - x_{j+1/2}), \\ \rho \epsilon = (\rho \epsilon)_{j+1/2} + \frac{\partial (\rho \epsilon)}{\partial x}|_{j+1/2}(x - x_{j+1/2}), \end{cases} \qquad \forall x \in (x_{j-1/2}, x_{j+3/2}),$$

where $\rho_{j+1/2}, (\rho U)_{j+1/2}, (\rho \epsilon)_{j+1/2}$ are mass, momentum and energy densities located at the cell boundary, and $\partial \rho / \partial x, \partial (\rho U)/\partial x, \partial (\rho \epsilon)/\partial x$ the corresponding slopes. With these initial conditions, to the second order accuracy, the time-dependent numerical fluxes from any Generalized Riemann solver [4] and from the Lax-Wendroff scheme should be identical. So, the Riemann solver, even with the full set of characteristics, does not help us at all to avoid the oscillatory behavior. In other words, the Riemann solver is not

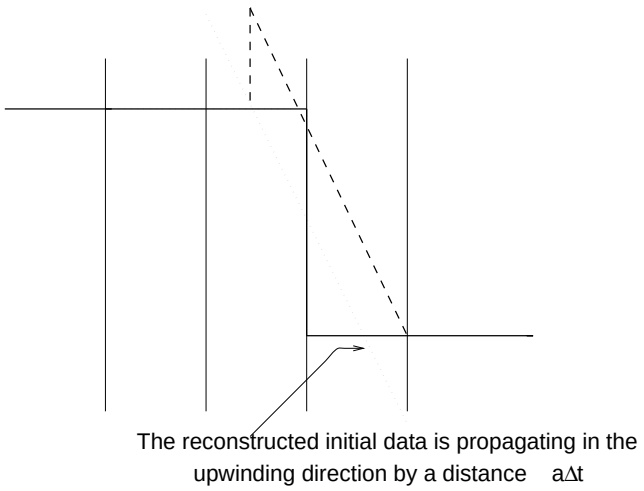

Figure 6.10: Numerical solution from an initial condition continuous across a cell interface

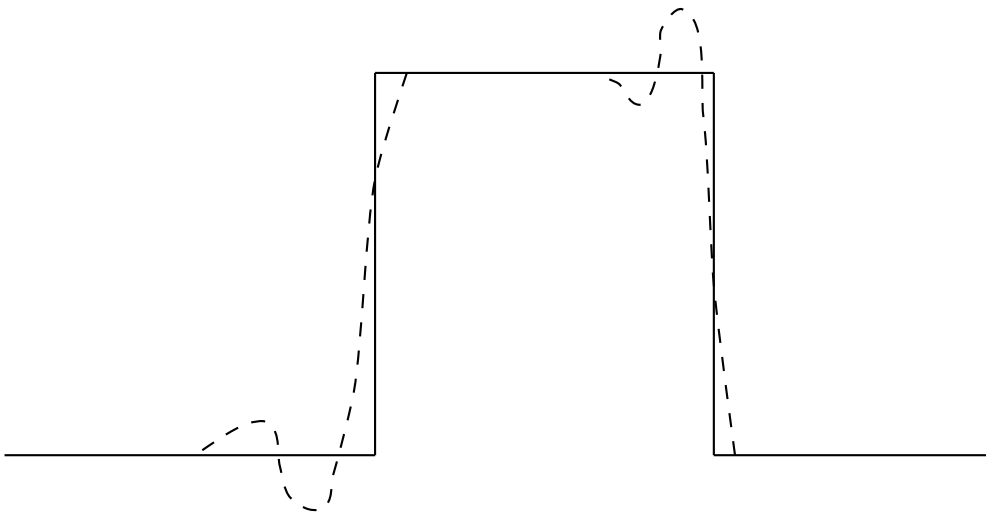

Figure 6.11: Numerical solution from an exact upwinding scheme with the initial condition of continuous flow distribution across a cell interface

critical for the capturing of monotonic shocks. To have a correct initial condition is more important than the fully upwinding characteristics.

The success for the Godunov method is mainly due to the introduction of initial discontinuities around each cell interface,

$$\text{IVP2:} \qquad \begin{cases} \rho = \rho_l \\ \rho U = (\rho U)_l \\ \rho\epsilon = (\rho\epsilon)_l \end{cases} \qquad x \le x_{j+1/2}, \qquad \begin{cases} \rho = \rho_r \\ \rho U = (\rho U)_r \\ \rho\epsilon = (\rho\epsilon)_r \end{cases} \qquad x \ge x_{j+1/2}.$$

Physically, the kinetic energy in the above initial data is much less than the kinetic energy contained in the initial data of the central scheme, *e.g.*

$$\int_{x_{j-1/2}}^{x_{j+3/2}} \frac{1}{2}\rho U^2|_{\text{IVP1}} dx > \int_{x_{j-1/2}}^{x_{j+3/2}} \frac{1}{2}\rho U^2|_{\text{IVP2}} dx.$$

Since the total energy is conserved, the reduction in the kinetic energy means an increase in the thermal energy, and this dissipation is critically needed in the construction of numerical shock structure. So, with the initial condition of two constant states, even if we never know what the Riemann solution is, we can still use other methods to construct approximate numerical fluxes in a short time period across the cell interface, and no oscillations will be generated. This explains that we can have many many approximate Riemann solvers and most of them work equally well. From this point of view, we can recognize the importance of the FCT concept in the development of modern high resolution shock capturing schemes. The slope-limiter approach was further developed by van Leer in a series of papers [122].

For schemes with a staggered mesh, due to the shifting of the numerical mesh, the projection dissipation is introduced more intensively than that with a non-staggered mesh. For example, for the simple linear advection equation, $u_t + au_x = 0$, in the special case of $a = 0$ and for an initial square wave, the upwinding scheme with a non-staggered mesh would only smear the discontinuity over two numerical cells and the square profile can be kept there forever. However, if we solve this problem with a staggered mesh, the alternative shifting of the mesh continuously smears any nonsmooth structure. As a result, even in the case of $a = 0$, the square wave will eventually disappear. So, the dynamical influence from the staggered mesh itself is to put additional numerical dissipations in the flow. Recently, Nessyahu and Tadmor [89] extended the Lax-Fridrichs scheme to high order by introducing higher order reconstruction of flow variables inside

each cell, where the dissipation effects from the staggered mesh are much reduced by using higher order interpolations.

6.3 Projection Dynamics

After reconstruction and gas evolution stages, we are going to discuss the projection dynamics in this section.

6.3.1 Introduction

It is well-known that the 1st-order Godunov-method always gives very dissipative numerical solutions, and it is interpreted as artificial viscosity effects. If the numerical fluxes are based on the exact Euler solutions, the dissipation must be added somehow in the projection stage. Our focal point in this section is to figure out qualitatively the dissipative mechanism in this stage[3], from which a few anomalous phenomena are well explained, including post-shock oscillations, density fluctuation in 2D shear waves, and pressure wiggles at a material interface in multicomponent gas flow. Since the projection process is intrinsically included in all shock capturing schemes, these phenomena are universal for both FVS and FDS schemes, even though the oscillations can be efficiently reduced in the KFVS scheme.

6.3.2 Dynamical Effects in the Projection Stage

In order to fully understand the dynamical effects in the projection stage, let's construct a physical model. This model not only can be applied to shocks, but also in general flow situations. Suppose there is a discontinuity in the flow distribution, and the location of the discontinuity is inside a numerical cell j. The left and right states in cell j are $(\rho_1, U_1, \rho_1\epsilon_1)$ and $(\rho_2, U_2, \rho_2\epsilon_2)$ in regions $[x_{j-1/2}, x_{j-1/2}+\alpha\Delta x]$ and $[x_{j-1/2}+\alpha\Delta x, x_{j+1/2}]$ respectively, where Δx is the cell size, see Fig.(6.12). In the following, we first assume $\alpha = \frac{1}{2}$.

The projection averaging is based on the conservation of total mass, momentum and

[3]Any truncation error analysis is only limited to regions with smooth flow. In order to analyze the dissipative flow behavior in discontinuous regions, a dynamical model has to be constructed.

energy,

$$\begin{cases} \frac{1}{2}\rho_1 + \frac{1}{2}\rho_2 = \bar{\rho}_j, \\ \frac{1}{2}\rho_1 U_1 + \frac{1}{2}\rho_2 U_2 = \bar{\rho}_j \bar{U}_j, \\ \frac{1}{2}\rho_1 \epsilon_1 + \frac{1}{2}\rho_2 \epsilon_2 = \bar{\rho}_j \bar{\epsilon}_j, \end{cases} \tag{6.3}$$

where $\bar{\rho}_j, \bar{\rho}_j \bar{U}_j, \bar{\rho}_j \bar{\epsilon}_j$ are averaged mass, momentum and energy densities in cell j. From the above equations, we can get the average velocity

$$\bar{U}_j = \frac{\rho_1 U_1 + \rho_2 U_2}{\rho_1 + \rho_2}. \tag{6.4}$$

After averaging, the kinetic energy in cell j becomes

$$\bar{E}_k = \frac{1}{4}(\rho_1 + \rho_2)\bar{U}_j^2. \tag{6.5}$$

However, before the averaging the original kinetic energy is

$$E_k = \frac{1}{4}\rho_1 U_1^2 + \frac{1}{4}\rho_2 U_2^2. \tag{6.6}$$

From Eq.(6.5) and Eq.(6.6), it can be proved that $E_k \geq \bar{E}_k$ and the lost kinetic energy is

$$\Delta E_k = E_k - \bar{E}_k = \frac{1}{4}\frac{\rho_1 \rho_2}{\rho_1 + \rho_2}(U_2 - U_1)^2. \tag{6.7}$$

Since the total energy is conserved in the projection stage, a decrease in the kinetic energy must be accompanied by an increase in the thermal energy. So, projection is actually a dissipative process in which kinetic energy is transferred into thermal energy. It is this dissipative mechanism that helps the Godunov method to capture "nonoscillatory" shocks.

From thermodynamics, we can prove that the entropy is increased in the above projection process. The transition from initial density distributions ρ_1 and ρ_2 to the final uniform density $\frac{1}{2}(\rho_1 + \rho_2)$ is achieved through an equivalent mass diffusion process.

The flow variables inside each cell are updated through the fluxes in the gas evolution stage and the averaging mechanism in the projection stage. If the exact Euler equations are solved in the gas evolution stage, the real governing equations in the whole updating process for a numerical scheme can be derived in the following. Fig(6.12) outlines an evolution process in an isolated cell from the initial flow distribution to the final constant

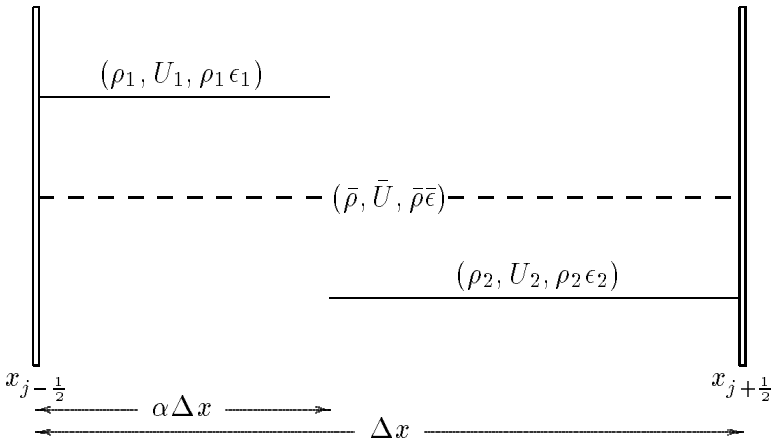

Figure 6.12: Subcell mixing in the averaging stage

state. This process is finished in a whole time step Δt. In the following, we are going to derive the approximate governing equations in this process. At the end, the convective fluxes from the exact Riemann solver in the gas evolution stage will be added.

1. Continuity Equation: In the subcell $x\epsilon[x_{j-1/2}, x_{j-1/2} + \alpha\Delta x]$, the density is changed from the initial ρ_1 to the final $\bar{\rho} = \alpha\rho_1 + (1-\alpha)\rho_2$ through the mass fluxes at $x = x_{j-1/2} + \alpha\Delta x$. If we assume that the diffusive mass flux is equal to $\eta_1\rho_x$, we have

$$\begin{aligned} \frac{\bar{\rho} - \rho_1}{\Delta t} &= \frac{\eta_1\rho_x}{\alpha\Delta x} \\ &= \frac{\eta_1(\rho_2 - \rho_1)}{\alpha\Delta x\frac{1}{2}\Delta x}, \end{aligned}$$

from which the mass diffusion coefficient η_1 can be obtained

$$\eta_1 = \frac{1}{2}\alpha(1-\alpha)\frac{(\Delta x)^2}{\Delta t}.$$

2. Momentum Equation: In the subcell $x\epsilon[x_{j-1/2}, x_{j-1/2} + \alpha\Delta x]$ again, the initial momentum $\rho_1 U_1$ is changed to $\bar{\rho}\bar{U}$ in a time step Δt. Denoting the viscous flux as $\eta_2 U_x$, we have

$$\begin{aligned} \frac{\bar{\rho}\bar{U} - \rho_1 U_1}{\Delta t} &= \frac{\alpha\rho_1 U_1 + (1-\alpha)\rho_2 U_2 - \rho_1 U_1}{\Delta t} \\ &= \frac{\eta_2 U_x}{\alpha\Delta x} \\ &= \frac{\eta_2(U_2 - U_1)}{\alpha\Delta x\frac{1}{2}\Delta x}. \end{aligned}$$

With the assumption

$$\rho_2 U_2 - \rho_1 U_1 \sim \rho(U_2 - U_1),$$

we have

$$\eta_2 = \frac{1}{2}\alpha(1-\alpha)\frac{(\Delta x)^2}{\Delta t}\rho.$$

3. Energy Equation: The dissipative effect in the energy equation is to translate kinetic energy into thermal energy. Heat conducting process can also be modeled by considering the smearing of two different temperature regions. In the whole numerical cell, we can write the energy dissipation process as

$$\frac{\partial E_k}{\partial t} = (\eta_3 U U_x)_x.$$

From the above equation and Eq.(6.7), we have

$$\begin{aligned}
\frac{\Delta E_k}{\Delta t} &= \frac{\frac{1}{4}\dfrac{\alpha\rho_1(1-\alpha)\rho_2}{\alpha\rho_1 + (1-\alpha)\rho_2}(U_2 - U_1)^2}{\Delta t} \\
&= \eta_3 \frac{(U_2 - U_1)U_x}{\frac{1}{2}\Delta x} \\
&= \eta_3 \frac{(U_2 - U_1)^2}{\frac{1}{2}\Delta x \frac{1}{2}\Delta x}.
\end{aligned}$$

So, with the assumption

$$\frac{\rho_1\rho_2}{\alpha\rho_1 + (1-\alpha)\rho_2} \sim \rho,$$

we can obtain

$$\eta_3 = \frac{1}{16}\alpha(1-\alpha)\frac{(\Delta x)^2}{\Delta t}\rho.$$

While the projection stage provides the dissipative mechanism to smear the subcell structure, the gas evolution stage influences the flow motion via the numerical fluxes across the cell interface. If the Euler equations are solved exactly in the gas evolution stage, the mass, momentum and energy transports through a cell interface are the fluxes $(\rho U, \rho U^2 + P, EU + PU)$. Combining the Euler fluxes with the diffusion and dissipative terms in the projection stage, we can get the following "Navier-Stokes" Equations, which

model the real governing equations in the Godunov method,

$$\begin{cases} \rho_t + (\rho U)_x = \epsilon \rho_{xx}, \\ (\rho U)_t + (\rho U^2 + P)_x = \epsilon (\rho U_x)_x, \\ E_t + (EU + PU)_x = \frac{1}{8}\epsilon (\rho U U_x)_x, \end{cases}$$

where

$$\epsilon = \frac{1}{2}\alpha(1-\alpha)\frac{(\Delta x)^2}{\Delta t} \tag{6.8}$$

depends on the location of the discontinuity. The dependence of ϵ on Δx and Δt is due to the fact that the actual averaging process is taking place dynamically over a whole time step inside each cell although it is often interpreted as an instantaneous process occuring at the end of each time step.

The diffusive and dissipative properties in the above model are not directly related to the specific Euler fluxes across each cell interface. Using Gilbarg and Paolucci's techniques[33], the stationary shock structure for Eq.(6.8) can be obtained[132], where the main conclusions are

(1) ρ increases monotonically while U decreases, as x varies from $-\infty$ to $+\infty$;

(2) the momentum ρU is not a monotonic function of x.

(3) the maximum value of the momentum ρU is independent of ϵ.

Points (1) and (2) have been analyzed based on the isentropic model in [53]. As pointed out by Jin and Liu, the momentum spike is solely related to the mass diffusion term in the continuity equation. Later, Karni and Canic found out that the the momentum spike has no direct contributions to the post-shock oscillations[57]. Numerically, a momentum spike has been observed using a 1st-order BGK scheme in chapter 4, where the momentum peak value is independence of the cell size Δx. The numerical results for other schemes have a similar property [53]. All these observations validate the governing equations (6.8). Also, based on Eq.(6.8), we can easily explain the fact that the momentum peak value $(\rho U)_{\max}$ is a constant. From the continuity equation, we have

$$(\rho U)_{\max} \sim \epsilon (\rho_x)_{\max}.$$

Note that the leading order term of the density variation across the shock layer is proportional to [140]

$$(\rho_x)_{\max} \sim \frac{\rho_2 - \rho_1}{\delta x} \sim \frac{(\rho_2 - \rho_1)^2}{l\rho_1} \sim \frac{C_1(\rho_2 - \rho_1)^2}{\epsilon \rho_1},$$

where δx is the shock thickness, l the mean free path, (ρ_1, ρ_2) the upstream and downstream densities, and C_1 the upstream sound speed. So, $(\rho U)_{\max}$ can be approximated as

$$(\rho U)_{\max} \sim \epsilon(\rho_x)_{\max} \sim \frac{C_1(\rho_2 - \rho_1)^2}{\rho_1},$$

which is independent of ϵ. So, even with a time-dependent ϵ in the moving shock case (Eq.(6.8)), $(\rho U)_{\max}$ keeps a constant value. Theoretically, the maximum momentum peak value $(\rho U)_{\max}$ should be a universal constant for all shock capturing schemes if only projection dissipation is involved.

Even though the Godunov-type schemes have become more and more popular in the CFD community, we have to agree that we understand much less than what we are supposed to understand from scalar equations to nonlinear systems. Basically, the great contribution of the Godunov method is the modeling of two constant states around a cell interface in the projection stage, which dramatically reduces the kinetic energy in the gas system. Also, this is the exact place where the implicit viscosity is coming from. The Euler equations never tell us that the numerical flow should be discontinuous at a cell boundary; the construction of constant states inside each cell is a numerical model of the real physics rather than any specific discretization of the governing equations. Also, this dissipative mechanism from the projection stage is more natural and complicated than the terms attributed to artificial viscosity [90, 91]. Even with the great success in the construction of the initial condition, the validity of the Godunov method for the numerical fluid is still questionable. Physically, the numerical fluid in the discontinuous regions will not follow the inviscid Euler equations.

It should be emphasized again that the FCT idea is a natural extension of the Godunov modeling to construct higher order accurate initial conditions [7]. The impact of nonlinear limiter is extraordinary in the development of modern shock capturing schemes. It seems that over the past twenty years, the importance of the limiters has been overtaken by the Riemann solvers. Frankly speaking, without constructing a good initial condition through nonlinear limiters, the numerical results will be disastrous regardless of whether exact or approximate Riemann solvers or any other generalized Riemann solvers are used in the gas evolution stage.

6.3.3 Post-Shock Oscillations

For the post-shock oscillations, Arora and Roe interpreted that the intermediate states inside the shock layer do not lie on the Hugoniot curve [2]. Hence, the Riemann solver generates a whole fan of waves and induces the post-shock oscillations. Jin and Liu explained this in the context of a traveling wave solution and suggested that the unsteadiness in the momentum spike is the cause of the oscillations [53]. Karni and Canic noticed that the upwind scheme and the Lax Friedrichs scheme behave differently here. They concluded that the vanishing viscosity in Roe's scheme at the shock region contributes to the oscillations, and derived a modified parabolic equation in the shock layer[57].

In [132], it is shown that there is a stationary "Navier-Stokes" shock structure for each constant ϵ. If ϵ were really a constant, such as in the stationary shock case, there would be no post-shock oscillations. However, for moving shocks, the discontinuity can be located at any place inside each cell $(x_{j-1/2} + \alpha\Delta x)$ and its location is changing with time. As a consequence, ϵ in the "Navier-Stokes" Equations (6.8) is a function of time t. For a moving shock, $\alpha(t)$ is a periodic function, with the period equal to the time interval for the shock to cross a numerical cell,

$$T = \frac{\Delta x}{U_s},$$

where U_s is the shock speed. So, the pulsating shock structure, obtained from the "Navier-Stokes" equations(6.8) with a unsteady viscosity coefficient, generates post-shock oscillations.

The continuing variation of kinetic energy due to averaging in the shock layer exerts a periodic force on the downstream flow motion, which is similar to exert a forcing term on one end of a string. The oscillations form and propagate along the string. This behavior is only related to the momentum spike superficially. Physically, even without the mass diffusion term in the continuity equation (6.8) and with a monotonic momentum distribution, post-shock oscillations will still be generated due to the unsteady nature in the momentum and energy equations. This is probably the reason why the momentum spike can be eliminated through a simple transformation $\rho u \rightarrow \rho u - \epsilon\partial_x\rho$, but the post-shock oscillations will remain the same[53]. We can validate the above observation in another way. When applying the projection model to a moving contact discontinuity wave, we can get the same mass diffusion term in the continuity equation and consequently obtain the momentum spike. However, we will not find any numerical oscillation there, because

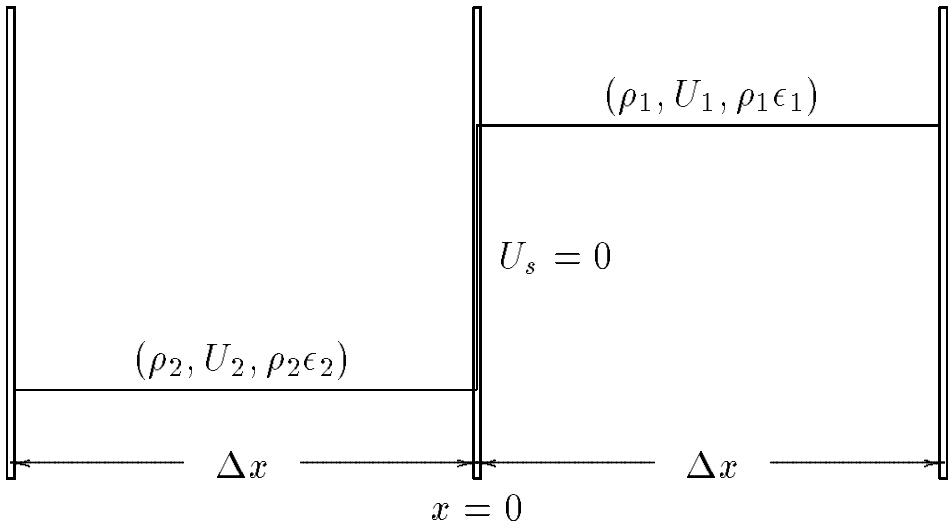

Figure 6.13: Stationary shock located at $x = 0$

there is no time-dependent nonlinear dissipative mechanism in the energy equation. Due to the equal velocities $U_1 = U_2$ on both sides of the contact discontinuity, $\Delta E_k = 0$ in Eq.(6.7) holds. So, it seems that the unsteady numerical dissipation from the projection stage is the real cause of the post-shock oscillations.

Based on the projection dynamics, the relation between the post-shock oscillation amplitude and the shock speed can be approximately obtained. As observed in [2, 73], very slow and fast moving shocks generate a smaller oscillating amplitude. In order to qualitatively evaluate the relation, let's consider the following model. Initially a stationary shock is located at cell interface $x = 0$ with distributions $(\rho_2, U_2, \rho_2\epsilon_2)$ and $(\rho_1, U_1, \rho_1\epsilon_1)$ on the left and right sides, as shown in Fig(6.13). The upstream and downstream flow conditions are

$$\begin{cases} \rho_1 = 1, \\ U_1 = -1, \qquad x \geq 0, \\ P_1 = \frac{1}{\gamma M^2}. \end{cases} \tag{6.9}$$

and

$$\begin{cases} \rho_2 = \dfrac{(\gamma+1)M^2}{2+(\gamma-1)M^2}\rho_1, \\ U_2 = (\dfrac{\gamma-1}{\gamma+1} + \dfrac{2}{(\gamma+1)M^2})U_1, \qquad x \leq 0, \\ P_2 = (\dfrac{2\gamma}{\gamma+1}M^2 - \dfrac{\gamma-1}{\gamma+1})P_1, \end{cases} \tag{6.10}$$

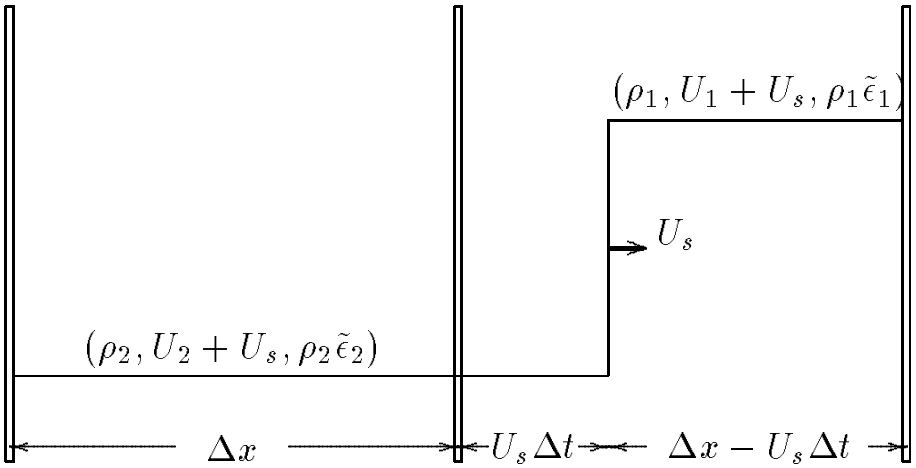

Figure 6.14: Moving shock with speed U_s at time Δt

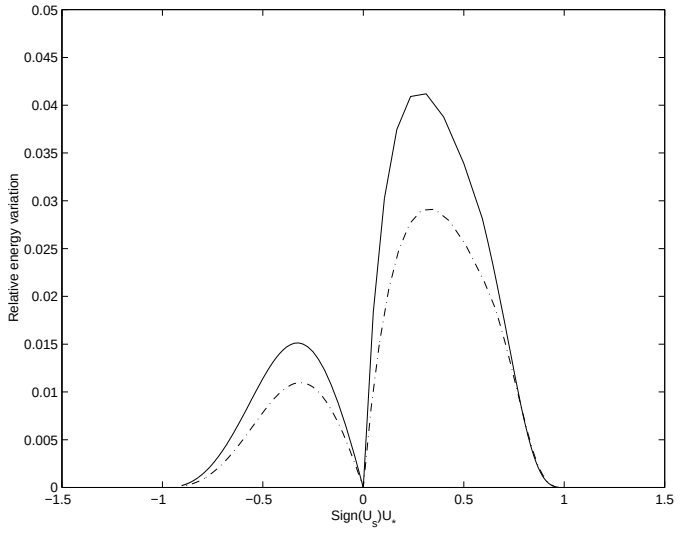

Figure 6.15: Relative energy variation $\frac{\Delta E_k}{\rho_2\tilde{\epsilon}_2\Delta x}$ vs. relative shock speed $\mathrm{Sign}(U_s)U_*$ for different Mach number M; dash-dotted line $M = 3.0$, solid line $M = 20.0$

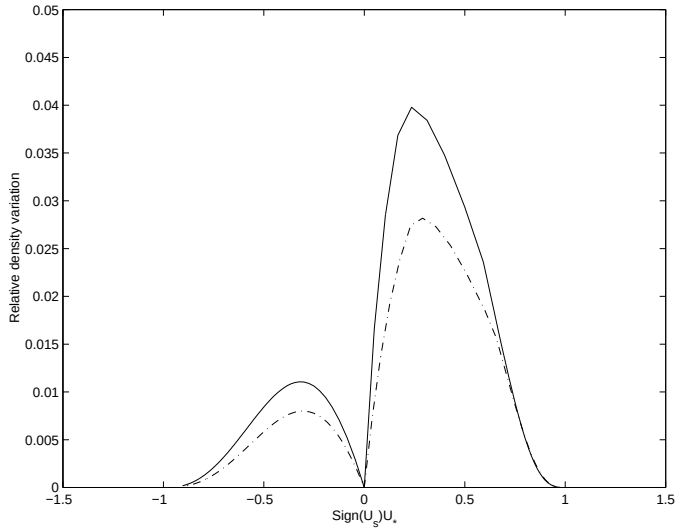

Figure 6.16: Relative density variation $\frac{\Delta\rho}{\rho_2}$ vs. relative shock speed $\mathrm{Sign}(U_s)U_*$ for different Mach number M; dash-dotted line $M = 3.0$, solid line $M = 20.0$.

where M is the upstream Mach number. From the above flow conditions, we can get the sound speeds C_1 and C_2 on both sides,

$$C_1 = \sqrt{\frac{\gamma P_1}{\rho_1}} \qquad \text{and} \qquad C_2 = \sqrt{\frac{\gamma P_2}{\rho_2}}.$$

For a moving shock, the flow velocities will be changed, *i.e.* $U_1 \to U_1 + U_s$ and $U_2 \to U_2 + U_s$, where U_s is the shock speed. After each time step Δt, the shock front will be located at $U_s\Delta t$, see Fig(6.14). In the numerical cell with shock, the lost kinetic energy due to the averaging is

$$\Delta E_k = \frac{1}{4}\frac{\rho_1\Delta t U_s\rho_2(\Delta x - \Delta t U_s)}{\rho_1\Delta t U_s + \rho_2(\Delta x - \Delta t U_s)}(U_1 - U_2)^2, \qquad \text{for} \quad U_s > 0. \tag{6.11}$$

Based on the CFL condition (CFL number=1), the time step is

$$\Delta t = \frac{\Delta x}{\mathrm{Max}(|U_1 + U_s| + C_1, |U_2 + U_s| + C_2)},$$

and Eq.(6.11) goes to

$$\Delta E_k = \frac{1}{4}\frac{\rho_1\rho_2 U_*(1 - U_*)}{\rho_1 U_* + \rho_2(1 - U_*)}(U_1 - U_2)^2\Delta x, \qquad \text{for} \quad U_s > 0, \tag{6.12}$$

where

$$U_* = \frac{|U_s|}{\mathrm{Max}(|U_1 + U_s| + C_1, |U_2 + U_s| + C_2)}.$$

Similarly, for $U_s < 0$, we have

$$\Delta E_k = \frac{1}{4}\frac{\rho_1\rho_2(1-U_*)U_*}{\rho_1(1-U_*)+\rho_2 U_*}(U_1-U_2)^2\Delta x, \qquad \text{for} \quad U_s < 0. \tag{6.13}$$

All noises generated in the shock region propagate downstream because of the following two reasons: (1). the kinetic energy variation in the shock layer perturb the flow motion, (2). there is no dissipative mechanism in the gas evolution stage for the inviscid Euler equations. The ratio of the energy variation ΔE_k to the total downstream energy density $\rho_2\tilde{\epsilon}_2\Delta x$ in each cell is

$$\frac{\Delta E_k}{\rho_2\tilde{\epsilon}_2\Delta x} = \frac{\frac{1}{4}\frac{\rho_1\rho_2 U_*(1-U_*)}{\rho_1 U_*+\rho_2(1-U_*)}(U_1-U_2)^2}{\frac{1}{2}\rho_2(U_2+U_s)^2+\frac{1}{\gamma-1}P_2}, \qquad \text{for} \quad U_s > 0, \tag{6.14}$$

similarly,

$$\frac{\Delta E_k}{\rho_2\tilde{\epsilon}_2\Delta x} = \frac{\frac{1}{4}\frac{\rho_1\rho_2(1-U_*)U_*}{\rho_1(1-U_*)+\rho_2 U_*}(U_1-U_2)^2}{\frac{1}{2}\rho_2(U_2+U_s)^2+\frac{1}{\gamma-1}P_2}, \qquad \text{for} \quad U_s < 0. \tag{6.15}$$

The energy fluctuation ratios in (6.14) and (6.15) depend mainly on the relative shock speed and velocities. Because of the independence of $\Delta E_k/\rho_2\tilde{\epsilon}_2\Delta x$ on the numerical cell size Δx, the post-shock oscillations can never be eliminated by refining the mesh. Fig.(6.15) is the plot of relative energy variation $\dfrac{\Delta E_k}{\rho_2\tilde{\epsilon}_2\Delta x}$ vs. the relative shock speed $\mathrm{Sign}(U_s)U_*$ for different Mach numbers. The relative energy fluctuation is smaller at both lower and higher shock speed. From the definition of total energy density $\rho\epsilon = \frac{1}{2}\rho U^2 + \frac{1}{\gamma-1}P$, we can derive the energy variation

$$\Delta(\rho\epsilon) = \rho U\Delta U + \frac{1}{2}U^2\Delta\rho + \frac{1}{\gamma-1}\Delta P.$$

Therefore, using $C^2 \sim \frac{\gamma\Delta P}{\Delta\rho}$ and the Riemann invariant $\Delta U \sim \frac{\Delta P}{\rho C}$, we have

$$\Delta(\rho\epsilon) \sim \Delta\rho(\frac{|U|C}{\gamma}+\frac{1}{2}U^2+\frac{C^2}{\gamma(\gamma-1)}),$$

from which the density fluctuation in the downstream can be obtained

$$\frac{\Delta\rho}{\rho_2} = \frac{1}{\rho_2}\frac{\Delta E_k/\Delta x}{\frac{|(U_2+U_s)|C_2}{\gamma}+\frac{1}{2}(U_2+U_s)^2+\frac{C_2^2}{\gamma(\gamma-1)}}.$$

Fig.(6.16) is the plot of density fluctuation for different Mach numbers. The numerical observations presented in [73, 2] confirm qualitatively the above theoretical analysis, where there is about $2-5\%$ density variation, and the amplitudes are different from $U_s > 0$ and $U_s < 0$. In real flow computations, a fast moving shock creates high frequency modes which are decaying much faster than low frequency modes due to the dissipation in both the gas evolution and the projection stage. As a result, the amplitude profile in the density variation has to be modified and shifted by considering the numerical dissipation in the whole downstream region. Also, the shock layer is smeared over several mesh points and the intermediate states in the shock layer are different from the upstream and downstream flow conditions. The final observation should be a statistical averaging over all possible states in the shock layer. For example, the kinetic energy fluctuation should be modified to

$$\overline{\Delta E_k} = \frac{1}{\beta - 1} \int_1^{\beta} \Delta E_k(\beta') d\beta',$$

which is an averaging over all possible density jumps,

$$\beta' = \frac{\rho_2}{\rho_1},$$

where β is the limit of highest density jump,

$$\beta = \frac{(\gamma+1)M^2}{2 + (\gamma-1)M^2}.$$

Remark(6.1)

The above explanation for the post-shock oscillations can be regarded as supplement to the explanations proposed in the literature [104, 53, 57, 2]. The projection dynamics is explicitly explored here. In order to understand this problem further, we need to consider the real physical properties in the shock region. Most shock capturing schemes usually smear the shock layer over a few grid points. The transition region in the shock layer has to be considered as points inside a numerical shock structure[4]. So, the non-equilibrium Navier-Stokes or Boltzmann equation have to be considered there in the gas evolution stage. Therefore, the use of the Euler equations in this region is physically inappropriate. The 1st-order BGK scheme basically solves the non-equilibrium Boltzmann equation in this region, which gives sharp and oscillation-free shock transitions. See Fig.(4.2)-(4.5) in chapter 4. This can be understood by noticing that the BGK fluxes are obtained from the

gas distribution function which is different from an exact Maxwellian in the shock region. This non-equilibrium property of using non-Maxwellian mimics the physical mechanism in the construction of a numerical shock front. The importance of a non-Maxwellian distribution has been well-recognized in the study of strong shock structure[88]. For high-order BGK method, the oscillation will still be generated because the dissipation from the reconstruction stage is a complicated function of flow distribution, limiter and the coupling between flow distribution and limiter. The artificial dissipation from the reconstruction stage can hardly be controlled in a reasonable way in the gas evolution stage to get oscillation free solution even though the oscillation can be efficiently dissipated afterwards. It is doubtful that there will exist any high-resolution schemes which are oscillation free for the moving shock case.

To have a consistent dissipative mechanism at the shock region in the gas evolution stage is crucial for any high resolution scheme; otherwise gigantic amount of dissipation is needed to smear a shock layer in order to get a smooth transition. Without solving the Navier-Stokes equations directly in the gas evolution stage, we have to carefully tune the artificial viscosity to mimic the physical viscous effects. Even solving the Navier-Stokes equations, the physical viscosity has to be amplified artificially to capture the shock with numerical thickness. It is reasonable for Karni and Canic to put additional viscous term in Roe's Riemann solver to reduce the amplitude in the post-shock oscillations [57]. However, without a reasonable governing equation, it is hard to determine the amount of dissipation needed. Arora and Roe concluded that the oscillation is due to the fact that the intermediate states in the shock regions are not located on the Hugoniot curve. This conclusion is based mainly on the Euler equations we are supposed to solve. Numerically, we are actually solving the "Navier-Stokes" solutions, the states inside the shock layer indeed would not stay on the Hugoniot curve, but they will not generate oscillations if the dissipative terms in the flux function are intrinsically consistent, such as in the 1st-order BGK method.

In summary, the dynamical effect in the projection stage for a nonlinear system provides an unsteady dissipative mechanism, which transfers kinetic energy into thermal energy. This feature is only observed in nonlinear systems, and this fact could probably

[4]Sometimes the transition from upstream to downstream in a numerical shock layer is considered to be connected by several small shocks. From a physical point of view, it is impossible to reach the same final state by compressing the gas through several shock waves as that reached by compressing with a single shock wave. For example, a strong shock wave propagating through a monatomic gas will yield a density ratio of 4, while two successive strong shock waves could result in a density ratio of 16. So, the transition cells in a numerical shock layer have to be regarded as points inside the shock structure. In other words, the intermediate states cannot stay on the Hugoniot curve connecting the upstream and downstream flow conditions in a nonlinear system.

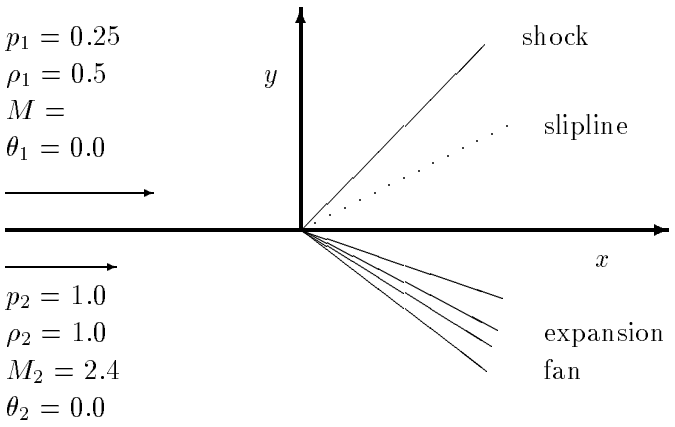

Figure 6.17: 2D Riemann problem

change our belief that any good numerical technique for solving the linear wave equation ($U_t + aU_x = 0$) could be extended by a simple mechanism into an equally good numerical technique for solving a system of nonlinear conservation laws [106].

6.3.4 Density Fluctuation in the 2-D Shear Wave

The idea of projection dynamics presented in the last section can also be used to explain the density fluctuations in a 2D shear wave. First, let's consider a 2-D test case, where the initial flow conditions are shown in Fig.(6.17)[45]. From these initial conditions, three waves will be formed, such as a shock, a slip line and an expansion fan.

Using a 2nd-order TVD scheme[117], the density distribution across these waves in the y-direction is shown in Fig.(6.18), where $M = 7$ is used for the initial Mach number of the flow in the upper part. The circles are numerical solutions and the solid lines are exact solutions. Similar spurious solution in the 2-D shear layer case has been reported in [120].

The density fluctuation around a slip line in the above figure is a common numerical phenomenon for all shock capturing schemes, except the Lagrangian one [44]. In order to understand this, we have to consider the projection dynamics again in the 2-D case. As a simple model, we consider a numerical cell which includes a slip line, as shown in Fig.(6.19). Here the velocities in the direction parallel to the cell interface are not equal $V_1 \neq V_2$ due to the slip condition and $U_1 = U_2$ holds in the normal direction. Due to the

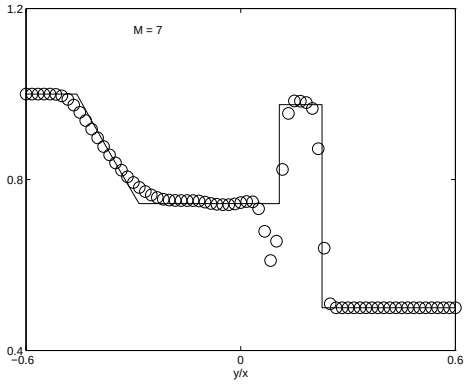

Figure 6.18: Density distribution for the case with Mach Number $M = 7$, where the solid line is the exact solution

dynamical averaging, kinetic energy is not conserved. Based on the same analysis as in the 1-D case, we can get the kinetic energy loss in the averaging stage

$$\Delta E_k = \frac{1}{4}\frac{\rho_1\rho_2}{\rho_1+\rho_2}(V_2 - V_1)^2, \tag{6.16}$$

where the location of the slip line is assumed to be at the center of the numerical cell. Due to the total energy conservation, the lost kinetic energy has to be transferred into thermal energy and heats the gas around the slip region. The magnitude of heating depends on the relative slip velocities. Due to this heating effect, the temperature and pressure around the slip line will increase, and the increased pressure pushes the gas away from each other. So, a density sink is formed, as shown in Fig.(6.18). The artificial heating effects can also be regarded as a result of the friction between different fluids around the slip line. In the 1-D case, we can not observe this phenomenon, because the equal velocity $U_1 = U_2$ at a contact discontinuity wave prevents the kinetic energy from being transferred into thermal energy. In conclusion, the projection stage provides not only a dissipative mechanism for numerical shocks, but also an artificial heating mechanism in multidimensional slip line regions. The only cure to reduce or eliminate the artificial heating effects around slip line is to solve it and avoid the projection dissipation. The generalized Langrangian method works very well in the slip region due to the fact that the slip line is always along the cell boundary [44, 78, 46].

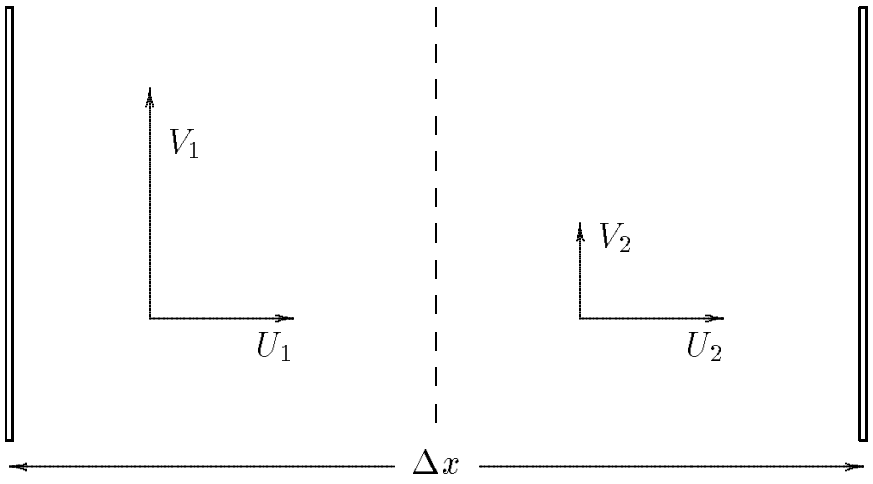

Figure 6.19: Slip Line inside a Numerical Cell.

6.3.5 Pressure Wiggles Around Material Interface in 2-Component Gas Flow

It is observed that for conservative Godunov-type schemes, pressure wiggles at a material interface are generated[3]. In order to explain these oscillatory behaviors across a material interface, let us study the projection dynamics again. Suppose a material interface is located inside a numerical cell and separates the whole cell into two parts with volumes V_1 and V_2, as shown in Fig.(6.20). The mass, momentum, energy densities, and specific heat ratio in both parts are

$$(\rho^{(1)}, \rho^{(1)}U^{(1)}, \rho^{(1)}\epsilon^{(1)}, \gamma^{(1)})$$

and

$$(\rho^{(2)}, \rho^{(2)}U^{(2)}, \rho^{(2)}\epsilon^{(2)}, \gamma^{(2)}).$$

The material interface is a contact discontinuity with equal velocities $U^{(1)} = U^{(2)}$ and equal pressures $P^{(1)} = P^{(2)}$ aross the interface. In order to simplify the derivation, we assume $U^{(1)} = U^{(2)} = 0$ here. This assumption will not change the applicability of the following analysis to the general case around a moving material interface.

The projection stage mixes different components and the mixing is based on the total mass, momentum and energy conservations. Since the momentum equation can be ignored here due to the equal velocities in the two components, the mass and energy

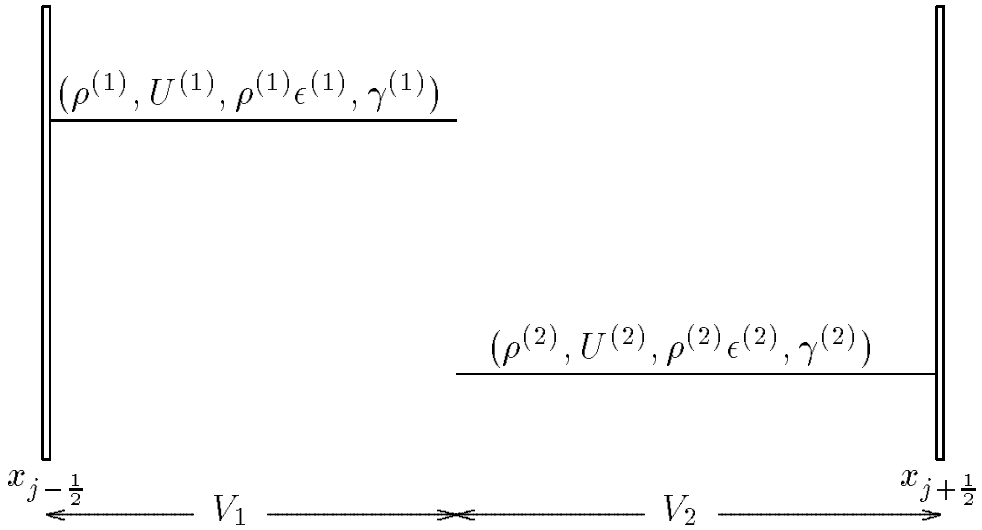

Figure 6.20: Multicomponent Subcell Mixing at Material Interface

conservations will be used. They are

$$\rho^{(1)}V_1 + \rho^{(2)}V_2 = \rho(V_1 + V_2), \tag{6.17}$$

and

$$\rho^{(1)}\epsilon^{(1)}V_1 + \rho^{(2)}\epsilon^{(2)}V_2 = \rho\epsilon(V_1 + V_2). \tag{6.18}$$

For a perfect gas, energy conservation reduces to

$$\begin{aligned} & \frac{kT^{(1)}}{\gamma^{(1)}-1}\frac{\rho^{(1)}V_1}{m_1} + \frac{kT^{(2)}}{\gamma^{(2)}-1}\frac{\rho^{(2)}V_2}{m_2} \\ = \;& T\left(\frac{k}{\gamma^{(1)}-1}\frac{\rho^{(1)}V_1}{m_1} + \frac{k}{\gamma^{(2)}-1}\frac{\rho^{(2)}V_2}{m_2}\right), \end{aligned} \tag{6.19}$$

where k is the Boltzmann constant, m_1 and m_2 the molecular weights for gas 1 and gas 2, $T^{(1)}, T^{(2)}$ and T are the temperatures in the initial two components and in the final equilibrium state. From Eq.(6.19), the common temperature after mixing (with the assumption $m_1 = m_2$) can be obtained,

$$T = \frac{(\gamma^{(2)}-1)T^{(1)}\rho^{(1)}V_1 + (\gamma^{(1)}-1)T^{(2)}\rho^{(2)}V_2}{(\gamma^{(2)}-1)\rho^{(1)}V_1 + (\gamma^{(1)}-1)\rho^{(2)}V_2}. \tag{6.20}$$

The equilibrium pressure $\tilde{P}$ in the whole cell $(V_1 + V_2)$ becomes

$$\tilde{P} \;=\; \tilde{P^{(1)}} + \tilde{P^{(2)}}$$

$$
\begin{aligned}
&= \frac{V_1}{V_1+V_2}\frac{T}{T^{(1)}}P^{(1)} + \frac{V_2}{V_1+V_2}\frac{T}{T^{(2)}}P^{(2)} \\
&= \frac{TP}{V_1+V_2}(\frac{V_1}{T^{(1)}} + \frac{V_2}{T^{(2)}}),
\end{aligned} \tag{6.21}
$$

where $\tilde{P^{(1)}}$ and $\tilde{P^{(2)}}$ are the partial pressure contributions from component 1 and 2 gases separately after mixing, and $P = P^{(1)} = P^{(2)}$ are the initial individual gas pressure before mixing. Substituting Eq.(6.20) into Eq.(6.21), we obtain

$$
\tilde{P} = P\frac{V_1T^{(2)} + V_2T^{(1)}}{T^{(1)}T^{(2)}(V_1+V_2)}\frac{(\gamma^{(2)}-1)T^{(1)}\rho^{(1)}V_1 + (\gamma^{(1)}-1)T^{(2)}\rho^{(2)}V_2}{(\gamma^{(2)}-1)\rho^{(1)}V_1 + (\gamma^{(1)}-1)\rho^{(2)}V_2}. \tag{6.22}
$$

Obviously, $\tilde{P} \neq P$ in general cases, which means that the final pressure after mixing is different from the initial pressure at the material interface. Once the pressure variation is formed near a material interface, it subsequently generates waves and contaminates the flow field. For a single component gas, ($\gamma^{(1)} = \gamma^{(2)}$), Eq.(6.22) gives $\tilde{P} = P$ automatically, and the equal pressure is kept. An alternative explanation for the above phenomena can be the following. For an ideal gas, each degree of freedom in a molecule has an equal amount of energy which is proportional to the temperature T. The total internal energy of each molecule is $e^{(1)} = \frac{kT^{(1)}}{\gamma^{(1)}-1}$ for component 1 gas, and $e^{(2)} = \frac{kT^{(2)}}{\gamma^{(2)}-1}$ for component 2 gas. Suppose that by collisions, these two molecules exchange their energies and equalize their temperature to a common temperature T. From energy conservation, we have

$$
\frac{k\Delta T^{(1)}}{\gamma^{(1)}-1} + \frac{k\Delta T^{(2)}}{\gamma^{(2)}-1} = \Delta e^{(1)} + \Delta e^{(2)} = 0. \tag{6.23}
$$

However, the pressure change due to the temperature variation is

$$
\begin{aligned}
\Delta P &\sim k\Delta T^{(1)} + k\Delta T^{(2)} \\
&= k\frac{\gamma^{(1)}-\gamma^{(2)}}{\gamma^{(1)}-1}\Delta T^{(1)} \\
&= (\gamma^{(1)}-\gamma^{(2)})\Delta e^{(1)} = (\gamma^{(2)}-\gamma^{(1)})\Delta e^{(2)},
\end{aligned} \tag{6.24}
$$

which can not be zero if $\gamma^{(1)} = \gamma^{(2)}$ is not satisfied.

6.3.6 Summary

In this section, we have analyzed the dynamical effects of the projection stage in Godunov-type schemes. The projection process is a purely numerical process due to the nonzero

cell size and time step. However it provides dynamical influence on the flow motion. Based on this, a few anomalous phenomena are well explained, which include post-shock oscillations, density fluctuation around a slip line, and pressure wiggles at a material interface.

6.4 Summary

Quite often, the requirements for robustness and accuracy in the design of a numerical scheme are in conflict with each other: if a scheme is robust, it is unnecessarily diffusive; if a scheme is accurate, it loses robustness. The balance between accuracy and robustness is equivalent to taking a choice between the FDS and FVS schemes.

The difference between the central scheme and the upwinding scheme is mainly on the differences of initial conditions around a cell interface. The use of a nonlinear limiter in modern shock capturing schemes is critically important. The failure of the traditional central scheme is due to the inappropriate initial condition, such as the artificial creation of kinetic energy in the initial data, rather than lack of upwinding in the gas evolution stage. With the same initial condition as the central schemes, even with the upwinding techniques and the use of full characteristics of the Euler equations, the results will still be disastrous. After having a correct initial flow reconstruction, we still need to choose the correct governing equations to solve the IVP. There is no physical reason to believe that the Euler equations give a correct physical representation of the numerical fluid. In order to capture the nonequilibrium flow property, a consistent dissipative mechanism must be included in the gas evolution stage. Due to the use of inviscid fluxes in the Godunov method, spurious solutions are automatically generated in certain flow situations. No perfect Riemann solver for the numerical fluid can be developed from the Euler equations, and the recent intensive attempts to construct hybrid schemes for unsteady compressible flow will not get any significant results if these attempts are only focusing on the modification of the flux functions rather than solving some more fundamental physical equations.

It is commonly agreed that in order to have an accurate Navier-Stokes solution, the property of an exact preservation of isolated contact and shear waves is an important attribute of a convective flux model. This property prevents the contamination of a boundary layer via artificial diffusion. However, as analyzed in section(6.3), the precise preservation of a slip line is also accompanied by an instability in the shock region.

So, to totally avoid dissipation in the convective flux function is not a good choice. In order to get a robust and accurate Navier-Stokes solver, we have to solve the governing equations with correct viscous term directly in the gas evolution stage. In some sense, the BGK method has a more fundamental physical basis than the Godunov method, it could capture both equilibrium and nonequilibrium flows.

Chapter 7

Conclusion

In recent years, the gas-kinetic schemes for unsteady compressible flow computations have become mature. The gas-kinetic scheme (GKS) not only provides a new physical picture about the time evolution of numerical fluid, it also provides an indispensable tool to analyze other shock-capturing schemes, such as the FVS and FDS schemes.

The BGK scheme presented in this lecture is based on the gas-kinetic BGK model, which is distinguished from other gas-kinetic schemes, such as the KFVS scheme, where the collisionless Boltzmann equation is solved in the gas evolution stage. The machinery for the BGK method consists of combining an explicit solution of the BGK model of the Boltzmann equation with the compatibility condition relating moments of the "real" distribution function to those of the equilibrium distribution towards which it continuously tends to relax. The result is a set of nonlinear integral equations for the parameters of the local Maxwell-Boltzmann distribution, or, equivalently, for the moments of this distribution, which are the mass, momentum and energy densities in the gas. The BGK model contains a relaxation time (or mean time between collisions), which decouples the connection between the viscous coefficient and the time step in the smooth flow regions. At the same time, the collision time couples the artificial viscous coefficient with the time step and cell size in the discontinuous flow region to describe the reality that the numerical discontinuous thickness is on the order of cell size rather than the real physical thickness. Theoretically, , the Navier-Stokes equations can be exactly recovered from the BGK model due to the connection between the viscosity coefficient and the relaxation time, where the Euler solutions are the limits when the viscosity is small in the Navier-Stokes solutions. From many numerical test cases, the robustness and accuracy of the BGK method have been fully approved.

The BGK method is different from central and upwinding schemes in the consider-

ations of both the initial condition and the governing equations. The initial condition in the BGK method not only keeps the pointwise values, but also the whole slopes in the left and right sides of a cell interface. Regarding the governing equations, the BGK model is valid for both the Navier-Stokes limit and the free particle transport limit, and could give a reasonable description for both near-equilibrium and nonequilibrium flow situations. Basically, the BGK method combines both the FVS and FDS philosophy in a nonlinear way. Due to the intrinsic dissipative nature in the BGK method, unphysical solutions, such as carbuncle phenomena and odd-even decoupling, have never been observed. Once concerning numerics, we have to always remember one fundamental limit that, for any discontinuous solution, the highest spatial resolution is the cell size Δx and the temporal resolution is the time step Δt. Any subcell resolution will be lost in the discretized space. Therefore, the governing equations for the numerical fluid must be intrinsically dissipative. For example, the numerical shock thickness is on the order Δx and physically it should be proportional to $1/\text{Re} \sim \nu$. So, the viscosity coefficient in the numerical shock region has to be $\nu \sim \Delta x$, which is achieved through the projection dissipation in the Godunov method, rather than the upwinding mechanism. In terms of the Euler equations, $\nu \sim \Delta x$ guarantees that in the discontinuity region any scheme has to be 1st-order for the nonlinear system.

This lecture presents a physical understanding and numerical analysis about the FVS and FDS schemes. The dissipative mechanism in the FVS and FDS schemes has been qualitatively evaluated. To understand the governing equations from discretized scheme is one of the important issues we need to face. It is the starting point to fully understand current schemes and to develop more robust and accurate ones. The artificial viscosity concept in upwinding scheme has been clarified instead of using the words "implicit". From the analysis in chapter 6, it is realized that the carbuncle phenomena and odd-even decoupling is intrinsically rooted in the Godunov method once the inviscid Euler equations are solved in the gas evolution stage. So, a positive suggestion from this lecture is that we have to find and solve viscous governing equations directly in the gas evolution stage, rather than keep on fixing the existing flux function. The modification of the exact Riemann solver and the formulation of hybrid scheme to get more robust and accurate numerical methods are actually a process to solve some other equations rather than the inviscid Euler equations, although it is not explicitly pointed out. The gas-kinetic BGK model probably provides such an equation. The search for perfect Riemann solver will not have any positive conclusion if the inviscid Euler equations are only used to describe

the numerical fluid.

Currently, extensions of gas-kinetic schemes to multiphase, chemical reactive, relativistic, inhomogeneous, semiconductor, phase transition, ..., have attracted much attention. Hopefully, in the near future, the gas-kinetic schemes could provide a useful tool for a wide variety of science and engineering applications.

Bibliography

[1] M. Arora (1996), "Explicit Characteristic-Based High-Resolution Algorithms for Hyperbolic Conservation Laws with Stiff Source Terms", Ph.D Thesis, University of Michigan.

[2] M. Arora and P. Roe (1997), "On Postshock Oscillations Due to Shock Capturing Schemes in Unsteady Flows", *J. Comput. Phys.*, **130**, 25-40.

[3] R. Abgrall (1996), "How to Prevent Pressure Oscillations in Multicomponent Flow Calculations: A Quasi Conservative Approach", J. Comput. Phys., **125**, 150-160.

[4] M. Ben-Artzi and J. Falcovitz (1986), "An Upwind Second-order Scheme for Compressible Duct Flows", SIAM J. Sci. Stat. Comput., **7**, No.3, 744-768.

[5] P.L. Bhatnagar, E.P. Gross, and M. Krook (1954), "A Model for Collision Processes in Gases I: Small Amplitude Processes in Charged and Neutral One-Component Systems", *Phys. Rev.* , **94**, 511-525.

[6] G. Bienkowski (1964), "Propagation of An Initial Density Discontinuity", in the proceeding of Rarefied Gas Dynamics.

[7] J.P. Boris and D.L. Book (1973), "Flux-Corrected Transport, I. SHASTA. A Fluid Transport Algorithm that Works", *J. Comput. Phys.*, Vol.11, 38.

[8] A. Bourlioux (1991), "Numerical Study of Unsteady Detonations", Ph.D Thesis, Princeton University.

[9] C. Cercignani (1988), "The Boltzmann Equation and its Applications", Springer-Verlag.

[10] S. Chapman, and T.G. Cowling, "the Mathematical theory of Non-Uniform Gases", third edition, Cambridge University Press, 1990.

[11] S. Chen and G. doolen, " Lattice Boltzmann Method for Fluid Flows", preprint submitted to *Annual Review of Fluids Mechanics*, (1997).

[12] C. Chiu and X. Zhong (1995), "Simulation of Transient Hypersonic Flow Using the ENO Schemes", AIAA-95-0469, 33rd Aerospace Sciences Meeting and Exhibit.

[13] S.Y. Chou and D. Baganoff (1997), "Kinetic Fluc-Vector Splitting for the Navier-Stokes Equations", *J. Comput. Phys.*, Vol.130, 217-230.

[14] C. K. Chu (1965), *Phys. Fluids*, **8**, 12.

[15] P. Colella (1990), "Multidimensional Upwind Methods for Hyperbolic Conservative Laws", *J. Comput. Phys.*, **87** , 171.

[16] P. Colella, A. Majda, and V. Roytburd, "Theoretical and Numerical Structure for Reacting Shock Waves", *SIAM J. Sci. and Stat. Comput.*, **7**, 1059-1080.

[17] P. Colella and P. Woodward (1984), "The Piecewise Parabolic Method(PPM) for Gas Dynamical Calculations", *J. Comput. Phys.* **54**, 174.

[18] F. Coquel and M-S. Liou (1994), "A Reliable and Efficient Upwind Scheme by a Field by Field Decomposition - Hydrid Upwind Slitting (HUS)", NASA preprint.

[19] J.P. Croissille and P. Villedieu (1992), "Kinetic Flux Splitting Schemes for Hyperbolic Flows", Lecture Notes in Physics, 414, Springer-Verlag.

[20] H. Deconinck, K.G. Powell, P.L. Roe, and R. Struijs (1991), "Multi-dimensional Schemes for Scalar Advection", *AIAA J*, **91**, 1532.

[21] H. Deconinck, P.L. Roe, and R. Struijs (1993), "Multi-dimensional Generalisation of Roe's Flux Difference Splitter for the Euler Equations", *Computers and Fluids*, **22**, 215-222.

[22] S.M. Deshpande (1986), "A Second Order Accurate, Kinetic-Theory Based, Method for Inviscid Compressible Flows," NASA Langley Tech. paper No. 2613.

[23] S.M. Deshpande, A.K. Ghosh, and J.C. Mandal (1989), "Least Squares Weak Upwind Method doe Euler Equations", 89 FM 4, Fluid Mechnics Reports, Dept. of Aerospace Engineering, Indian Institute od Science, Bangalore, India.

[24] J.R. Edwards (1997), "A Low-Diffusion Flux-Splitting Scheme for Navier-Stokes Calculations", *Computers & Fluids*, **26**, No.6, 635-659.

[25] B. Einfeldt (1991), "On Godunov-type Methods for Gas Dynamics", *SIAM J. Numer. Anal.*, **25**, 294-318.

[26] B. Einfeldt, C.D. Munz, P.L. Roe, and B. Sjögreen (1991), "On Godunov-type Methods near Low Density", *J. Comput. phys.* **92**, 273.

[27] T.G. Elizarova and B.N. Chetverushkin (1985), "Kinetic Algorithms for Calculating Gas Dynamic Flows", *J. Comput. Math. and Math. Phys.*, **25**, 1526-1533.

[28] S. Engquist and B. Sjögreen, "Robust Difference Approximations of Stiff Inviscid Detonation Waves", UCLA CAM Report 91-03, 1991.

[29] W. Eppard and B. Grossman (1993), "A multidimensional kinetic-based upwind solver for the Euler equations", AIAA 11th CFD Conference, Orlando, FL.

[30] J. L. Estivalezes and P. Villedieu, "High-order positivity-preserving kinetic schemes for the compressible Euler equations", *SIAM J. Numer. Anal.*, **33**, 2050-2067, 1996.

[31] U. Frisch, B. Hasslacher, and Y. Pomeau, *Phys. Rev. Lett.*, **56**, 1505 (1986).

[32] M. Ghidaoui, K. Xu, and K.L. Cheung (1997), "Analysis of Unsteady Open Channel by the Boltzmann Irreversible Kinetic Theory", submitted to *J. Hydraulic Engineering*.

[33] D. Gilbarg and D. Paolucci (1953), "The Structure of Shock Waves in the Continuum Theory of Fluids", *J. Rational Mech. Anal.*, **2**, 617.

[34] S.K. Godunov (1959), " A Difference Scheme for Numerical Computation of Discontinuous Solutions of Hydrodynamic Equations", *Math. Sbornik*, **47**, 271.

[35] J. Gressier and J.M. Moschetta (1998), " On the Pathological Behavior of Upwind Schemes", AIAA 98-0110, 36th AIAA Aerospace Sciences Meeting and Exhibit.

[36] A.K. Gunstensen, D.H. Rothman, S. Zaleski, and G. Zanetti (1991), "Lattice Boltzmann Model of Immiscible Fluids", *Phys. Rev. A*, **43(8)**, 4320-4327.

[37] S. Harris (1971), "An Introduction to the Theory of the Boltzmann Equation", Holt, Rinehart and Winston, Inc.

[38] X. He and L. Luo (1996), "On the Theory of the Lattice Boltzmann Method. Part I. From the Boltzmann Equation to the Lattice Boltzmann Equation", Preprint.

[39] A. Harten (1983), "On the symmetric form of systems of conservation laws with entropy", *J. of Comput. Phys.*, **49**, 151-164.

[40] A. Harten, B. Engquist, S. Osher, and S. Chakravarthy (1987), "Uniformly High Order Accurate Essentially Non-Oscillatory Schemes, III", *J. Comput. Phys.*, **71**, 231-303.

[41] A. Harten, P. D. Lax, and B. Van Leer (1983), "Upstream differencing and Godunov-type schemes for hyperbolic conservation laws," *SIAM Rev.*, **25**.

[42] C. Hirsch (1990), "The Numerical Computation of Internal and External Flows", John Wiley & Sons, Vol. 1 and 2.

[43] S. Hou, Q. Zou, S. Chen, G. Doolen, A.G. Cogley (1995), "Simulation of cavity flow by the lattice Boltzmann method", *J. Comput. Phys.*, **118**, 329-347.

[44] W.H. Hui (1995), "Generalized Lagrangian Formulation of Computational Fluid Dynamics", Computational Fluid Dynamics Review-1995.

[45] W.H. Hui (1996), "Accurate Computation of Discontinuous Flow – The Role of Coordinates", 2nd Asia CFD Conference, Tokoyo.

[46] W.H. Hui and C.Y. Loh (1992), "A New Lagrangian Method for Steady Supersonic Flow Computation, Part III: Strong Shocks", *J. Comput. Phys.*, **103**, 465-471.

[47] H.T. Huynh (1995), "Accurate Upwind Methods for the Euler Equations", *SIAM J. Numer. Anal.*, **32**, No.5, 1565-1619.

[48] A. Jameson (1993), "Solution of the Euler equations by a multigrid method", *Appl. Math. and Comp.*, **13**, 327-356.

[49] A. Jameson (1995), "Positive Schemes and Shock Modeling for Compressible Flows", *Int. J. Num. Met. in Fluids*, **20**, 743-776.

[50] A. Jameson, W. Schmidt and E. Turkel, "Numerical solutions of the Euler equations by finite volume methods using Runge-Kutta time-stepping schemes", AIAA paper 81-1259, 1981.

[51] G.-S. Jiang and E. Tadmor, *Non-oscillatory central schemes for multidimensional hyperbolic conservation laws*, UCLA Report.

[52] S. Jin (1995), "Runge-Kutta Methods for Hyperbolic Conservation Laws with Stiff Relaxation Terms", *J. Comput. Phys.*, **122**, 51-67.

[53] S. Jin and J. Liu (1996), *The Effects of Numerical Viscosity I: Slowly Moving Shocks*, *J. Comput. Phys.*, **126**, 373-389.

[54] S. Jin and Z.P. Xin (1995), "The Relaxation Schemes for Systems of Conservation Laws in Arbitrary Space Dimension", *Commun. Pure Appl. Math.*, **48**, 235.

[55] S. Kaniel (1988), "A Kinetic Model for the Compressible Flow Equations", *Indiana University Mathematics Journal*, **27**, 537-563.

[56] S. Karni (1994), "Multicomponent Flow Calculations by a Consistent Primitive Algorithm", *J. Comput. Phys.*, **112**, 31-43.

[57] S. Karni and S. Canic (1997), " Computations of Slowly Moving Shocks", *J. Comput. Phys.*, **136**, 132-139.

[58] C.A. Kim (1997) "Robust and Accurate Numerical Methods for High Speed Unsteady Flows", Ph.D Thesis, Department of Mechanical and Aerospace Engineering, Princeton University.

[59] C.A. Kim and A. Jameson (1997), "A Robust and Accurate LED-BGK Solver on Unstructured Adaptive Meshes", accepted by *J. Comput. Phys.*.

[60] C.A. Kim, A. Jameson, L. Martinelli, and K. Xu (1997), "An Accurate LED-BGK Solver on Unstructured Adaptive Meshes", *AIAA-97-0328*.

[61] C.A. Kim, K. Xu, L. Martinelli, and A. Jameson(1997), "Analysis and Implementation of the Gas-kinetic BGK Scheme for Computational Gas Dynamics", *Int. J. Num. Met. in Fluids*, **25**, 21-49.

[62] Kogan, M.N. (1969), "Rarefied Gas Dynamics", Plenum Press, New York.

[63] A.D. Kotelnikov and D.C. Montgomery (1997), "A Kinetic Method for Computing Inhomogeneous Fluid Behavior", *J. Comput. Phys.*, **134**, 364-388.

[64] A.D. Kotelnikov and D.C. Montgomery (1997), "Turbulent Shocks in Composite Materials", submitted to *Phys. Fluids*.

[65] B. Larrouturou (1991), "How to Preserve the Mass Fraction Positive When Computing Compressible Multi-component Flow", *J. Comput. Phys.*, **95**, 59-84.

[66] P.D. Lax (1972), "Hyperbolic Systems of Conservation Laws and the Mathematical Theory of Shock Waves", in *Regional Conference Series Lecture in Applied Math*, **11** (SIAM, Philadelphia).

[67] P.D. Lax and B. Wendroff (1964), "Difference Schemes for Hyperbolic Equations with High Order Accuracy", *Comm. Pure and Applied Mathematics*, **17**, 381-398.

[68] L.D. Landau and E.M. Lofshitz (1987), "Fluid Mechanics", 2nd edition, Pergamon Press.

[69] R.J. LeVeque (1990), "Numerical Methods for Conservation Laws", Birkhäuser Verlag.

[70] R.J. LeVeque and H. Yee (1990), "A Study of Numerical Methods for Hyperbolic Conservation Laws with Stiff Source Terms", *J. Comput. Phys.*, **86**, 187-210.

[71] Levermore, C.D. (1995), "Moments Closure Hierarchies for Kinetic Theory", submitted to *J. of Statistical Physics*.

[72] H.W. Liepmann, R. Narasimha and M.T. Chahine (1962), "Structure of a Plane Shock Layer", *Phys. of Fluids*, **5**, P1313.

[73] H.C. Lin (1995), *Dissipation Additions to Flux-Difference Splitting*, *J. Comput. Phys.*, **117**, 20-27.

[74] D. Lindstrom (1996), *Numerical Computation of Viscous Detonation Waves in Two Space Dimensions*, Report No. 178/1996, Department of Computing, Uppsala University.

[75] M.S. Liou and C.J Steffen (1993), "A New Flux Splitting Scheme", *J. Comput. Phys.*, **107**, 23.

[76] M.S. Liou (1997), "Probing Numerical Fluxes, Positivity, and Entropy-satisfying Property", AIAA 97-2035 (unpublished).

[77] X.-D. Liu and P. D. Lax, *Positive schemes for solving multi-dimensional hyperbolic sysytems of conservation laws*, Courant Maths and Computing Lab. Report, NYU, 95-003 (1995), and submitted to CPAM.

[78] C.Y. Loh and W.H. Hui (1990), "A New Lagrangian Method for Steady Supersonic Flow Computation, Part I: Godunov Scheme", *J. Comput. Phys.*, **89**, 207-240.

[79] S.H. Lui and K. Xu (1997), "Simulation of Cavity Flow by BGK-type Schemes", in preparation.

[80] P. Lyra, K. Morgan, J. Peraire, and J. Peiro (1994), " TVD Algorithms for the Solution of the Compressible Euler Equations on Unstructured Meshes", *Int. J. for Num. Met. in Fluids*, **19**, 827-847.

[81] R.W. MacCormack (1969), "The effect of viscosity in hypervelocity impact gratering", AIAA paper 69-354.

[82] R.W. MacCormack and G.V. Candler (1989), "The solution of the Navier-Stokes equations using Gauss-Seidel Line Relaxation", *Computer & Fluids*, **17**, No.1, P135.

[83] M.N. Macrossan (1989), "The Equilibrium Flux Method for the Calculation of Flows with Non-Equilibrium Chemical Reactions", *J. of Comput. Phys.*, **80**, 204-231.

[84] Macrossan, M.N. and Oliver, R.I. (1993), "A Kinetic Theory Solution Method for the Navier-Stokes Equations", *Int. J. for Num. Method in Fluids*, **17**, 177.

[85] Mandal, J.C. and Deshpande, S.M. (1994), "Kinetic Flux Vector Splitting for Euler Equations", *Computers and Fluids*, **23** , No.2, 447.

[86] J.M. Moschetta and D. Pullin (1997), "A Robust Low Diffusive Kinetic Scheme for the Navier-Stokes/Euler Equations", *J. Comput. Phys.*, **133**, 193-204.

[87] J.M. Moschetta and J. Gressier (1997), "A Cure for the Sonic Point Glitch", submitted to *Int. J. Comput. Fluid Dynamics*.

[88] H.M. Mott-Smith (1951), *Phys. Rev.*, **82**, 885.

[89] H. Nessyahu and E. Tadmor (1990), "Non-Oscillatory Central Differencing for Hyperbolic Conservation Laws", *J. Comput. Phys.*, **87**, 408-463.

[90] J.V. Neumann and R.D. Richtmyer (1950), *J. Appl. Phys.*, **21**, 232.

[91] W.F. Noh (1987), "Errors for Calculations of Strong Shocks Using an Artificial Viscosity and an Artificial Heat Flux", *J. Comput. Phys.*, **72**, 78-120.

[92] S. Osher and J.A. Sethian (1988), "Front Propagating with Curvature-Dependent Speed: Algorithms Based on Hamilton-Jacobi Formulations", *J. Comput. Phys.*, **79**, 12-49.

[93] R.B. Pember (1993), "Numerical Methods for Hyperbolic Conservation Laws with Stiff Relaxation, I. Spurious Solutions", *SIAM J. Applied Math.*,**53**, 1293-1330.

[94] R.B. Pember (1993), "Numerical Methods for Hyperbolic Conservation Laws with Stiff Relaxation, II. Higher-Order Godunov Methods", *SIAM J. Sci. Comput.*, **14**, No.4, 824-859.

[95] B. Perthame (1992), "Second-Order Boltzmann schemes for compressible Euler equation in one and two space dimensions", *SIAM J. Numer. Anal.* **29**, No.1.

[96] B. Perthame and C. W. Shu (1996), "On positivity preserving finite volume schemes for Euler equations", *Numer. Math.*, **73**, 119-130.

[97] B. Perthame and E. Tadmor (1991), "A Kinetic Equation with Kinetic Entropy Functions for Scalar Conservation Laws", *Commun. Math. Phys.* , **36**, 501-517.

[98] K.H. Prendergast and K. Xu (1993), "Numerical Hydrodynamics from Gas-Kinetic Theory", *J. of Comput. Phys.* **109**, 53.

[99] D.I. Pullin (1980), "Direct Simulation Methods for Compressible Inviscid Ideal Gas Flow", *J. Comput. Phys.*, **34**, 231-244.

[100] Quirk, J. (1994), "A Contribution to the Great Riemann Solver Debate", *Int. J. Num. Met. in Fluids*, **18**, no.6.

[101] S.V. Raghurama Rao and S.M. Deshpande (1994), "Peculiar Velocity based Upwind Method for Inviscid Compressible Flows", *Comput. GFluid Dynamics Journal*, **3**, No.4, 415-432.

[102] Reitz, R.D. (1981), "One-Dimensional Compressible Gas Dynamics Calculations Using the Boltzmann Equations", *J. of Comput. Phys.*, **42**, 108-123.

[103] R.D. Richtmyer (1962), "A survey of different methods for non-steady fluid dynamics", NCAR Technical report 63-2, Boulder, Colorado.

[104] T.W. Roberts (1990), "The Behavior of Flux Difference Splitting Near Slowly Moving Shock Waves", *J. Comput. Phys.*, **90**, 141-160.

[105] P.L. Roe (1981), "Approximate Riemann Solvers, Parameter Vectors and Difference Schemes", *J. Comput. Phys.*, **43**, 357.

[106] P.L. Roe (1986), "Characteristic-based schemes for the Euler equations", *Ann. Rev. Fluid Mech.*, **18**, 337.

[107] P.L. Roe (1997), "A Brief Introduction to High-Resolution Schemes", *Upwind and High-Resolution Schemes*, eds. M. Y. Hussaini, B. van Leer and J. van Rosendale.

[108] R.H. Sanders and K.H. Prendergast (1974), "The possible relation of the three-kiloparsec arm to explosions in the galactic nucleus," in *Astrophysical Journal,* **188**.

[109] H. Schlichting (1979), "Boundary-Layer Theory", McGraw-Hill, Inc.

[110] X. Shan and H. Chen (1993), "Lattice-Boltzmann Model for Simulating Flows with Multiple Phases and Components", *Phy. Rev. E*, **47(3)**, 1815-1819.

[111] X. Shan and G. Doolen (1995), "Multicomponent Lattice-Boltzmann Model with Interparticle Interactions", *J. Stat. Phys.*, **81**, 379.

[112] Shu, C.W. and Osher, S. (1989), "Efficient Implementation of Essentially Non-Oscillatory Shock-Capturing Schemes II", *J. Comput. Phys.*, **83**, 32-78.

[113] Sod, G.A. (1978), "A Survey of Several Finite Difference Methods for System of Nonlinear Hyperbolic Conservation Laws", *J. Comput. Phys.*, **27**, 1-31.

[114] J. L. Steger and R. F. Warming (1981), "Flux vector splitting of the inviscid gas-dynamic equations with applications to finite difference methods", *J. Comput. Phys.*, **40**, 263-293.

[115] J.D. Sterling and S. Chen (1996), "Stability Analysis of Lattice Boltzmann Methods", *J. Compu. Phys.*, **123**,196-206.

[116] R.C. Swanson and E. Turkel (1992), "On Central-Difference and Upwind Schemes", *J. Comput. Phys.*, **101**, 297-306.

[117] P.K. Sweby (1984), "High Resolution Schemes Using Flux Limiters for Hyperbolic Conservation Laws", *SIAM J. Numer. Anal.*, **21**.

[118] T. Tang and K. Xu (1997), "Gas-kinetic Schemes fro the Compressible Euler Equations I: Positivity-Preserving Analysis", Preprint.

[119] G. Toth and D. Odstrcil (1996), "Comparison of some flux corrected transport and total variation diminishing numerical schemes for hydrodynamic and magnetohydrodynamic problems", *J. Comput. Phys.*, **128**, 82-100.

[120] E. Toro (1995), "Some IVPs for Which Conservative Methods Fail Misserably", *Proceedings of the Sixth Int. Symp. on CFD*, 1294.

[121] E. Toro (1997), "Riemann Solvers and Numerical Methods for Fluid Dynamics", Springer.

[122] Van Leer, B. (1977), "Towards the Ultimate Conservative Difference Scheme IV, A New Approach to Numerical Convection", *J. Comput. Phys.*, **23**, 276.

[123] B. van. Leer (1982), "Flux-Vector Splitting for the Euler Equations", ICASE report, NO.82-30, September.

[124] B. van. Leer , J.L. Thomas, P.L. Roe and R.W. Newsome (1987), "A Comparison of Numerical Flux Formulas for the Euler and Navier-Stokes Equations", AIAA paper 87-1104.

[125] W.G. Vincenti, C.H. Kruger (1965), " Introduction to Physical Gas Dynamics", Krieger.

[126] P. Woodward and P. Colella (1984), "Numerical Simulations of Two-dimensional Fluid Flow with Strong Shocks", *J. Comput. Phys.*, **54**, 115.

[127] G.H. Xu (1997), "Hydrodynamic and N-body Schemes on an Unstructured, Adaptive Mesh with Application to Cosmological Simulations", *Monthly Notices of Royal Astronomical Society*, **288**, 903-919.

[128] K. Xu (1993), "Numerical Hydrodynamics from Gas-Kinetic Theory", Ph.D. thesis, Columbia University.

[129] K. Xu (1997), "BGK-based Scheme for Multicomponent Flow Calculations", *J. Comput. Phys.*, **134**, 122-133.

[130] K. Xu (1997), "A Gas-Kinetic Scheme for the Euler Equations with Heat Transfer", accepted by *SIAM J. on Scientific Computing*.

[131] K. Xu (1996), "Unsplitting BGK-type Schemes for the Shallow Water Equations", http://www.math.ntnu.no/conservation/, paper 1996-035.

[132] K. Xu and J. Hu (1997), "Projection Dynamics in Godunov-type Schemes I: to the Physical Understanding of Post-Shock Oscillations", http://www.math.ntnu.no/conservation/, paper 1997-001

[133] K. Xu and J. Hu(1997) "Projection Dynamics in Godunov-type Schemes", accepted by *J. Comput. Phys.*.

[134] K. Xu and A. Jameson (1995), "Gas-Kinetic Relaxation (BGK-Type) Schemes for the Compressible Euler Equations", AIAA 95-1736, 12th AIAA CFD Conference.

[135] K. Xu, C. Kim, L. Martinelli,and A. Jameson (1996), "BGK-Based Schemes for the Simulation of Compressible Flow" *Int. J. Comput. Fluid Dynamics*, **7**, 213-235.

[136] K. Xu, L. Martinelli,and A. Jameson (1995), "Gas-Kinetic Finite Volume Methods, Flux-Vector Splitting and Artificial Diffusion", *J. Comput. Phys.*, **120**, 48-65.

[137] K. Xu and K.H. Prendergast (1994), "Numerical Navier-Stokes Solutions from Gas-Kinetic Theory", *J. Comput. Phys.*, **114**, 9-17.

[138] H.Q. Yang and A.J. Przekwas (1992), "A Comparison Study of Advanced Shock-Capturing Schemes Applied to the Burgers' Equation", *J. Comput. Phys.*, **102**, 139.

[139] H.C. Yee and J.L. Shinn (1989), " Semi-implicit and Fully Implicit Shock Capturing Methods for Nonequilibrium Flows", *AIAA J.*, **27**, 299-307.

[140] Ya.B. Zel'dovich and Yu. P. Raizer (1966), "Physics of Shock Waves and High-Temperature Hydrodynamic Phenomena", Academic Press.

Appendix A

Connection between BGK, Navier Stokes and Euler Equations

Derivation of the Navier-Stokes equations from the Boltzmann equation can be found in Kogan[62], Chapman and Cowling[10] and from the Bhatnagar-Gross-Krook equation in Cercignani[9] and Vincenti and Kruger[125] for the case of perfect monotonic gases. Here we reconsider the derivation of the Navier-Stokes and Euler equations from the BGK equation, right from the outset for polyatomic gases.

To derive the Navier-Stokes equations, let $\tau = \epsilon\widehat{\tau}$ where ϵ is a small dimensionless quantity, and suppose that g has a Taylor series expansion about some point x_i, t. Since τ depends on the local thermodynamic variables, and since these depend on the moments of g, we may assume that τ and consequently $\widehat{\tau}$ can be expanded about the point x_i, t. Now consider the formal solution of the BGK equation for f, supposing that g is known, and suppose that $t >> \tau$; *i.e.* that the initial condition were imposed many relaxation times ago. We can then ignore the initial value of f, and, with negligible error, the difference between $t' = 0$ and $t' = -\infty$ in the integral solution of the BGK model. It can be shown from the integral solution that the Taylor series expansion of τ and g about x_i, t may be written as power series in ϵ, and therefore f has an expansion in powers of ϵ. We can find the terms in this expansion from the formal solution for f , or, more easily, by putting

$$f = f_0 + \epsilon f_1 + \epsilon^2 f_2 ...$$

and $\tau = \epsilon\widehat{\tau}$ into the BGK equation directly. Let

$$D_{\mathbf{u}} = \frac{\partial}{\partial t} + u_i \frac{\partial}{\partial x_i},$$

and write the BGK equation as $\epsilon\widehat{\tau} D_{\mathbf{u}} f + f - g = 0$. An expansion of this equation in

powers of ϵ yields

$$f = g - \epsilon\hat{\tau} D_{\mathbf{u}} g + \epsilon^2 \hat{\tau} D_{\mathbf{u}}(\hat{\tau} D_{\mathbf{u}} g) + ...$$

and the compatibility condition, after dividing by $\epsilon\hat{\tau}$, give

$$\int \psi_\alpha D_{\mathbf{u}} g d\Xi = \epsilon \int \psi_\alpha D_{\mathbf{u}}(\hat{\tau} D_{\mathbf{u}} g) d\Xi + \mathcal{O}(\epsilon^2). \tag{A.1}$$

We define $\mathcal{L}_\alpha$ to be the integral on the left side of this equation, and $\mathcal{R}_\alpha$ to be the integral on the right, so that Eq.(A.1) can be written as

$$\mathcal{L}_\alpha = \epsilon \mathcal{R}_\alpha + \mathcal{O}(\epsilon^2). \tag{A.2}$$

We show that these equations give the Euler equations if we drop the term of $\mathcal{O}(\epsilon)$, and the Navier-Stokes equations if we drop terms of $\mathcal{O}(\epsilon^2)$. To simplify the notation, let

$$< \psi_\alpha(...) > \equiv \int \psi_\alpha(...) g d\Xi,$$

and consider

$$\begin{aligned} \mathcal{L}_\alpha &\equiv \int \psi_\alpha D_{\mathbf{u}} g d\Xi \\ &= \int \psi_\alpha (g_{,t} + u_l g_{,l}) d\Xi \\ &= < \psi_\alpha >_{,t} + < \psi_\alpha u_l >_{,l}, \end{aligned}$$

since ψ_α is independent of x_i and t. Now Eq.(A.2) shows that

$$< \psi_\alpha >_{,t} + < \psi_\alpha u_l >_{,l} = \mathcal{O}(\epsilon) \tag{A.3}$$

for all α, and therefore, in reducing $\mathcal{R}_\alpha$ on the right side of Eq.(A.2), which is already $\mathcal{O}(\epsilon)$, we can drop $\mathcal{O}(\epsilon)$ quantities and their derivatives. Put differently, we first reduce the $\mathcal{L}_\alpha$ to find that $\mathcal{L}_\alpha = 0$ ($\alpha = 1, 2, ...5$) is identical to the Euler equations; then we use the fact that $\mathcal{L}_\alpha$ is $\mathcal{O}(\epsilon)$ to simplify $\mathcal{R}_\alpha$ — the result is the Navier-Stokes equations.

The expression for $\mathcal{R}_\alpha$ contains time derivatives which must be eliminated. We have, from the definition of $\mathcal{R}_\alpha$,

$$\begin{aligned} \mathcal{R}_\alpha &= \hat{\tau}[< \psi_\alpha >_{,tt} + 2 < \psi_\alpha u_k >_{,tk} + < \psi_\alpha u_k u_l >_{,lk}] \\ &\quad + \hat{\tau}_{,t}[< \psi_\alpha >_{,t} + < \psi_\alpha u_l >_{,l}] + \hat{\tau}_{,k}[< \psi_\alpha u_k >_{,t} + < \psi_\alpha u_k u_l >_{,l}]. \end{aligned} \tag{A.4}$$

According to Eq.(A.3) the coefficient of $\widehat{\tau}_{,t}$ in this expression is $\mathcal{O}(\epsilon)$, and can therefore be neglected. As for the first term, consider

$$\begin{aligned}\frac{\partial}{\partial t}[< \psi_\alpha >_{,t} + < \psi_\alpha u_k >_{,k}] &= < \psi_\alpha >_{,tt} + < \psi_\alpha u_k >_{,kt} \\ &= \mathcal{L}_{\alpha,t} = \mathcal{O}(\epsilon)\end{aligned}$$

Then the first term in Eq.(A.4) is

$$\widehat{\tau}\frac{\partial}{\partial x_k}[< \psi_\alpha u_k >_{,t} + < \psi_\alpha u_k u_l >_{,l}] + \mathcal{O}(\epsilon),$$

which can be combined with the third term to give

$$\mathcal{R}_\alpha = \frac{\partial}{\partial x_k}\{\widehat{\tau}[< \psi_\alpha u_k >_{,t} + < \psi_\alpha u_k u_l >_{,l}]\} + \mathcal{O}(\epsilon),$$

which eliminates the second time derivatives from $\mathcal{R}_\alpha$; the first time derivatives will be removed by using $\mathcal{L}_\alpha \simeq 0$.

The Euler equations follow from putting $\mathcal{L}_\alpha = 0$. To see this, consider

$$\mathcal{L}_1 = < \psi_1 >_{,t} + < \psi_1 u_k >_{,k} = \rho_{,t} + (\rho U_k)_{,k},$$

since $\psi_1 = 1$; $\mathcal{L}_1 = \mathcal{O}(\epsilon)$ is the continuity equation if we neglect $\mathcal{O}(\epsilon)$. For $\alpha = 2, 3, 4$, it is convenient to define $\mathcal{L}_i$ and $\mathcal{R}_i$ such that $i = \alpha - 1$ and to let $w_i = u_i - U_i$. Then

$$\mathcal{L}_i = < u_i >_{,t} + < u_i u_k >_{,k} = (\rho U_i)_{,t} + [\rho U_i U_k + < w_i w_k >]_{,k},$$

since all moments of g odd in w_l vanish. The pressure tensor is defined by

$$p_{ik} = < w_i w_k > \equiv p\delta_{ik}.$$

(The diagonal form of p_{ik} is obvious from the fact that g can be written as a function of w_k^2.) Then

$$\mathcal{L}_i = (\rho U_i)_{,t} + (\rho U_i U_k + p\delta_{ik})_{,k} \tag{A.5}$$

and $\mathcal{L}_i = 0$ is the Euler equation for the conservation of momentum. For the energy equation we have

$$\mathcal{L}_5 = \frac{1}{2}< {u_n}^2 + \xi^2 >_{,t} + \frac{1}{2}< u_l({u_n}^2 + \xi^2) >_{,l}$$

or

$$\mathcal{L}_5 = \left(\frac{1}{2}\rho {U_n}^2 + \frac{K+3}{2}p\right)_{,t} + \left(\frac{1}{2}\rho U_k {U_n}^2 + \frac{K+5}{2}pU_k\right)_{,k}.$$

Setting $\mathcal{L}_5 = 0$ gives the energy equation in the absence of dissipation.

We proceed to eliminate the time derivatives from $\mathcal{R}_\alpha$ using the fact that $\mathcal{L}_\alpha = \mathcal{O}(\epsilon)$. For $\alpha = 1$, we have

$$\mathcal{R}_1 = \{\widehat{\tau}[< u_k >_{,t} + < u_k u_l >_{,l}]\}_{,k}$$

The quantity in square brackets is $\mathcal{L}_k$, which implies that $\mathcal{R}_1 = \mathcal{O}(\epsilon)$, and $\mathcal{L}_1 = \epsilon\mathcal{R}_1 = \mathcal{O}(\epsilon^2)$. Hence, to the order we have retained, $\mathcal{R}_1 = 0$ and $\mathcal{L}_1 = 0$, or

$$\rho_{,t} + (\rho U_k)_{,k} = 0, \tag{A.6}$$

which is the continuity equation. We can use the continuity equation to simplify the momentum equations and the energy equation. Multiplying the continuity equation by U_i and the subtracting the result from $\mathcal{L}_i$ gives, according to Eq.(A.5),

$$\mathcal{L}_i = \rho U_{i,t} + \rho U_k U_{i,k} + p_{,i} + \mathcal{O}(\epsilon^2). \tag{A.7}$$

For $\mathcal{L}_5$, we group the terms as follows:

$$\begin{aligned}\mathcal{L}_5 &= \frac{1}{2}{U_n}^2[\rho_{,t} + (\rho U_k)_{,k}] + \rho U_n U_{n,t} + \rho U_k U_n U_{n,k} + U_k p_{,k} \\ &\quad + \frac{K+3}{2}[p_{,t} + U_k p_{,k}] + \frac{K+5}{2}pU_{k,k}\end{aligned}$$

The first term is $\frac{1}{2}{U_n}^2\mathcal{L}_1$ which is $\mathcal{O}(\epsilon^2)$, and the next three are $U_n\mathcal{L}_n$, and are therefore $\mathcal{O}(\epsilon)$. Then

$$\mathcal{L}_5 = \frac{K+3}{2}[p_{,t} + U_k p_{,k}] + \frac{K+5}{2}pU_{k,k} + U_n\mathcal{L}_n. \tag{A.8}$$

We can drop the last term in the reduction of $\mathcal{R}_\alpha$, but the term $U_n\mathcal{L}_n$ must be retained in the reduction of $\mathcal{L}_5$ when we finally write $\mathcal{L}_5 = \epsilon\mathcal{R}_5$ in detail.

For the right sides of the momentum equations, consider $\mathcal{R}_j = (\widehat{\tau}F_{jk})_{,k}$, where

$$F_{jk} \equiv < u_j u_k >_{,t} + < u_j u_k u_l >_{,l}$$

or

$$\begin{aligned}F_{jk} &= U_j[(\rho U_k)_{,t} + (\rho U_k U_l + p\delta_{kl})_{,l}] \\ &\quad + \rho U_k U_{j,t} + (\rho U_k U_l + p\delta_{kl})U_{j,l} \\ &\quad + (p\delta_{jk})_{,t} + (U_l p\delta_{jk} + U_k p\delta_{jl})_{,l},\end{aligned}$$

using the fact that all moments odd in w_k vanish. The term in square brackets multiplying U_j is $\mathcal{L}_k$, *i.e.* it is $\mathcal{O}(\epsilon)$, and can therefore be ignored. Then, after gathering terms with coefficients U_k and p, we have

$$F_{jk} = U_k[\rho U_{j,t} + \rho U_l U_{j,l} + p_{,j}] + p[U_{k,j} + U_{j,k} + U_{l,l}\delta_{jk}] + \delta_{jk}[p_{,t} + U_l p_{,l}].$$

The coefficient of U_k is $\mathcal{L}_j$, according to Eq.(A.7), and can therefore be neglected. To eliminate $p_{,t}$ from the last term we use the Eq.(A.8) for $\mathcal{L}_5$; this gives

$$p_{,t} + U_k p_{,k} = -\frac{K+5}{K+3} p U_{k,k} + \mathcal{O}(\epsilon).$$

Finally, we decompose the tensor $U_{k,j}$ into its dilation and shear parts in the usual way, which gives

$$F_{jk} = p[U_{k,j} + U_{j,k} - \frac{2}{3}U_{l,l}\delta_{jk}] + \frac{2}{3}(\frac{K}{K+3})pU_{l,l}\delta_{jk}. \tag{A.9}$$

The last term is due to bulk viscocity; it vanishes, as it should, for $K = 0$, since the physical mechanism for bulk viscosity involves energy sharing between translational and internal degrees of freedom of the molecules, and $K = 0$ corresponds to a monoatomic ($\gamma = \frac{5}{3}$) gas.

For $\alpha = 5$, we write

$$\mathcal{R}_5 = (\widehat{\tau} N_k)_{,k} \tag{A.10}$$

where

$$N_k \equiv < u_k \frac{({u_n}^2 + \xi^2)}{2} >_{,t} + < u_k u_l \frac{({u_n}^2 + \xi^2)}{2} >_{,l}$$

which can be written as ${N_k}^{(1)} + {N_k}^{(2)}$, where

$${N_k}^{(1)} = [U_k \frac{< {u_n}^2 + \xi^2 >}{2}]_{,t} + [U_k < u_l \frac{({u_n}^2 + \xi^2)}{2} >]_{,l}$$

and

$${N_k}^{(2)} = < w_k \frac{{u_n}^2 + \xi^2}{2} >_{,t} + < w_k u_l \frac{({u_n}^2 + \xi^2)}{2} >_{,l}$$

For ${N_k}^{(1)}$ we have

$$\begin{aligned} {N_k}^{(1)} &= U_k[\frac{< {u_n}^2 + \xi^2 >_{,t}}{2} + \frac{< u_l({u_n}^2 + \xi^2) >_{,l}}{2}] \\ &\quad + [\frac{1}{2}\rho {U_n}^2 + \frac{K+3}{2}p]U_{k,t} + \frac{1}{2}\rho U_l[{U_n}^2 + \frac{(K+5)p}{\rho}]U_{k,l}. \end{aligned}$$

The coefficient of U_k in the equation above is $\mathcal{L}_5$, and can therefore be neglected, and the remaining terms can be rewritten as

$$[\frac{1}{2}\rho {U_n}^2 + \frac{K+3}{2}p][U_{k,t} + U_l U_{k,l}] + pU_l U_{k,l},$$

or, using the fact that $\mathcal{L}_k = \mathcal{O}(\epsilon)$,

$${N_k}^{(1)} = -[\frac{1}{2}{U_n}^2 + \frac{K+3}{2}\frac{p}{\rho}]p_{,k} + pU_l U_{k,l}.$$

For ${N_k}^{(2)}$, remembering that moments odd in w_k vanish, we have

$$\begin{aligned} {N_k}^{(2)} &= < U_n w_n w_k >_{,t} + < U_l U_n w_n w_k >_{,l} \\ &\quad + \frac{1}{2} < {U_n}^2 w_k w_l >_{,l} + \frac{1}{2} < w_k w_l ({w_n}^2 + \xi^2) >_{,l}, \end{aligned}$$

or

$${N_k}^{(2)} = (pU_k)_{,t} + (pU_k U_l)_{,l} + \frac{1}{2}({U_n}^2 p)_{,k} + \frac{K+5}{2}(\frac{p^2}{\rho})_{,k}.$$

This result can rewritten as

$$\begin{aligned} {N_k}^{(2)} &= p[U_{k,t} + U_l U_{k,l} + U_k U_{l,l} + U_l U_{l,k}] \\ &\quad + U_k(p_{,t} + U_l p_{,l}) + \frac{1}{2}{U_l}^2 p_{,k} + \frac{K+5}{2}(\frac{p^2}{\rho})_{,k}, \end{aligned}$$

and the time derivatives can be removed by using $\mathcal{L}_k = \mathcal{O}(\epsilon)$, and $\mathcal{L}_5 = \mathcal{O}(\epsilon)$, neglecting $\mathcal{O}(\epsilon)$, since we are evaluating $\mathcal{R}_5$. Finally, ${N_k}^{(1)} + {N_k}^{(2)}$ can be combined to give (after some algebra)

$$N_k = \frac{K+5}{2}p(\frac{p}{\rho})_{,k} + p[-\frac{2}{K+3}U_k U_{l,l} + U_l(U_{k,l} + U_{l,k})]. \tag{A.11}$$

All time derivatives have now been removed from $\mathcal{R}_\alpha$ (for all α). The remaining steps in the derivation of the Navier-Stokes equations may be summarized briefly as follows:

1). Drop $\mathcal{O}(\epsilon^2)$ in Eq.(A.2).

2). Combine ϵ and $\widehat{\tau}$ to recover $\tau = \epsilon\widehat{\tau}$.

3). Define the stress tensor

$${\sigma'}_{jk} = \eta[U_{j,k} + U_{k,j} - \frac{2}{3}U_{l,l}\delta_{jk}] + \varsigma U_{l,l}\delta_{jk},$$

where

$$\eta = \tau p$$

and

$$\varsigma = \frac{2}{3}\frac{K}{K+3}\tau p$$

are the dynamic viscosity and second viscosity coefficients respectively.

4). From Eq.(A.7) for $\mathcal{L}_j$ and Eq.(A.9) for F_{jk}, it follows that $\mathcal{L}_j = \epsilon\mathcal{R}_j$ may now be written as

$$\rho U_{j,t} + \rho U_k U_{j,k} + p_{,j} = \sigma'_{jk,k},$$

which is the Navier-Stokes equation.

5). The energy equation follows from $\mathcal{L}_5 = \epsilon\mathcal{R}_5$ by using Eq.(A.8), (A.7) and (A.6) to write $\mathcal{L}_5$ in detail, and using Eq.(A.10) and (A.11) for $\mathcal{R}_5$. The result is

$$\frac{K+3}{2}(p_{,t} + U_k p_{,k}) - \frac{K+5}{2}p(\rho_{,t} + U_k\rho_{,k}) = (\kappa T_{,k})_{,k} + (U_l\sigma'_{lk})_{,k},$$

where

$$\kappa = \frac{K+5}{2}\frac{k}{m}\tau p$$

is the thermal conductivity, k is the Boltzmann constant, m is the mass of a molecule and T is the temperature. The equations can be written in terms of γ instead of K by using $K = (5-3\gamma)/(\gamma-1)$ for 3-Dimensional gas flow.

Appendix B

Moments of the Maxwellian Distribution Function

In the gas-kinetic scheme, we need to evaluate moments of the Maxwellian distribution function with bounded and unbounded integration limits.

In the 1-D case, the Maxwellian distribution function is

$$g = \rho(\frac{\lambda}{\pi})^{\frac{K+1}{2}} e^{-\lambda((u-U)^2+\xi^2)},$$

where ξ has K degrees of freedom. With the introduction of the following notation,

$$\rho < ... >= \int\int_{-\infty}^{+\infty} (...) g du d\xi,$$

the general integration formula becomes

$$< u^n \xi^l >=< u^n >< \xi^l >,$$

where n is an integer, and l is an even integer (owing to the symmetrical property of ξ). The moments of $< \xi^l >$ are:

$$< \xi^2 >= (\frac{K}{2\lambda})$$

$$< \xi^4 >= (\frac{3K}{4\lambda^2} + \frac{K(K-1)}{4\lambda^2})$$

The values of $< u^n >$ depend on the integration limits. If the limit is from $-\infty$ to $+\infty$, we have

$$< u^0 >= 1,$$

$$< u >= U,$$

$$< u^2 >= (U^2 + \frac{1}{2\lambda}),$$

$$< u^3 >= (U^3 + 1.5\frac{U}{\lambda}),$$

$$< u^4 >= (U^4 + \frac{3U^2}{\lambda} + \frac{0.75}{\lambda^2}),$$

$$< u^5 >= (U^5 + 5\frac{U^3}{\lambda} + 3.75\frac{U}{\lambda^2}),$$

$$< u^6 >= (U^6 + 7.5\frac{U^4}{\lambda} + 11.25\frac{U^2}{\lambda^2} + \frac{1.875}{\lambda^3}),$$

$$...$$

$$< u^{n+2} >= U < u^{n+1} > + \frac{n+1}{2\lambda} < u^n > .$$

If the integration limit for u is from 0 to $+\infty$, such as

$$\rho < ... >_{u>0} = \int\int_0^{+\infty} (...) g du d\xi,$$

or from $-\infty$ to 0,

$$\rho < ... >_{u<0} = \int\int_{-\infty}^{0} (...) g du d\xi,$$

the error function and the complementary error function have to be used. The moments for u^n in the half space are,

$$< u^0 >_{>0} = \frac{1}{2}\mathrm{erfc}(-\sqrt{\lambda}U)$$

$$< u >_{>0} = U < u^0 >_{>0} + \frac{1}{2}\frac{e^{-\lambda U^2}}{\sqrt{\pi\lambda}}$$

$$...$$

$$< u^{n+2} >_{>0} = U < u^{n+1} >_{>0} + \frac{n+1}{2\lambda} < u^n >_{>0} .$$

Similarly,

$$< u^0 >_{<0} = \frac{1}{2}\mathrm{erfc}(\sqrt{\lambda}U)$$

$$< u >_{<0} = U < u^0 >_{<0} - \frac{1}{2}\frac{e^{-\lambda U^2}}{\sqrt{\pi\lambda}}$$

...

$$< u^{n+2} >_{<0} = U < u^{n+1} >_{<0} + \frac{n+1}{2\lambda} < u^{n} >_{<0} .$$

In the 2-D and 3-D cases, the equilibrium state can be decomposed into the form of the 1-D case, and the above integration formula can be used too. For example, in the 3-D case we have

$$\rho < ... >= \int (...) g du dv dw d\xi,$$

and

$$< u^m v^n w^p \xi^l >=< u^m >< v^n >< w^p >< \xi^l >,$$

where the integration limits can be the whole or half velocity space.